Modeling and measurement of the b-jet nuclear modification factor in p-Pb collisions at 5.02 Tev with ALICE at the LHC

Hadi Hassan

Communauté UNIVERSITÉ Grenoble Alpes

الجامعة اللبنانية
UNIVERSITE LIBANAISE

THÈSE

Pour obtenir le grade de

DOCTEUR DE LA COMMUNAUTE UNIVERSITE GRENOBLE ALPES

préparée dans le cadre d'une cotutelle entre la Communauté Université Grenoble Alpes et l'Université Libanaise

Spécialité : **Physique Subatomique et Astroparticules**
Arrêté ministériel : le 6 janvier 2005 – 25 mai 2016

Présentée par

Hadi HASSAN

Thèse dirigée par **Ingo Schienbein** et **Rachid Guernane**
codirigée par **Haitham Zaraket**

Préparée au sein des **Laboratoire de Physique Subatomique et de Cosmologie** et **Multi Displinary Physics Lab**

dans les **École Doctorale de Physique** et **École Doctorale des Sciences et de Technologie**

Modélisation et mesure des facteurs de modification nucléaire des jets issus de quarks beaux dans les collisions p-Pb à 5.02 TeV avec l'expérience ALICE auprès du LHC

Thèse soutenue publiquement le **19 Février 2019**,
devant le jury composé de :

Monsieur Tatsuya CHUJO
Professeur, Université de Tsukuba, Membre
Monsieur Benoît CLÉMENT
Maître de Conférences, Université Grenoble Alpes, Invité
Monsieur Johann COLLOT
Professeur, Université Grenoble Alpes, Président
Monsieur Cvetan CHESKOV
Chargé de recherche, IPNL, Rapporteur
Monsieur Rachid GUERNANE
Chargé de recherche, LPSC, Membre
Madame MinJung KWEON
Professeur, Université Inha, Rapporteur
Monsieur Stéphane PEIGNÉ
Chargé de recherche, Subatech, Membre
Monsieur Yves SCHUTZ
Directeur de Recherche, IPHC, Membre
Monsieur Haitham ZARAKET
Professeur, Université Libanaise, Membre

Modeling and measuring the b-jet nuclear modification factor in p–Pb at $\sqrt{s_{\mathrm{NN}}} = 5.02$ TeV with ALICE experiment at the LHC

Hadi Hassan

Supervisor: Ingo Schienbein
Haitham Zaraket
Rachid Guernane

Ecole Doctorale de physique
Université Grenoble Alpes

EDST Liban
Université Libanaise

This dissertation is submitted for the degree of
Doctor of Philosophy

LPSC Grenoble

February 2019

Abstract

In Pb–Pb collisions at the LHC, a hot and dense medium of deconfined quarks and gluons is formed, the so-called Quark-Gluon Plasma (QGP). The QGP is conjectured to be the state of matter of the early Universe up to few microseconds after the Big Bang and may still exist in the core of neutron stars. One of the most striking signatures of the QGP formation in heavy-ion collisions is the suppression of jet production. This phenomenon, called jet quenching, is ascribed to the energy lost by the initial parton while traveling through the QGP medium.

In the last two decades, many theoretical developments of the theory of jet quenching have been formulated within pQCD.

The main energy loss mechanisms proposed in the literature are attributed to radiative and collisional processes. Another kind of energy loss is developed in this work comprises a background field induced radiative energy loss which additionally includes scattering effects. Under the suggested model, a fast parton propagating through the medium will feel the effect of the color magnetic and the color electric fields while undergoing multiple scatterings with the particles in the medium.

Besides, theoretical models predict that energy loss depends on the color charge and mass of the hard-scattered parton traversing the medium. Such mass dependence can be studied by measuring the production of hadrons and jets containing heavy-quarks in pp, p–Pb and Pb–Pb collisions at the LHC.

In this thesis report, a new model for the medium is presented, which is described as a collection of static colored scattering centers in the presence of a chromomagnetic field, together with the description of the related energy loss mechanism. The ALICE measurement of b-jet production cross section in pp and p–Pb collisions at $\sqrt{s_{\mathrm{NN}}} = 5.02$ TeV and nuclear modification factor using an impact parameter based tagger is also presented.

Résumé

Dans les collisions Pb–Pb au LHC, un milieu chaud et dense formé de quarks et de gluons déconfinés est formé, communément appelé Plasma de Quarks et de Gluons (PQG). Le PQG est l'état hypothétique de l'univers primordial quelques microsecondes après le Big Bang et constituerait encore à ce jour le coeur des étoiles à neutrons. Une des signatures les plus frappantes de l'occurrence du PQG lors de collisions d'ions lourds est la suppression des jets. Ce phénomène appelé étouffement des jets, est attribué au mécanisme de perte d'énergie du parton à l'origine du jet lors de son trajet au travers du milieu formé par le PQG.

Les deux dernières décennies ont vu l'émergence d'une formulation théorique du phénomène d'étouffement des jets dans le cadre de la ChromoDynamique Quantique. La perte d'énergie étant le plus fréquemment attribuée dans la littérature à des processus radiatifs et collisionnels. Un nouveau mécanisme de perte d'énergie à été étudié dans ce travail de thèse qui outre la description des effets de diffusions multiples, met en oeuvre une perte d'énergie radiative induite par un champ chromomagnétique, de sorte qu'un parton rapide se propageant au travers du milieu ressentira l'effet des champs magnétique et de couleur tout en subissant des diffusions multiples avec les particules du milieu.

De plus, les modèles théoriques prédisent une dépendance de la perte d'énergie avec la charge de couleur et la masse du parton issu d'une diffusion à grand transfert d'impulsion lors de sa traversée du milieu. Une telle dépendance en masse peut être étudiée en mesurant la production de hadrons et de jets contenant des quarks lourds dans les collisions pp, p–Pb et Pb–Pb au LHC.

Dans cette thèse, un modèle original du milieu est présenté, décrit comme un ensemble de centres de diffusion statiques colorés en présence d'un champ chromomagnétique, de même qu'une description du mécanisme de perte d'énergie associé. Enfin, la mesure de la production de jets issus de quarks beaux avec le détecteur ALICE dans les colllsions pp et p–Pb à l'énergie de 5.02 TeV au LHC à l'aide d'une méthode d'étiquetage utilisant le paramètre d'impact des traces est présenté dans cette thèse.

Acknowledgements

First and foremost I would like to express my thanks to God because of His love and strength that He has given to me to finish this thesis report. I do thank for His blessings to my daily life, good health, healthy mind and good ideas.

The joint PhD I had between the Lebanese University and Grenoble University, and also at the LPSC in Grenoble and with ALICE collaboration at CERN was a great chance for learning and professional development. Therefore, I consider myself as a very lucky individual as I was provided with an opportunity to be a part of it. I am also grateful for having a chance to meet so many wonderful people and professionals who led me though this thesis.

Then, I would like to thank to my supervisors: Prof. Ingo Schienbein and Prof. Haitham Zaraket and my co-supervisor Dr. Rachid Guernane for the valuable guidance and advice. They inspired me greatly to work, commit in this PhD. Their willingness to motivate me contributed tremendously to my thesis.

Special thanks to all my friends for sharing their experiences, time and commitment especially during finishing this PhD. I am grateful because I have a lot of friends helping and supporting me throughout the course of completing this PhD.

Thanks to my parents and to my family, who have been there with me all along the way. They have been supportive of every choice I have made, and forgiving of every mistake I have made.

I am also thankful for the Lebanese CNRS and to the Lebanese university for providing me with the scholarship that allowed me to do this thesis and produce these results.

Table of contents

List of figures

List of tables

Introduction

Our universe was created in an event called the Big-Bang. The Big Bang theory is a cosmological model which states that few microseconds after the Big Bang, the universe was in a very high-density and high-temperature state roughly 13.7 billion years ago. The main fundamental constituents of this high-density and high-temperature state were the deconfined quarks, anti-quarks and gluons, this state of matter was called the quark-gluon plasma (QGP). After the QGP the universe starts to cool down and the quarks and gluons began to hadronize and then baryogensis and nucleosynthesis started.

This QGP can be created In relativistic heavy-ion collisions at RHIC and at the LHC. After the QGP cools down the particles hadronize and the final state particles can be seen by a particle detector (Fig. 1). So heavy-ion collisions can be used as a tool to create and study the quark gluon plasma.

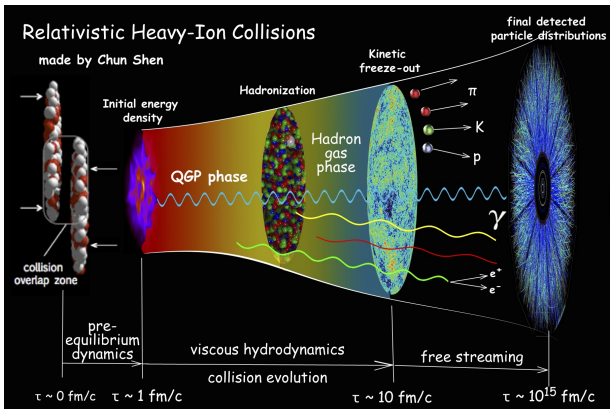

Fig. 1 The QGP evolution in heavy-ion collision [1].

One of the most important signatures for the QGP formation in heavy-ion collisions is jet quenching [2] [3] [4]. Jet quenching is the suppression of the particle and jet production in heavy-ion collisions compared to pp collisions.

A jet [5] is a narrow cone of particles which are produced in the hadronization (process of the formation of hadrons out of quarks and gluons) and fragmentation of the hard scattered partons see Fig. 2. Interactions of hard-scattered partons with the colored medium created in a heavy-ion collision may lead to in-medium partonic energy loss, resulting in a suppression of jet production at high p_T in heavy-ion collisions with respect to jets in pp collisions where the QGP is not produced. So the investigation of jet suppression at high p_T and internal structure modification (nuclear modification) provides information about the parton energy loss and thus on the QGP properties (transport coefficient $\hat{q}$, medium density, etc..). The transport coefficient $\hat{q}$ encodes the medium

scattering power of the medium. It is the transverse momentum squared transferred to the particle per unit path length.

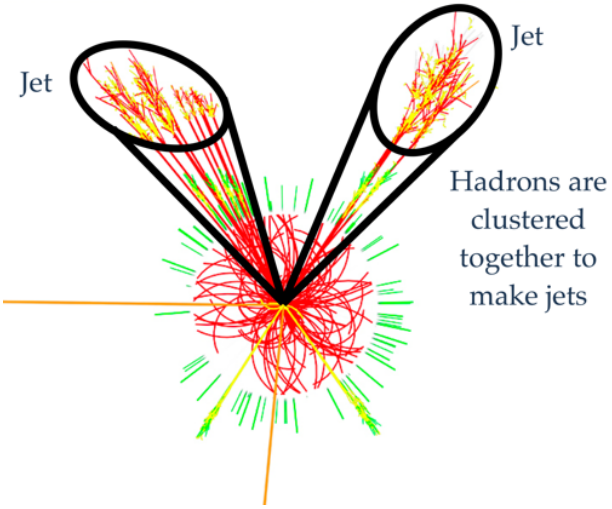

Fig. 2 Simulated event from ATLAS Experiment © 2011 CERN.

Investigating the QGP medium in heavy-ion collisions is the main goal of the ALICE experiment at the LHC. Its capabilities allows to perform this study using different probes including reconstructed jets and identified particles in a broad range of momentum.

Heavy quarks (charm and beauty) are excellent probes for the study of the QGP, because they are mainly produced in the hard scattering in a short time scale before the QGP formation, meaning the heavy quark number after the initial hard scattering is essentially fixed. Also their production cross section is calculable with pQCD theoretical models (FONLL [6, 7], GM-VFNS [8, 9], POWHEG [10], ...) and they can be experimentally tagged using special tagging algorithms. Tagging the heavy-flavor (HF)-jets allows for the study of the mass and the color charge dependence of parton energy loss. Figure 3 shows the mass dependence of the nuclear modification factor R_{AA}. As can be seen for very high momentum $p_T > 50$ GeV/c R_{AA} for light-flavor jet and b-jet is very similar, while at low momentum $p_T < 50$ GeV/c the R_{AA} for the b-jet is larger than that of the light-flavor jet.

Figure 3 also shows that R_{AA} is dependent on the mass of the parton in the low momentum region $p_T < 60$ GeV/c, which is the ALICE capability since ALICE can track the charged particle down to a very low momentum ($p_T > 0.15$ GeV/c). Unlike ATLAS and CMS where they study the high momentum region $p_T > 60$ GeV/c.

In this thesis, the study of the b-jet production and the nuclear modification factor in pp and p–Pb collisions at a center of mass energy $\sqrt{s_{\mathrm{NN}}} = 5.02$ TeV is presented. This thesis also presents a theoretical calculation for the partonic energy loss in QGP medium by the effect of the background field with scattering.

This thesis is arranged as follows: Chapter 1 gives a brief introduction about the standard model of particle physics, the QCD phase diagram, an introduction to heavy-ion collisions, partonic energy loss (jet quenching) and about heavy-flavor production. Chapter 3 presents the ALICE detector and its sub-detectors and the softwares that were used in this analysis. Chapter 2 represents a new model for the partonic energy loss in QGP medium. Chapter 4 shows the data sets used in this analysis and the event selection. Also the same chapter gives an overview about the b-jet tagging algorithms used in the

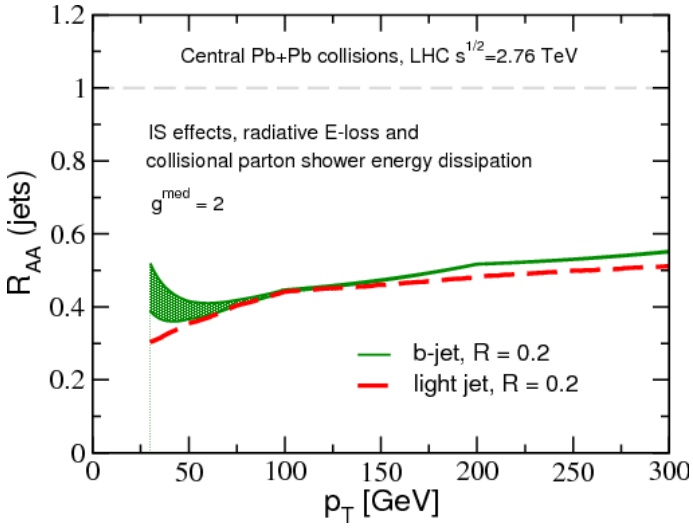

Fig. 3 The mass dependence of R_{AA} [11].

literature. Chapter 4 also shows the ways used for correcting the b-jet spectrum until finding the final jet spectrum in pp and p–Pb collisions. Chapter 5 reveals the systematic uncertainties of the current study for p–Pb and pp collisions. And the final result, the b-jet production cross section and the nuclear modification factor of the b-jet R^b_{pPb} is shown in Chapter 6.

Chapter 1

Theoretical background

In this chapter, an introduction to the standard model of particle physics will be shown, the QCD phase diagram and the QGP properties will be presented and an overview of the the particle production in heavy-ion collisions and in particular of heavy-flavor particles at the LHC will be presented.

1.1 Standard Model

Our understanding of the building blocks of matter in the universe is governed by the Standard model (SM) of particle physics [12]. This model describes the fundamental interactions of elementary particles in the universe. It is not complete because it doesn't describe the gravitational interaction, but it has predicted several properties of weak neutral currents and the W and Z bosons with great accuracy.

The SM is a combination of related theories developed over the 20th century including Quantum Electrodynamics (QED), the Glashow-Weinberg-Salam theory of electro-weak processes and Quantum Chromodynamics (QCD). The SM consists of three kinds of elementary particles, quarks, leptons (fermions) and the gauge bosons which are the mediators of the different interactions. An overview of these particles is given in Fig. 1.1. Fermions are half "$\frac{1}{2}$" spin particles, while bosons are integer "1" spin particles except for the Higgs which has "0" spin.

The QED is the theory of electromagnetic interaction, it describes the interaction of the electrically charged particles by the exchange of photons, the carrier of the electromagnetic force. It is responsible for the repulsion of electrons or the orbiting of an electron around the nucleus. Photons are massless, uncharged, and have an unlimited range of interaction.

Electric charge is the property of matter that generates the electric and magnetic phenomena (known as electromagnetism). Charge is quantized, i.e it can only take discrete values. Particles that exist freely (the electron, muon, and tau) carry multiples of the elementary charge ($-1e$), while quarks carry fractions of the elementary charge ($+\frac{2}{3}e$ or $-\frac{1}{3}e$). We don't measure directly fractional charge because quarks always tend to bind together in groups in which the total charge is an integer times the elementary charge.

The QCD is the theory of strong interaction, it describes the interaction of colored particles by the exchange of gluons. This is also called the strong nuclear force since it causes the force in the nucleus that stronger than the electromagnetic force, without it the nucleus would explode into protons and neutrons. The colored particles are the quarks

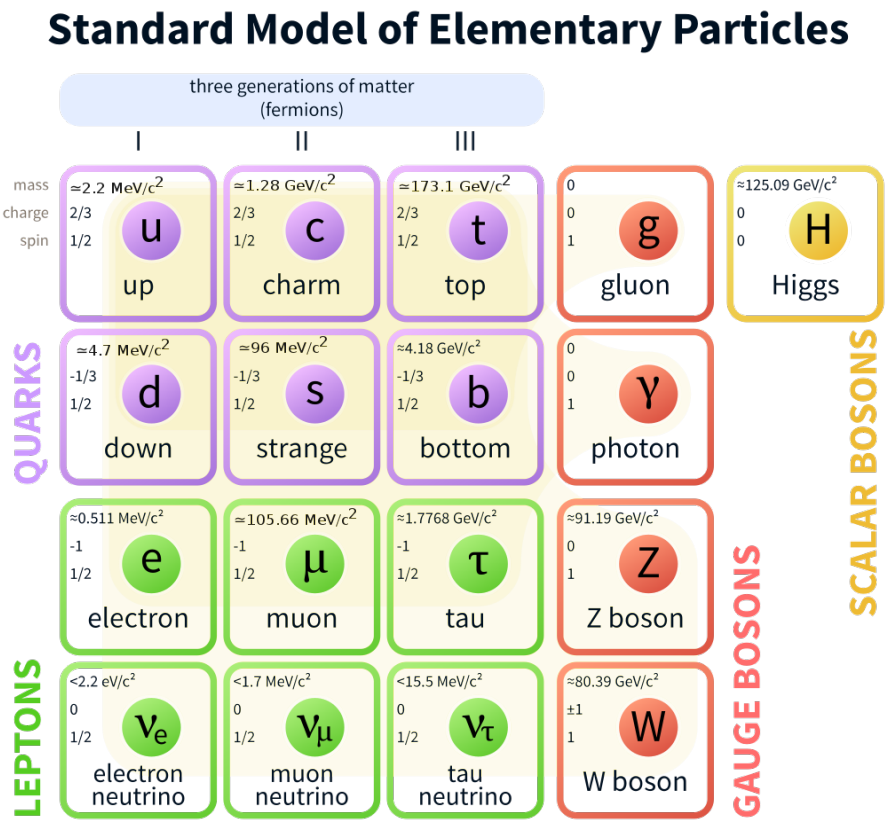

Fig. 1.1 The standard model of elementary particles.

and they can be arranged as in Fig. 1.1 (the purple colored particles). Each quark carries a color charge: red, green, blue. Quarks are always confined with each other inside the nucleon (which are color neutral). Gluons have eight colors and they are named like this because they glue the quarks together inside the nucleon as well as gluing themselves together.

The electro-weak theory is the theory that describes the weak interactions between flavored particles by the exchange of $W^{\pm}$ or Z bosons which are the carriers of the weak force. When a neutron decays into a proton it gives a W^{-} boson which decays into an electron and an anti-neutrino. The $W^{\pm}$ and Z bosons have masses as mentioned in Fig. 1.1. They were discovered in 1983 at CERN. Due to their very high mass their lifetime is very short of the order of $\approx 2.6 \times 10^{-25}$s for the ($Z^0$) and 3.1×10^{-25}s ($W^{\pm}$) [13] [14].

Neutrinos are fermions that interact via the weak force and via the gravitational force. They were first proposed by Wolfgang Pauli to explain the energy, momentum, and angular momentum conservation of the beta decays $n \rightarrow p^{+}e^{-}\bar{\nu}$. In 1942, Wang Ganchang suggested to detect the neutrinos experimentally using the beta capture to detect neutrinos [15], and it was detected later in 1956. Neutrinos play a major role in the study of charge and neutral current electro-weak processes. According to the standard model these neutrinos are massless. But after the experimental discovery of neutrino oscillations by Super-Kamiokande [16] and the Sudbury Neutrino Observatory [17], they discovered that the neutrinos have a very small non-zero mass. These experiments also measured the

flux of atmospheric neutrinos and solar electron neutrinos and discovered that neutrinos change their flavor over long distances in a process called neutrino oscillation, and they were awarded the Nobel prize of physics in 2005 for this discovery.

The Higgs boson is a massive spin zero elementary particle, it was proposed by Peter Higgs in 1964. The Higgs boson is the key building block in the Standard Model, it explains why the elementary particles like W and Z bosons are massive while the photons and the gluons have no mass. In the SM, the Higgs interacts with the other particles and itself so it gives them and itself a mass, except photons and gluons. Due to its very large mass and its fast decay, only very large and powerful particle accelerators can observe and study the Higgs. In 2012, two of the LHC experiments (ATLAS and CMS) pointed out the discovery of a new particle with a mass of about $125.09 \pm 0.21(\text{stat.}) \pm 0.11(\text{syst.})$ GeV/c^2 which is consistent with the theoretical Higgs boson [18] [19]. After the Higgs discovery the Standard Model is complete.

1.2 QCD phase diagram and the QGP

The QCD elementary particles "quarks and gluons" can't be seen freely moving or directly observed because they are confined in a bound state particle which is called "hadron". At high temperature, a phase transition occurs to a deconfined plasma of quarks and gluons, in which they behave as quasi-free particles. This phase transition leads to the creation of the the quark-gluon plasma. It is also believed that the QGP was formed in the early universe few microseconds after the Big Bang, which makes the QGP study important for our understanding of the early universe [20].

The phase transition from hadronic matter to the strongly interacting QGP phase can be represented as a diagram in (temperature T, baryon chemical potential μ_B) plane shown in Figure 1.2. This figure also shows that the phase transition could happen if we compress the hadronic matter to a high baryon density (large μ_B) or by heating to a higher temperature. Lattice QCD calculation at zero μ_B predicts that the phase transition occurs at a critical temperature $T_c \approx 155$ MeV or at a critical baryon density $e_c \approx 0.6 - 0.7$ GeV/fm^3 [21].

If we go to a lower temperature and much larger energy density region of the QCD phase diagram, we find a phase of color-superconductor or color-flavor locked quark matter. Color superconducting phases are the opposite of the normal phase of quark matter, it is a weakly interacting Fermi liquid of quarks. In theory, a color superconductor phase is a state in which the quarks near the Fermi surface become unstable leading to the formation of condensate quark Cooper pairs. In phenomenology, a color superconducting phase is a state which breaks some of the symmetries of the underlying theory, and has a very different transport properties from the hadronic phase.

1.3 Relativistic heavy-ion collisions

In order to create a QGP in the laboratory, we have to collide heavy ions at relativistic energies. The main target of the heavy-ion physics is to study the phase transition from hadronic matter to QGP and to study the properties of the QGP. The first high-energy heavy-ion collisions were made at the Bevelac experiment at the LBNL (Lawrence Berkeley

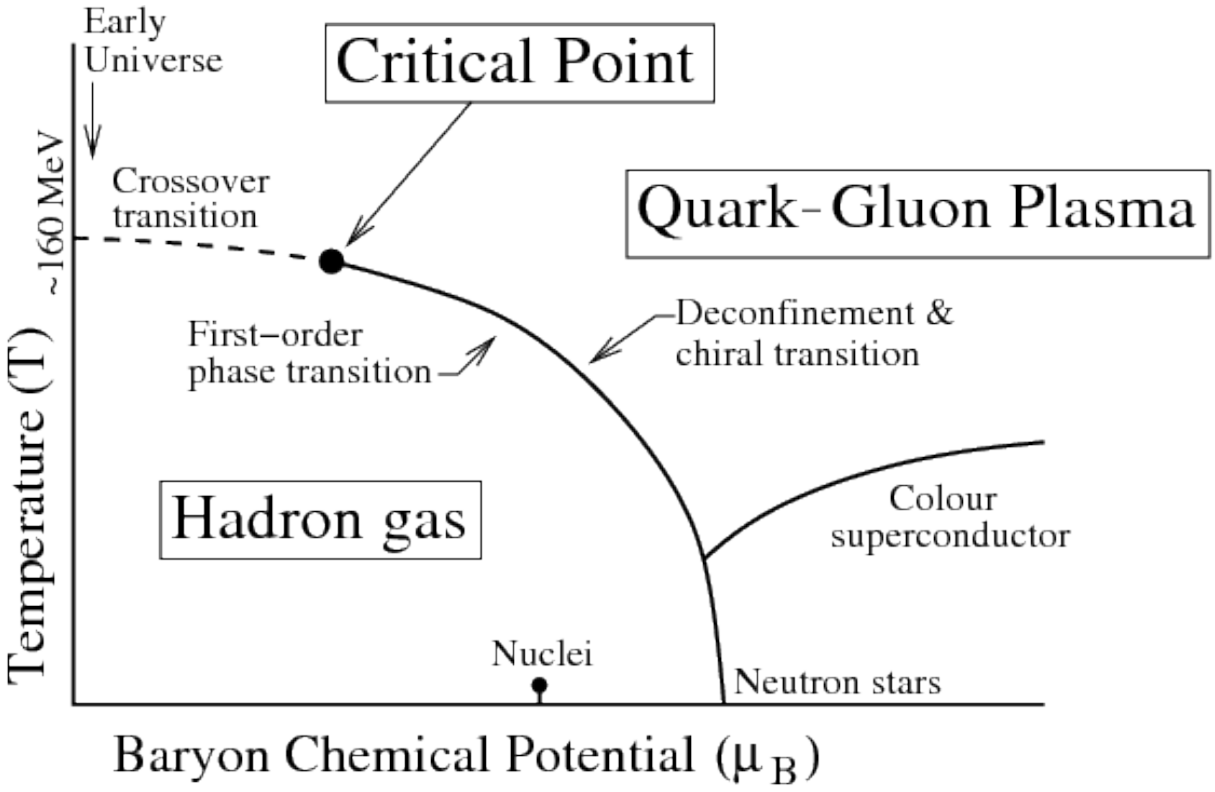

Fig. 1.2 The QCD phase diagram of hadronic matter [22].

national laboratory) and at the joint institute for nuclear research in Dubna (Russia) in which they collided heavy-ions at center-of-mass energy of 1 GeV. But the first program dedicated to create and study the QGP in relativistic heavy-ion collisions was the fixed target experiment at Super Proton Synchrotron (SPS) at CERN which collided Pb ions at center of mass energy between 8-17.3 GeV. After the SPS the Alternating Gradient Synchrotron (AGS) began operation by colliding ions in the mass range between the proton and ^{32}S with a center-of-mass energy up to 28 GeV which is found at the vicinity of the phase transition (by looking at the QCD phase diagram). Later in 2000 the AGS was upgraded to the Relativistic Heavy Ion Collider (RHIC) which delivers ^{197}Au-^{197}Au collisions at energies up to 200 GeV which goes deeper in the QGP region. Ten years after the success of the RHIC and exploring so many properties of the QGP, the Large Hadron Collider (LHC) was built at CERN which delivered Pb–Pb collisions at center of mass energy equals to 2.76 TeV in 2010 and 2011 during 1 month of data taking and it was upgraded later to increase the energy to 5.02 TeV in 2015 and 2018.

1.3.1 Medium evolution

It is necessary to have a good understanding of the evolution of the system formed in heavy-ion collisions to explore the QGP properties. The evolution of a nucleus-nucleus collision can be shown in a space-time diagram as Fig. 1.3.

The right-hand side of the figure shows the evolution of a heavy-ion collision in which QGP is formed according to Bjorken's model [23].

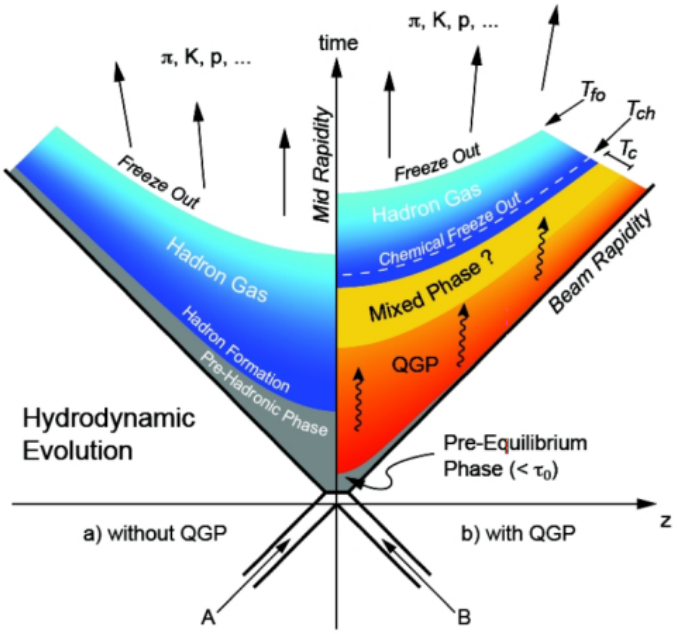

Fig. 1.3 Evolution of a central heavy ion collision in a Minkowski-like plane. The two scenarios with and without QGP are pointed out. The critical temperature is indicated by T_c, while the freeze-out and chemical freeze-out temperatures, are pointed out with T_{fo}, and T_{ch}, respectively.

- In the pre-equilibrium phase ($t < t_0$), the hard scattering process of the partons occurs, in this phase high-p_T probes are created, like jets, heavy quarks or prompt photons.
- In the thermalization and QGP phase ($t_{th} \approx 1$ fm/c), a thermal equilibrium occurs after multiple scattering between the constituents of the system produced in the heavy-ion collision after time t_{th}. If the energy density is larger than the critical value ($\epsilon_c \sim 1$ GeV/fm^3) the mean free path in the QGP medium is expected to be smaller than the medium size leading to a thermalized hydrodynamical QGP expansion which cools down the system.
- In the hadronization phase, the expanding medium temperature starts to decrease and phase transition occurs when the temperature steps down the critical temperature T_c making the quarks and gluons confined again into hadrons. The system is still in thermal equilibrium since inelastic scatterings between hadrons occur.
- In the chemical freeze-out phase ($T = T_{ch}$), the system continues to expand and the temperature keeps dropping resulting in the stopping of the inelastic processes between the hadrons. This stop of inelastic scattering process leads to the fixing of the relative abundances of the different hadron species.
- In the kinetic freeze-out phase ($T = T_h$), the elastic collision between the produced particles is stopped. Thus, the momentum spectra are fixed until the produced particles reach the different sub-detectors.

The left-hand side of Fig. 1.3 shows the evolution of a collision where no QGP is formed. In this case, the protons collide at the origin of the diagram, and hadrons are created after the initial scattering takes place. After that, a short-lived hadron gas phase is formed in which the gas constituents can be modified by the elastic scatterings between the particles. Finally, the system gets cold leading to its freeze-out into the final state particles which can be seen by a particle detector.

It is important to study the parameters of the medium produced in heavy-ion collisions in order to describe it. These parameters like chemical potential, flow velocity (velocity of the medium expansion), medium length and the transport coefficient $\hat{q}$ (transverse momentum transfer squared per unit path length) can be derived from different experimental observables (R_{AA}, ...).

1.3.2 Nucleon-Nucleus collisions

In nucleon-nucleus collisions, the effects coming from the creation of a QGP is expected to be smaller than that of nucleus-nucleus collisions. So nucleon-nucleus collisions can be used as a probe to distinguish between hot and cold nuclear matter effects. In general, the structure of the event of nucleon-nucleus collisions is very similar to the nucleon-nucleon collisions.

The effect of the QGP occurs after the collisions, while the effect of the nuclear parton distribution function (which describes the partonic structure in the nuclues) occurs before the collisions.

QGP is not expected be produced in p–Pb collisions, while in Pb–Pb collisions both QGP and nPDF are present.

1.3.2.1 Nuclear parton distribution functions

Parton distribution functions describe the inner structure of the nucleon, it gives the probability density to find a parton with a certain virtuality (squared momentum transfer Q^2) and a certain Bjorken-x in a nucleon. The Bjorken-x is the nucleon momentum fraction carried by the parton.

A nuclear parton distribution function (nPDF) is the probability density to find a parton in a nucleus. Or in other words it is a nuclear modified PDF of a free nucleon. It is determined based on the free nucleon PDF like in the following equation 1.1 for a nucleus A:

$$f^{n/A}(x, Q^2) = R^A(x, Q^2) f^n(x, Q^2) \tag{1.1}$$

where f^n is free nucleon PDF, $f^{n/A}$ is the nuclear modified nucleon PDF and R^A is the nuclear modification factor of the PDF (describes how the nucleus changes the nucleon PDF). Different were made to constrain the nPDF, one of them is nCTEQ nPDF [24]. Figure 1.4 shows an example of nuclear PDF fit, the left side of the figure shows the nuclear modification factors R^A and the right side shows the bound proton PDFs $f^{p/Pb}(x, Q^2)$ for the lead ion.

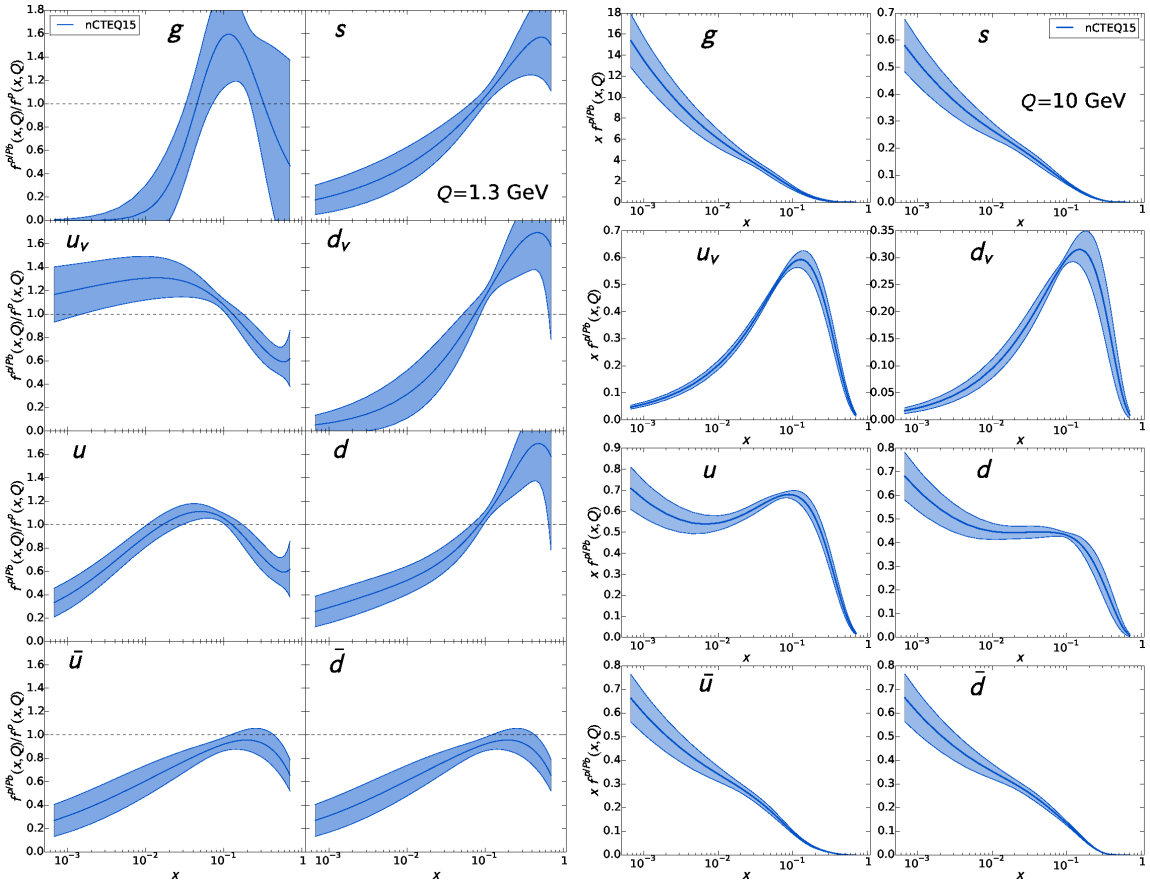

Fig. 1.4 Results of the nCTEQ fit. On the left the nuclear modification factors defined as ratios of proton PDFs bound in lead to the corresponding free proton PDFs is shown, and on the right the actual bound proton PDFs for lead is shown [24].

1.3.2.2 Cold nuclear matter effects

Cold nuclear matter effects are effects that alter the measurements by modifying the environment before the collision (by creating nuclear environment) and they can be described by nPDF.

Studies in the 1970's made by Cronin et al [25] on the cold nuclear matter effects resulted in the discovery that the low momentum hadrons get suppressed and intermediate momentum hadrons around 3 to 6 GeV/c get enhanced, compared to the proton-proton results.

There are four different effects on nuclear modification factors $R^A(x, Q^2)$ of the PDF in four different x regions:

- For small Bjorken-x values $x < 0.01$, the nuclear modification is smaller than unity, so this means a suppression of the PDF was observed. This is called **Shadowing** and it was studied since the 1970's [27].
- For Bjorken-x is the region $0.01 < x < 0.2$, the nuclear modification factor is larger than unity, which means that an enhancement on the PDF was measured. This is called **Anti-Shadowing**. It is less understood than shadowing.

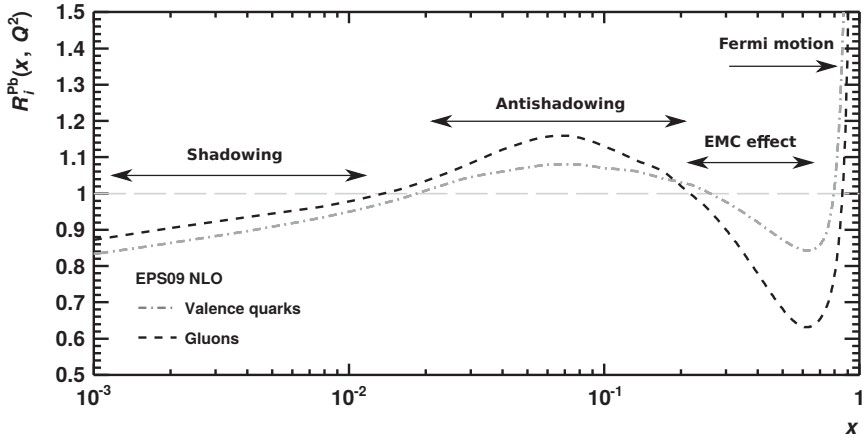

Fig. 1.5 The nuclear modification factor of the nucleon PDF at $Q^2 = 100$ GeV^2 for valence quarks and gluons. Figure adapted from [26].

- For Bjorken-x in the range $0.2 < x < 0.8$, the nuclear modification is again below unity, a suppression of the PDF again is observed. This is called **EMC effect**, which is named after the **European Muon Collaboration** who was the first to observe such effect [28] by comparing the Deep inelastic Scattering (DIS) of a muon on an iron atom and on a deuterium ion.
- The last region for Bjorken-x $x > 0.8$, corresponds to the **Fermi Motion**. Fermi motion of a parton inside the nucleus leads to an expansion of the momentum distribution compared to a free nucleon, which results in an enhancement [29] in the PDF at high x .

1.4 Jet Production

Jets are collimated bunches of particles that are tracked inside the detector at the final state of a high energy collision. They are produced after the hadronization and fragmentation of the particles produced from the initial partons.

The initial partons and their interaction cannot be directly observed, so the jets are reconstructed from the final state particles detected inside the detector in order to study the properties of the interacting partons, keeping in mind that the jets and the partons are different objects, but they share the same kinematic properties.

Actually, the above definition of the jet is what we want the jet to be (perfect jet finder), but the truth is, a jet is what the jet finder finds, given an array of particles, by applying the jet finder these particles are clustered into a jet.

Jets are produced in QCD hard scattering processes, and the probability of creating a certain set of jets is described by the jet production cross section shown in equation 1.2

$$\sigma_{ij\to k} = \sum_{i,j} \int dx_1 dx_2 d\hat{t} f_i^1(x_1, Q^2) f_j^2(x_2, Q^2) \frac{d\hat{\sigma}_{ij\to k}}{d\hat{t}} \tag{1.2}$$

where $\hat{\sigma}_{ij\to k}$ is the pQCD cross section for the reaction $ij \to k$.

The most important requirement for a jet algorithm is that it should be infrared and collinear (IRC) safe in order to guarantee that the experimentally measured jet can be linked to a theoretical observable.

IRC safe means that the clustering of the jet should not be affected by a collinear splitting or emission of a soft gluon which makes the set of hard jets in the event unchanged.

Figure 1.6 shows the configurations when we have a collinear safe and unsafe algorithm. If configuration (a) gives a single jet, then configuration (b) with a collinear splitting should also result in one jet leading to the cancellation of the divergence in pQCD. Unlike configurations (c,d) where the collinear splitting results in the clustering of two jets, leading to non-cancellation of the divergences. Figure 1.7 shows an illustration of an infrared safe and unsafe algorithm, in configuration (c), adding a soft gluon results in the clustering of one jet instead of two.

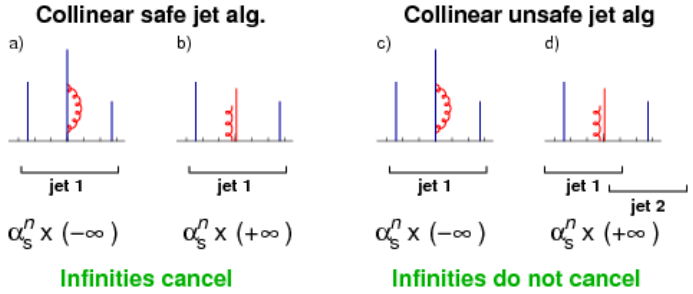

Fig. 1.6 Illustration of collinear safety (left) and collinear unsafety (right) [30].

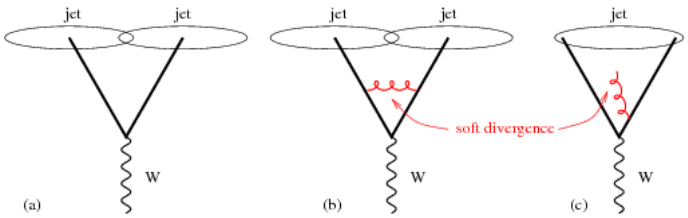

Fig. 1.7 Configurations illustrating IR unsafety of IC-SM algorithms in events with a W and two hard partons [30].

In order to reconstruct jets a set of mathematical tools are used, that allow us to reconstruct the properties of the jets, these tools are called jet algorithms.

We have two main types of jet algorithms: Cone Algorithms and the Sequential Clustering Algorithms.

1.4.1 Cone Algorithms

In this algorithm the jets are defined as a cone with definite radius in the $\eta - \phi$ plane and its direction is in the direction of the dominant energy flow. We have many types of cone algorithms:

Iterative Cone Progressive Removal (ICPR): In Iterative Cone (IC) we take the particle with the highest momentum in the event as a seed and we draw a cone of radius R around it. Sum all the momenta of the particles inside the cone and call it a "trial jet", and compare the hardest particle momentum axis with the seed axis.

If they are identical then this cone is said to be stable cone. If it is stable then all the particles inside the cone are removed from the event and then take the next most energetic particle as a seed and continue in the same way.

If not, iterate with the trial jet as new seed and continue in the same way, until we are left with no seed above the threshold (minimum momentum of the seed).

This algorithm suffers from a collinear unsafety.

Iterative Cone Split Merge (ICSM): It is similar to the ICPR except that the particles inside the stable cone are not removed. So we may have an overlapping between stable cones, this overlapping can be solved by using the split merge procedures:

1. First start using the list of all the protojets (the list of stable cones).
2. Take the protojet with the highest p_T, and call it i.
3. Take the next hardest protojet that overlap with protojet i and call it j, if j does not exist, then remove i from the list of protojets and add it to the list of the final jets then restart from step 2.
4. Calculate the sum of the p_T's of the shared particles between the overlapped cones. If $p_T^{share}/p_T^j > f$, where f is the overlap threshold replace i and j by a single merged protojet.
5. If not, split the protojets by taking the shared particles with the closest protojet.
6. Repeat from step 2 until no protojets are left.

This algorithm suffers from infrared divergence.

SISCone Algorithm: SISCone is a solution to the IRC unsafety also it is the only IRC safe cone algorithm. It is exactly seedless because it avoids the usage of seed. The procedure of jet reconstruction are as the following:

1. Let the number of the current particles equal to the number of all the particles in the event.
2. Find all the stable cones of these particles.
3. Add these stable cones to list of protojets.
4. Remove all the particles in the stable cones from the list of current particles.
5. If new stable cones are found repeat from step 2.
6. Apply the split-merge procedures with overlap parameter f

for more details on the cone algorithms refer to [30].

1.4.2 Sequential clustering algorithms

Clustering Sequence Algorithms are IRC safe algorithms and simple to use. These algorithms are based on two parameters, the distance d_{ij} between two particles i, j and the distance d_{iB} between particle i and the beam B. The distance d_{ij} can be written as:

$$d_{ij} = min(k_{Ti}^p, k_{Tj}^p)\frac{\Delta_{ij}^2}{R^2} \tag{1.3}$$

where $\Delta_{ij} = \sqrt{(y_i - y_j)^2 + (\phi_i - \phi_j)^2}$ is the distance between the pairs of particles i, j, p is the an algorithm-specific parameter (will be discussed later), R is the angular radius in $\eta - \phi$ plane i.e the minimal distance between jets in analogy with the jet radius and $k_{ti,j}$ is the particle i, j transverse momentum. The distance d_{iB} between particle i and the beam B can be written as:

$$d_{iB} = k_{Ti}^p \tag{1.4}$$

The jet clustering procedure of this algorithm is as follows:

1. Calculate the distances d_{ij} and d_{iB} for all particles: If d_{ij} is the smallest, then combine i and j into one single particle using a certain recombination scheme[1], and continue by finding the next smallest. If d_{iB} is smallest then remove particle i and call it a jet.

2. Repeat these procedures until no particles are left.

We have 3 sequential clustering algorithms:

- k_T **algorithm**: In this algorithm, the parameter p in equation 1.4 is equal to $p = 2$. So it takes the softer particles and clusters all the other particles on them, it doesn't have a definite shape for the area (see section 1.4.3 for details on the jet area). Also, it is good for background estimation and subtraction, more details about the algorithm can be found in [30].

- **Cambridge/Aachen**: In this algorithm, the parameter p is set to zero $p = 0$. It clusters the particles according to the spatial separation without taking into account the energy/momentum $d_{ij} = \frac{\Delta_{ij}^2}{R^2}$. It doesn't have a definite area shape also it is good for background estimation and subtraction [30].

- **Anti-k_T algorithm**: In this algorithm, the parameter p is equal to $p = -2$, so it takes the hard particles and cluster all the soft particles at a distance R on the hard particles. It gives a circular cone shape (it reconstructs the hard jets in a circular shape). Also, it is slightly sensitive to the underlying events and pileup. Its passive area (see section 1.4.3) is around $A_{Anti-k_T} = \pi R^2$. More details about the Anti-k_T algorithm can be found here [31].

[1]The recombination scheme determines how the the particles are combined. There are several recombination schemes, examples are the p_T-scheme which recombines the particles by summing the transverse momentum of the particles. Another example is the E-scheme which sums over the energy of the particles.

The k_T algorithm is used to estimate the backgrounds in heavy-ion collisions, after that, the background is subtracted from the anti-k_T clustered jets on event-by-event basis. This will be explained in detail in chapter 4.5.

1.4.3 Jet area

Jet area gives the measure of the surface in the $\eta - \phi$ plane the jet covers. Within the framework of FastJet package [32] several jet definitions can be used in order to define the area of a reconstructed jet. There are three definitions for the jet area:

- **Active area**: This method fills the space with uniformly distributed infinitesimally soft particles in the event, called ghosts. The jet area is determined by the number of ghost particles inside the jet cone. The accuracy of area determination is governed by the number of ghosts per unit area. The smaller the ghost area is, the more ghost particles used.
- **Passive area:**: This method adds a single ghost in a random place in the event. After that, the jet which the ghost ends up with is checked. Then, another ghost is randomly added and the same thing is done again. This process is repeated several times and the jet passive area is then determined from the probability that the jet contains a ghost scaled by the ghost area.
- **Voronoi area**: It is the sum of the Voronoi areas of the constituent particles of the jet. Voronoi area of a particle is measured using the Voronoi diagram for the whole event. For the k_T algorithm, the Voronoi area gives the same measurement as the passive area determination.

1.5 Jet quenching and parton energy loss in QGP

High-p_T jets and high mass particles (p_T, $m > 2$ GeV/c^2) i.e "Hard Probes" are excellent probes for the study of the hot and dense QGP medium, because they are originated from partonic interactions with a large momentum transfer Q^2, they are produced on a very short time scale ($\tau \approx 1/p_T \lesssim 0.1$ fm/c) after the collision takes place, which allow them to propagate through the medium and interact with its constituents, and also their cross section is calculable within pQCD framework and it is a well calibrated probe.

When a parton propagates through the medium, it strongly interacts with the medium constituents, through this interaction this parton loses energy, leading to the attenuation or the disappearance of the hadrons produced from the fragmentation of the parton that suffered from energy loss a shown in Fig. 1.8. This phenomenon is called "jet quenching".

The partonic energy loss ΔE depends on the particles properties (mass m and energy E) and the medium characteristics (temperature T, coupling between the particles and the medium α, and medium length L). But there are other extremely useful variables that characterize the energy loss [33]:

- The **mean free path** $\lambda = 1/(\rho\sigma)$, where σ is the integrated cross section of the interaction between the particle and the medium, and ρ is the medium density ($\rho \propto T^3$)

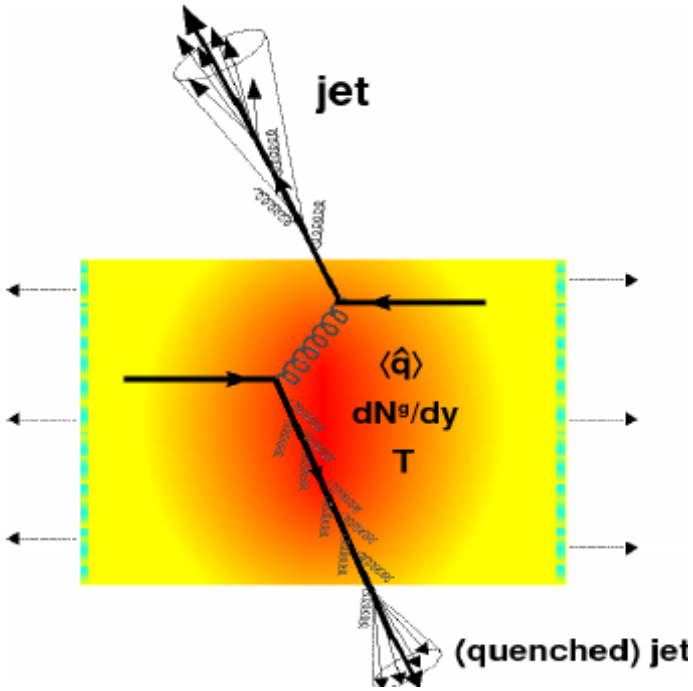

Fig. 1.8 Jet quenching in a head-on nucleus-nucleus collision. Two quarks suffer a hard scattering: one goes out directly to the vacuum, radiates a few gluons and hadronises, the other goes through the dense plasma formed in the collision (characterized by transport coefficient $\hat{q}$ and gluon density dN^g/dy), suffers energy loss due to medium-induced gluonstrahlung and finally fragments outside into a (quenched) jet. Figure adapted from [33].

- The **Opacity**, it is the number of scattering centers in a medium with length L, $N = L/\lambda$.
- The **Debye mass**, is the inverse of the screening length for the electric (chromo) field in the plasma, $m_D(T) \sim gT$, where g is the coupling parameter in QCD. m_D characterizes the lowest momentum exchanged with the medium.
- The **Transport Coefficient** $\hat{q} = m_D^2/\lambda$, is the squared average momentum transferred to the medium per unit path length, which gives the scattering power of the medium.
- The **Diffusion Coefficient** D gives the dynamical properties of the heavy non-relativistic particles (with mass M and speed v) traveling through the medium. Using Einstein's equation D can be written as $D = 2T^2/\kappa = T/(M\eta_D)$, where κ is the **momentum diffusion coefficient** (which is the average momentum gain of the particle per unit time and it is related to $\hat{q}$ by $\kappa \approx \hat{q}v$), and η_D is the **momentum drag coefficient**.

1.5.1 Energy loss mechanisms

There are two main kinds of parton energy loss in the medium: **radiative** and **collisional** energy loss. So the total energy loss is the sum of the two energy losses i.e $\Delta E = \Delta E_{coll} + \Delta E_{rad}$.

- **Collisional energy loss**: The parton loses energy through elastic scatterings with the medium particles Fig. 1.9 (left). It is the dominant process for low momentum particles. In depends on the parton energy E and on the medium temperature T. It was originally predicted by Bjorken [34] and Braaten-Thoma [35], and it was improved later [36–38]. The average energy loss per single scattering is :

$$\langle \Delta E_{coll}^{1scat} \rangle = \frac{1}{\sigma T} \int_{m_D^2}^{t_{max}} t \frac{d\sigma}{dt} dt, \tag{1.5}$$

  where $\frac{d\sigma}{dt}$ is the cross section and t is the momentum transfer squared.

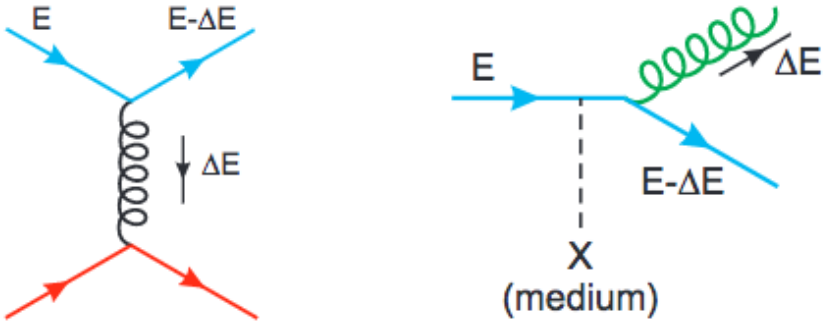

Fig. 1.9 Diagrams for collisional (left) and radiative (right) energy losses of a quark of energy E traversing a quark-gluon medium [39].

- **Radiative energy loss**: The parton loses energy through inelastic scattering with the medium particles as in Fig. 1.9-right, and it is the dominant process for the high momentum particles. The parton traversing the QGP medium loses energy through multiple medium-induced gluon emissions. It can be found by the corresponding differential gluonstrahlung spectrum $w\mathrm{d}I_{rad}/\mathrm{d}\omega$

$$\Delta E_{rad}^{1scat} = \int^{E} \omega \frac{\mathrm{d}I_{rad}}{\mathrm{d}\omega} \mathrm{d}\omega \tag{1.6}$$

  where ω is the energy of the radiated gluon. In case of incoherent scatterings (case where there is no interference effects between successive emissions) $\Delta E^{tot} = N.\Delta E^{1scat}$, where N is opacity ($N = L/\lambda$, λ is the parton mean free path). So the stopping power (energy loss per unit length) will be:

$$-\frac{\mathrm{d}E}{\mathrm{d}l} = \frac{\langle \Delta E^{tot} \rangle}{L} = \frac{\langle \Delta E^{1scat} \rangle}{\lambda} \tag{1.7}$$

  In the radiative energy loss case, the number of emitted gluons depends on the medium thickness and the gluon formation time (t_f). Three regimes were identified:

1. Bethe-Heitler (BH) regime ($L \ll \lambda \ll t_f$): For a thin medium, the parton traversing the medium experience only one scattering. In other words, each scattering center radiates independently:

$$\omega \frac{\mathrm{d}I_{rad}}{\mathrm{d}\omega} \approx \alpha_s C_R \hat{q} L^2/\omega \quad \Rightarrow \quad \Delta E^{BH}_{rad} \approx \alpha_s C_R \hat{q} L^2 \ln(E/m_D^2 L)). \tag{1.8}$$

2. Landau-Pomeranchuk-Migdal (LPM)($L \gg t_f \gg \lambda$): for a thick medium, the parton traveling through the medium undergoes N (opacity) scattering and the gluon radiation spectrum will be suppressed by the LPM [40] effect. In other words, each group of (t_f/λ) scattering centers act as a single source of radiation, which results in the suppression of gluon emission compared to that of the BH regime:

$$\omega \frac{\mathrm{d}I_{rad}}{\mathrm{d}\omega} \approx \alpha_s C_R \begin{cases} \sqrt{\hat{q}L^2/\omega} & (\omega < \omega_c) \\ \hat{q}L^2/\omega & (\omega > \omega_c) \end{cases} \Rightarrow \Delta E^{BH}_{rad} \approx \alpha_s C_R \begin{cases} \hat{q}L^2 & (\omega < \omega_c) \\ \hat{q}L^2 \ln(E/(\hat{q}L^2)) & (\omega > \omega_c) \end{cases} \tag{1.9}$$

   where $\omega_c = \frac{1}{2}\hat{q}L^2$ is the characteristic gluonstrahlung energy.

3. Long formation time ($t_f \gg \lambda$): at large gluon momenta $k^+ \gg \hat{q}L^2$, all the scattering centers are treated coherently as a source of radiation. This is regime is also called the factorization regime.

- In this thesis another kind of energy loss was proposed, which is **Synchrotron radiation energy loss**: In this model, when a fast parton propagates through the QGP medium, it will feel the effect of a chromomagnetic field produced by the color charges of the particles in the medium. This color charged parton will interact with the chromomagnetic field leading to a gluon radiation while undergoing multiple scatterings with the medium particles. This kind of energy loss will be discussed in details in chapter 2.

1.5.2 Dead cone effect

The gluon emission process for a heavy quark is different from that of a light parton (up, down, strange, and gluons). The gluon emission is suppressed at small angles ($\theta \ll M/E$) due to kinematic constraints. The empty cone around the heavy-quark direction is called the "dead-cone" region [41–43]. The gluon emission spectrum for a heavy quark ($\mathrm{d}P_{HQ}$) is different from that of a light quark ($\mathrm{d}P_{LQ}$) by [42]:

$$\mathrm{d}P_{HQ} = \left(1 + \frac{\theta_0^2}{\theta^2}\right)^{-2} \mathrm{d}P_{LQ} \quad , \theta \equiv \frac{M}{E}. \tag{1.10}$$

where θ is the radiation angle. The factor $D = \left(1 + \frac{\theta_0^2}{\theta^2}\right)^{-2}$ is called the "dead-cone" factor which is responsible for the suppression of the gluon emission. This factor is coming from the soft-eikonal-collinear approximation. Since the radiated gluons are assumed to be soft, the recoil between the projectile and the target partons is neglected, and the radiated gluons are assumed to be predominantly emitted collinearly with the parent parton. The

gluon emission spectrum was calculated in [43] by removing the collinearity assumption, and they have found a collinearity removed dead cone factor:

$$D_{NC} = \left(1 + \frac{m^2}{s} e^{2\eta}\right)^{-2} \tag{1.11}$$

where the "NC" means non-collinear.

Recently, few analyses were trying to go beyond the eikonal approximation when finding the radaitive energy loss for a heavy quark [44]. They showed that by proposing a large angle scattering correction in the gluon emission spectrum of the heavy-quark interacting with light quark and by removing the non-eikonality lead to a non-empty region around the direction of propagation of the heavy quark.

The dead-cone effect has some interesting implications such as the suppression of the gluon emissions for heavy-quarks makes the energy loss of the heavy quark different from that of a light quark (mass dependent). This makes the energy loss for the gluon larger than that of the light quark which in turn larger than that of the heavy quark $\Delta E_{gluon} > \Delta E_{LQ} > \Delta E_c > \Delta E_b$.

1.5.3 Energy loss formalisms

Four main phenomenological approaches have been developed to link the QCD calculations of in-medium energy loss with the experimental observables:

- **BDMPS-Z** (LCPI/ASW) [45–48].
- **DGLV** [49–53].
- **Higher twist (HT)** [54–59].
- **AMY** [60, 61].

All the formalisms are based on pQCD calculations. The difference between these models are the approximation of medium structure, they also differ in the dependence on the various medium parameters (initial parton's energy E, virtuality Q^2, typical momentum μ and the medium length L). The effect of the energy loss is centered in the parton medium-modified fragmentation function into hadrons $D^{vac}_{c\to h}(z) \to D^{med}_{c\to h}(z', \hat{q})$. The hadronization of the parton occurs in the vacuum after the parton has escaped the medium, with smaller energy ($z' < z$), see Fig. 1.10.

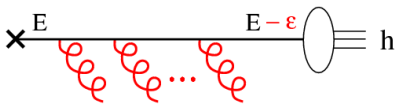

Fig. 1.10 Diagrams for parton energy loss leading to a medium-modified fragmentation function [62].

1.5.3.1 BDMPS-Z (LCPI/ASW)

This approach done by Baier, Dokshitzer, Müller, Peigné, and Schiff (BDMPS) and the light-cone path integral (LCPI) by Zakharov (Z) calculates the energy loss of parton in a colored medium using the multiple soft scattering approximation.

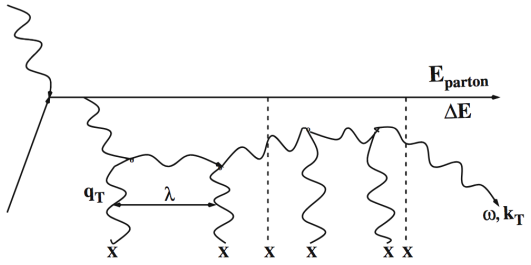

Fig. 1.11 Diagrams for gluon radiation in the BDMPS approach [33].

When a hard parton traverses the medium, it will interact with N scattering centers and radiate a gluon as shown in Fig. 1.11. The path integral over the field was used in order to obtain a Green's function which was used to express the propagation of the parton and the radiated gluon. Then they calculate the gluon emission spectrum $\omega\frac{dI}{d\omega}$.

BDMPS discusses three regimes, the Bethe-Heitler (BH) regime with small gluon energy ω, the LPM regime for intemediate ω it is also called the coherent regime, and the which corresponds to the factorization limit for very high energies $\omega > \omega_{fact} \propto \frac{\mu^2 L^2}{\lambda}$ where μ is the Debye mass of the medium.

The BH and LPM regime are identified by the dimensionless parameter $\kappa = \frac{\lambda\mu^2}{2\omega}$. If $\kappa > 1$ then this is the BH, if $\kappa < 1$ then this is LPM case.

The energy of the emitted gluon ω allows to quantify the radiation behavior:

- $\omega < \omega_{BH} \sim \lambda\mu^2$ for (BH).
- $\omega_{BH} < \omega < \omega_{fact}$ for (LPM).
- $\omega > \omega_{fact}$ for the emissions above the factorization limit.

The BDMPS found the gluon emission probability for the LPM regime as:

$$\left(\omega\frac{\mathrm{d}I}{\mathrm{d}\omega dz}\right) = \frac{3\alpha_s}{2\pi}\frac{C_R}{\lambda_g}\sqrt{\tilde{\kappa}ln(\frac{1}{\tilde{\kappa}})} \tag{1.12}$$

where $\tilde{\kappa} = \frac{2C_F}{N_C}\kappa$, and where $\lambda_g = \lambda\frac{C_F}{N_C}$ is the gluon mean free path. At this scale $\omega_{BH} < \omega < \omega_{fact}$ the total in-medium energy loss was found to be linearly dependent on L for all the incident quark energies. Above this scale (the factorization scale $\omega > \omega_{fact}$) the energy loss was found to be independent of L and linearly dependent on E.

This model also computed the medium-modified fragmentation function:

$$D^{med}_{i\to h}(z, Q^2) = P_E(\epsilon; \hat{q}) \otimes D^{vac}_{i\to h}(z, Q^2), \tag{1.13}$$

where $P_E(\epsilon;\hat{q})$ is the quenching weights computed by Armesto, Salgado, and Wiedemann (ASW) [46, 63, 64]. The quenching weight is the probability that a propagating parton loses energy fraction $\epsilon = \Delta E/E$ as a result of gluon radiation in N collisions:

$$P_E(\epsilon;\hat{q}) = \sum_{N=0}^{\infty} \frac{1}{N!} \left[\prod_{i=1}^{N} \int \mathrm{d}\omega_i \frac{\mathrm{d}I^{med}(\hat{q})}{d\omega}\right] \delta\left(\epsilon; -\sum_{i=1}^{N} \frac{\omega_i}{E}\right) \exp\left[-\int d\omega \frac{dI^{med}}{d\omega}\right] \tag{1.14}$$

There is an implementation of the quenching weights in a MC model, called the parton quenching model [65, 66], which gives a realistic approach for parton production in heavy-ion collisions.

1.5.3.2 DGLV formalism

The formalism of Djordjevic, Gyulassy, Levai and Vitev (DGLV) [49–53] computes the energy loss of a propagating parton in a hot and dense medium containing static scattering centers (Fig. 1.12) which results in a screened Yukawa potential (same case of BDMPS-Z). The DGLV starts with a single-hard emission spectrum (different to BDMPS which starts

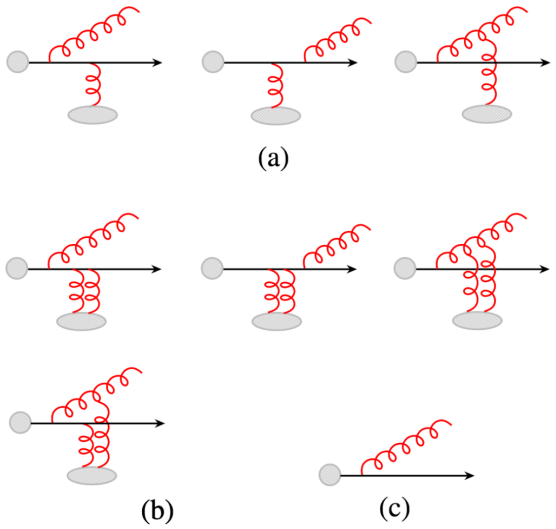

Fig. 1.12 Diagrams contributing to the lowest order in opacity energy loss expansion [67].

from multiple-soft emissions) and expands it to account for gluon radiation from multiple scattering through diagrammatic approach [51]. A fast parton propagating through the dense QGP medium will gain a transverse momentum $\mathbf{q}_\perp$ and emits a gluon with momentum $\mathbf{k} = (xE, \frac{k_\perp^2}{xE}\mathbf{k}_\perp)$. The gluon radiation spectrum at first order opacity is [50]

$$x\frac{\mathrm{d}I^{(1)}}{\mathrm{d}x\mathrm{d}k_\perp^2} = x\frac{\mathrm{d}I^{(0)}}{\mathrm{d}x\mathrm{d}k_\perp^2}\frac{L}{\lambda_g}\int_0^{q_{max}^2} \mathrm{d}^2q_\perp \frac{\mu_D^2}{\pi(q_\perp^2+\mu_D^2)^2}\frac{2k_\perp\cdot q_\perp(k-q_1)^2L^2}{16x^2E^2+(k-q)_\perp^2L^2} \tag{1.15}$$

where $\frac{\mathrm{d}I^{(0)}}{\mathrm{d}x\mathrm{d}k_\perp^2}$ is leading order gluon emission spectrum, λ_g is the mean free path of the emitted gluon. Every emission at a certain opacity is supposed to be independent and it

will setup a new scheme in which the partonic energy loss (with radiated energy fraction ϵ in N opacity) is given by a Poissonian distribution [51]

$$P_N(\epsilon, E) = \frac{e^{\langle N^g \rangle}}{N!} \prod_{i=1}^{N} \left[\int dx_i \frac{dN^g}{dx_i} \right] \delta \left(\epsilon - \sum_{i=1}^{n} x_i \right), \tag{1.16}$$

where $\langle N^g \rangle$ is the average number of gluons emitted per coherent set of scatterings. By summing over N we get the probability $P(\epsilon)$ for a parton to radiate (lose) a gluon with energy fraction ϵ via its passage through the QGP medium. This probability is then used to compute the medium-modified FF by modifying the energy of the fragmented parton as in Eq. 1.13.

1.5.3.3 Higher Twist (HT)

The higher twist approach was formulated by Guo, Wang and Majumder [54–59]. It characterizes the parton multiple scattering with medium particles as a power correction to the leading-twist cross section Fig. 1.13.

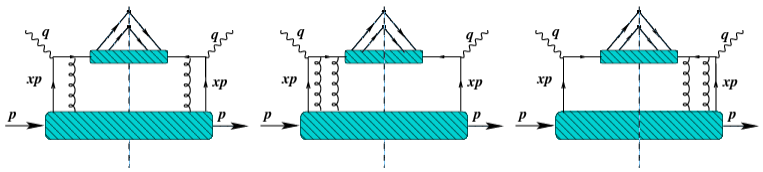

Fig. 1.13 LO and NLO diagrams contributing to the medium-modified FF [68].

This model takes the medium properties into account in the calculation of the higher twist matrix elements. Originally this formalism was applied to compute the medium-modified fragmentation function in order to derive the total cross section in nuclear DIS of $e - A$ collisions.

In this approach the Feynman diagrams of Fig 1.13 were computed and then added coherently in order to compute the medium-modified FF by adding the medium dependent contributions to vacuum term $D^{med}_{i\to h} = D^{vac}_{i\to h} + \Delta D^{med}_{i\to h}$,

$$\Delta D^{med}_{i\to h}(z, Q^2) = \int_0^{Q^2} \frac{\mathrm{d}k_\perp^2}{k_\perp^2} \frac{\alpha_s}{2\pi} \left[\int_{z_h}^1 \frac{\mathrm{d}x}{x} \sum_{j=q,g} \left\{ \Delta P^{med}_{i\to j} D_{j\to h}\left(\frac{z_h}{x}\right) \right\} \right], \tag{1.17}$$

where $\Delta P_{i\to j} \propto P_{i\to j} C A \alpha_s T^A_{qg}$ is the medium-modified splitting function for a parton i splitting into parton j, x is the momentum fraction carried by j from i and $k_\perp$ is the transverse momentum of the emitted gluon. The factor T^A_{qg} is the quark-gluon correlation factor that represents the whole medium effect. The term C is the normalization factor to the correlation coefficient T^A_{qg}, which is determined by fitting the experimental data it is also used to compute the partonic energy loss in a medium. Eq. 1.17 can be used to compute the medium-modified fragmentation functions and derive the final hadron spectra.

1.5.3.4 AMY

The formalism of Arnold-Moore-Yaffe [60, 61, 69, 70] is a quantum field theory approach of a parton losing energy in a weakly-coupled medium in thermal equilibrium. The colored medium properties are described by its temperature. AMY combines the multiple scatterings of the emitted gluon and the incident quark in order to obtain the LO gluon emission spectrum. By computing the imaginary parts of the ladder diagrams in Fig 1.14 using the integral equations that give $q \to qg$ transition rate Γ^a_{bg}, Where a is the incident quark and b is the outgoing quark and g is the emitted gluon.

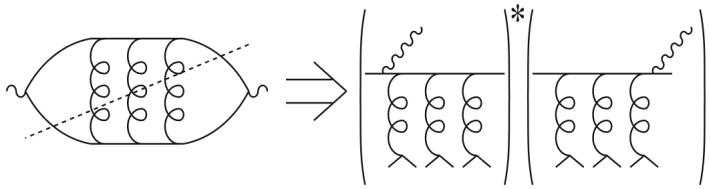

Fig. 1.14 Ladder diagram for the AMY calculations [61].

The Fokker-Planck equation [71] was used to evolve the original gluon emission spectrum over the medium length and also by using transition rates Γ^a_{bg}, then gluon radiation spectrum becomes:

$$\frac{\mathrm{d}P_a(p)}{\mathrm{d}t} = \int dk \sum_{b,c} \left[P_b(p+k) \frac{\mathrm{d}\Gamma^b_{ac}(p+k,p)}{\mathrm{d}k\mathrm{d}t} - P_a(p) \frac{\mathrm{d}\Gamma^a_{bc}(p,k)}{\mathrm{d}k\mathrm{d}t} \right]. \tag{1.18}$$

After that the vacuum FF was convoluted with the hard parton after going through the QGP medium, the medium-modified FF was found as:

$$D^{med}_{a\to h}(z) = \int \mathrm{d}p_f \frac{z'}{z} \sum_a P_a(p_f; p_i) D^{vac}_{a\to h}(z') \,, \tag{1.19}$$

where $z = p_h/p_i$ and $z' = p_h/p_f$, and p_i is the momentum of the parton after the hard scattering and p_f is the momentum of the parton before exiting the plasma. The AMY model for the QGP is basically governed by space-time profile decided for the underlying temperature showing up in the transition rates.

1.5.4 Models Comparison

All the energy loss models discussed above can be divided into two categories: the models that calculate the energy loss through the gluon emission spectrum like the BDMPS-Z and GLV, and the models that directly calculate the final medium-modified spectra of the parton traveling through the medium. Each model has its pros and cons and some of them are shown in the following table:

All four formalisms were successful by comparing them to the data from RHIC and LHC (see Fig. 1.15). One parameter in each model was tuned such that the models perfectly fit the experimental observable: transport coefficient $\hat{q}$ in the BDMPS-Z formalism, the initial gluon density dN^g/dy in GLV, energy loss ϵ_0 in HT, and the medium temperature

Model	Advantages	Disadvantages
BDMPS-Z	It can be applied to the different medium lengths L	It doesn't account for elastic energy loss
GLV	It is applicable to confined and deconfined media	It lacks the implementation of the energy flow into the medium
Higher Twist	It directly calculates the medium modified FF and allows for the analysis of multi-hadron correlations	It is not appropriate for thick media
AMY	It accounts for the absorption of a quark or a thermal gluon by the hard parton, and elastic energy loss is included	It can't be applied to non-thermalized media

Table 1.1 Table summarizing the advantages and disadvantages of the energy loss formalisms

T in AMY. So this means all models with medium parameters consistent with QGP (at temperature T above the QCD phase transition) can produce all the jet quenching observables in Au-Au collisions at $\sqrt{s_{\mathrm{NN}}} = 200$ GeV at RHIC. The resulting R_{AA} of the four models are equivalent, but they cannot be compared in details (in theory) since these models, use different approximations in the calculation, the list of physical processes are not the same, also various fitting parameters were used to describe the medium and they are using different space time profiles.

The equivalence between the four different formalisms has been looked into within a 3D hydrodynamical approach Fig. 1.15 [73] by connecting the different medium characteristics through thermodynamical relations also using the same space-time evolution. But the extracted values of $\hat{q}$ vary by factors of 2-3. By requiring the reproduction of the quenched di-hadron azimuthal correlation, further constraints on the transport coefficient can also be set.

1.5.5 The nuclear modification factor R_{AA}

Partonic energy loss in AA collisions leads to different effects that can be observed experimentally by comparing to pp collisions where no QGP is created. The most

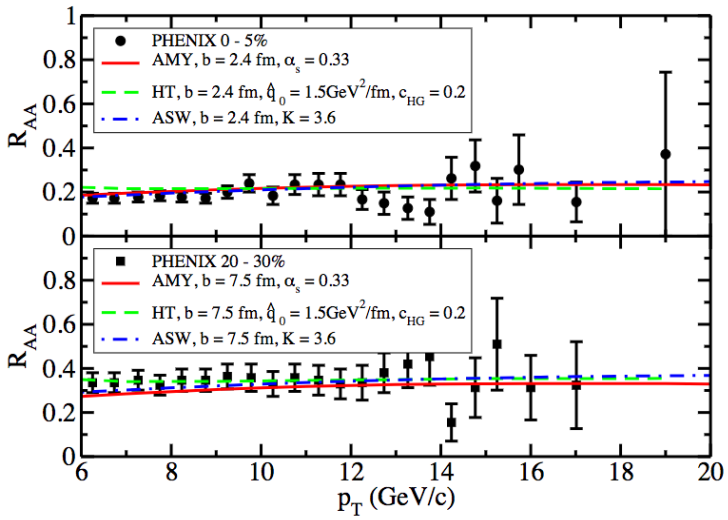

Fig. 1.15 Nuclear modification factor R_{AA} of pions in central (top) and semicentral (bottom) $Au - Au$ at RHIC [72] compared to the BDMPZ, HT, and AMY energy loss formalisms [73].

direct approach to study jet quenching is the suppression of the high-p_T hadrons spectra $\mathrm{d}N_{AA}/\mathrm{d}p_T$ or the so called nuclear modification factor R_{AA}. With the use of the QCD factorization theorem [74], the production cross section of a hight-p_T hadron "h" or a heavy-flavor hadron in pp collisions can be written as:

$$\mathrm{d}\sigma^{hard}_{AB\to h} = f_{a/A}(x_1, Q^2) \otimes f_{b/B}(x_2, Q^2) \otimes \mathrm{d}\sigma^{hard}_{ab\to c}(x_1, x_2, Q^2) \otimes D_{c\to h}(z, Q^2)\,, \qquad (1.20)$$

where $\sigma^{hard}_{ab\to c}(x_1, x_2, Q^2)$ is the perturbative partonic cross section, $f_{a/A}(x_1, Q^2)$ is the PDF of a parton "a" inside the nucleon "A" and $D_{c\to h}(z, Q^2)$ is the FF of a parton "c" fragmenting into hadron "h". The PDFs for a parton inside a free nucleon and FFs cannot be calculated in the pQCD framework, but they can be extracted from the experimental data.

The partonic cross section of Eq. 1.20 is the short distance cross section. It was obtained by removing the mass and collinear singularities related to the light quark and the gluon through the mass-factorization procedure, which makes the partonic cross section dependent on the factorization scale μ_F. The partonic cross section is also dependent on the coupling constant, which is evaluated at a certain renormalization scale μ_R. The renormalization scale μ_R is a factor which was introduced in pQCD calculation in order to cure the UV divergence of which the strong coupling α_s will become function of it. The factorization scale is an energy scale that was introduced in pQCD calculations in order to cure the IR divergences of which the parton distribution and fragmentation functions will become a function of it. These scales are chosen to be on the order of the hard scale to avoid large logarithmic contributions, and for heavy quark production these scales are chosen to be of the order of the heavy quark mass. In general, if the hard scale of the scattering process is larger than the QCD scale ($\mu_F, \mu_R > \Lambda_{QCD}$), the pQCD calculations are applicable. In the case of heavy-flavor production the masses of the heavy quarks are larger than Λ_{QCD} so the pQCD is always applicable down to low p_T regions.

In AA collisions each nucleus is assumed to be as a collection of free partons. So the partonic density in a nucleus of mass number "A" is supposed to be similar to the superposition of "N_A" independent nucleons $f_{a/A}(x_1, Q^2) = A \cdot f_{a/N}(x_1, Q^2)$. So the prodution cross section of high-p_T hadrons in heavy-ion collision would be:

$$\mathrm{d}\sigma^{hard}_{AB\to h} = A \cdot B \cdot f_{a/N_A}(x_1, Q^2) \otimes f_{b/N_B}(x_2, Q^2) \otimes \mathrm{d}\sigma^{hard}_{ab\to c}(x_1, x_2, Q^2) \otimes D_{c\to h}(z, Q^2)\,, \quad (1.21)$$

Equation 1.21 shows that the inclusive production cross section in heavy-ion collisions scales as $A \cdot B$ times the cross section in pp collisions:

$$\mathrm{d}\sigma^{hard}_{AB} = A \cdot B \cdot \mathrm{d}\sigma^{hard}_{pp}. \quad (1.22)$$

Since in heavy-ion collisions experiments we measure yields in different centrality bins (or impact parameter "b"), so the equation 1.22 becomes:

$$\mathrm{d}N^{hard}_{AB} = \langle T_{AB}(b) \rangle \cdot \mathrm{d}\sigma^{hard}_{pp}, \quad (1.23)$$

where $T_{AB}(b)$ is the nuclear overlap function which describes the surface profile of the two beams of ions colliding at a distance "b" from each other and it can be calculated by Glauber model [75]. The nuclear overlap function can also be written as: $T_{AB}(b) = \langle N_{coll}(b) \rangle / \sigma^{inel}_{NN}$, where $N_{coll}(b)$ is the number of inelastic nucleon-nucleon collisions at "b", and σ^{inel}_{NN} is the total inelastic nucleon-nucleon cross section.

The nuclear modification factor which is used to identify the effects of the QGP on the spectra of the hard probes in heavy-ion collisions can be written as:

$$R_{AA}(p_T, y; b) = \frac{\mathrm{d}^2 N_{AA}/\mathrm{d}y\mathrm{d}p_T}{\langle T_{AA}(b) \rangle \times \mathrm{d}^2\sigma_{pp}/\mathrm{d}y\mathrm{d}p_T}. \quad (1.24)$$

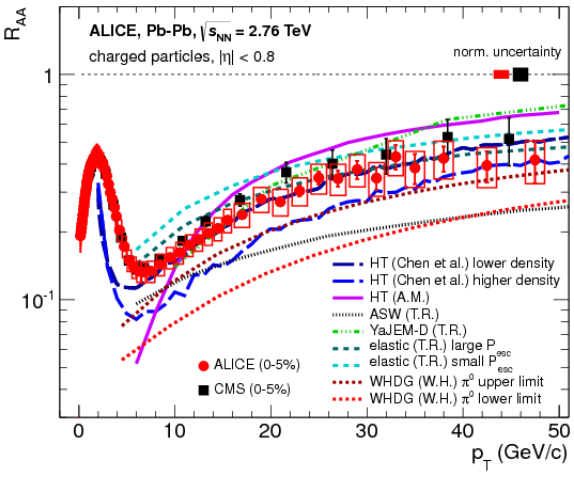

Fig. 1.16 Charged particles measured by ALICE in the most central Pb–Pb collisions (0–5%) in comparison to results from CMS and Theory models.

By definition, if the R_{AA} is close to unity then this means there is no medium effect, no nPDF effect, and no cold energy loss. If the R_{AA} is larger than unity then this means the yield was enhanced by the medium effect, if the R_{AA} is less than unity then this

means there is a suppression of the particle spectra. The R_{AA} has been measured for the inclusive hadron spectra by the ALICE collaboration [76] (Fig. 1.16). The R_{AA} of Fig. 1.16 shows a strong suppression in the whole p_T range, and it is also p_T dependent. The strongest suppression is observed at $p_T = 6 - 7$ GeV/c, and above this limit the R_{AA} starts to increase significantly until it reaches $R_{AA} \approx 0.4$.

Also the R_{AA} of the inclusive jets has been measured by the ALICE, ATLAS and CMS collaborations [77] (Fig. 1.17). This figure shows that R_{AA} is largely suppressed in the full p_T range and it is slightly increasing with the p_T, also this figure shows that the R_{AA} is independent from the jet radius R used for the jet reconstruction.

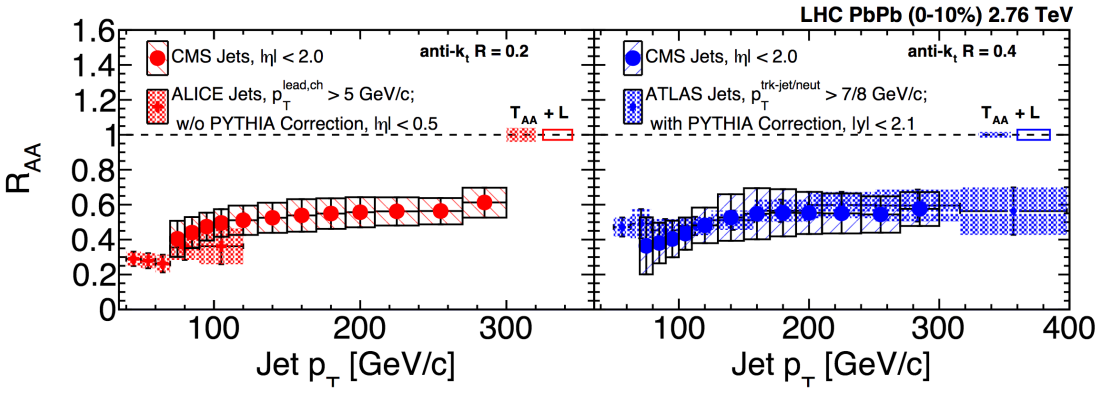

Fig. 1.17 The Inclusive jet R_{AA} as a function of the jet p_T for $R = 0.2$ in the (0–10%) central Pb–Pb for ALICE and CMS (left), and for jets with $R = 0.4$ for ATLAS and CMS (right). The error bar below T_{AA} is the uncertainty on the nuclear overlap function, and L is the uncertainty on the luminosity determination.

This strong suppression in R_{AA} shows that kinematics and the fragmentation of the hard partons are modified by the QGP medium. Any theory model studying jet quenching should be able to describe the above measurements.

1.6 Open heavy flavor production

One the most important tools to characterize Quantum Chromodynamics (QCD) in high-energy hadronic collisions, are the heavy-flavor hadrons, which are particles that contain open or hidden charm or beauty quarks. They are important to study in the different collision systems, their production mechanism in pp, their modification in p–Pb collisions, and they also important to study the properties of the strongly-interacting hot and dense QGP medium in heavy-ion collisions.

The heavy-quark mass can be treated as a long distance cutoff in such a way that the partonic hard scattering process can be computed in the pQCD framework to a low transverse momentum region (p_T).

Heavy-flavor quarks are produced in the early stage of the collision prior to the QGP thermalization time. Disentangling the medium induced effect (final state effects) and connecting them to the QGP properties needs a good understanding of the so-called cold

nuclear matter effect (section 1.3.2), which affects the heavy-flavor production in p–Pb collisions compared to the pp collisions.

In high energy heavy-ion collisions, the produced heavy quarks interact with the medium particles leading to the loss of their energy, which reveals some of the properties of the QGP. Theory predicts that the partonic energy loss is dependent on the mass and the color charge of the propagating parton. So charm and beauty quarks are important probes for the study of the partonic energy loss and also for the QGP properties.

1.6.1 Open heavy-flavor production in pp collisions

Open-heavy-flavor production in pp collisions improves our understanding of the different aspects of QCD at different scales. Also open-heavy-flavor production in pp collisions allows for the study of the perturbation series in various kinematic regions ($p_T < m_Q$, $p_T \sim m_Q$, $p_T \gg m_Q$) due to the existence of multiple hard scales (m_Q, p_T). These multiple hard scales are also found in other physics processes of high interest like the weak boson production, Higgs boson production and several cases of physics Beyond the Standard Model.

Since the production cross section is sensitive to the gluon and the heavy-quark contents in the nucleon, the production cross section evaluation at the LHC can give a useful constrain on the PDFs inside the proton and inside the nucleus. The differential cross section measurement of open-heavy-flavor production in pp and in p–Pb collisions can also be used as reference for the study of the heavy-flavor production in heavy-ion collisions.

1.6.1.1 Heavy-quark production

The production of a heavy quark occurs at the partonic level in the hard scattering process between two quarks or gluons, or in general two partons as shown in Fig. 1.18.

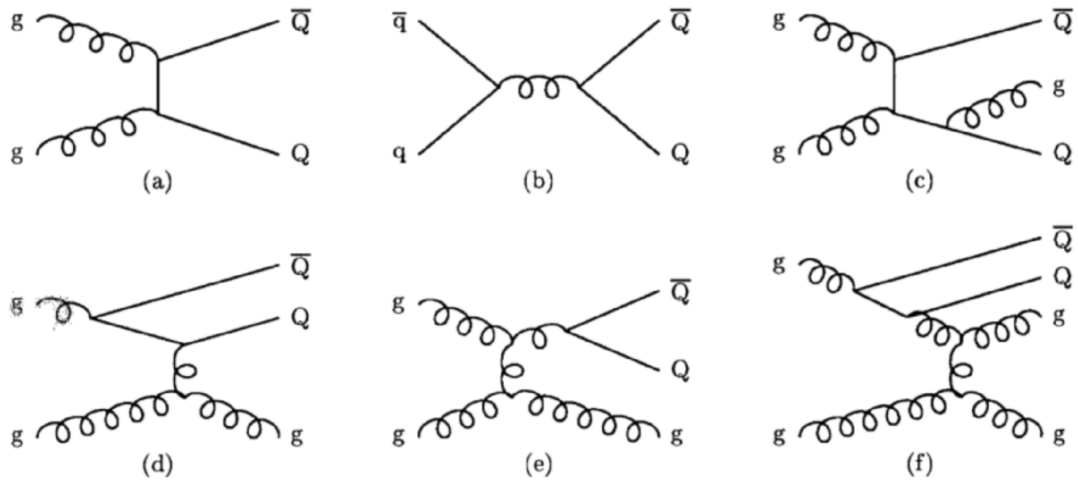

Fig. 1.18 Main Feynmann Diagrams involved in the computation of a heavy-flavour quark pair production. Diagrams (a) and (b) are for LO contribution. Diagrams (c) (d) (e) and (f) are for NLO contribution.

Diagrams (a) and (b) of Fig. 1.18 represent the leading order diagrams contributing to the HF production. Diagrams (c) (d) and (e) are the NLO contribution to the HF production, diagram (c) for gluon emission, diagram (d) for flavor excitation, and diagram (e) for gluon splitting. On the other hand diagram (f) represents higher order flavor excitation events. The contribution of the various diagrams is predicted to be dependent on the kinematics of the parton and also on the center-of-mass energy of the collisions, and can be calculated with the pQCD framework.

In the kinematic regime of the LHC, in the LO processes the dominant contribution for the heavy-flavor production is predicted to be the gluon fusion process (since the gluon PDF is larger than that of the quark). While for the NLO contributions, the gluon splitting process is expected to be the dominant contribution at very high energies, flavor excitation is the dominant at intermediate energies, and at low energies the dominant process is the pair production.

The reason that makes the NLO contribution larger than the LO contribution is related to the soft and collinear logarithms related to the gluon slitting into $b\bar{b}$-pairs. The flavor excitation contribution is $(\alpha_s \ln p_T/m_b)^n$ and the gluon splitting contribution is $(\alpha_s \ln p_T/m_b)^{2n-1})$ with respect to the leading order $O(\alpha_s)$. And since $m_b \ll p_T$ these contribution are enhanced.

1.6.1.2 Experimental results

Since the heavy-flavor particles have a short lifetime, their production is studied through their decay products. The main techniques used are:

1. Full reconstruction of the exclusive decay channels, such as $D^0 \to K^-\pi^+$ or $B^0 \to J/\psi K^0_s$.

2. Studying the semi-inclusive decays, for example for the beauty decays, we look for a certain particle and require it to point to the secondary vertex of the b-quark decay.

3. Selection of leptons from HF decay. This can be done by two ways:

   - Removing all the particles with known sources from the inclusive yields.
   - Choosing the leptons that point to the secondary vertex.

4. Reconstructing the c- and b-jets. When the heavy-flavor jet (HF-jet) is reconstructed, several objects like secondary vertices, track impact parameters, and identified leptons, are used to discriminate the HF-jets from the light flavor jets. These method will be discussed in details in chapter 4.4.

These methods are used in different conditions, depending on the different detectors and sub-detectors, different triggers, the statistics (number of events), the precision and the kinematical range.

The heavy-flavor decay analysis is performed at RHIC by PHENIX [78], and at the LHC by the ATLAS [79] and ALICE [80–82].

Figure 1.19 shows the result for the p_T differential production cross section of heavy-flavor decay leptons in pp collisions at different center-of-mass energies and rapidities. In this figure the differential cross section is well described by the pQCD predictions by

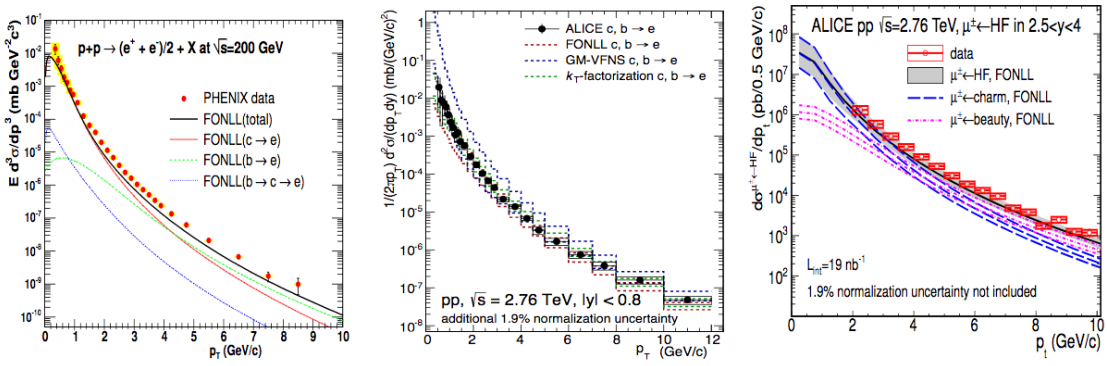

(a) PHENIX, HF → $e^{\pm}$, $\sqrt{s}$ = 200 GeV (b) ALICE, HF → $e^{\pm}$, $\sqrt{s}$ = 2.76 TeV (c) ALICE, HF → $\mu^{\pm}$, $\sqrt{s}$ = 2.76 TeV

Fig. 1.19 $\mathrm{d}\sigma/\mathrm{d}p_T$ for heavy-flavor decay leptons, (a) electrons at mid-rapidity for PHENIX [78], (b) electrons at mid-rapidity with ALICE [80], (c) muons at forward rapidity with ALICE [81].

FONLL [6, 7] panels (a) and (c) in Fig. 1.19, GM-VFNS [8, 9] and k_T factorization [83] for panel (c) besides FONLL.

It is also possible to separate leptons from open charm and beauty production through:

- Cutting on the impact parameters of the leptons (distance of closest approach between the lepton and the primary vertex).
- Fitting templates of the impact parameter distribution for the different lepton sources to inclusive yield.
- Analysis of the azimuthal correlations between the HF-leptons and charged hadrons.

These measurments were done by the ALICE collaboration [84, 85] at the LHC and are also well described by the theoretical predictions.

D-mesons have been studied recently at RHIC, Tevatron and LHC energies [86–93]. The D-meson were studied by fully reconstructing the hadronic decay using particles identification capabilities of the different sub-detectors to reduce the combinatorial background.

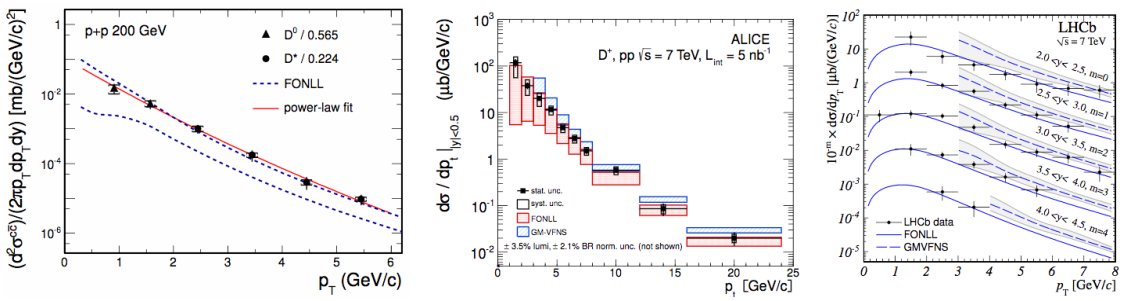

Fig. 1.20 $\mathrm{d}\sigma/\mathrm{d}p_T$ for D meson prdouction in pp, (a) D^0 and D^{*+} with STAR detector [86], (b) D^+ with the ALICE detector [90], (c) D_s^+ with the LHCb detector [92].

Figure 1.20 shows the D-meson measurements compared to the pQCD calculation. The differential production cross section measurements are described by the theory calculations

within uncertainties, but FONLL [6, 7] calculations underestimate the data, whereas GM-VFNS [8, 9] calculations overestimate the data. In addition, it is also possible to separate primary and secondary charm hadrons, they are also called *prompt* (coming from the hard scattering) and $non - prompt$ (which are coming from weak decays of the b hadrons). The non-prompt contribution to the charmed hadrons yields can be subtracted by:

- Fitting templates of the impact parameter distribution for both the prompt and non-prompt charmed hadrons to the inclusive yield (exploiting the larger life time of "b" than "c" flavored hadrons) [87, 88, 92].
- Estimating the non-prompt contribution using pQCD calculation [89–91, 93] (it doesn't work if the pQCD fails to describe data).

Charm baryons production is also measured at hadron colliders. The C- and B-factories and fixed target experiments studied the branching ratios and the properties of Λ_c, Σ_c and Ξ_c particles. Example results done by the Fermilab E791 in [94], FOCUS in [95], and CLEO in [96] collaboration. The charmed baryons were studied by the CDF collaboration [97] in $p\bar{p}$ collisions at $\sqrt{s} = 1.96$ TeV. The Λ_c baryon differential production cross section was measured in pp collisions at $\sqrt{s} = 7$ TeV by LHCb [92] and by ALICE [98] collaboration at the LHC. The ALICE collaboration also studied the Ξ_c^0 production in pp collisions at $\sqrt{s} = 7$ TeV [99].

The b-quark production is usually predicted by measuring b-jets or b-hadrons through their hadronic decay. Their properties and branching ratios are being studied at the e^-e^+ B-factories, where the large luminosity allows for precise measurements, in-spite of the small b-quark production cross section. High-energy collisions increase the production cross section for the b-quarks, but their reconstruction is more difficult compared to the e^-e^+ environment due to the large combinatorial background.

The beauty mesons (like $B^{\pm}$, B^0 and B_s^0) production cross section measurement has been done at the Tevatron and at the LHC [100–106]. Figure 1.21 show the differential production cross section for the B^+ meson in pp collisions at $\sqrt{s} = 7$ TeV measured by the ATLAS and CMS collaborations compared to the theory prediction. The PYTHIA leading order prediction fails to describe the data, this could be due to the choice of the heavy-quark mass m_b, while POWHEG, FONLL and MC@NLO provide a good description of the data within uncertainties.

The beauty baryons production were also measured at the LHC in pp collisions at $\sqrt{s} = 7$ TeV, for example the Λ_b baryon production cross section was measured by the CMS [107], where theory predictions (PYTHIA and POWHEG) fail to describe the data.

The b-jet cross section measurement was done in the ATLAS and CMS collaborations [108, 109], and they were also compared with the theory prediction which computes fully exclusive final states, which can be done by matching NLO prediction to a shower Monte Carlo (MC) [110]. In this thesis, same things was done, POWHEG was used to generate the hard scattering of the event, and then it was matched PYTHIA8 shower MC which is used for showering the hard scattered partons.

Figure 1.22 presents the b-jet differential cross section analyzed by the ATLAS and CMS experiments in pp at $\sqrt{s} = 7$ TeV. The data are found to be described by the theory calculation from POWHEG [10] (showered by PYTHIA [111]) and MC@NLO calculation [112, 113] (showered by HERWIG [114]).

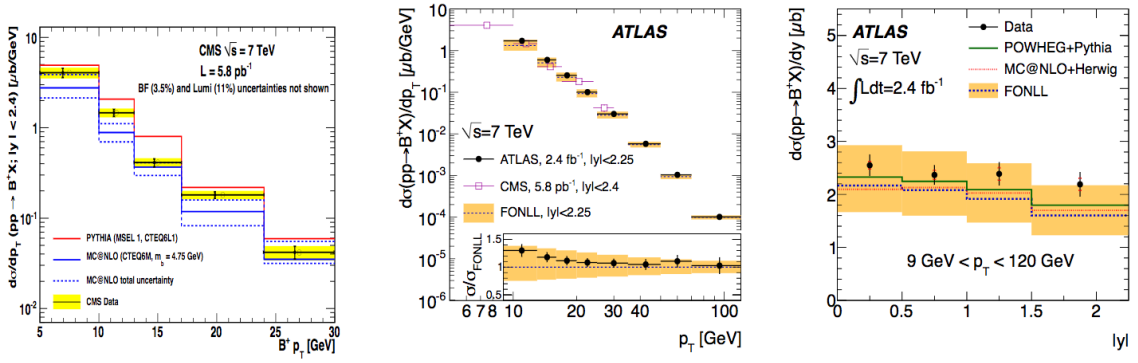

(a) CMS, p_{T} differential (b) ATLAS, CMS, p_{T} differential (c) ATLAS, y differential

Fig. 1.21 (a),(b) $\mathrm{d}\sigma/\mathrm{d}p_T$ for B^+ meson prdouction in pp with the ATLAS and CMS detectors, (c) $\mathrm{d}\sigma/\mathrm{d}y$ with the ATLAS detector [100, 101].

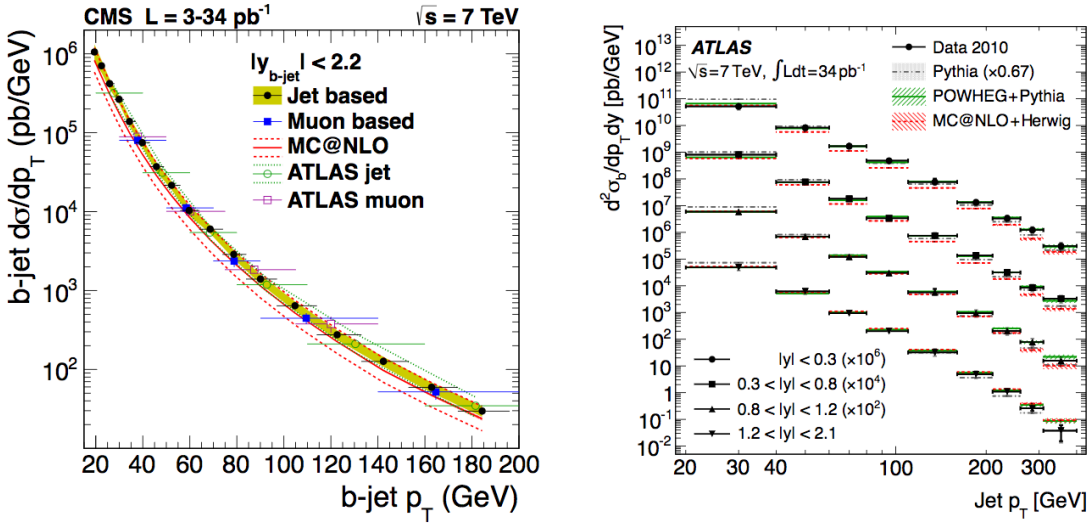

Fig. 1.22 b-jet cross section as a function of p_T in pp collisions at $\sqrt{s} = 7$ TeV, (a) $\mathrm{d}\sigma/\mathrm{d}p_T$ measured by the CMS collaboration [108], (b) $\mathrm{d}\sigma/\mathrm{d}p_T\mathrm{d}y$ measured by the ATLAS collaboration [109].

In summary, the differential production cross sections of the open charm and beauty are described by pQCD prediction, despite the fact that the theoretical uncertainties are quite large at low p_T. The LHC Run 3 will give strong constraints on the theoretical calculation and more understanding of the production mechanism.

1.6.2 Open heavy-flavor production in p–Pb collisions

Studying the hot and dense medium produced in heavy-ion collisions needs a good understanding of the initial state effect caused by the cold nuclear matter (CNM) effects due to presence of a nucleus in the high-energy collisions. In order to see the CNM effects, we have to measure the nuclear modification factor R_{pA}^C of the studied objects (defined in 1.5.5), which is the ratio of the production yield N_{pA}^C in p-A collisions, over the pp cross

section σ_{pp} at the same center-of-mass energy, divided by the nuclear overlap function $\langle T_{pA} \rangle_C$ which is obtained from the Glauber model [75] in a given centrality class "C",

$$R_{pA}^{C} = \frac{N_{pA}^{C}}{\langle T_{pA} \rangle_C \sigma_{pp}}. \tag{1.25}$$

Centrality is a measure to quantify how central or peripheral the p-Pb or Pb-Pb collisions are. It is related to the overlaping of the colliding nuclei and also to the impact parameter of the collisions. The impact parameter is the distance the centers of the two colliding nuclei in the transverse plane to the beam direction.

In case of minimum bias p-A collisions the nuclear modification factor is independent of the centrality "C" so R_{pA}^{C} will be reduced to R_{pA},

$$R_{pA} = \frac{\sigma_{pA}}{A\,\sigma_{pp}} \tag{1.26}$$

where "A" is the mass number of the colliding nucleus. In the absence of cold nuclear matter effect R_{pA} will become equal to unity.

1.6.2.1 Recent experimental results

The production cross section of lepton from charm and beauty decays (heavy-flavor decay leptons), has been measured at the RHIC in d-Au collisions at $\sqrt{s_{\rm NN}} = 200$ GeV and at the LHC in p–Pb collisions at $\sqrt{s_{\rm NN}} = 5.02$ TeV. The HF-lepton spectrum is measured by subtracting the non-heavy-flavor contribution from the inclusive yield.

The R_{dAu} was studied by STAR and PHENIX in [115, 116] for the heavy-flavor decay leptons in different rapidity regions and in minimum bias and in different centralities in d-Au collisions at $\sqrt{s_{\rm NN}} = 200$ GeV. These results show an enhancement of the HF electrons production for central and forward rapidities, and a small suppression at backward rapidity for central collisions. While in peripheral collisions all the results are consistent and they show no nuclear modification for the HFe spectrum. The data at backward rapidity were not described by the model calculation considering nPDF only.

At the LHC, the ALICE collaboration measured the R_{pPb} for the heavy-flavor decay leptons [117, 118] at central rapidity for electrons and forward ($-4.46 < y_{cms} < -2.96$) and backward ($2.03 < y_{cms} < 3.53$) rapidity for the muons as shown in Fig. 1.23. This figure shows no nuclear modification for the HF electrons at mid-rapidity, and also the R_{pPb} for muons at forward rapidity is equal to unity, while slight enhancement was observed at low momenta for the backward rapidity HF muons which could be caused by the Cronin effect [25]. The data was described by the model calculation with nPDFs at high p_T which is different for RHIC case.

The ALICE collaboration also measured the nuclear modification R_{pPb} of the beauty-hadron decay electrons [119] at mid-rapidity, and the result was no modification observed for the beauty decay electrons within uncertainties. These results from RHIC and the LHC at low p_T on the HF leptons are not describes by the models that consider the nPDF only. This means that the nPDF is not the dominant effect in the heavy-flavor production. Other effects could be present like k_T-broadening or initial or final state energy loss.

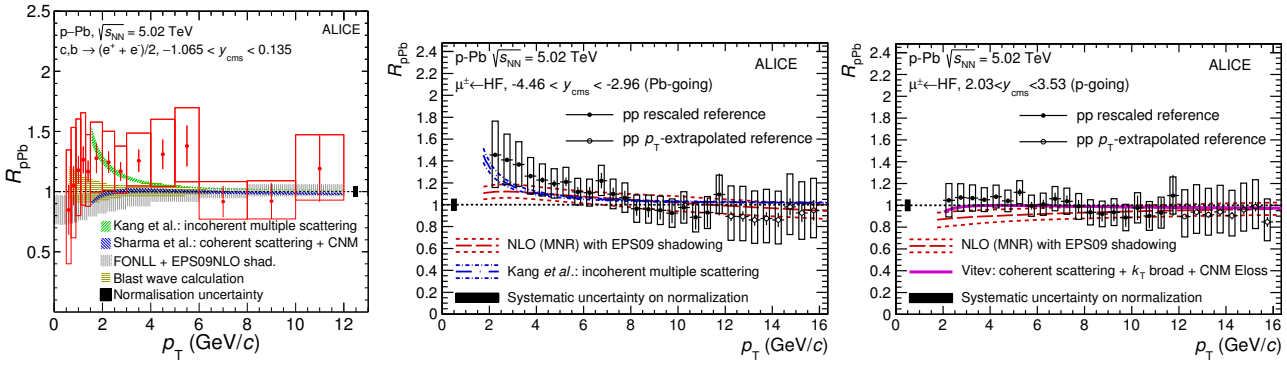

(a) (b) (c)

Fig. 1.23 Nuclear modification factor for (a) HF electrons in central rapidity [118] (b) HF muons at forward rapidity (c) HF muons at backward rapidity [117].

The production cross section of the D^0, D^+, D^{*+} and D_s^+ mesons was measured by ALICE in minimum bias p–Pb collisions at $\sqrt{s_{\rm NN}}$ = 5.02 TeV [120, 121] and also as a function of multiplicity [122]. D mesons are reconstructed through their hadronic decay, and the prompt D-meson spectrum is obtained by removing the contribution from non-prompt D-mesons from B-hadron decay, which is estimated by the pQCD. Figure 1.24 shows the nuclear modification factor R_{pPb} for the average prompt D (D^0, D^+, D^{*+} and D_s^+) mesons compared to the theory predictions. The R_{pPb} was close to unity within uncertainties which means that no nuclear modification of the D-meson production was observed and was also well described by the theory prediction.

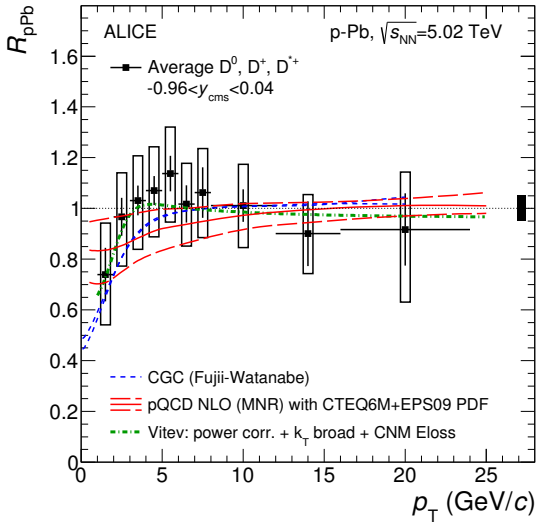

Fig. 1.24 Nuclear modification factor R_{pPb} of prompt D mesons in p–Pb collision as a function of p_T measured by the ALICE detector [121].

The ALICE collaboration also measured the production cross section and the nuclear modification factor R_{pPb} of the charmed baryon Λ_C^+ in minimum bias p–Pb collisions [98], and the result was also similar to the D meson, no nuclear modification was observed for the Λ_c production within uncertainties.

The charm jet production cross section (c-jet) was also measured by the CMS detector in p–Pb collision at $\sqrt{s_{\rm NN}} = 5.02$ TeV [123]. A charm jet or c-jet is defined as a jet that contains a c-quark within the jet cone. The c-jets are identified through tagging the secondary vertex consistent with the charmed hadrons decay vertices. Figure 1.25 shows the differential production cross of the c-jet compared with the pp data (top), and the R_{pPb}^{c-jet} (bottom). From this figure, it is clear that there is no nuclear modification for the c-jet in p–Pb collisions within the measured uncertainties.

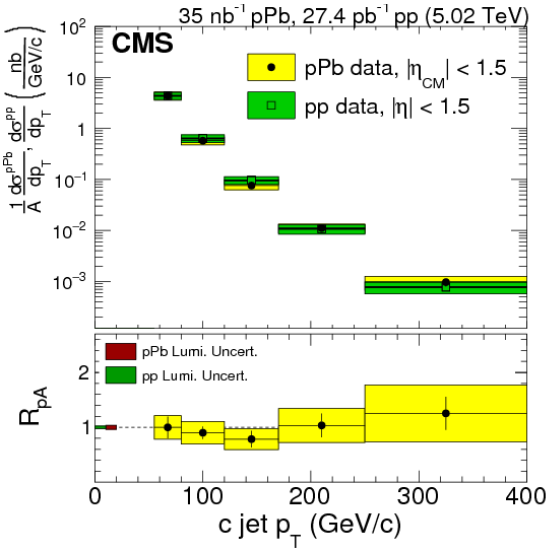

Fig. 1.25 Production cross section of the c-jet (top) and the R_{pPb} of the c-jet (bottom) as a function of p_T in p–Pb collisions measured by the CMS detector [123].

The beauty quark production was measured by LHCb in p–Pb collisions at $\sqrt{s_{\rm NN}} = 5.02$ TeV [124]. This measurement done by analyzing the non-prompt J/ψ mesons, the fraction of non-prompt J/ψ coming from b-hadron decays, was estimated from fitting templates of the pseudo-proper lifetime of the J/ψ. The result was that, in the backward rapidity region, the R_{pPb} was close to unity, while in the forward rapidity region, small suppression was observed.

The CMS collaboration measured the production of B mesons in p–Pb collisions [125, 126], the B^0, B^+ and B_s^0 mesons were reconstructed at mid-rapidity through their hadronic decays to $J/\psi + K$ or to $J/\psi + \phi$. The production cross section was described by FONLL prediction within uncertainties, and there was no nuclear modification observed for the b-meson production.

The b-jet production cross section was measured by the CMS in p–Pb collisions at $\sqrt{s_{\rm NN}} = 5.02$ TeV [127]. The tagging of the b-jet was performed by the secondary vertex algorithm and the cross section was described by PYTHIA simulation. Figure 1.26 shows the nuclear modification factor R_{pPb}^{b-jet} for the b-jets. According to [127], no nuclear modification occurred for the b-jet spectra. Also in [127] they studied the nuclear modification factor of the b-jets in different rapidity regions and the result was no nuclear modification has occurred for the b-jets.

The b-jet measurements in p–Pb done by the CMS is for the high p_T jets. The aim of this thesis is to measure the b-jet production cross section in the low p_T region where the b-quark mass dependence of the R_{pPb}^{b-jet} can be seen.

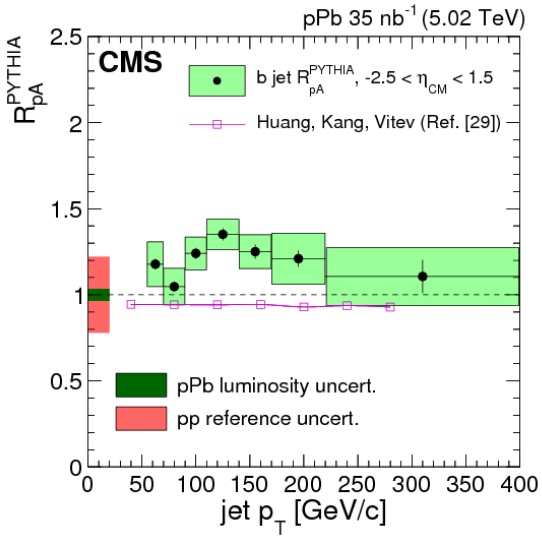

Fig. 1.26 Nuclear modification factor of the b-jet as a function of p_T in p–Pb at $\sqrt{s_{\rm NN}} = 5.02$ TeV [127].

In summary, nuclear modification factor of the heavy-flavor decay leptons and the D-mesons, is consistent with unity within uncertainties. As a result, the cold nuclear matter effect has no influence on the open heavy-flavor particle production in nucleon-nucleus collisions.

1.6.3 Open heavy-flavor production in A-A collisions

Heavy-flavor hadrons are important probe for the study of the hot and dense medium formed in ultra relativistic heavy-ion collisions.

The nuclear modification factor R_{AA} of the heavy-quarks (Eq. 1.24) can be used as an observable for the study of the energy loss. At high transverse momentum, the R_{AA} is very sensitive to the heavy-quark energy loss in the medium.

One of the targets for the heavy-flavor analysis in heavy-ion collisions, is the study of the characteristic of the produced QCD medium or generally studying the transport coefficient. By comparing the experimental result with the different outcomes resulting from the choices of the transport coefficient in the theoretical calculations, then it is possible to constraint the transport coefficient of the QGP through the interaction of heavy-quarks with the medium. This is similar to the extraction of the QGP viscosity by comparing the soft particles spectra from data with the theory prediction from the fluid dynamic models.

1.6.3.1 Recent experimental results

The production cross section of the electrons from heavy-flavor decays was measured by the STAR [128] and PHENIX [129–131] collaborations in different systems and different energies at different centralities. These results show a clear suppression of the heavy-flavor electrons in Au-Au collision at $\sqrt{s_{\rm NN}} = 200$ GeV, which was observed in Au-Au collision at $\sqrt{s_{\rm NN}} = 62.4$ GeV. The STAR and PHENIX results show that the R_{AA} of the electrons

is dependent on the center-of-mass energy, dependent on the colliding system and it also depends on the centrality of the collisions.

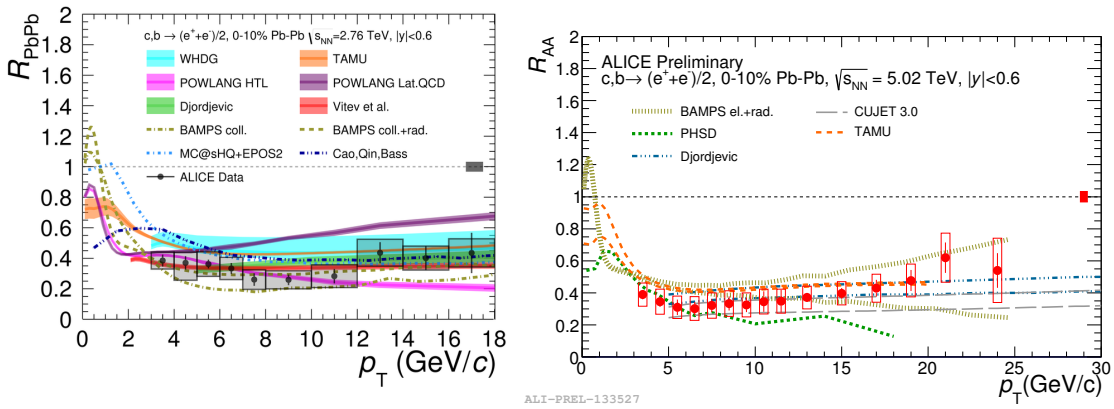

(a) (b)

Fig. 1.27 Nuclear modification factor for HF electrons in central Pb-Pb collisions at (a) $\sqrt{s_{\rm NN}} = 2.76$ TeV [132] (b)$\sqrt{s_{\rm NN}} = 5.02$ TeV [133].

At the LHC the production cross section of the heavy-flavor decay leptons was measured in Pb-Pb collisions at $\sqrt{s_{\rm NN}} = 2.76$ TeV [132, 81, 134] and at $\sqrt{s_{\rm NN}} = 5.02$ TeV [133]. Figure 1.27 shows the nuclear modification factor R_{AA} for electron from heavy flavor decays in Pb–Pb collisions at $\sqrt{s_{\rm NN}} = 2.76$, 5.02 TeV compared to the theory predictions. This figure shows that the HF electrons are largely suppressed in central Pb–Pb , and there is no significant increase in the R_{AA} by increasing the center-of-mass energy. This figure also shows that the R_{AA} of the electrons is well described by the theory prediction.

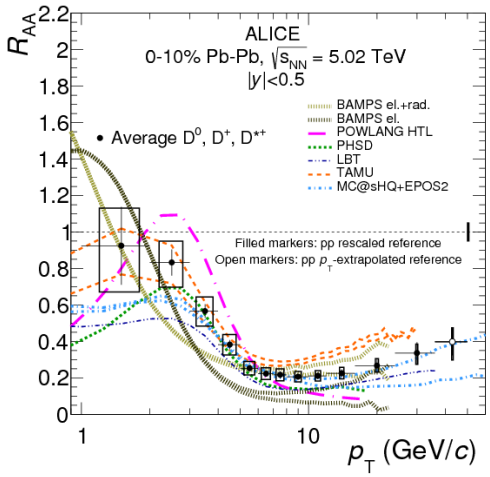

Fig. 1.28 Nuclear modification factor R_{AA} of the D mesons in Pb–Pb collision as a function of p_T measured by the ALICE detector [135].

The production cross section for the open charm mesons (D^0, D^+ and D^{*+}) was measured by the ALICE [136, 137, 135], CMS [138, 139] and STAR collaborations through their hadronic decay channels. Figure 1.28 show the nuclear modification R_{AA} of the D

mesons measured by ALICE in central Pb–Pb collisions at $\sqrt{s_{\rm NN}} = 5.02$ TeV compared with the theory prediction. This figure shows a large suppression of the D meson in central Pb–Pb collisions, this suppression is largely dependent on the p_T of the D mesons. The R_{AA} of the D-mesons is described by the theory prediction. The result of [137] also shows that the R_{AA} of the D mesons is increasing with centrality, so the $R_{AA}^{D-meson}$ is dependent on the multiplicity of the system.

The beauty hadrons are identified and detected by exploiting their long life time, and it requires strong tracking and vertexing capabilities. The ALICE collaboration measured the beauty hadrons through their semi-leptonic decay in Pb–Pb at $\sqrt{s_{\rm NN}} = 2.76$ TeV [119]. In order to extract the "b" contribution, templates of the impact parameter distribution for the different electron sources are fitted to the inclusive yield. The result shows a strong suppression of the electrons from beauty-hadron decays.

Another method for studying beauty hadron is through the measurement of the non-prompt D^0 mesons [140] and also through the study of the non-prompt J/ψ.The first method (non-prompt D^0 mesons) was applied by the CMS, and second method (non-prompt J/ψ) was applied by the ALICE collaborations in the central rapidity region [141] and by the CMS collaborations [142] in forward rapidity. In order to extract the non-prompt contribution of the J/ψ we fit templates of the lifetime for the different source of J/ψ to the inclusive yield.

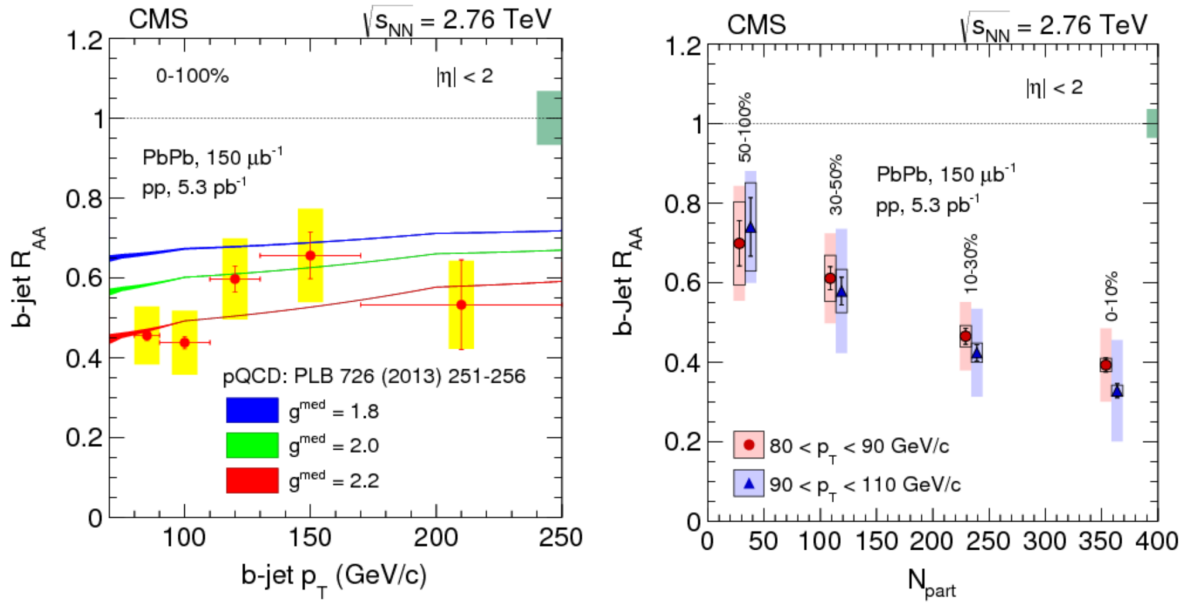

(a) (b)

Fig. 1.29 Nuclear modification factor of the b-jets as a function of (a) p_T (b)Centrality in Pb–Pb collisions at $\sqrt{s_{\rm NN}} = 2.76$ TeV measured by CMS [143].

The differential production cross section of the b-jet was measured by the CMS in Pb–Pb collisions at $\sqrt{s_{\rm NN}} = 2.76$ TeV by reconstructing the displaced secondary vertices related to the jet [143]. Figure 1.29 show the nuclear modification factor of the b-jet as a function of centrality (right) and p_T (left). This figure (left panel) shows a strong suppression of the b-jet in Pb–Pb and it was described by the theory prediction of [11].

The right panel of Fig. 1.29 shows that the b-jet suppression is largely dependent on the centrality of the collision.

For more details on the quarkonium and heavy-flavor production and nuclear modification factor refer to [144].

In summary, the nuclear modification R_{AA} shows a strong suppression of the heavy-flavor particles production in A–A collisions. Also, the R_{AA} is consistent with the different energy loss models within uncertainties.

Chapter 2

New partonic energy loss model

A new model for the medium is proposed in this thesis, in which the medium is considered as a collection of static colored scattering centers in the presence of a background chromomagnetic field. In this scenario a new energy loss mechanism can be studied: a background field induced radiative energy loss which will also include the effect of the scattering with the medium particles. In [145, 146] using numerical simulations it was shown that a strong chromomagnetic field is created in a relativistic heavy-ion collisions and it can be treated as a classical background field. Hence, a fast parton traversing the medium will feel the effect of the color magnetic and the color electric fields while undergoing multiple scatterings with the particles in the medium. Therefore, in this case, a radiative energy loss will be obtained with a certain dependence on the energy of the incident parton and the medium size.

This chapter is organized as follows: In Sec. 2.1 the general theoretical framework will be introduced base on the light-cone approach in the presence of a classical background field. The main target of this section is to be as pedagogic and self-contained as possible since the existing descriptions of this formalism in the literature are not easily accessible. In Sec. 2.2, the general framework to derive expressions for the parton energy loss will be shown in the presence of the following three background field configurations:

1. *An impulse field configuration.* The impulse field approximation for an arbitrary field can be seen as a succession of N impulse fields at different locations. In this thesis, the case of only one impulse in a small localized region of space will be considered.

2. *A zero background field and taking into account a single scattering.* As expected, in this limit the same radiation spectrum as in [147] is recovered with the same energy, color and energy fraction (x) dependences.

3. *A constant background field.* In this case, the parton in a constant chromomagnetic background field undergoing a single scattering with a static scattering center will be considered. Note that the case of a constant background field has been studied before by Zakharov [148], however, without including medium effects.

2.1 Theoretical framework

This section provides an overview of required ingredients entering the theoretical framework, in order to be self-contained as much as possible.

The different elements have to be taken into account:

- Firstly, describe the interaction of the colored parton with a colored background field. For this purpose, the "color part" of the interaction has to be described.
- Secondly, the kinematics has to be described. a) Propagation of the parton in a background field. b) Kinematics of the scattering with the static scattering centers. For this purpose, the light-cone formalism is used.

2.1.1 Color charge "representation"

As described in [149] the coupling between partons and the chromomagnetic background field is characterized through a color charge. The color charge can be explicitly obtained by starting from the QCD Lagrangian, decomposing the gauge field into quantum fluctuations and a classical background field, then regrouping terms that couple to a given background color index. The coupling constant g is then found to be multiplied by a number which can be interpreted as a color charge.

A more formal approach is to use the Cartan subalgebra of SU(3). Indeed, each state in an irreducible representation of the SU(3) color algebra is characterized by a weight which encodes the information on the quantum numbers of the state with respect to the commuting (diagonal) generators in the Cartan subalgebra. Choosing as a basis of the Cartan subalgebra the usual generators $\mathcal{H}_1 = T_3$ and $\mathcal{H}_2 = T_8$ the weights are represented by two-dimensional weight vectors which can be interpreted as color charges (Q_3, Q_8). This is quite general and holds in particular for the quarks in the fundamental representation and the gluons in the adjoint representation (where the weights are called roots). Defining the following complex linear combinations of the remaining six generators as

$$E_{\pm\alpha} = T_1 \pm iT_2\,, E_{\pm\beta} = T_6 \pm iT_7\,, E_{\pm\gamma} = T_4 \pm iT_5\,, \tag{2.1}$$

these new matrices will play the role of raising and lowering operators satisfying

$$[\mathcal{H}_i, E_\xi] \equiv \mathrm{ad}(\mathcal{H}_i)E_\xi = \xi(\mathcal{H}_i)E_\xi\ .$$

Hence the E_ξ are eigenvectors of the elements of the Cartan subalgebra in the adjoint representation, $ad(\mathcal{H}_1)$ and $ad(\mathcal{H}_2)$. The weights ξ of the adjoint representation are called the roots. They represent the color charges of the eight gluons in the adjoint representation. A simple calculation gives two neutral gluons (G_3 and G_8) and six charged gluons with the following charges $(\xi(\mathcal{H}_1), \xi(\mathcal{H}_2) = (Q_3, Q_8))$:

$$(1,0)\ ,\ (-1,0)\ ,\ (-\frac{1}{2}, \frac{\sqrt{3}}{2})\ ,\ (\frac{1}{2}, -\frac{\sqrt{3}}{2})\ , (\frac{1}{2}, \frac{\sqrt{3}}{2})\ ,\ (-\frac{1}{2}, -\frac{\sqrt{3}}{2})\ .$$

The quarks are found in the fundamental representation with the following weights/charges:

$$(\frac{1}{2}, \frac{\sqrt{3}}{6}) \ , \ (-\frac{1}{2}, \frac{\sqrt{3}}{6}) \ , \ (0, -\frac{\sqrt{3}}{3}) \ .$$

The color charges appear always in combination with the strong interaction coupling constant g, such that it is possible to absorb the effect of the "charge" in the coupling and define a new coupling $g_A^i = gQ_i$ for gluons and $g_q^i = gq_i$ for the quarks.

For simplicity, in the following, we consider a background field which is in color space either proportional to T_3 or to T_8 but not to a linear combination of the two. As a consequence only the color charge Q_3 respectively Q_8 of the vector (Q_3, Q_8) will appear in the interaction Lagrangian.

2.1.2 Background field propagator

The propagation of a highly energetic parton of color charge Q in an external field can be understood in terms of wave functions. The equation of motion for a fast quark can be derived using the QCD Lagrangian with a background field. In the following, we use light-cone variables $z := (t+x_3)/2$ and $\xi := t-x_3$ formed out of the space-time coordinates $x^\mu = (t, x_1, x_2, x_3) = (t, \boldsymbol{\rho}, x_3)$ so that $x^\mu = (z, \xi, \boldsymbol{\rho})$. Furthermore, the momentum space variables are given by

$$p^\mu = (E, \boldsymbol{p}_\perp, p_L) = (p^+, p^-, \boldsymbol{p}_\perp) = (p^+, \frac{\boldsymbol{p}_\perp^2 + m^2}{2p^+}, \boldsymbol{p}_\perp)$$

with $p^+ := (E + p_L)/2$, $p^- := E - p_L$.

For a highly energetic parton moving essentially in longitudinal direction we have $E \simeq p_L \gg |\boldsymbol{p}_\perp|$ such that $p^+ \simeq E$ and $p^- \simeq 0$.

For the wave function of the quark, the following ansatz can be made assuming a plane wave in the ξ direction (and omitting the color factor):

$$\psi(z, \xi, \boldsymbol{\rho}) = \exp[-ip^+\xi]\hat{u}_{\lambda_q}\phi(\boldsymbol{\rho}, z)/\sqrt{2p^+} \ \simeq \ \exp[-iE\xi]\hat{u}_{\lambda_q}\phi(\boldsymbol{\rho}, z)/\sqrt{2E} \ , \tag{2.2}$$

where $\hat{u}_{\lambda_q}$ is the Dirac spinor operator for a quark of helicity $\lambda_q = \pm 1/2$. The $1/\sqrt{2E}$ normalization factor is included in the wave function and not in the Lorentz invariant phase space which will lead later to a normalization factor for the vertex operator.

Given the simple factorized ξ dependence, the evolution in the z variable can be worked out with ξ constant. Hence z can be understood interchangeably as either x_3 or t ($z = x_3 + \xi/2 = t - \xi/2$, hence $\partial_z = \partial_3 = \partial_t$). The z evolution equation for the function $\phi(\boldsymbol{\rho}, z)$ in external magnetic and electric fields $\boldsymbol{B}$ and $\boldsymbol{\varepsilon}$, respectively, represented by a gauge field A^μ, is given by the two-dimensional Schrödinger-like equation [148]

$$i\frac{\partial\phi}{\partial z} = \left\{ \frac{(\mathbf{p} - gQ\mathbf{A})_\perp^2 + m^2}{2E} + gQ(A^0 - A^3) \right\} \phi \ , \tag{2.3}$$

where m is the mass of the quark parton.

For constant chromo-magnetic/-electric fields perpendicular to the z direction, the vector potential can be written as $A^0 = -\boldsymbol{\rho}\cdot\boldsymbol{\varepsilon}$, $\mathbf{A}_\perp = 0$, and $A^3 = [\mathbf{B}\times\boldsymbol{\rho}]_3$. Then it is easy to see that (for this field configuration) the potential energy term in Eq. (2.3) takes the form $gQ(A^0 - A^3) = -\mathbf{F}\cdot\boldsymbol{\rho}$ with $\mathbf{F} = gQ(\boldsymbol{\varepsilon} + \boldsymbol{v}\times\mathbf{B})$ where $\boldsymbol{v} \simeq (0,0,1)$ is the velocity of the fast incoming parton. Hence, $gQ(A^0 - A^3)$ can be interpreted as the potential energy $U(\boldsymbol{\rho}, z) = -\mathbf{F}\cdot\boldsymbol{\rho}$ with a constant Lorentz force $\mathbf{F} = (F_x, F_y, 0)$ in the transverse plane acting on a particle with a color charge gQ.

Using the path integral approach, the z evolution can be written in terms of the kernel K_F as

$$\phi(\tau_f, z_f) = \int d^2\tau_i K_F(\tau_f, z_f; \tau_i, z_i)\phi(\tau_i, z_i)\ . \tag{2.4}$$

The propagator K_F can be obtained with the assumption that the classical force $\boldsymbol{F}$ is $\boldsymbol{\rho}$ independent and hence it acts as a classical source. The particle propagator with an external source can be written in the generic form [150]:

$$\begin{aligned} K_F(\boldsymbol{\rho}_2, z_2; \boldsymbol{\rho}_1, z_1) \;=\; & \frac{m_{\text{eff}}}{2\pi i(z_2 - z_1)} \exp\left[\frac{i}{(z_2 - z_1)}\left\{\frac{m_{\text{eff}}}{2}(\boldsymbol{\rho}_2 - \boldsymbol{\rho}_1)^2 + \int dz \mathbf{F}(z)\cdot\boldsymbol{\rho}_1(z_2 - z)\right.\right. \\ & + \int dz \mathbf{F}(z)\cdot\boldsymbol{\rho}_2(z - z_1) - \frac{\epsilon^2}{2m_{\text{eff}}}(z_2 - z_1)^2 \\ & \left.\left. - \frac{1}{m_{\text{eff}}}\int_{z_1}^{z_2} dz \int_{z_1}^{z} dz' \mathbf{F}(z)\cdot\mathbf{F}(z')(z_2 - z)(z' - z_1)\right\}\right], \end{aligned} \tag{2.5}$$

where m_{eff} is the effective mass of the particle. For a single particle in the eikonal approximation m_{eff} is the energy of the particle ($m_{\text{eff}}^2 = E^2$) while for a composite system it will be a combination of particle masses as we will see later.

The same steps are followed for the gluon. The gluon wave function can be written in a similar form as in Eq. (2.2) up to the replacement of the spinor operator by the polarization vector and the appropriate normalization. A similar two dimensional Schrödinger-like equation is derived for the gluon ϕ-field starting from the Yang-Mills Lagrangian after separating the background field from the quantum fluctuations.

Gluon radiation processes are obtained when we couple the quark to quantum fluctuations of the gluon (A^μ_{quantum}). For instance, a quark q can split into a gluon g and another quark q' with different energy and colour due to the interaction Lagrangian

$$g_s Q_q \bar{\Psi}\gamma_\mu A^\mu_{\text{quantum}}\Psi\ ,$$

where g_s is the strong coupling constant and Q_q (i.e. Q_q^3 or Q_q^8) is the color charge of the initial quark which can be expressed in terms of the color charges of the gluon and the final quark due to charge conservation at the vertex, $Q_q = Q_g + Q_{q'}$.

"Feynman rules" are derived using the light-cone setting introduced at the beginning of this section where also the gamma matrices are decomposed into light-cone components as done for the momenta. For each vertex, products of spinors of different momenta with gamma matrices are computed using the helicity amplitudes given in [151] (see Tab. 2).

One can choose also to work in the light cone gauge with $\eta \cdot k = k^+$ and with a circular polarization ε for the gluon such that the polarization tensor reads:

$$d_{\mu\nu} = -g_{\mu\nu} + \frac{\eta_\mu k_\nu + \eta_\nu k_\mu}{\eta \cdot k} = \sum_{\lambda_g=\pm}\left[-\eta_\mu \frac{\varepsilon^{(\lambda_g)} \cdot k}{\eta \cdot k} + \varepsilon_\mu^{(\lambda_g)}\right] \cdot \left[-\eta_\nu \frac{\varepsilon^{(\lambda_g)} \cdot k}{\eta \cdot k} + \varepsilon_\nu^{(\lambda_g)}\right]. \quad (2.6)$$

A gluon is then characterized by a helicity $\lambda_g = \pm 1$. The qqg vertex can be decomposed into a non spin flip (nsf) contribution, where the helicity of the initial quark is not affected by gluon radiation, and a spin flip (sf) term, where the helicity is reversed after gluon emission. Using the helicity amplitude method, the nsf-vertex in momentum space with its Lorentz and spinor structure can be represented by (without colour structure yet)

$$V_{\text{nsf}}^{\lambda_g\lambda_q}(x) = i\sqrt{\frac{\alpha_s}{2x}}\left[2\lambda_q x + \lambda_g(2-x)\right]\frac{[q_x - i\lambda_g q_y]}{2\mu}, \quad (2.7)$$

$$V_{\text{sf}}(x) = im\frac{\sqrt{2\alpha_s x^3}}{2\mu} \quad (2.8)$$

where $\mathbf{q} = (1-x)\mathbf{p}_g - x\mathbf{p}_{q'}$, $x = E_g/E_q$ is the gluon energy fraction, m is the quark mass and $\mu = E_q x(1-x)$ is the Schrödinger mass. The propagator has a simple coordinate space representation, hence it is convenient to also have the vertex structure in coordinate space. The Dirac spinor used to construct the vertex is an eigenvector of the momentum operator in the impact parameter space.

In case of incident gluon, the ggg nsf vertex in momentum space can be written as:

$$\vec{V}_{\text{nsf}}^{ggg}(x) = i\sqrt{\frac{\alpha_s}{2x(1-x)}}\left[2x(1-x) - 2\right]\frac{\mathbf{q}}{2\mu}, \quad (2.9)$$

$\mathbf{q} = (1-x)\mathbf{p}_{g'} - x\mathbf{p}_{g''}$ in which $\mathbf{p}_{g'}$ is the momentum of the radiated gluon and $\mathbf{p}_{g''}$ is the momentum of the outgoing gluon, $x = E_{g'}/E_g$ is energy fraction carried by the radiated gluon from the incident gluon.

The vertex operator can then be obtained using

$$q_{x,y} \to \frac{1}{i}\partial_{x,y}.$$

This should be done for the quark and the gluon momenta $\mathbf{p}_{q'}$ and $\mathbf{p}_g$, respectively. Using the change of variables

$$\begin{aligned} \boldsymbol{\rho} &= \boldsymbol{\rho}_g - \boldsymbol{\rho}_{q'}, \\ \boldsymbol{\rho}_{C.M.} &= x\boldsymbol{\rho}_g + (1-x)\boldsymbol{\rho}_{q'}, \end{aligned} \quad (2.10)$$

we can show that the vertex operator has the form

$$\hat{V}^{\lambda_g\lambda_q} = \hat{V}_{\text{nsf}}^{\lambda_g\lambda_q} + \hat{V}_{\text{sf}}^{\lambda_g\lambda_q} = (\boldsymbol{\rho}, x) = P(x)\left[\frac{\partial}{\partial\rho_x} - i\lambda_g\frac{\partial}{\partial\rho_y}\right] + P_{\text{sf}}(x), \quad (2.11)$$

where the factor $P(x)$ is

$$P(x) = \sqrt{\frac{\alpha_s}{2x}}\,[2\lambda_q x + \lambda_g(2-x)]\,\frac{1}{2\mu} \;\text{ and }\; P_{\rm sf}(x) = m\frac{\sqrt{2\alpha_s x^3}}{2\mu}.$$

In the low mass limit, the contribution of the spin flip term can be neglected and we can keep only the non-spin flip (nsf) contribution.

In the case of a propagating gluon, the vertex operator of ggg system has the form

$$\hat{V}^{ggg}_{\rm nsf}(\boldsymbol{\rho}, x) = P_g(x)\left[\frac{\partial}{\partial\boldsymbol{\rho}}\right]\,, \tag{2.12}$$

where the factor P_g is

$$P(x) = \sqrt{\frac{\alpha_s}{2x(1-x)}}\,[2x(1-x)-2]\,\frac{1}{2\mu}\,.$$

Since the quark and gluon cases are very similar, in what follows everything will be done for the quark case unless there was a difference, in that case it will be mentioned.

The gluon-quark-quark vertex represents a local interaction, *i.e.*, $\boldsymbol{\rho}_g = \boldsymbol{\rho}_{q'}$. Hence in constructing Feynman diagrams this vertex will be proportional to the Dirac delta function $\delta^2(\boldsymbol{\rho})$. The position of the quark q can be safely taken as $\boldsymbol{\rho}_{C.M.}$ since at the vertex derivatives with respect to the outgoing quark and gluon are used only.

The Feynman rules in the impact parameter space are summarized in Fig.2.1.

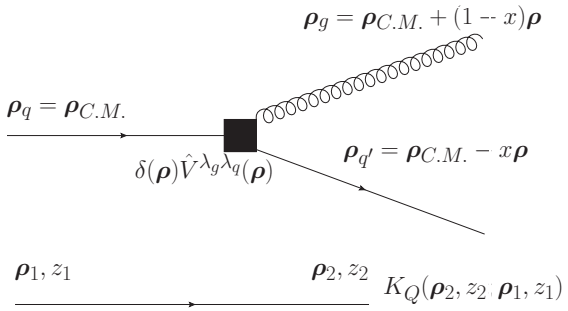

Fig. 2.1 Feynman rules in the impact parameter space for the light cone path approach. The vertex $\hat{V}^{\lambda_g\lambda_q}_{\rm nsf}(\boldsymbol{\rho}, x)$ is given in Eq. (2.11) and $K_Q \equiv K_F$ represents the propagator in a background field given in Eq. (2.5) (which depends on the colour charge Q).

Physical processes can be derived using the Feynman rules cited above either in coordinate space or in (transverse) momentum space. We have absorbed all the $1/(2E)$ factors into the definition of the vertex.

The propagator K_F will receive quantum corrections at higher orders due to the interaction with the quantum field $A_{\rm quantum}$. The first order quantum correction to K_F is shown in Fig. 2.2.

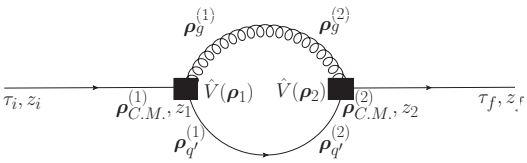

Fig. 2.2 One loop quantum corrections to the quark propagator.

Applying Feynman rules to the one loop diagram, and summing over the quark and gluon helicities and colors, we obtain the quantum correction for the propagator δK:

$$\delta K(\boldsymbol{\tau}_f, z_f; \boldsymbol{\tau}_i, z_i) = \int dx d^2\boldsymbol{\rho}_{C.M.}^{(1)} d^2\boldsymbol{\rho}_{C.M.}^{(2)} d^2\boldsymbol{\rho}_1 d^2\boldsymbol{\rho}_2 dz_1 dz_2 \delta^2(\boldsymbol{\rho}_1)\delta^2(\boldsymbol{\rho}_2)\hat{g}_q(\boldsymbol{\rho}_1, \boldsymbol{\rho}_2, x)$$
$$K_q(\boldsymbol{\rho}_{C.M.}^{(1)}, z_1; \boldsymbol{\tau}_i, z_i) K_g(\boldsymbol{\rho}_g^{(2)}, z_2; \boldsymbol{\rho}_g^{(1)}, z_1) K_{q'}(\boldsymbol{\rho}_{q'}^{(2)}, z_2; \boldsymbol{\rho}_{q'}^{(1)}, z_1) K_q(\boldsymbol{\tau}_f, z_f; \boldsymbol{\rho}_{C.M.}^{(2)}, z_2) \quad (2.13)$$

Here, the new operator $\hat{g}_q$ is the product of the two vertex factors with the sum over color and helicities performed:

$$\begin{aligned} \hat{g}_q(\boldsymbol{\rho}_1, \boldsymbol{\rho}_2, x) &= C_F \sum_{\lambda_q \lambda_g} \hat{V}^{\lambda_q \lambda_g}(\boldsymbol{\rho}_1, x)(\hat{V}^{\lambda_q \lambda_g}(\boldsymbol{\rho}_2, x))^\dagger \\ &= G_q(x) \frac{1}{\mu^2} \frac{\partial}{\partial \boldsymbol{\rho}_1} \cdot \frac{\partial}{\partial \boldsymbol{\rho}_2}, \end{aligned} \quad (2.14)$$

with

$$G_q(x) = \alpha_s C_F [1 - x + x^2/2]/x = \frac{\alpha_s}{2} P_{gq}^{(0)}(x), \quad (2.15)$$

where $P_{gq}^{(0)}(x) = C_F[1 + (1-x)^2]/x$ is the well-known leading order splitting function $P_{gq}^{(0)}(x) = C_F[1 + (1-x)^2]/x$ describing the branching $q \to gq$ of a quark into a collinear gluon carrying a momentum fraction x of the quark momentum.

And for the gluon case (ggg) the operator $\hat{g}$ can be written as:

$$\hat{g}_g(\boldsymbol{\rho}_1, \boldsymbol{\rho}_2, x) = G_g(x) \frac{1}{\mu^2} \frac{\partial}{\partial \boldsymbol{\rho}_1} \cdot \frac{\partial}{\partial \boldsymbol{\rho}_2}, \quad (2.16)$$

with

$$G_g(x) = \alpha_s C_A \frac{x^4 + (1-x)^4 + 1}{4x(1-x)} = \frac{\alpha_s}{4} \hat{P}_{gg}^{(0)}(x), \quad (2.17)$$

where $\hat{P}_{gg}^{(0)}(x)$ is the regular part ($x < 1$) of the leading order splitting function $P_{gg}^{(0)}(x)$ describing the collinear branching $g \to gg$ of a gluon into a gluon with a momentum fraction x; it is symmetric under the exchange $x \leftrightarrow 1 - x$.

It should be noted that $\hat{P}_{gg}^{(0)}(x)$ is divergent in the limit $x \to 1$. This soft gluon divergence gets canceled once the virtual contributions to the splitting function are taken into account. The splitting function $P_{gg}^{(0)}(x)$ then turns into a distribution which is

well-behaved in the limit $x \to 1$:

$$P_{gg}^{(0)}(x) = 2C_A \left[\frac{x}{(1-x)_+} + \frac{1-x}{x} + x(1-x) \right] - \left[\frac{11}{6} C_A - \frac{2}{3} T_R N_F \right] \delta(1-x) \tag{2.18}$$

where the '+'-distribution is defined in the usual way [152], $T_R = 1/2$, and N_F is the number of active quark flavours. Consequently, in the following, we identify the function $G_g(x)$ with the full splitting function:

$$G_g(x) = \frac{\alpha_s}{4} P_{gg}^{(0)}(x) \,. \tag{2.19}$$

The propagators for the quark q, the quark q' and the gluon g in the background field are denoted now by $K_{q,q',g}$ with the appropriate color charge of the particle replaced in K_F in Eq. (2.5). As said above, the vertex operator, V, does not act on the external quark propagator with $(\boldsymbol{\rho}_{C.M.}^{(1)}, \boldsymbol{\rho}_{C.M.}^{(2)})$ dependence.

Using the explicit form of the propagator Eq. (2.5) and the change of variables in Eq. (2.10) the product of the gluon-quark propagators in the loop can be written as:

$$K_g(\boldsymbol{\rho}_g^{(2)}, z_2; \boldsymbol{\rho}_g^{(1)}, z_1) K_{q'}(\boldsymbol{\rho}_{q'}^{(2)}, z_2; \boldsymbol{\rho}_{q'}^{(1)}, z_1) = K_q(\boldsymbol{\rho}_{C.M.}^{(2)}, z_2; \boldsymbol{\rho}_{C.M.}^{(1)}, z_1) \mathcal{K}_f(\boldsymbol{\rho}_2, z_2; \boldsymbol{\rho}_1, z_1) \,. \tag{2.20}$$

where $\mathcal{K}_f$ is the effective propagator for a three body system $\bar{q}gq'$ in the presence of the external field. It can be shown that the propagator $\mathcal{K}_f$ takes the same form as K_F in Eq. (2.5) but with the replacement of the classical Lorentz force $\mathbf{F}$ by an effective force $\mathbf{f}$. The new "force" is a linear combination of the Lorentz forces on the quark q' and on the gluon: $\mathbf{f} = (1-x)\mathbf{F}_g - x\mathbf{F}_{q'}$. It should be added that the dynamics of the new three body system will have an effective mass $m_{\text{eff}}(x) = Ex(1-x) = \mu$, and $\epsilon^2 = m_g^2(1-x) + m_q^2 x^2$.

2.1.3 Propagator in a random scattering background

The construction made in the previous subsection can be modified to include medium effects. Physically, we have the propagation of a colored particle in a medium while being under the action of a chromomagnetic field. The particle will undergo scattering off particles in the medium. A common simplification is to model the medium by a (random) set of static scattering centers.

In this case, the only modification needed is to replace the propagator $\mathcal{K}_f$ of the three body $q\bar{q}g$ system discussed in Sec. 2.1.2 by a modified (medium-averaged) propagator $\mathcal{K}_s$. $\mathcal{K}_s$ can be obtained by averaging over the medium static centers using the approximation

$$\langle\langle \exp\left(iQA(\boldsymbol{\rho}_q, z) - iQA(\boldsymbol{\rho}_{\bar{q}}, z) + iQ_g A(\boldsymbol{\rho}_g, z)\right)\rangle\rangle \quad \approx \exp(iv(\boldsymbol{\rho}, z, x)) \tag{2.21}$$

with the two dimensional effective potential v being complex

$$v(\boldsymbol{\rho}, z, x) = -i \frac{n(z)\sigma_3(\boldsymbol{\rho}, x)}{2} \,.$$

Here $n(z)$ is the density of the medium and σ_3 is the cross section of the interaction of the $qg\bar{q}$ system with the medium color centers [45, 153]. Analytical evaluation of $\mathcal{K}_s$ is possible when using the dipole approximation, where $\sigma_3 \sim \boldsymbol{\rho}^2$. K_s will then be the non relativistic kernel for a two dimensional harmonic oscillator [150].

2.1.4 Gluon emission probability

As shown in [45, 153] the gluon emission probability can be written as

$$dP = 2\mathrm{Re}\int d^2\boldsymbol{\tau}_i d^2\boldsymbol{\tau}_f \phi_q^*(\boldsymbol{\tau}_f, z_f)\phi_q(\boldsymbol{\tau}_i, z_i) \times \delta K(\boldsymbol{\tau}_f, z_f; \boldsymbol{\tau}_i, z_i)\ . \tag{2.22}$$

Substituting the propagator correction δK given in Eq. (2.13) and the relation in Eq. (2.20) and the fact that

$$\int d^2\boldsymbol{\tau}_f d^2\boldsymbol{\rho}^{(2)}_{C.M.} d^2\boldsymbol{\rho}^{(1)}_{C.M.} \phi_q^*(\boldsymbol{\tau}_f, z_f) K_q(\boldsymbol{\tau}_f, z_f; \boldsymbol{\rho}^{(2)}_{C.M.}, z_2)$$
$$K_q(\boldsymbol{\rho}^{(2)}_{C.M.}, z_2; \boldsymbol{\rho}^{(1)}_{C.M.}, z_1) K_q(\boldsymbol{\rho}^{(1)}_{C.M.}, z_1; \boldsymbol{\tau}_i, z_i) = \phi_q^*(\boldsymbol{\tau}_i, z_i)$$

one can easily see that the dependence on the wave functions will be factored out leading to

$$\frac{dP}{dx} = \left(\int d^2\boldsymbol{\tau}_i \phi_q^*(\boldsymbol{\tau}_i, z_i)\phi_q(\boldsymbol{\tau}_i, z_i)\right) 2\mathrm{Re}\left(\int dz_1 dz_2 \left[\hat{g}_q(\boldsymbol{\rho}_1, \boldsymbol{\rho}_2, x) K_s(\boldsymbol{\rho}_2, z_2; \boldsymbol{\rho}_1, z_1)\right]_{\boldsymbol{\rho}_2, \boldsymbol{\rho}_1 = 0}\right). \tag{2.23}$$

The wave functions are then eliminated by the normalization condition

$$\forall z_i : \quad \int d^2\boldsymbol{\tau}_i \phi_q^*(\boldsymbol{\tau}_i, z_i)\phi_q(\boldsymbol{\tau}_i, z_i) = 1\ . \tag{2.24}$$

The medium induced gluon emission probability by a propagating quark has to exclude the vacuum effects. The fact that the initial/final quark wave function dependence has been eliminated leads to a simple subtraction of the vacuum probability through the propagator only such that

$$\frac{dP}{dx} = 2\mathrm{Re}\int dz_1 dz_2\, \hat{g}_q(\boldsymbol{\rho}_1, \boldsymbol{\rho}_2, x) \times \left(\mathcal{K}_s(\boldsymbol{\rho}_2, z_2; \boldsymbol{\rho}_1, z_1) - \mathcal{K}_s(\boldsymbol{\rho}_2, z_2; \boldsymbol{\rho}_1, z_1)|_{n=0}\right)_{\boldsymbol{\rho}_2, \boldsymbol{\rho}_1 = 0} \tag{2.25}$$

The integration bounds in Eq. (2.25) depend on the initial parton production location. We consider an asymptotic parton that is produced outside the medium as in [154]. A more physically transparent form of the emission probability can be derived where the light cone wave function of the $q\bar{q}g$ is used. Using the approximation shown in Fig. 2.3, the (medium, background) modified propagator is split into a medium modified and a field modified part. Hence, the emission probability can be written as

$$\frac{dP}{dx} = \int_0^L dz\ n(z)\frac{d\sigma_{eff}(x, z)}{dx}\ , \tag{2.26}$$

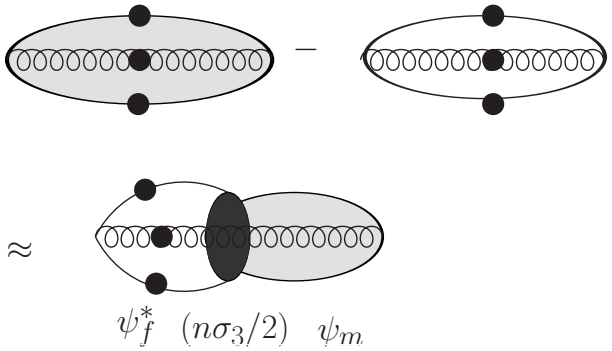

Fig. 2.3 The approximated factorization: the blob indicated background effect, the shaded area is the effect of the multiple soft scatterings in the medium. ψ_f is the light-cone wave function of the three body $q\bar{q}g$ system in the background field, ψ_m is the three body light-cone medium modified wave function.

where the effective cross section is approximated by

$$\frac{d\sigma_{eff}}{dx} = \mathrm{Re}\int d^2\boldsymbol{\rho} \sum_{\text{color,helicity}} \psi_m^*(\boldsymbol{\rho},x)\sigma_3(\boldsymbol{\rho},x)\psi_f(\boldsymbol{\rho},x,z)\,. \tag{2.27}$$

Here, ψ_f is the light-cone wave function of the three body system $q\bar{q}g$ in the background field,

$$\psi_f(\boldsymbol{\rho},x,z) \;=\; P(x)\left(\frac{\partial}{\partial\rho'_x} - i\lambda_g\frac{\partial}{\partial\rho'_y}\right)\int_0^\infty d\xi\mathcal{K}_f(\boldsymbol{\rho},z|\boldsymbol{\rho'},z-\xi)\Big|_{\rho'=0}\,, \tag{2.28}$$

where $P(x)$ is defined below Eq. (2.11) and Eq. (2.12) while ψ_m is the three-body light-cone medium modified wave function given by [147]

$$\psi_m(\boldsymbol{\rho},x,z) \;=\; P(x)\left(\frac{\partial}{\partial\rho'_x} - i\lambda_g\frac{\partial}{\partial\rho'_y}\right)\int_0^\infty d\xi\mathcal{K}_m(\boldsymbol{\rho},z+\xi|\boldsymbol{\rho'},z)\Big|_{\rho'=0}\,. \tag{2.29}$$

The color factor will be embedded later in the production probability. The three body scattering cross section $\sigma_3(\boldsymbol{\rho},x)$ will be further discussed in the following subsection.

2.1.5 σ_3 in the quasi-dipole approximation

The three body cross section σ_3 is dominated by the diagrams shown in Fig. 2.4. Figures 2.4a)-c) show the process where the same particle undergoes the scattering with the medium while Figs. 2.4d)-e) depict the interference terms between amplitudes where two different particles undergo a scattering with the medium. The ggg three body scattering cross section has similar diagrams with the replacement of the incident and outgoing quarks with gluons.

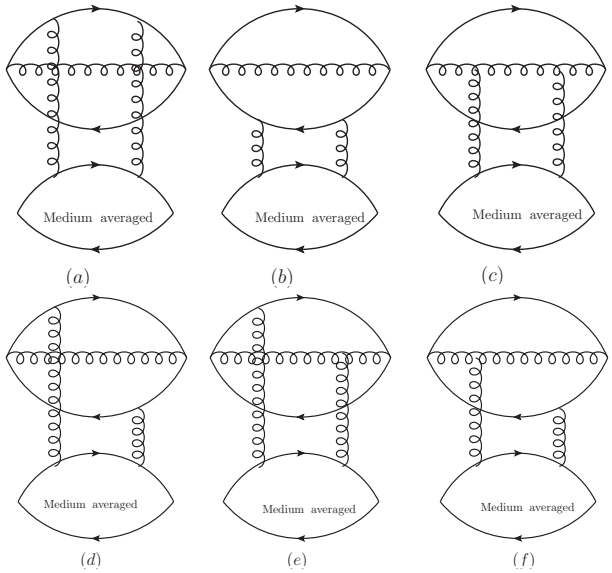

Fig. 2.4 Diagrams contributing to the three body ($qg\bar{q}$) cross section σ_3. Figures a)-c): Square of the same probability amplitude. Figures d)-e): Interference terms between different amplitudes where the exchange gluon is attached to different particles in the upper part of the diagram.

The $qg\bar{q}$ three body scattering cross section can be written in terms of the two body $q\bar{q}$ (dipole) scattering cross section as [155]

$$\sigma_3^{(q\bar{q}g)}(\boldsymbol{\rho}, x) = \frac{N_c}{2C_F}\left[\sigma_2((1-x)\boldsymbol{\rho}) + \sigma_2(\boldsymbol{\rho}) - \frac{1}{N_c^2}\sigma_2(x\boldsymbol{\rho})\right] . \tag{2.30}$$

The ggg three body scattering cross section can be also written in terms of the two body $q\bar{q}$ (dipole) scattering cross section as:

$$\sigma_3^{(ggg)}(\boldsymbol{\rho}, x) = \frac{N_c}{2C_F}[\sigma_2((1-x)\boldsymbol{\rho}) + \sigma_2(\boldsymbol{\rho}) + \sigma_2(x\boldsymbol{\rho})] . \tag{2.31}$$

This should be compared to the three scattering diagrams considered by Gunion and Bertsch [156].

The two body $q\bar{q}$ dipole scattering cross section by a color center is given by [147]

$$\sigma_2(\boldsymbol{\rho}) \approx C_T C_F \alpha_s^2 \int d^2l \frac{1 - e^{i\boldsymbol{l}\cdot\boldsymbol{\rho}}}{(l^2 + \mu_s^2)^2} , \tag{2.32}$$

where μ_s is the screening mass and C_T is the color Casimir of the scattering center ($C_T = C_F$ for a quark, $C_T = C_A$ for a gluon).

For ρ^2 small, and for arbitrary x, the $q\bar{q}g$ three-body cross section can be written in terms of the dipole cross section as:

$$\sigma_3^{(q\bar{q}g)/(ggg)}(\boldsymbol{\rho}, x) = A(x)\sigma_2(\boldsymbol{\rho}) , \tag{2.33}$$

where the factor $A(x)$ reads for the $qg\bar{q}$ case:

$$A_q(x) = \frac{C_A}{2C_F}(1 + (1-x)^2 - \frac{x^2}{N_C^2})\,. \tag{2.34}$$

and for the ggg case $A(x)$ reads:

$$A_g(x) = \frac{C_A}{2C_F}(1 + (1-x)^2 + x^2)\,, \tag{2.35}$$

Performing then the k-integration in σ_2, the effective cross section can then be approximated by

$$\frac{d\sigma_{eff}}{dx} \approx \frac{\alpha_s^2 C_T C_F A(x)}{(2\pi)^2}\mathrm{Re}\int \frac{d^2l d^2k}{(l^2+\mu_s^2)^2} \sum_{\text{color,helicity}} \left[\psi_m^*(k,x,z) - \psi_m^*(k-l,x,z)\right]\psi_f(k,x,z)\;, \tag{2.36}$$

In what follows we use the expression in Eq. (2.36) for the cross section to facilitate the comparison with existing results in the literature.

2.2 Analytical results for parton energy loss

Using the general framework reviewed in Sec. 2.1 we now turn to the derivation of analytic expressions for parton energy loss including the effects of a background field and the scattering of the propagating parton with particles in the medium. We consider three different background field configurations. We start in Sec. 2.2.1 with an impulse configuration. Then we turn to a zero background field in Sec. 2.2.2. Finally, the case of a constant background field will be studied in Sec. 2.2.3. Equation (2.46) constitutes the main result of these theory calculations.

2.2.1 Impulse configuration

In the impulse field configuration it is assumed that the effect of the background field is to give the particle a "kick" at some instant of time ξ_s. This can be mimicked by an impulse $\boldsymbol{H}(\xi) = \boldsymbol{H}_o\delta(\xi - \xi_s)$ where the constant ξ_s represents the location where the background impulse acts. This leads to an effective force $\boldsymbol{f}(\xi) = \boldsymbol{f}_o\delta(\xi - \xi_s)$ acting on the dipole.

We chose the magnetic field to be in one of the following configurations:

- either a background field in the transverse plane,
- or a background field in the longitudinal direction.

For a background field in the transverse plane, the momentum change $\boldsymbol{f}_o$ can be written as

$$\boldsymbol{f}_o = (1-x)\boldsymbol{f}_o^g - x\boldsymbol{f}_o^{q'} \approx g[(1-x)Q - xq']\boldsymbol{e}_z \wedge \boldsymbol{H}_o\;, \tag{2.37}$$

where Q is the radiated gluon color charge and q' is the outgoing quark color charge.

However, in the case of a longitudinal background field $\boldsymbol{f}_o$ will be related to particle momenta shifts

$$\boldsymbol{f}_o = (1-x)\boldsymbol{q}_g - x\boldsymbol{q}_{q'} \,, \tag{2.38}$$

where $\boldsymbol{q}_g$ and $\boldsymbol{q}_{q'}$ are the momenta transferred to the radiated gluon and the outgoing quark by the impulse field, respectively.

Integrating over ξ in Eq. (2.28) will lead to a dependence of ψ_f on ξ_s, i.e., $\psi_f = \psi_f(\boldsymbol{\rho}, x, z-\xi_s)$. Furthermore, ψ_m in Eq. (2.29) will be evaluated assuming a single scattering in the region $z \approx \xi_s$. This assumption in turn leads to a simplified expression for ψ_f.

Then the gluon emission will be induced by a single soft scattering and an impulse exchange with the field. The differential cross section of radiation will be

$$\left.\frac{d\sigma_{eff}}{dx}\right|_{N=1,z\approx\xi_s} \approx \frac{\alpha_s^2 C_T C_F A_q(x) G_q(x)}{2\pi} \int \frac{dl^2 dk^2 F_f(k,l)}{(l^2+\mu_s^2)^2} \,. \tag{2.39}$$

where the factors $G_q(x)$ and $A_q(x)$ can be found in Eqs. (2.15) and (2.34), respectively. The function F_f is given by

$$F_f(k,l,\boldsymbol{f}_0) = \frac{1}{2\pi}\int_0^{2\pi} d\phi_k \int_0^{2\pi} d\phi_l \left(\frac{\boldsymbol{k}}{\boldsymbol{k}^2} - \frac{\boldsymbol{k}-\boldsymbol{l}}{(\boldsymbol{k}-\boldsymbol{l})^2}\right)\cdot \frac{\boldsymbol{k}-\boldsymbol{f}_o}{(\boldsymbol{k}-\boldsymbol{f}_o)^2} \,, \tag{2.40}$$

where ϕ_k and ϕ_l are the azimuthal angles of $\boldsymbol{k}$ and $\boldsymbol{l}$ in the transverse plane, respectively.

In order to further evaluate Eq. (2.40) one has to specify the direction of $\boldsymbol{f}_0$. For a background field $\boldsymbol{H}$ in the transverse plane $\boldsymbol{f}_0 \propto \boldsymbol{e}_z \wedge \boldsymbol{H}_o$ lies also in the transverse plane and it is useful to perform an average over all possible azimuthal angles ϕ_f leading to

$$\langle F_f\rangle|_\perp(k,l,x) = \int \frac{d\phi_f}{2\pi} F_f(k,l,\boldsymbol{f}_0) \,, \tag{2.41}$$

where $\boldsymbol{f}_o$ is given in the right side of Eq. (2.37).

In the longitudinal case with $\boldsymbol{f}_0 = (1-x)\boldsymbol{q}_g - x\boldsymbol{q}_{q'}$, the averaging should be made over the directions of the exchanged momenta $\boldsymbol{q}_g$ and $\boldsymbol{q}_{q'}$:

$$\langle F_f\rangle \qquad |_\parallel(k,l,x) = \int \frac{d\phi_g}{2\pi}\frac{d\phi_{q'}}{2\pi} F_f(k,l,\boldsymbol{f}_0) \,, \tag{2.42}$$

where ϕ_g is the azimuthal angle of the gluon momentum exchange $\boldsymbol{q}_g$ and $\phi_{q'}$ is that of the quark momentum exchange $\boldsymbol{q}_{q'}$ in the transverse plane.

This equation contains two ϕ integrals which makes any further integral very difficult to deal with. So for this reason, the longitudinal $\boldsymbol{f}_0$ was written in another form

$$\boldsymbol{f}_o = ||(1-x)\boldsymbol{q}_g - x\boldsymbol{q}_{q'}||\vec{a} \,, \tag{2.43}$$

where $||(1-x)\boldsymbol{q}_g - x\boldsymbol{q}_{q'}||$ is the norm of $\boldsymbol{f}_o$ and $\vec{a}$ is the resultant vector of $-x\boldsymbol{q}_{q'}$ and $(1-x)\boldsymbol{q}_g$. This form of $\boldsymbol{f}_o$ summarizes Eq. (2.42) into only one ϕ integral.

After integrating over the azimuthal angle, the function $\langle F_f \rangle$ can be written in a compact way as

$$\langle F_f \rangle(k,l,x) = \frac{2\pi}{k^2}\theta(l^2-k^2)\theta(k^2-\tilde{f}^2)\,, \tag{2.44}$$

where we use the notation $\tilde{f}$ for the two considered cases

$$\tilde{f}^2 = \begin{cases} [Q(1-x)-xq']^2 g^2 H_o^2 \text{ for } \boldsymbol{H} \text{ transverse}\,, \\ \\ \left((1-x)\boldsymbol{q}_g - x\boldsymbol{q}_{q'}\right)^2 \text{ for } \boldsymbol{H} \text{ longitudinal}\,, \end{cases} \tag{2.45}$$

After integration over l and k in Eq. (2.39) and using a constant scattering density n in Eq. (2.26), the medium induced radiation spectrum can be written as

$$x\frac{dP}{dx} \approx \frac{2xG_q(x)}{\alpha_s}\frac{\alpha_s}{\pi}\frac{A_q(x)}{A_q(0)}\frac{L}{\lambda_g}\ln\left(1+\frac{\mu_s^2}{\tilde{f}^2}\right)\,, \tag{2.46}$$

where [147]

$$\frac{1}{\lambda_g} = \frac{\alpha_s^2 \pi C_F C_T A_q(x=0) n}{2\mu_s^2}\,.$$

Eq. (2.46) constitutes our main result for the quark energy loss.

But if $\tilde{f}^2$ for the longitudinal field is expanded, it will be noted that it contains an angle inside, which is the angle between $\boldsymbol{q}_g$ and $\boldsymbol{q}_{q'}$. So this angle has to be averaged in order to be removed from Eq. (2.46):

$$\int_0^{2\pi}\frac{d\phi_{gq'}}{2\pi}\ln\left(1+\frac{\mu_s^2}{q_g^2(1-x)^2+q_{q'}^2x^2-2q_gq_{q'}x(1-x)cos(\phi_{gq'})}\right)\,. \tag{2.47}$$

After solving the above integral and taking the limit of small μ_s^2 the result will be:

$$\ln\left(1+\frac{\mu_s^2}{|q_g^2(1-x)^2-q_{q'}^2x^2|}\right)\,. \tag{2.48}$$

So the gluon emission probability for the longitudinal field case becomes:

$$x\frac{dP}{dx} \approx \frac{2xG_q(x)}{\alpha_s}\frac{\alpha_s}{\pi}\frac{A_q(x)}{A_q(0)}\frac{L}{\lambda_g}\ln\left(1+\frac{\mu_s^2}{|f'|}\right)\,, \tag{2.49}$$

with $f' = q_g^2(1-x)^2 - q_{q'}^2x^2$.

Figure 2.5 shows (in logarithmic scale) the gluon emission spectrum for the quark in the transverse H case (upper panel) where μ_s/gH was varied between, $\mu_s/gH = 0.005$, $\mu_s/gH = 0.025$, and $\mu_s/gH = 0.05$. The radiation spectrum was measured for different color charges of the outgoing quark and the radiated gluon like:

- Blue curve, $q' = 0.5$ and $Q = 0$.

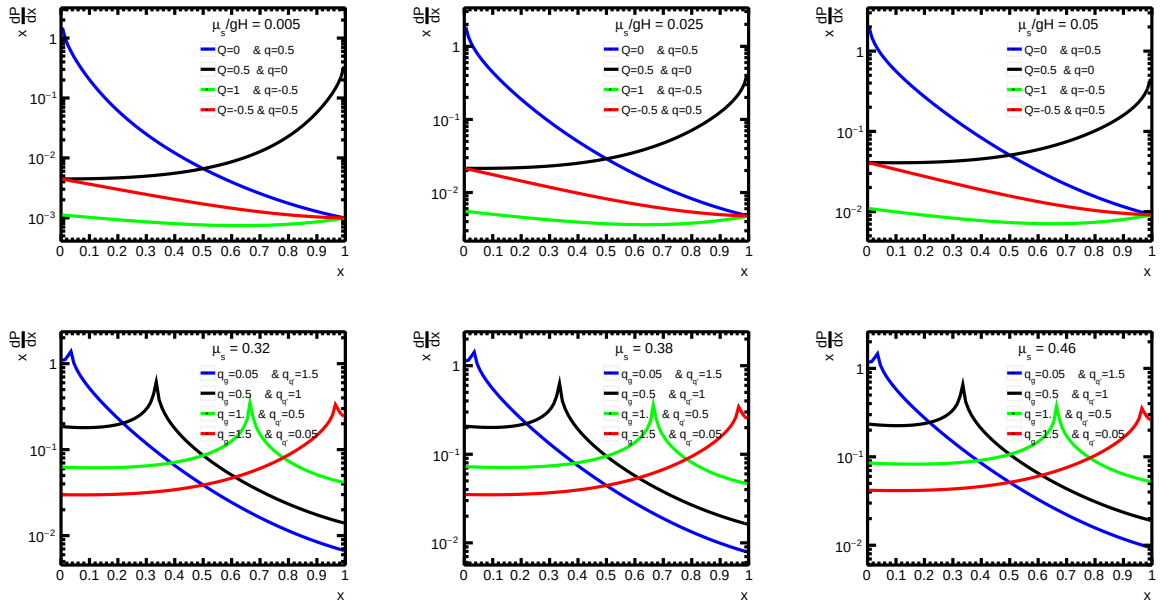

Fig. 2.5 The gluon emission spectrum in the transverse H case (upper plots) for different μ_s/gH, and for the longitudinal H case (lower plots) for different μ_s.

- Black curve, $q' = 0$ and $Q = 0.5$.
- Green curve, $q' = -0.5$ and $Q = 1$.
- Red curve, $q' = 0.5$ and $Q = -0.5$.

In this figure the following parameters were chosen, $L = 1$ fm, $N = 3$, $C_F = 4/3$, $C_A = 3$, and $\alpha_s = 0.3$. The rising lines in the figures corresponds to soft limits where one need to re-sum in order to absorb all the divergences.

The lower panel of Fig. 2.5 corresponds to the gluon radiation spectrum in the longitudinal H case, where μ_s was varied as follows; $\mu_s = 0.32$ (GeV), $\mu_s = 0.38$ (GeV), and $\mu_s = 0.46$ (GeV). Where the values of μ_s are taken from [157] Fig. (1) at fixed $\mu_b = 600$ MeV and at three temperature $T = 50$ MeV, $T = 100$ MeV and $T = 150$ MeV. The emission spectrum was measured for different values of $q_{q'}$ and q_g as:

- Blue curve, $qq_{q'} = 1.5$ GeV$/c$ and $q_g = 0.05$ GeV$/c$.
- Black curve, $q_{q'} = 1.$ GeV$/c$ and $q_g = 0.5$ GeV$/c$.
- Green curve, $q_{q'} = 0.5$ GeV$/c$ and $q_g = 1.$ GeV$/c$.
- Red curve, $q_{q'} = 0.05$ GeV$/c$ and $q_g = 1.5$ GeV$/c$.

The peaks in the figures corresponds to soft limits which can be absorbed by resummation.

The associated energy loss can be obtained by integrating Eq. (2.46) over x:

$$\Delta E \equiv E \int_0^1 dx\; x\; \frac{dP}{dx}\,. \tag{2.50}$$

In the transverse field case, in the limit of small $\mu_s/q'_\perp$ the result in Eq. (2.50) can be further simplified and one easily finds

$$\Delta E \approx \mathcal{C}\alpha_s \frac{L}{\lambda_g}\frac{\mu_s}{q'_\perp}E \ , \tag{2.51}$$

where the factor $\mathcal{C}$ is given by:

$$\mathcal{C} = C_F \frac{sign(Q)+sign(q')}{2q^5}\left(q^2+q'^2\right)\left(q^2+q'^2-\frac{Q^2}{N^2}\right) \tag{2.52}$$

which is linear in μ, with $q = Q + q'$ and $q'_\perp = gH$.

In case $Q = 0$, the factor $\mathcal{C}$ becomes $\mathcal{C} = 2C_F/|q'|$, and in case $q' = 0$ the factor $\mathcal{C}$ becomes $\mathcal{C} = C_F(1-1/N^2)/(2|Q|)$. But if the two color charges are different from zero, looking at the different color charge combination in 2.1.1 we see that it is impossible for Q and q' to have the same sign, they always have an opposite sign, so the linear term in μ will be equal to zero. So in this case the energy loss will be suppressed by a quadratic term in μ. The general form of this energy loss can be found in the appendix (see appendix E). Another case can be studied which is when $(Q + q') = 0$, in this case the energy loss can be written as:

$$\Delta E \approx \frac{(56N^2-11)}{60\pi N^2 Q^2}\alpha_s \frac{L}{\lambda_g}(\frac{\mu_s}{q'_\perp})^2 E \ . \tag{2.53}$$

For the longitudinal case, if we take the case where $q_g = 0$ or $q_{q'} = 0$ and then the limit of small μ_s, Eq. (2.50) will be simplified to:

$$\Delta E \approx \mathcal{C}'\alpha_s \frac{L}{\lambda_g}\frac{\mu_s}{q'_\perp}E \ , \tag{2.54}$$

where $\mathcal{C}' = 2C_F$and $q'_\perp = q_{q'}$ when $q_g = 0$, and $\mathcal{C}' = C_F(1-1/N^2)/2$ and $q'_\perp = q_g$ when $q_{q'} = 0$.

But if we take both q_g or $q_{q'}$ different from zero then we have to take the general case without any approximations. Since the general form was involved it was added into the appendix (appendix E) and plotted in Fig. 2.6.

Figure 2.6 shows (in logarithmic scale) the quark energy loss in the transverse H case (upper panel) where μ_s/gH was varied between, $\mu_s/gH = 0.005$, $\mu_s/gH = 0.025$, and $\mu_s/gH = 0.05$. The energy loss was plotted for different color charges of the outgoing quark and the radiated gluon like:

- Blue curve, $q' = 0.5$ and $Q = 0$.
- Black curve, $q' = 0$ and $Q = 0.5$.
- Green curve, $q' = -0.5$ and $Q = 1$.
- Red curve, $q' = 0.5$ and $Q = -0.5$.

In this figure the following parameters were chosen, $L = 1$ fm, $N = 3$, $C_F = 4/3$, $C_A = 3$, and $\alpha_s = 0.3$.

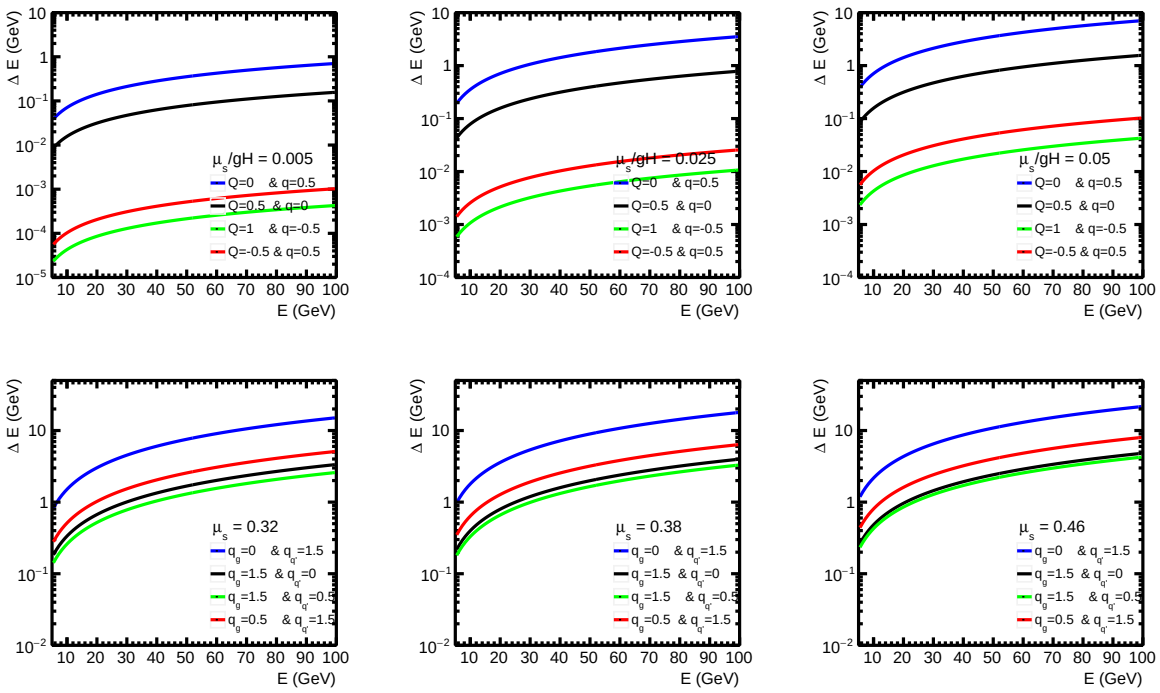

Fig. 2.6 The quark energy loss in the transverse H case (upper plots) for different μ_s/gH, and for the longitudinal H case (lower plots) for different μ_s.

The lower panel of Fig. 2.6 corresponds to the quark energy in the longitudinal H case, where μ_s was varied as follows; $\mu_s = 0.32$ (GeV), $\mu_s = 0.38$ (GeV), and $\mu_s = 0.46$ (GeV). Where the values of μ_s are taken from [157] Fig. (1) at fixed $\mu_b = 600$ MeV and at three temperature $T = 50$ MeV, $T = 100$ MeV and $T = 150$ MeV. The energy loss was computed for different values of $q_{q'}$ and q_g as:

- Blue curve, $qq_{q'} = 1.5$ GeV$/c$ and $q_g = 0.$ GeV$/c$.
- Black curve, $q_{q'} = 0.$ GeV$/c$ and $q_g = 1.5$ GeV$/c$.
- Green curve, $q_{q'} = 0.5$ GeV$/c$ and $q_g = 1.5$ GeV$/c$.
- Red curve, $q_{q'} = 1.5$ GeV$/c$ and $q_g = 0.5$ GeV$/c$.

As can be seen on the figures 2.6, as the value of μ_s increases the energy loss also increases.

As can be seen the energy loss is inversely proportional to $q'_\perp$ which can be interpreted as the "kick" received from the background by the softest outgoing particle. Furthermore, the energy loss depends linearly on the size of the medium (L) and the energy (E) of the propagating quark. The linear energy dependence of the energy loss was also obtianed in [154] for a propagating parton.

The previous calculations were done for the propagation of a quark. The gluon case can be treated in a similar way.

In the gluon case, only the transverse field case was considered, and $\tilde{f}$ in this case is given by:

$$\tilde{f}^2 = [Q_{g'}(1-x) - xQ_{g''}]^2 g^2 H_o^2 \tag{2.55}$$

where $Q_{g'}$ is the color charge of the radiated gluon, and $Q_{g''}$ is the color charge of the outgoing gluon.

The radiation rate for the gluon will then be

$$x\frac{dP}{dx} \approx \frac{2xG_g(x)}{\alpha_s}\frac{\alpha_s}{\pi}\frac{A_g(x)}{A_g(0)}\frac{L}{\lambda_g}\ln\left(1+\frac{\mu_s^2}{\tilde{f}^2}\right). \tag{2.56}$$

This equation is similar to Eq. (2.46) for a propagating quark except that the coefficients $A_q(x)$ and $G_q(x)$ are replaced by $A_g(x)$ which was given in Eq. (2.35) and $G_g(x)$ which was given in Eq. (2.19).

The associated gluon energy loss can be obtained by integrating Eq. (2.56) over x:

$$\Delta E \equiv E\int dx x\frac{dP}{dx} \approx \mathcal{C}\alpha_s\frac{L}{\lambda_g}\frac{\mu_s}{q'_\perp}E\,, \tag{2.57}$$

which is formally the same as Eq. (2.51) for a propagating quark except that the factor $\mathcal{C}$ is now given by

$$\mathcal{C} = C_A\frac{(Q_{g''}^2+Q_{g''}Q_{g'}+Q_{g'}^2)}{Q_{g''}(Q_{g''}+Q_{g'})^6}(sign(Q_{g'})+sign(Q_{g''}))$$

and $q'_\perp = gH$. If the color charge of the radiated gluon was zero $Q_{g'}=0$ the factor $\mathcal{C}$ will be reduced to $\mathcal{C}=C_A/Q_{g''}$.

As can be seen, in the impulse field approximation, the energy loss is again linearly dependent on L and E similar to the quark case.

2.2.2 Zero background field configuration

Consider now the case where the scattering event and the impulse event are too far from each other, i.e. $z-\xi_s\to\infty$, keeping only the contribution from a single scattering ($N=1$). This term can be also obtained by turning off the background field, i.e., by setting $\boldsymbol{f}_o=0$. The formation length will be kept to avoid infrared divergences, so the effective cross section will be

$$\left.\frac{d\sigma_{eff}}{dx}\right|_{N=1} \approx \frac{\alpha_s^2 C_T C_F A(x)G(x)}{2\pi}\int\frac{dl^2dk^2F(k,l,z)}{(l^2+\mu_s^2)^2}\,, \tag{2.58}$$

where the function F is given as:

$$F(k,l,z) = \mathrm{Re}\left[1-\exp\left(\frac{-izk^2}{2\mu(x)}\right)\right]\int_0^\pi d\phi\left(\frac{\boldsymbol{k}}{\boldsymbol{k}^2}-\frac{\boldsymbol{k}-\boldsymbol{l}}{(\boldsymbol{k}-\boldsymbol{l})^2}\right)\cdot\frac{\boldsymbol{k}}{\boldsymbol{k}^2}\,, \tag{2.59}$$

where ϕ is the angle between the vectors $\boldsymbol{k}$ and $\boldsymbol{l}$.

This expression was obtained in [147] which leads to the energy loss

$$\Delta E \equiv E\int dx x\frac{dP}{dx} \approx \frac{C_F\alpha_s}{4}\frac{L^2\mu_s^2}{\lambda_g}\ln\left(\frac{E}{\omega_{cr}}\right) \tag{2.60}$$

where ω_{cr} is the limit at which we still have the diffusive regime, or the large formation length regime.

For the gluon case the energy loss will be:

$$\Delta E \equiv E \int dx x \frac{dP}{dx} \approx \frac{C_A \alpha_s}{8} \frac{L^2 \mu_s^2}{\lambda_g} \ln\left(\frac{E}{\omega_{cr}}\right) \tag{2.61}$$

which again differs from the quark case by only a color factor ($C_A/2$ for the gluon and C_F for the quark).

In the zero background field case the energy loss is logarithmically dependent on the energy E and quadratically dependent on the medium length L.

2.2.3 Constant field configuration: synchrotron radiation with scattering

In this case a constant background field will be considered [158, 148, 149]. The propagator in the presence of a constant field can be easily evaluated without the medium effect or with the medium effect but in the dipole approximation. Taking the $N = 1$ term, the effective cross section can be written in the coordinate space as

$$\left.\frac{d\sigma_{eff}}{dx}\right|_{N=1} \approx \mathrm{Re} \int d^2\boldsymbol{\rho} \psi_f(\boldsymbol{\rho}, x, z)^* \sigma_3(\boldsymbol{\rho}, x) \psi_f(\boldsymbol{\rho}, x, z) \tag{2.62}$$

where the light-cone wave function ψ_f is

$$\psi_f(\boldsymbol{\rho}, x, z) = P(x) \left(\frac{\partial}{\partial \rho'_x} - i\lambda_g \frac{\partial}{\partial \rho'_y}\right) \int_0^\infty d\xi \mathcal{K}_f(\boldsymbol{\rho}, z | \boldsymbol{\rho}', z - \xi) \Big|_{\rho'=0} , \tag{2.63}$$

and the constant background field propagator can be written as:

$$\begin{aligned} \mathcal{K}_f(\boldsymbol{\rho}_f, z_f; \boldsymbol{\rho}_i, z_i) &= \frac{\mu}{2\pi(z_f - z_i)} \exp i\Bigg\{ \frac{\mu}{2(z_f - z_i)} (\boldsymbol{\rho}_f - \boldsymbol{\rho}_i)^2 + \frac{z_f - z_i}{2} \mathbf{f} \cdot (\boldsymbol{\rho}_f + \boldsymbol{\rho}_i) \\ &\quad - \frac{\mathbf{f}^2 (z_f - z_i)^3}{24\mu} - \frac{\epsilon^2}{2\mu} (z_f - z_i) \Bigg\} . \end{aligned} \tag{2.64}$$

In momentum space representation, the effective cross section for the radiation can be written as:

$$\left.\frac{d\sigma_{eff}}{dx}\right|_{N=1} \approx \alpha_s^2 C_T C_F A(x) \mathrm{Re} \int \frac{d^2\boldsymbol{l}}{(l^2 + \mu_s^2)^2} (\mathcal{P}_m - \mathcal{P}_{vac}) \tag{2.65}$$

where $\mathcal{P}_m(x,\mathbf{l})$ is the medium modified synchrotron quasi-probability:

$$\begin{aligned}\mathcal{P}_m(x,\mathbf{l}) &= \frac{i\mu}{\pi}\int_0^\infty dL\int_{-\infty}^{\infty}\frac{d\tau}{\tau}\left[\frac{g_1}{\mu^2}\left(\frac{2i\mu}{\tau}+\frac{\mathbf{f}^2\tau^2}{4}\ -\frac{\tau}{2}\mathbf{l}\cdot\mathbf{f}+\left(\frac{1}{4}-\frac{L^2}{\tau^2}\right)\mathbf{l}^2\right)\right] \\ &\exp\left\{-i\left[\frac{\epsilon^2\tau}{2\mu}+\frac{\mathbf{f}^2\tau^3}{24\mu}\right]\right\}\exp\left\{-\frac{i}{2}\left[\frac{L^2}{\mu}\mathbf{l}\cdot(\mathbf{f}-\frac{\mathbf{l}}{\tau})-\frac{\tau^2}{4\mu}\mathbf{l}\cdot(\mathbf{f}-\frac{\mathbf{l}}{\tau})\right]\right\}\end{aligned} \tag{2.66}$$

and $\mathcal{P}_{vac}(x)$ is the vacuum contribution obtained by setting to zero the exchange momentum of the scattering ($\boldsymbol{l}\to 0$) in $\mathcal{P}_m$:

$$\mathcal{P}_{vac}(x)=\frac{i\mu}{\pi}\int_0^\infty dL\int_{-\infty}^{\infty}\frac{d\tau}{\tau}\left[\frac{g_1}{\mu^2}\left(\frac{2i\mu}{\tau}+\frac{\mathbf{f}^2\tau^2}{4}\right)\right]\exp\left\{-i\left[\frac{\epsilon^2\tau}{2\mu}+\frac{\mathbf{f}^2\tau^3}{24\mu}\right]\right\}. \tag{2.67}$$

Here, $g_1=C_F\alpha_s(1-x+x^2/2)/x=G_q(x)$ (non-spin-flip vertex factor) in the notation used in [148]. The general expression in Eq. (2.65) for a single scattering in the presence of a constant background field is a new result and could be evaluated numerically. We leave this for a future publication where we plan to implement the theoretical expressions for the energy loss in a numerical code.

However, the expression for $\mathcal{P}_{vac}(x)$ can be compared with known results in the literature: Taking the real part of P_{vac} and doing an integration by parts one can show that the synchrotron radiation probability in the vacuum is given by

$$\left.\frac{dP}{dxdL}\right|_{synch}=\mathrm{Re}\frac{d\mathcal{P}_{vac}}{dL}=\frac{i\mu}{2\pi}\int_{-\infty}^{\infty}\frac{d\tau}{\tau}\left[\frac{g_1}{\mu^2}\left(\epsilon^2+\frac{\mathbf{f}^2\tau^2}{2}\right)\right]\exp\left\{-i\left[\frac{\epsilon^2\tau}{2\mu}+\frac{\mathbf{f}^2\tau^3}{24\mu}\right]\right\} \tag{2.68}$$

which coincides with the result of [148] after neglecting the spin flip terms in the vertex.

Chapter 3

Experimental setup

This chapter will give an overview of the structure of ALICE experiment. The main characteristics of the LHC machine will be introduced in section 3.1. Section 3.2 will give an overview about the ALICE sub-detectors that will be used in this thesis. After that, section 3.3 will outline how these sub-detectors are used for triggering and event reconstruction. Then the software used in this analysis will be mentioned in section 3.4. Finally, section 3.5 will talk about the Monte Carlo (MC) generators that were used in this thesis.

3.1 The Large hadron collider

The Large Hadron Collider (LHC) is the largest particle accelerator in the world and the most powerful, which is 27 km in circumference and 100 m underground [159]. It is located at the French Swiss boarder at CERN. Inside the accelerator, two high-energy particle beams travel at a speed close to the speed of light before they are made to collide. The beams travel in opposite directions in separate beam pipes in two tubes kept at ultrahigh vacuum. They are guided around the accelerator ring by a strong magnetic field maintained by superconducting electromagnets.

The electromagnets are built from coils of special electric cable that operates in a superconducting state. All the controls of the accelerator are based at the CERN control center (CCC), from this center all the beam particles are made to collide at four locations around the accelerator ring corresponding to the position of four large detectors ATLAS [160] (A Toroidal LHC ApparatuS), CMS [161] (Compact Muon Solenoid), LHCb [162] (LHC beauty) and ALICE (A Large Ion Collider Experiments).

The LHC consists of many parts [159]: the dipole magnets, the quadrupole magnets, radio frequency cavities, cryogenic systems and the vacuum pipes:

- **Dipole magnet**: The magnetic dipole is needed in order to bend the beam particles such that they are in a closed loop of fixed radius determined by the superconducting dipoles.
- **Quadropole magnets**: The quadrupole magnets are used for extra focusing in the transverse plane to pull the particles back to the ideal trajectory when they drift away.

- **Radiofrequency cavity**: A radiofrequency (RF) cavity is a metallic chamber that contains an electromagnetic field. Its primary purpose is to accelerate charged particles.
- **Cryogenic system**: The LHC's main magnets operate at a temperature of 1.9 K (-271.3^0 C), colder than the 2.7 K (-270.5^0 C) of outer space. The cryogenic system is used to cool the magnets to make them work in a superconductor state in order to avoid overheating of the coils.
- **Vacuum pipes**: To avoid colliding with gas molecules inside the accelerator, the beams of particles in the LHC must travel in a vacuum pipe which is as empty as interplanetary space.

3.1.1 Injection chain

Protons and lead ions are injected into the LHC via slightly different injection chains, as shown in Fig. 3.1.

The injection of the protons is done as follows:

- Hydrogen atoms are taken from a bottle containing hydrogen. The protons are obtained by stripping orbiting electrons from hydrogen atoms.
- The obtained protons are injected into LINAC2 (LINear ACcelerator) which accelerates the protons to 50 MeV.
- Then the protons are transferred to the PS booster (PSB) which accelerates the protons to 1.4 GeV and consistently focus them.
- After that the protons are fed to the proton synchrotron (PS) where they are accelerated to 25 GeV.
- The beam is then injected to the super proton synchrotron (SPS) and accelerated more to 450 GeV.
- Finally, the beam leaves the SPS and enters the LHC to be accelerated to their maximum energy at 14 TeV before they are made to collide.

The lead ion injection is quite different:

- The Pb ions are taken from a source of vaporized lead (Pb^{27+}) with energy 2.5 KeV/nucleon.
- These Pb ions enter a different accelerator LINAC 3, where they are accelerated to 4.2 MeV/n (Pb^{54+}).
- After that they are collected from LINAC3 and injected into the lower energy ion ring (LEIR), where they are accelerated to 72 MeV/n (Pb^{54+}).
- The beam is then fed to the PS where it is accelerated to 6 GeV/n (Pb^{54+}).

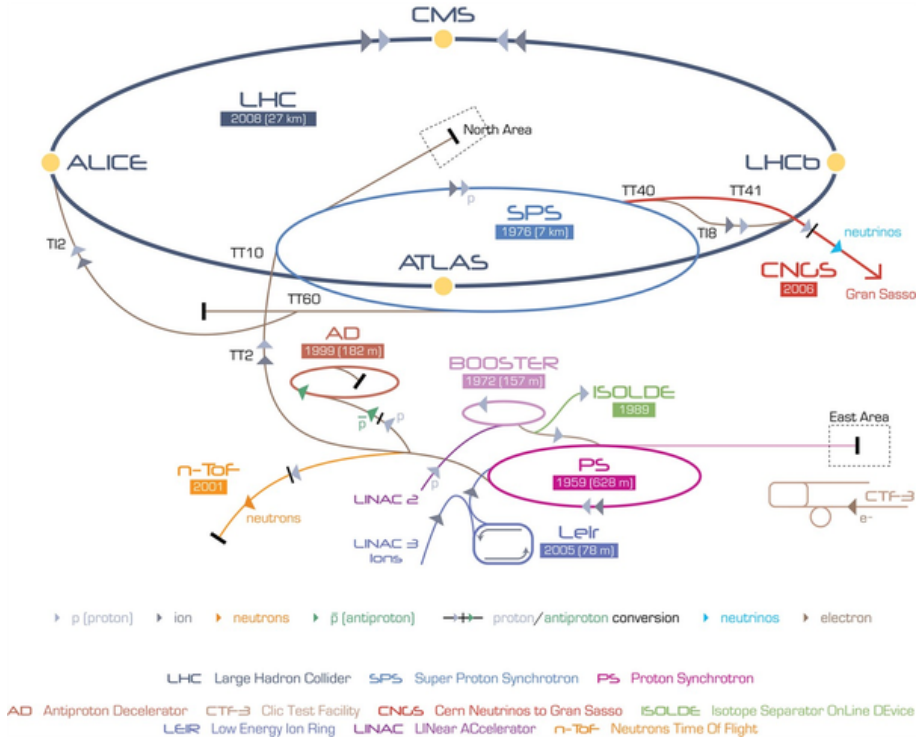

Fig. 3.1 The layout of the LHC injection chain for protons and lead ions.

- Protons are then sent to the SPS which accelerates the lead ions to 177 GeV/n (Pb^{82+}).
- Finally, the lead beams are transferred to the LHC, where they are accelerated to their maximum energy of 5.02 TeV/n (Pb^{82+}).

3.2 The ALICE detector

ALICE [163] (A Large Ion Collider Experiment) is a heavy-ion detector that measures the product of pp, Pb–Pb and p–Pb collisions.

The positions in the ALICE detector are indicated by the cylindrical coordinates. The angle in the (x-y) plane is the azimuthal angle. The pseudo-rapidity can be written as:

$$\eta = -\ln\left(\tan\frac{\theta}{2}\right) \tag{3.1}$$

where θ is the polar angle (angle with respect to the z-axis). The pseudo-rapidity can also be written as a function of the particle's total momentum p and the longitudinal momentum p_L:

$$\eta = -\frac{1}{2}\ln\left(\frac{p+p_L}{p-p_L}\right). \tag{3.2}$$

A general layout of the ALICE detector is shown in Fig. 3.2. The detector is formed mainly of two parts: the central part consists of detectors especially made to measure and

identify the hadronic signals, electrons, jets, and also photons down to very low transverse momenta in full azimuth. And the second part located in the forward region consists of the muon spectrometer which is built asymmetrically on the C side of the detector and it was made to study the Quarkonia behavior. The second part also consists of the V0 and the ZDC (Zero Degree Calorimeter) which are needed for the centrality determination.

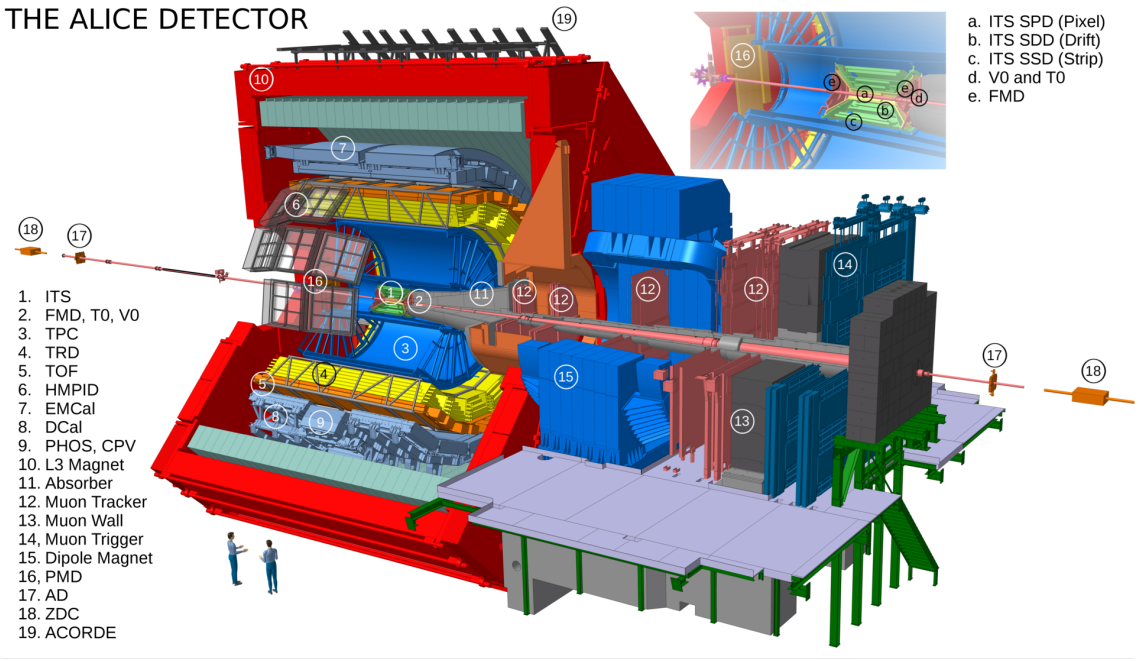

Fig. 3.2 The general layout of the ALICE detector at the LHC.

The central barrel detector is made from the Inner Tracking system (ITS), Time Projection Chamber (TPC), Time Of Flight (TOF), the ElectroMagnetic Calorimeter (EMCal), and several other detectors. For more details on each sub-detector you can refer to [163].

3.2.1 V0

The V0 detector system provides a minimum bias triggering in Pb–Pb , p–Pb and pp collisions events. The V0 is also used to measure the multiplicity of the event in Pb–Pb and p–Pb collisions which allows for the determination of the centrality.

The V0 consists of two sub-detector V0A and V0C, each consist of two disks of scintillator counters and each disk consists of 32 counters divided into 4 rings. V0A and V0C are located asymmetrically on two sides of the interaction point and they cover a pseudo-rapidity range of $2.8 < \eta_{V0A} < 5.1$ and $3.7 < \eta_{V0C} < 1.7$.

When a particle traversing the detector hits the V0, it will produce a scintillator light which is propagated to the photomultiplier tubes. The signal created in the photomultiplier is proportional to the number of particles interacting with the detector materials, which is proportional to the number of particles produced in the heavy-ion collision allowing for multiplicity estimation using Glauber model [75].

3.2.2 Inner Tracking System (ITS)

The Inner Tracking System (ITS) [163] is located close to the interaction point. It consists of six concentric layers of silicon detectors. It is located close to the beam pipe in order to allow precise reconstruction of the primary and secondary vertices with a reconstruction resolution of 100 μm which supports the detection of charm and beauty hadrons. The ITS also contributes to the tracking and particle identification of the low momentum particles (below 200 MeV/c) and improves the momentum resolution of the TPC tracks (tracks reconstructed at the TPC).

The ITS covers the full azimuth range and rapidity region of $|\eta| < 0.9$ which allows for a good efficiency in detecting high mass and low p_T particles. The ITS high granularity and good two-track separation resolution is optimized for the very high track multiplicity in heavy-ion collisions. The spatial resolution for the ITS allows for the very small impact parameter resolution needed for the reconstruction of the short-lived particles.

The ITS consists of three different types of detector, the Silicon Pixel Detector (SPD) which is the closest to the interaction point, the Silicon Drift Detector (SDD), and the Silicon Strip Detector (SSD) as shown in Fig. 3.3.

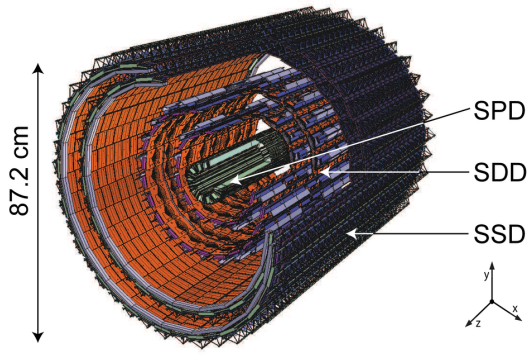

Fig. 3.3 The general layout of the ALICE inner tracking systems.

- The **Silicon Pixel Detector (SPD)** makes up the two innermost layers of the ITS located at an average distance of 3.9 cm (inner layer) and 7.6 cm (outer layer) from the beam axis which makes it fundamental in determining the primary vertex. The SPD is a hybrid silicon pixels, which consists of a matrix of two-dimensional reverse biased silicon diode . The rapidity coverage of the SPD ($|\eta| < 1.98$) allows for continues coverage of the charged-particles multiplicity measurement.

- The **Silicon Drift Detector (SDD)** constitutes the two middle layers of the ITS which surround the SPD located at 15 and 23.9 cm from the beam axis. The SDD provides particle identification through the $\mathrm{d}E/\mathrm{d}x$ measurements. SDD benefits from the measurement of the transport time of the charge deposited by a traversing particle to localize the impact point in one dimension. Thus enhancing resolution and multitrack capability at the expense of speed. They are therefore well suited to this experiment in which very high particle multiplicities are coupled with a relatively low event rates.

- The **Silicon Strip Detector (SSD)** it constitutes the two outer layers of the ITS located at 38 and 43 cm from the interaction point. The SSD provides a good position resolution and identification of low-momentum particles through $\mathrm{d}E/\mathrm{d}x$ information. It is also important for the track matching from the TPC to the ITS.

3.2.3 Time Projection Chamber (TPC)

The TPC is the main tracking system in the ALICE central barrel detector. Its main goal is to provide charged-track reconstruction in the transverse momentum range of $0.1 < p_T < 100$ GeV/c and Particle Identification (PID) for low momentum particles up to $p_T = 20$ GeV/c. It covers full azimuthal range and pseudo-rapidity range $|\eta| < 0.9$ for charged tracks traversing the full TPC, for tracks only partially reconstructed inside the TPC (*i.e* that are not reaching the outer layers of the TPC) $|\eta| < 1.5$ is covered but with worse momentum resolution.

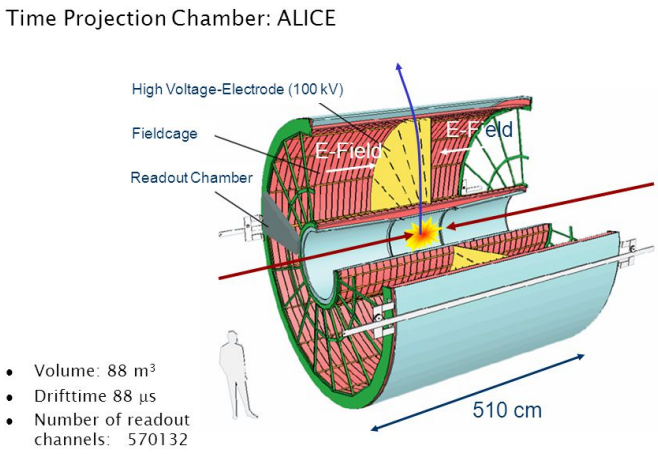

Fig. 3.4 The general layout of the ALICE time projection chamber.

The TPC is made up of a cylindrical barrel with a length of 5 meters (along the beam direction), an outer radius of 280 cm and an inner radius of about 80 cm w.r.t the beam pipe. Figure 3.4 shows the TPC of the ALICE detector. The TPC is filled with 90 m^3 of a gas mixture of primarily Ar or Ne. Charged particles traversing the TPC volume will ionize the gas. The ionized electrons are then drifted at a speed of 2.7 cm/s under the high voltage 100 kV towards the readout channels on one of the two end plates, which are constituted by Multi-Wire Proportional Chambers (MWPCs). The electrons cause an electron avalanche in the MWPC which reaches the cathode pad readout. The position of the charged deposition on the cathode gives the two-dimensional track position in $r\phi$ and the time taken for the electrons to drift to the end plates gives the track position in z. In this way, a position resolution of 1100 (800) μm in $r\phi$ and 1250(1100) μm in z is achievable for tracks in inner (outer) layers of the TPC.

PID is performed by the TPC through the measurement of the energy loss per unit length $\mathrm{d}E/\mathrm{d}x$, which is directly related to the number of electrons ionized by the charged

particle propagating through the TPC. A distribution of the TPC $\mathrm{d}E/\mathrm{d}x$ signal as a function of the momentum p is shown in Fig. 3.5. The various particle species are seen as bands that are well described by the ALEPH parametrization of the Bethe-Bloch curve [164].

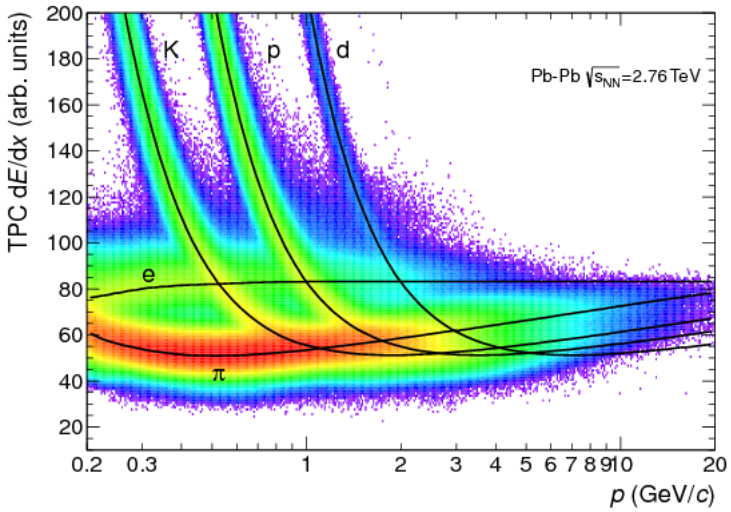

Fig. 3.5 Specific energy loss ($\mathrm{d}E/\mathrm{d}x$) in the TPC vs. particle momentum in Pb–Pb collisions at $\sqrt{s_{\mathrm{NN}}} = 2.76$ TeV [165]. The lines show the parametrizations of the expected mean energy loss.

The TPC PID information was used in this thesis to identify the proton and pions coming from strange hadrons for the V0 rejection analysis in section 5.1.6.

3.3 Event reconstruction

The first step in the event reconstruction is the conversion of the detector raw data into "clusters". The clusterization is executed for each detector separat The next step is locating the interaction vertex (SPD vertex) using clusters in the SPD layers, defined as the convergence point of the maximum number of SPD tracklets (which are the lines defined by pairs of clusters, one in each SPD layer). The determination of the SPD primary vertex provides the input for the next offline reconstruction of tracks and vertices.

Afterward, track determination and fitting in the central barrel is done following a three stages inward-outward-inward plane. The first inward stage starts with looking for tracks in the outer region of the TPC, where the track density is lower. Track seeds are built using TPC clusters and the position of the SPD primary vertex. The seeds are propagated inward and at each stage the nearest found clusters are connected to them. The track that are propagated to inner TPC region are those reconstructed from at least 20 clusters in the outer TPC regions. The built TPC tracks are then extrapolated to the outer layer of SSD and become the seeds for track finding in the ITS. The seeds are then propagated inward the ITS and are updated at each layer by associating ITS clusters within a proximity cut considering positions and errors. The propagated TPC-to-ITS track candidates are arranged according to the reduced χ^2 and after that the tracks are

added to reconstructed event only if they are high quality tracks. The track reconstruction efficiency in the TPC sharply drops down at low p_T.

In order to retrieve the low momentum particles, a standalone ITS reconstruction is done by using the remaining clusters of the combined TPC+ITS tracking procedure. The outward propagation starts when the reconstruction in the ITS is complete and all the tracks are extrapolated to the point of closest approach to the SPD vertex. The propagated tracks are then fitted by the Kalman filter [166] in the outward direction using the clusters determined by the previous procedure. At each outward step, the track length integral and the time of flight predicted for the different particle types are improved for the later particle identification with TOF and TRD. Then tracks are propagated for matching with signals in EMCal, PHOS, and HMPID. The kinematic parameters are determined and the particle identification is performed at the final stage of the track reconstruction.The track position, direction, inverse curvature and its associated covariance matrix are found by propagating all the tracks inward beginning with the outer layer of the TPC and refitted with the previously found clusters.

The reconstructed global tracks in the TPC and ITS, are used to determine the interaction vertex with a higher precision than with SPD alone tracklets. The approximate point of closest approach of validated tracks is found through the extrapolation of the tracks to the point of closest approach to the beam line and subtracting far outliers. Then the precise vertex fit is executed using track weighting to remove the contribution of the remaining outliers.

After determining the tracks and the interaction vertex for the event reconstruction, a look for secondary vertices from particle decays is started. The selected tracks for the secondary vertex reconstruction are the ones with a distance of closest approach to the interaction vertex exceeding a certain minimum value (0.5 mm in pp and 1 mm in Pb–Pb). For every unlike-sign pair of these tracks, called V^0 candidate, the point of closest approach between the two tracks is computed. An optimized set of cuts is applied to the V^0 candidates to select K^0_s and Λ, and support the later search for cascade decays. After determining the V^0 candidates, the search for the Ξ^- cascade decays is performed. The reconstruction of the complex secondary vertices is done later at the analysis stage. For the analysis of heavy-flavor decays close to the interaction point, the secondary vertices is searched for by taking into account all unlike-sign track pairs and selecting those passing a set of topological cuts.

3.4 Analysis Framework

3.4.1 ROOT

ROOT is an oject oriented data analysis framework developed by CERN written in the C++ computing language [167] and it was originally made for particle physics data analysis. The packages provided by ROOT include several ways of user interaction: graphic interface, command line, histograms, curve fitting statistics, interface with python, etc. ROOT packages also provide data processing, statistical analysis, visualisation and storage. ROOT provides a set of methods to handle and analyze large amounts of data in an efficient way. A key property of ROOT is the data container called tree, with its

substructures branches and leaves. A tree can be seen as a sliding window to the raw data, as stored in a file. Data from the next entry in the file can be retrieved by advancing the index in the tree.

3.4.2 AliROOT

AliRoot [168] is an Off-line framework designed for the reconstruction and analysis of simulated and real data from the ALICE detector. AliRoot is based on the ROOT framework and it consists of several modules providing software for detector simulation, event generation and data analysis. It is also the software responsible for the event reconstruction mentioned in section 3.3. This framework is based on the object oriented programming type, and it is written in C++.

AliROOT stores the outputs of the reconstruction of the real and simulated data in an Event Summary Data (ESD) output files which are detector independent. The ESDs are the starting point for the analysis. ESDs are filtered into Analysis Object Data (AOD) in order to reduce the data szie and increase the speed of the data analysis. The event from ESD are filtered to AOD by applying quality selection on the reconstructed tracks.

3.5 MC Generators

Monte Carlo (MC) simulation is important for particle physics in many situations: compare the theory prediction to the data and see whether our understanding for the physics is correct, the detector design and facilities, the optimization development of the softwares of the data reconstruction.

The simulation chain consists of: the generation of the events, the detector simulation, reconstructing the simulator events in the same way as for the raw data. All the particles in the generated events are called MC truth particles. After passing all these particles into the simulated detector they get affected by the tracking efficiency and resolution (through interaction with the detector materials), these particles will be called reconstructed particles.

For this thesis the event generators that were used are: PYTHIA, POWHEG and GEANT (for detector simulation).

3.5.1 PYTHIA

PYTHIA [111] is a software used to generate high energy collisions and the outgoing particles produced in the hard scattering. It also simulates the evolution of these hard scattered particles into multi-hadronic final state. The program contains theory models for the different physics processes, including hard and soft interactions, parton distributions, initial- and final-state parton showers, multiple interactions, fragmentation and decay. PYTHIA also contains a combination of analytical results and different QCD-based models because not all the physics processes can be calculated perturbatively. PYTHIA is a leading order MC generator, but the parameters used for the initial and final state emissions are tuned to describe the next-to-leading-order (NLO) pQCD predictions.

In order to have good description of the experimental data, the free parameters of PYTHIA must be perfectly tuned. These parameters tune the parton cascades and the non-perturbative hadronization process of the simulated event. Example of these parameters are: the p_T distribution in the hadron fragmentation and baryon- to meson-ratios, these parameters are related to phenomenological non-perturbative processes. Modeling the underlying event in PYTHIA is dependent on the theoretical expectation like the PDFs of the partons inside the colliding hadrons and the mechanism of multiple parton interactions. The underlying event tunes in PYTHIA were determined based on experimental observables at the Tevatron and LHC. In this thesis PYTHIA6 with EPOS-LHC were used for the simulation of p–Pb collisions and PYTHIA8 simulation for pp collisions. These simulation were used in the extraction of the tagging efficiency and purity (using data-driven methods) and also used for the unfolding. PYTHIA8 was used with POWHEG for theory prediction of the b-jet spectrum.

3.5.2 EPOS-LHC

EPOS [169, 170] is a phenomenological approach based on the parton model which tries to understand the pp, n-A, A-A collisions. In particular the transverse momentum results from RHIC and LHC experiments. EPOS is a minimum bias Monte-Carlo event generator, used for both heavy ion collisions and cosmic ray air shower simulations. Since its release in 2009, the LHC experiment provided an interesting results compromises pp and p–Pb and Pb–Pb collisions. EPOS-LHC is an upgraded version of the old EPOS [169] which is made to describe the LHC results, it also describes all the minimum bias results for all particles with transverse momentum of $p_T = 0$ GeV/c to few GeV/c.

When PYTHIA is embedded inside the EPOS-LHC, EPOS generates a soft particles which embeds the PYTHIA signal to simulate the environment in heavy-ion collisions.

3.5.3 POWHEG

POWHEG [10] (stands for POsitive Weight Hardest Emission Generator) is a set of methods for performing perturbative QCD calculations of the hard hadron–hadron scatterings up to next-to-leading order (NLO). The POWHEG BOX framework is a software for implementing these methods. It allows the user to interface the calculated NLO emissions (the generated matrix element) to a Shower Monte Carlo programs (SMC) like HERWIG and PYTHIA, in order to generate final hadronic collision events with this chain process.

Various SMC framework implement some NLO corrections like gluon radiation in the final state. As a result of that, MC@NLO matching can lead to a double counting of these NLO correction. In early stage of the implementation, the double counting is corrected by removing the NLO corrections from SMC side. This subtraction of the NLO correction is not totally positive, so it results in about 10 to 15% of the total events to be negative-weighted.

The POWHEG box guarantee all the event weights to be positive-weighted by generating the hard emissions first and describing a hardness matching criterion. Emissions computed in POWHEG should be above a certain threshold. The interfaced SMC program after that vetoes all the emissions above the defined threshold.

The matching of POWHEG calculations to a SMC is typically realized by LHE files for particle listing [171]. This is done in this thesis using POWHEG BOX and PYTHIA8, in which the generated NLO hard scattering in POWHEG replaces the LO hard process generated by PYTHIA.

3.5.4 Detector simulation with GEANT

GEANT (for GEometry ANd Tracking) is a software used for simulating the passage of particles through matter using MC methods. Geant includes methods for handling geometry, tracking, detector response, run management, visualization and user interface. For many physics needs, *i.e* researchers can spend less time on the low level details, and can start directly on the more important aspects of the simulation.

In experimental particle physics GEANT is used to simulate the passage of final-state particles through the different materials of sub-detector in the presence of a magnetic field similar to the L3 magnet in ALICE, so accurate illustration of the detector is need. The detector simulation consists of: potential decays of the particles and modeling of the energy loss of each particle depending on the particle species and the material it pass through. In order to model the detector response, the electronic signal of each particle passing through the detector is simulated similar to what is recorded in data. GEANT3 was used in this thesis.

Chapter 4

Datasets and analysis method

In the present thesis, several data sets have been analyzed: the ALICE data sets used for the b-jets in pp and p–Pb collisions and the corresponding Monte Carlo simulations (used for systematic uncertainty estimate, theoretical predictions, and correction techniques).

The analysis was performed on data recorded with the ALICE detector at the LHC. p–Pb collisions were taken at a center-of-mass energy of $\sqrt{s_{\mathrm{NN}}} = 5.02$ TeV in year 2016 and pp collisions at $\sqrt{s} = 5.02$ TeV in year 2017. Around 700 million minimum-bias p–Pb events were recorded and 1 billion pp events were recorded [1].

The p–Pb MC productions used in this thesis at a center-of-mass energy of $\sqrt{s_{\mathrm{NN}}} = 5.02$ TeV are generated using PYTHIA6 [111] and EPOS-LHC [170]:

- $b\bar{b}$ production contains around 20M events. In this production, the final state partons were forced to be beauty partons ($b\bar{b}$). This MC was used for determining the b-jet tagging efficiency (section 4.5.2) and for determining the b-jet finding efficiency used after unfolding.

- $c\bar{c}$ production contains around 20M events. In this production, the final state partons were forced to be charmed partons ($c\bar{c}$). This MC was used for determining the c-jet mistag rate.

- di-jet production which contains about 74M events. This MC was used for creating the response matrix which was used for unfolding in section 4.5.7. This MC was also used for determining the mistag rate for the light-flavor jets and also used for determining the b-jet purity in section 4.5.6.

The MC productions that are anchored to the pp data are generated using PYTHIA8 [172]:

- di-jet production which contains about 160M events. This MC was used for creating the response matrix which was used for unfolding in section 4.6.6. This MC was also used for determining the b-jet tagging efficiency (section 4.6.2), charm/light-flavor-jet (c/lf-jets) mistagging rate and for determining the b-jet purity. It was also used for the definition of the templates that were used in the data driven efficiency and purity determination in section 4.6.4.

[1] A detailed description on the data samples used in this analysis is given in Appendix A.2.

4.1 Event selection

In order to select the good events, several event selection criteria have been applied. The first selection is the trigger selection in order to select specific events for the physics we are interested in. The second selection is to reject the pileup events. Finally, the selected events must pass primary vertex selection cuts. The number of selected events should be taken into account for the normalization of the b-jet spectra (see section 6.1).

4.1.1 Trigger selection

The Minimum Bias (MB) triggered events were used in this analysis. In pp and in p–Pb collisions, the events that have at least one hit in both V0 detectors are selected by the minimum bias trigger. The total inelastic cross section for the MB trigger is determined by the Van der Meer scans and it is equal to $\sigma_{V0} = 2.09 \pm 0.07$ b [173] for p–Pb collisions and $\sigma_{V0} = 51.2 \pm 1.2$ mb [174] for pp collisions.

4.1.2 Pileup rejection

A pileup event is an event with multiple reconstructed primary vertices, this event may include two or more collisions in the same bunch crossing. These event should be rejected from the analysis. Due to specific ALICE beam conditions (the average number of inelastic collisions per bunch crossing $\mu \ll 1$), this pileup rejection has a very small effect. Only around 0.022% in p–Pb collisions and 0.041% in pp collisions of the total MB events were recognized as pileup events.

4.1.3 Vertex selection

All the selected events must have a reconstructed primary vertex. The vertex definition used in this analysis can be found in [175]. The z-position of the primary vertex along the beam axis is required to be within $|z_{vertex}| < 10$ cm only around interaction point. This cut is applied to ensure a uniform detector acceptance.

An event is selected if its vertex fulfills the following the requirement:

- The primary vertex must be reconstructed from SPD tracklets.
- The minimum number of contributors for the vertex reconstruction is one contributor.
- If SPD vertex has only reconstructed z coordinate and it is determined with poor resolution $\sigma_{Z^{SPD}_{vertex}} > 0.25$, then the event should be rejected.
- The distance between the SPD vertex and track vertex must not exceed 0.5 cm.

More details on the event selection criteria can be found in [175]. The event statistics after each selection are:

- p–Pb : Total events: 723.3M, after pileup rejection: 723.1M (99.97%), and after all vertex selections: 612.4M (84.66%).
- pp: Total events: 1.06B, after pileup rejection: 1.06B (99.959%), and after all vertex selections: 897.2M (84.07%).

4.2 Track selection

Charged jets consist of charged tracks reconstructed by the ALICE sub-detectors. The reconstruction of tracks in the ALICE detector was discussed in details in section 3.3. But they cannot be directly used in the jet finding, several quality selection criteria should be used before (see appendix A.4).

In order to select high quality tracks, a certain cut should be applied on the reconstructed tracks. Some tracks can be reconstructed in a pseudorapidity region up $|\eta| < 1.4$, but the tracking efficiency sharply falls in the outer regions of the detector. For this reason, tracks are limited to the pseudorapidity region $|\eta| < 0.9$. Furthermore, the tracking efficiency sharply decreases in the low track-p_T region. A $p_{T,min} > 0.15$ GeV/c cut was applied close to the natural cut-off of the ALICE detector (due to the energy loss and multiple scattering in the detector material).

4.3 Jet reconstruction

The jets used in the analysis were reconstructed using the anti-k_T jet clustering algorithm [31] with resolution parameter/radius $R = 0.4$. The k_T algorithm [30] was applied to reconstruct k_T-clustered jets which were used for the background estimation and subtraction.

For the b-jet analysis not all the reconstructed jets were be considered. Several cuts were applied.

Firstly, a pseudorapidity cut is applied on the reconstructed jet axis. The jet axis is determined using p_T-weighted direction of the constituent particles. This cut is applied to reject partially reconstructed jets in the TPC acceptance which fall on the edge of the TPC. The η cut was chosen to be$|\eta_{jet}| < 0.9 - R = 0.5$.

Secondly, p_T cuts were applied on the jets. These are a needed by the unfolding algorithms such that only jets above a certain threshold can enter the unfolding procedure. These cuts were also applied because most of the jets in the low p_T regions are combinatorial jets, or in other words they were not created in the hard scattering. A p_T threshold was chosen to be $p_{T,min} = 5$ GeV/c. A $p_{T,max}$ cut was chosen such that the bin entries of the highest transverse momentum p_T bin should be larger than 10, because if it is less it cannot enter the unfolding procedure.

Thirdly, an area cut was applied on the jets. The jet area should larger than $A_{jet} > 0.6\pi R^2$, πR^2 is the expected area of the jet cone. This cut was applied because it subtracts some of the low p_T jets coming from the background.

4.4 b-jet tagging algorithm

Building an observable which discriminates between b, c, and light parton jets requires a variety of reconstructed objects like: tracks, vertices, and identified leptons. There are algorithms that use only one observable for the tagging, and there are algorithms that combine several objects into one tagger to ensure a higher discriminating power. Each algorithm has a specific discriminator value for each jet. All the algorithms described

below uses the kinematic properties of the charged particles (charged tracks), including identified leptons in a jet.

The impact parameter is the distance of closest approach between the track and the primary vertex as illustrated in Fig. 4.1.

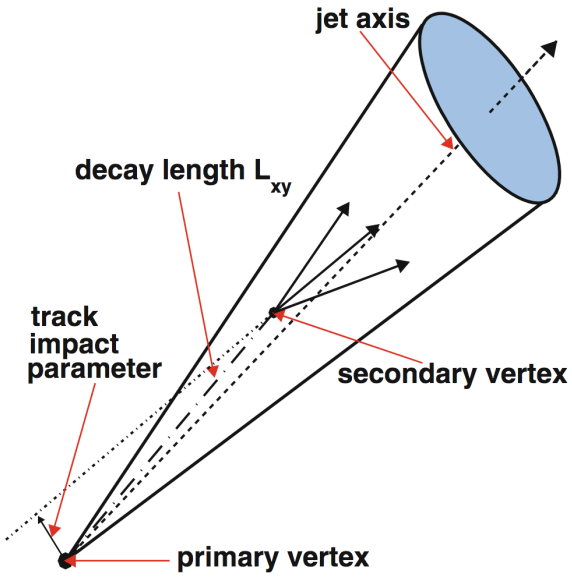

Fig. 4.1 Objects used for the identification of a jet originating from the fragmentation of a b-quark (figure adapted from [176]).

The b-jet tagging algorithms request a sample of high quality tracks. More quality requirements are applied to the selected tracks used in the jet finding:

- The track transverse momentum p_T should be larger $p_{T,min}^{track} = 0.5$ GeV in order to reduce the fraction of poorly reconstructed tracks.
- The track should have at least two hits in the ITS (it should be 4 but due to the absence of the SDD it was reduced to 2).
- The minimum number of the track's TPC clusters is 80.
- The track must not have a $\chi^2/n.d.f$ larger than 5 (where $n.d.f$ is the number of degrees of freedom) to ensure a good fit quality.
- The track should have at least one hit in the SPD, since these tracks provide most of the discriminating power.
- The 2D impact parameter (or DCA distance of closet approach of the track to the primary vertex) of the track must be $d_{xy} < 1$ cm, this loose selection on the track impact parameters was used for the purpose of increasing the fraction of well-reconstructed tracks and to reduce the long-lived particles decay products (V^0 decay) contamination.
- The track z impact parameter must be $d_z < 2$ cm, for the same reasons.

- The distance of closest approach between the jet axis and the track $\mathrm{DCA}_{jet-track}$ must be within 0.07 cm. This cut was applied such that the number of tracks coming from pileup is reduced.
- The $\mathrm{DCA}_{jet-track}$ must be within 5 cm from the primary vertex.

These cuts are different from the track cuts introduced in section 4.2, since the track cuts are applied on the tracks inside the jets to be selected for tagging. While the tracks in section 4.2 are used for the jet finding.

These cuts on the tracks inside the jets are the basis for all algorithms that use impact parameters information like the track counting and jet probability algorithms used in this work.

For more information about b-jet tagging algorithms see [177, 176, 178].

4.4.1 Track counting algorithm

In order to distinguish the b- or c-hadron decay products from other particles originating from light-flavour jets, the impact parameter of the track with respect to the primary vertex can be used. The impact parameter - defined as the distance of closest approach of the track to primary vertex - can be calculated either in two dimensions or three dimensions, but due to the poor resolution along the z-axis, the 2D impact parameter (d_{xy}) will be used in this thesis. The sign of the impact parameter can be determined as the sign of the scalar product of the jet axis and the impact parameter *i.e* the vector pointing from the primary vertex of the point of closest approach (DCA). Figure 4.2 shows the impact parameter sign for the secondary particles from b or c decays (a) and impact parameter sign of primary tracks (b). As shown in the figure part (a) due to decay length (long lifetime) the tracks originating from the secondary vertex tend to have positive impact parameter values. While part (b) of the same Fig. 4.2 shows that due to resolution effect (which is symmetric around the primary vertex) the tracks originating from the primary vertex can have both positive and negative impact parameter values.

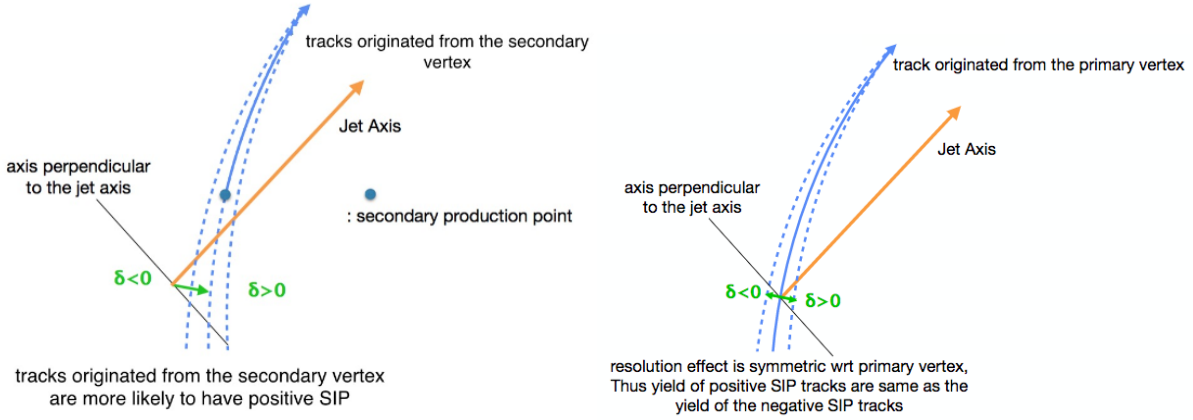

(a) (b)

Fig. 4.2 The sign of the impact parameter (a) for secondary particles (b) primary particles. Figure taken from Minjung Kim.

The impact parameter significance Sd_{xy} which is the ratio of the impact parameter over its estimated uncertainty (resolution), is usually used as discriminator. The impact parameter resolution largely depends on the η and the p_T of the tracks. Figure 4.3 shows the probability distribution of impact parameter and impact parameter significance taken from PYTHIA6+EPOS simulation for the different jet flavors. It is clear that the impact parameter (Sd_{xy}) of the b-jets is larger than the impact parameter Sd_{xy} of the c-jet which is in turn larger than the impact parameter of the light-flavor-jets, which shows that the impact parameter has a strong discriminating power in distinguishing between the different jet flavors.

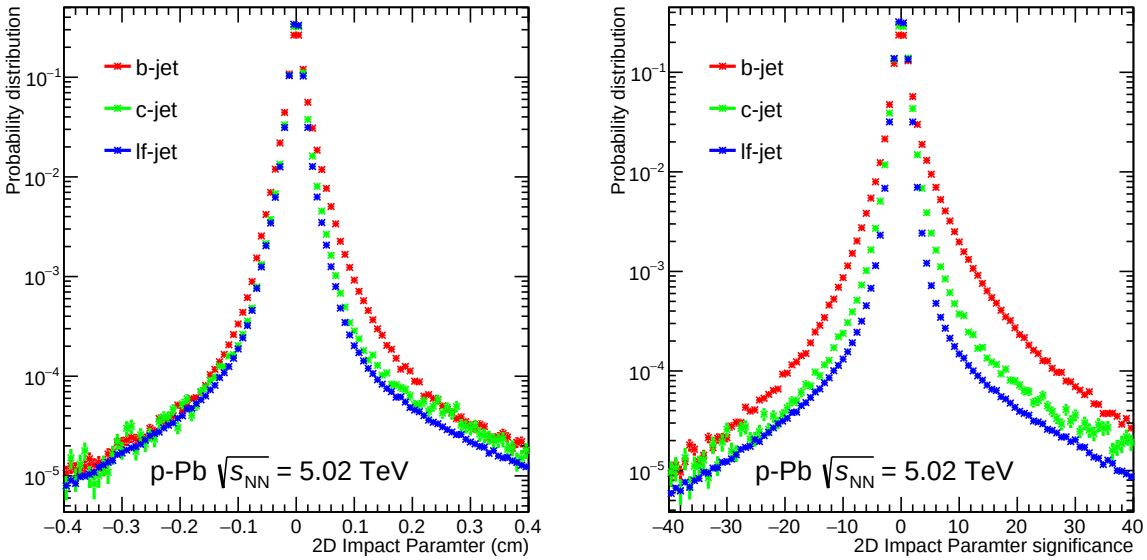

Fig. 4.3 The impact parameter (left), and the impact parameter significance (right) for the tracks inside the different jet flavors

The Track Counting (TC) algorithm arranges the impact parameters (d_{xy}) or the Sd_{xy} values of tracks in the jet in descending order. Despite the fact that the ranking biases the values for the first track to high positive d_{xy}, the possibility to have several tracks with high positive d_{xy} values is low for light-flavor jets. Therefore the three different versions of the TC algorithm use the d_{xy} of the first, second and third (Nth) largest d_{xy} value of the tracks as the discriminator value. These versions of the TC algorithm are called $N = 1$, $N = 2$, and $N = 3$, respectively. A jet is tagged as a b-jet if the Nth largest d_{xy} value is larger than a certain threshold parameter $d_{xy}^{threshold}$. The $N = 4$ was also tested but present in this thesis, it gives a very high purity and very low tagging efficiency. The $N = 4$ tagger stands for rare decays in which the b-hadrons decay into four particles.

Figure 4.4 shows the first, second and third largest d_{xy} values for the tracks inside the jet for the different jet flavors. This figure shows that, the $N = 1$ tagger rejects a small number of c and lf-jets so it gives a largely contaminated sample with non b-jets, while the $N = 2$ tagger rejects a significant amount of light and charm jets and it also keeps a large number of b-jets. But the $N = 3$ tagger reject a very large fraction of the light and charm jets, and keep a significant number of b-jets which makes it the highest purity tagger.

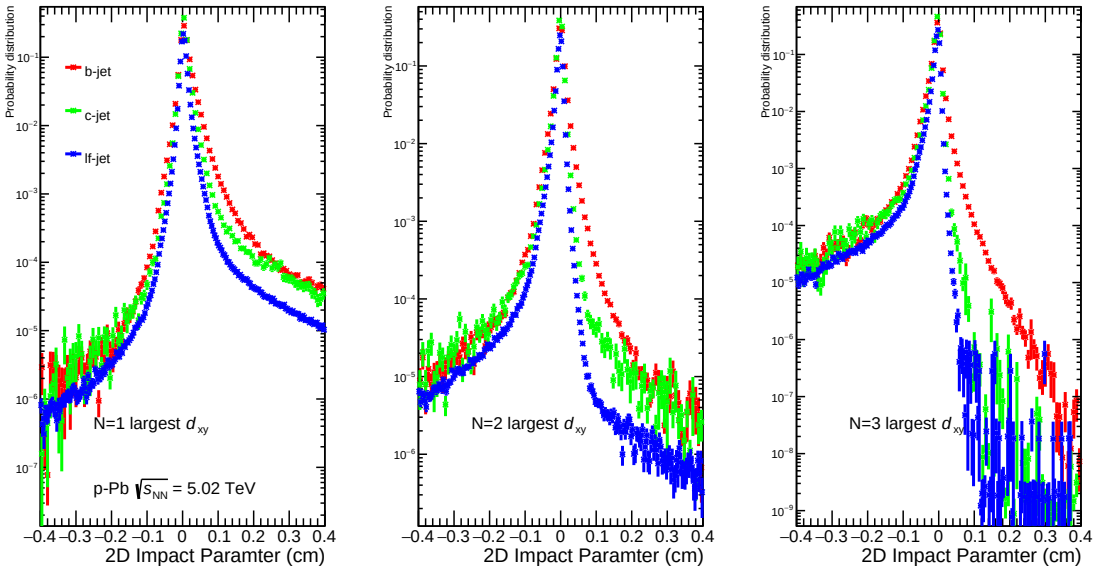

Fig. 4.4 The impact parameter of the first, second, and third largest d_{xy} of the tracks inside the jet for the different jet flavors.

4.4.2 Jet probability algorithm

The jet probability algorithm will be introduced in section 4.5.3, since it will be used in the data-driven methods for extracting the b-jet tagging efficiency in section 4.5.5.

4.4.3 Heavy-flavor decay electrons

This method was not used in this analysis, it was presented just to show the different tagging algorithms used in ALICE collaboration.

Large percentages of charm and beauty quarks decay semileptonically (around 10% probability). The jets originating from charm and beauty quarks can be tagged by identifying the electrons from heavy-flavor decays [179]. First, electrons are identified with the TPC and EMCal. The TPC track's ionization energy loss (per unit length) $\mathrm{d}E/\mathrm{d}x$ in the electron expectation region was used to select electron candidates and reject the hadronic background as shown in Fig. 4.5 (a). The shower of the electron is totally contained and precisely measured by the EMCal, so the ratio of the EMCal measured energy over the ITS+TPC measured momentum is close to unity for an electron, as shown in Fig. 4.5 (b). Hadrons, on the other hand, tend to pass through the EMCal loosing a small fraction of their energy (minimum ionizing particles), so they tend to have have an $E/p \ll 1$ (Fig. 4.5 b). Because of that, the E/p of the electrons was used to select electron candidates and reduce the hadron contamination. Then, the residual hadronic contamination was subtracted using data driven methods by fitting templates of the E/p of the electrons and hadrons extracted from MC to the data E/p. After that, the photonic electrons contamination was identified using the invariant mass method. All the inclusive electrons were paired with other track in the event. The like-sign distribution of

electrons estimates the uncorrelated pairs. Subtracting these from the unlike-sign pairs yields the number of electrons with a photonic partner. Finally the inclusive electrons yield is corrected from these identified photonic electrons.

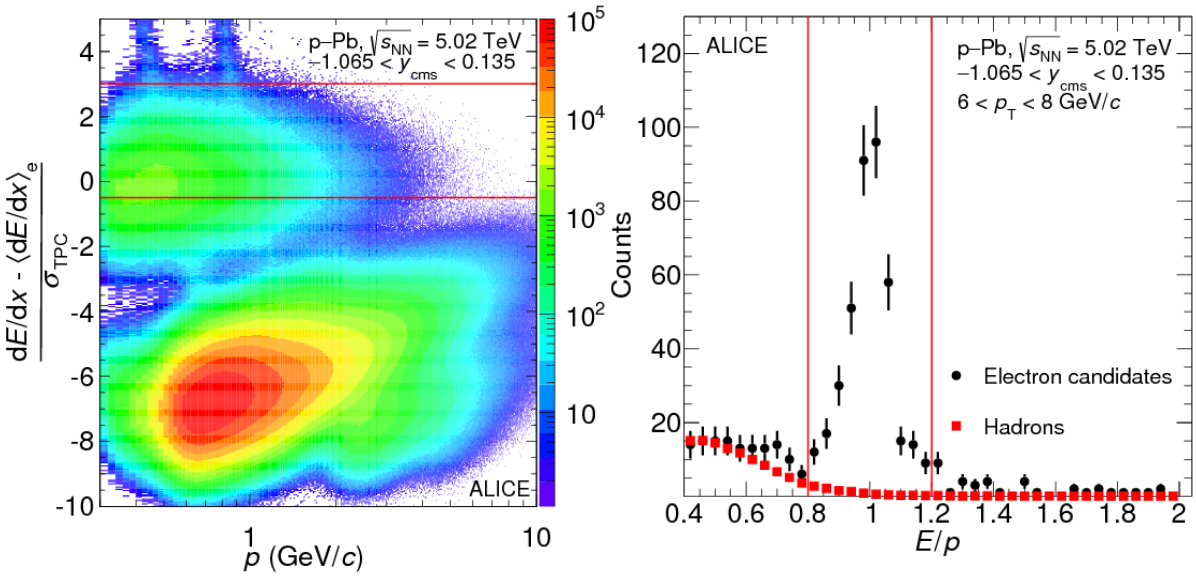

(a) (b)

Fig. 4.5 (a) Measured dE/x in the TPC as function of momentum p expressed as a deviation from the expected energy loss of electrons, normalized by the energy-loss resolution. (b) E/p of the electrons and the hadrons. The solid lines indicate the applied electron selection criteria. Figures adapted from [118].

The heavy-flavor-electron-jet (HFe-jet) tagging is carried out by matching the momentum between the identified heavy-flavor decay electrons and the track constituents of the reconstructed charged jet.

4.4.4 Secondary vertex algorithm

The secondary vertices of the B hadrons in most cases are well displaced from the primary vertex of the collision due to their long lifetime ($\approx 10^{-12}$ s). The SV [180] algorithm reconstructs the secondary vertices inside the jets using their associated tracks. Only vertices reconstructed from three tracks in the jets are selected. This algorithm reconstructs all the possible secondary vertices from three tracks, and the most displaced vertex is selected for the tagging. The vertex reconstruction quality is described by the dispersion of the vertex's tracks $\sigma_{vtx} = \sqrt{d_1^2 + d_2^2 + d_3^2}$, where $d_{1,2,3}$ are the distances of closest approach of the three track to the secondary vertex.

This algorithm uses the decay length to discriminate the b-jets from the charm/light jets. The decay length is the distance between the primary vertex and the secondary vertex. The sign of the decay length can be determined as the sign of the scalar product of the jet axis with the flight distance $i.e$ the vector pointing from the primary vertex to the position of the secondary vertex $L = |\vec{L}| \cdot sign(\vec{L} \cdot \vec{p}_{jet})$. This algorithm tags the b-jets by cutting on the SV dispersion σ_{vtx} and on the flight distance significance which

the flight distance divided by its uncertainty $SL_{xy} = L_{xy}/\sigma_{L_{xy}}$ (Fig. 4.6). As shown in Fig. 4.6, the decay length of the b-jets is larger than that of the charm and light flavor jets, which shows that the SL_{xy} can be used as a discriminator for b-jets. The larger the SL_{xy}, the more charm and light jet rejection, which improves the discrimination power.

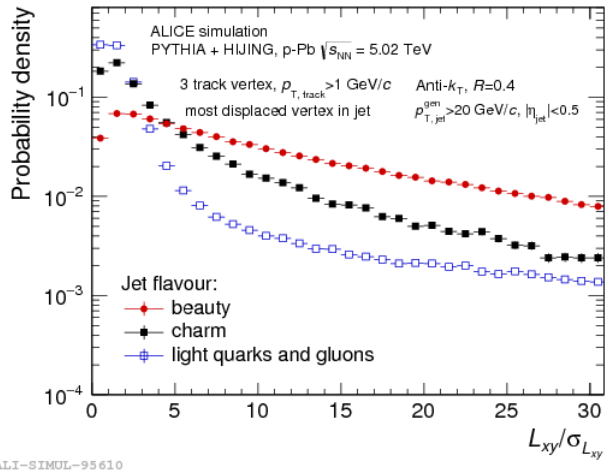

Fig. 4.6 Probability distribution of the signed flight distance significance of the most displaced secondary vertex [180].

Figure 4.7 shows the SV algorithm tagging performance through measuring mistagging rate of the c/lf-jets vs the tagging efficiency of the b-jets for different tagger working points. The different working point were obtained by varying the SL_{xy} cuts from 2 to 14, while the $\sigma_{vtx} < 0.02$ cm was fixed. As shown in the figure, stronger cuts result in a lower tagging efficiency, but also much lower mistagging rates for the c/light-flavor-jets, which therefor increase the purity of the sample.

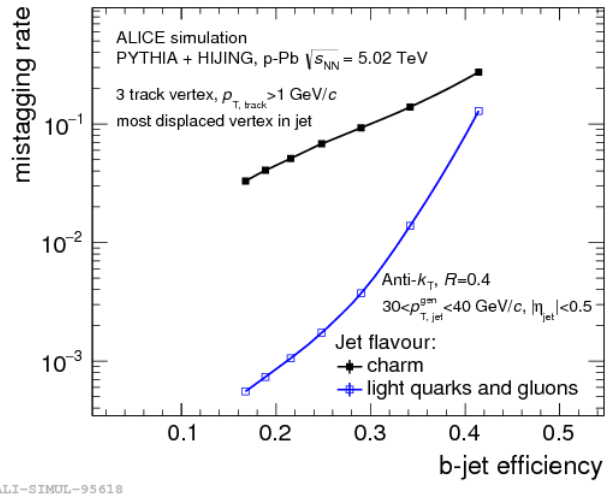

Fig. 4.7 Mistagging rate vs the b-tagging efficiency of SV tagging algorithm for different operating points for jets with $30 < p_{T,jet} < 40$ GeV/c [180].

Comparing the plots of Fig. 4.7 with the performance plots of the track counting tagger in Fig. 4.12, it seems that the secondary vertex tagger which is a main stream tagger in ALICE has approximately similar performance as the track counting tagger.

It should be noted that this algorithm was not used in this analysis, it was presented just to show the different tagging algorithms investigated in ALICE collaboration.

4.5 b-jet spectrum in p–Pb collisions

The aim of this thesis is to measure the p_T-differential production cross section for b-jets. This is achieved in different steps:

- The underlying event background is subtracted from the raw tagged p_T spectrum.
- After applying the b-jet tagging algorithm described in section 4.4, the raw tagged jets has to be corrected from tagging efficiency and purity.
- Then, the raw b-jet spectrum has to be corrected from detector effects and background fluctuation (in p–Pb collisions) using the unfolding procedure.

4.5.1 Underlying event subtraction

In p–Pb collisions, the reconstructed jets which are made from constituents originating from the hard scattering are not the only jets present in the events, there are softer contributions present in the event which are coming from the underlying events, mainly semi-hard parton scattering at p_T's of the order of a few GeV/c.

In Pb–Pb collisions, the clustered jet momentum is largely affected by the huge background which is mainly coming from the underlying events. The common method used in such systems for estimating the background is a statistically robust median of all k_T-clustered jet transverse momenta per area per event.

For pp and p–Pb , which have sparser environment, various techniques for a valid background estimate have been developed and have been used for systematic uncertainty studies. The default method that will be used in this thesis is the CMS method [181].

The CMS collaboration introduced a method especially made for sparse systems [181]. Its main idea is that it accounts for the empty spaces not by adding ghost jets (jets with no particles) but by implementing a factor correcting for the empty spaces in the event.

The CMS method defines the background density ρ as:

$$\rho_{CMS} = \text{Median}\left\{\frac{p_{T,i}}{A_i}\right\} \cdot C\,, \quad \text{where } C = \frac{\text{Covered Area}}{\text{Total Area}} \tag{4.1}$$

where i is the index of the k_T jets with $p_T > 0.150$ GeV/c, and C is the charged tracks occupancy factor, accounting for the fraction of the occupied area by charged particles. This occupied area by the particles is determined by the k_T jet finding algorithm [30]. Generally, the C factor shows how full or empty the event is.

The corrected jet transverse momentum $p^{corr}_{T,ch.jet}$ is determined by subtracting the average background density times the area of the jet from the raw jet p_T as:

$$p^{corr}_{T,chjet} = p^{raw}_{T,ch.jet} - \rho A_{jet}. \tag{4.2}$$

For a specific use, this method can be redefined. By excluding the hardest two k_T jets from the jets set in equation 4.1, the signal is suppressed, enhancing the background quality, which makes the background estimation more precise. The background density ρ is shown in Fig. 4.8.

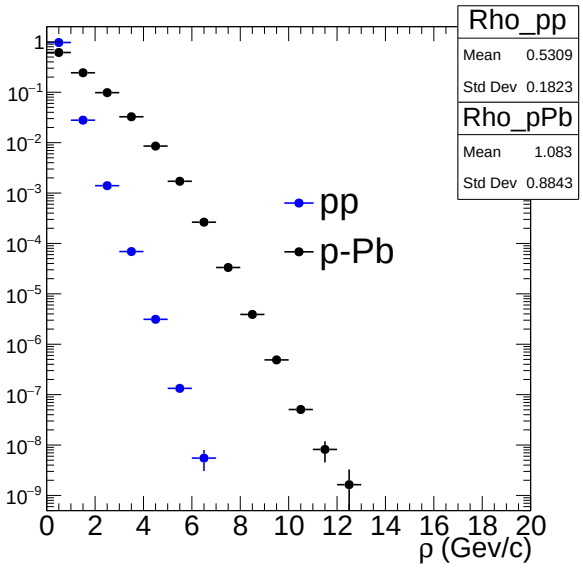

Fig. 4.8 The background density ρ in pp and p–Pb collisions.

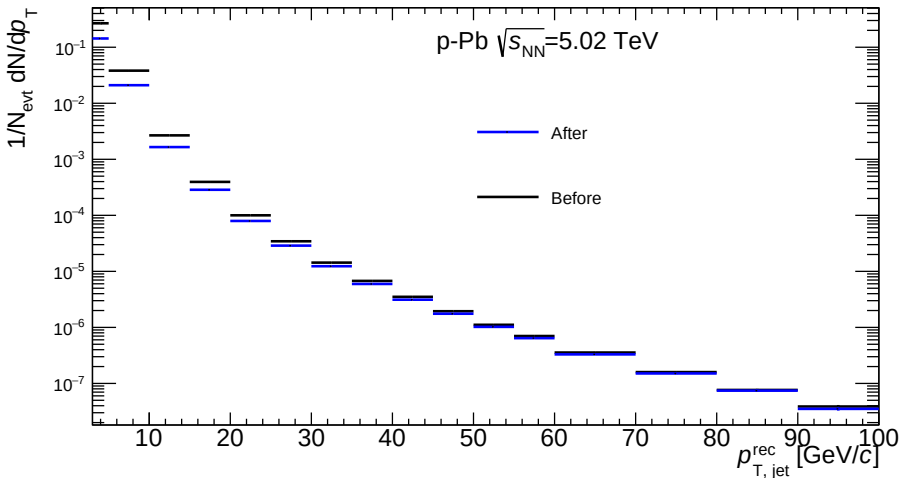

Fig. 4.9 The raw inclusive jet spectrum after and before subtracting the underlying events.

Fig. 4.9 shows the raw inclusive jet spectrum after and before subtracting the underlying events in p–Pb collisions.

4.5.1.1 Background fluctuation

The background density is estimated using the particles in the jet acceptance on an event-by-event basis. Assuming a uniform background distribution, every jet is corrected

depending on its area. This is an assumption, since it is impossible to calculate the real background of a single jet - in reality the true background density for a given jet, fluctuates around the calculated value, and should be corrected for. Random uncorrelated fluctuations in particle production process results in a Poissonian distribution of the particle count.

The Random Cone (RC) approach [182] is used in this thesis in order to estimate the background fluctuation.

For each event, a cone is placed in a random position in the $\eta - \phi$ plane inside the jet detector acceptance region. After all, the tracks in the event that have a $\Delta R < R_{cone}$ are selected in the analysis, with R_{cone} equal to jet resolution parameter, and ΔR is the distance between the track and the random cone:

$$\Delta R_{track,cone} = \sqrt{(\eta_{track} - \eta_{cone})^2 + (\phi_{track} + \phi_{cone})^2}. \tag{4.3}$$

The transverse momentum of all the selected tracks are summed and then the background density is subtracted from the summed p_T. The background fluctuation δp_T can be defined by:

$$\delta p_T = p_{T,RC} \; - \; \rho \pi R^2_{cone} \tag{4.4}$$

For each tagger, certain events were selected for the background estimation. Only events that contains a tagged b-jet (using the N_{th} tagger) were selected for the background estimation.

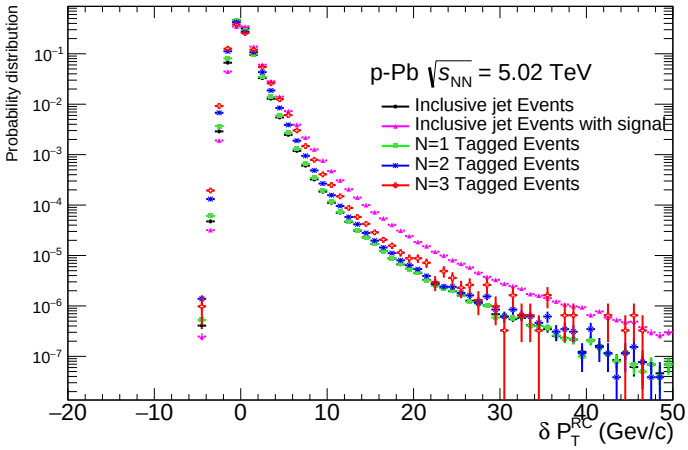

Fig. 4.10 The background fluctuations (δp_T distribution) for the different tagged jet events compared to that of the inclusive jet event in p–Pb collisions.

Figure 4.10 shows the background fluctuation δp_T distribution for the different event categories. As shown in the figure the statistical fluctuation can lead to negative and positive values of δp_T. The negative region of the δp_T distribution corresponds to fluctuations caused by soft scattering processes, while the positive side of the δp_T distribution corresponds to both background fluctuation and signal.

The main target of the random cones is to examine the background within a jet for different positions in the jet detector acceptance. Therefore the δp_T assesses how the background fluctuates within a jet in the event. The δp_T is estimated with a cone equal

to the jet radius, for such reasons. Since the random cones are randomly positioned in the event, the random cone may overlap with a signal jet (or with the hardest jet in the events), in this case the background estimation will be largely overestimated (Fig. 4.10).

To avoid such effect, a modified δp_T estimation was used in this thesis and the original δp_T estimation will be considered for systematic uncertainties. This modification discards all the random cones that overlap with the signal jets in the event. The signal jets here are defined as the leading and the sub-leading jets in the event (the hardest and the sub-hardest jets). Fig. 4.10 shows the difference the between the δp_T distributions with and without signal exclusion. As shows in the figure, it is clear that removing signal jets reduces the background estimation.

4.5.2 Tagging efficiency

The b-jet tagging algorithms discussed in chapter 4.4 don't tag all the b-jets in the events. For the purpose of using the b-tagging in a physics analysis, it is required to measure the tagging efficiency of the tagging algorithms to correctly identify a jet originated from a b quark as a b-jet (ϵ_b: b-efficiency) or to wrongly tag as a b-jet, a jet originated from a charm quark (ϵ_c: c-mistag-efficiency) or a jet originating from a light quark or a gluon (ϵ_{lf}: lf-efficiency or mistag rate). The tagger working point is defined by the threshold parameter (minimum value cut) that should be applied on the discriminator distribution (like impact parameter, JP, decay length, ...), in order to get the tagging efficiency and purity.

In this analysis, a PYTHIA6+EPOS-LHC MC simulations was used for the p–Pb data. At the generator level (particle level) a jet was identified as a b-jet if it contains a b-quark inside its cone through the equation:

$$\Delta R_{quark,jet} = \sqrt{(\eta_{quark} - \eta_{jet})^2 + (\phi_{quark} - \phi_{jet})^2} \tag{4.5}$$

where $\Delta R_{quark,jet}$ is the distance between quark and the jet in the $\eta - \phi$ plane, and $\eta_{quark/jet}$ and $\phi_{quark/jet}$ are the pseudo-rapidity and azimuthal angle of the quark/jet. Using equation 4.5 a particle level jet is defined as a b-jet if it satisfies the criteria $\Delta R_{quark,jet} < R_{jet}$ where $R_{jet} = 0.4$ is the jet resolution parameter (jet radius). The same thing was done in order to determine whether the particle level jet is a c-jet or lf-jet. For the detector level jets, in order to determine the jet flavor, jet matching between the detector and the generator level has been used. A detector level jet is matched to a particle jet through the matching procedure. The jet matching procedure matches two jets if their distance in equation 4.5 (instead of quark-jet it is jet-jet) is $\Delta R_{gen-jet,rec-jet} < 0.25$. If the matched particle level jet is b/c/lf-jet, the detector level jet should be b/c/lf-jet respectively.

After determining the jet flavors, the tagging algorithms are applied and the tagging/mistagging efficiency is calculated as:

$$\epsilon_i(p_T) = \frac{N_i^{Tagged}(p_T)}{N_i^{Total}(p_T)} \tag{4.6}$$

where i is the jet flavor (b, c, lf-jets), N_i^{Tagged} is the number of tagged i-jets, and N_i^{Total} is the total number of i-jets before tagging.

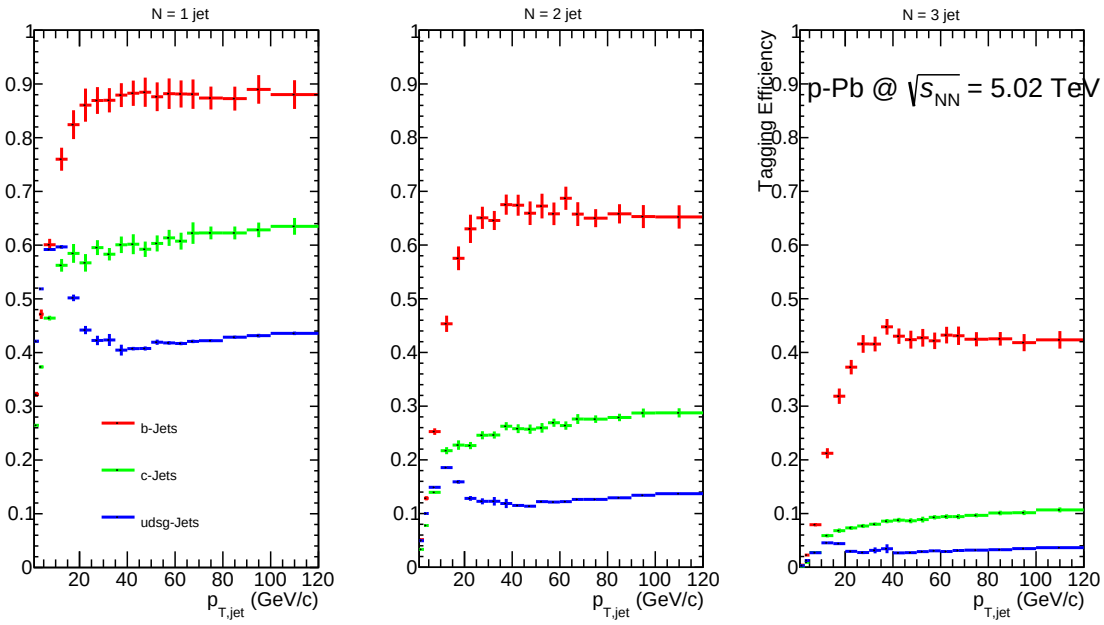

Fig. 4.11 The tagging efficiency and the mistagging rate of the b-jet and c/lf-jets respectively with the tagger working point $d_{xy}^{min} = 0.008$ cm, for the $N = 1$, $N = 2$, and $N = 3$ tagged jets.

Figure 4.11 shows the tagging efficiency for the different jet flavors as a function of p_T for the $N = 1$, $N = 2$, and $N = 3$ tagged jets. The b-jet tagging efficiency increases steeply at low p_T, and after 30 GeV/c it starts to get flat with p_T. The c-jet tagging efficiency has the similar shape as the b-jet (increasing and then flat). The efficiency to tag a b-jet is much larger than the efficiency to tag a c-jet, which is in turn larger than that of the lf-jets. The three taggers use the same working point but the b-jet tagging efficiencies are different such that the $N = 1$ b-jet tagging efficiency is larger than the $N = 2$ tagging efficiency, which in turn is larger than the $N = 3$ tagging efficiency, but the rejection of the c-jet and lf-jets is much larger for the $N = 3$.

Figure 4.12 shows the performance of the track counting taggers algorithm. The tagger working point for the track counting was varied between $0.0 < d_{xy}^{min} < 0.6$ cm. As we tighten the working point, the tagging efficiency decreases but concomitantly the light and charm rejection largely increase, which increases the b-jet purity. The charm-jet rejection shown in Fig. 4.12 left is very similar for all the taggers. The default working point for the track counting algorithm that was used in this thesis is $d_{xy}^{min} = 0.008$ cm (the dashed lines in Fig. 4.12).

4.5.3 Jet probability algorithm

The jet probability (JetProb) algorithm [178] [177] also uses the measured track impact parameter information. It extends the Track Counting tagger by using combined impact

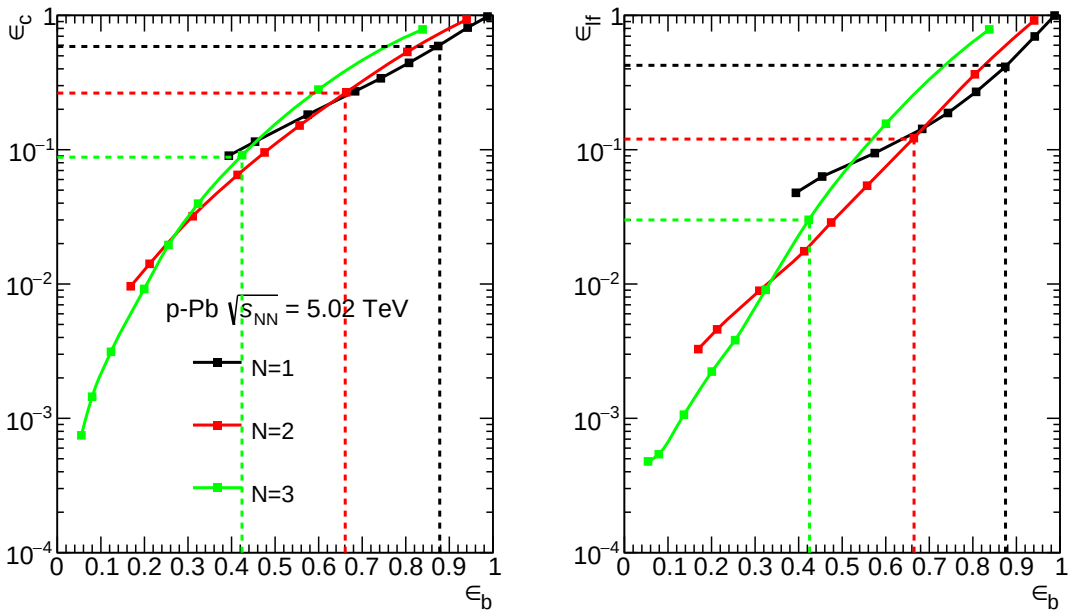

Fig. 4.12 The performance of the N_{th} track counting taggers algorithms for jet transverse momentum in the range $30 < p_T < 40$ GeV/c. The dashed colored line corresponds to the default tagger working point.

parameter significance Sd_{xy} of the tracks inside the jets. The JetProb algorithm uses an estimate of the likelihood that all tracks associated to the jet are originated from the primary vertex (from the interaction point). This algorithm defines a resolution function (R) by fitting the negative side of signed impact parameter significance distribution for different track quality categories. It fits the negative part of the distribution because all the tracks in that region are primary tracks originated from the primary vertex. The resolution function is parameterized as the sum of five exponential functions plus a Gaussian function as follows:

$$\begin{aligned} R \quad = \quad & exp([0] + [1] * x) + exp([2] + [3] * x) + exp([4] + [5] * x) + exp([6] + [7] * x) + \\ & + exp([8] + [9] * x) + [10] * exp(-0.5 * ((x - [11])/[12]) * *2). \end{aligned} \tag{4.7}$$

Seven track quality categories were defined (Fig. 4.13):

- Tracks that have a $\chi^2/NDF > 2$ where NDF is the number of degree of freedom.
- Tracks with $\chi^2/NDF < 2$, 2 hits in the ITS and $p_T < 2$ GeV/c.
- Tracks with $\chi^2/NDF < 2$, 2 hits in the ITS and $p_T > 2$ GeV/c.
- Tracks with $\chi^2/NDF < 2$, 3 hits in the ITS and $p_T < 2$ GeV/c.
- Tracks with $\chi^2/NDF < 2$, 3 hits in the ITS and $p_T > 2$ GeV/c.
- Tracks with $\chi^2/NDF < 2$, 4 hits in the ITS and $p_T < 2$ GeV/c.

- Tracks with $\chi^2/NDF < 2$, 4 hits in the ITS and $p_T > 2$ GeV/c.

The different categories were adjusted to describe the geometric and tracking effects as much as possible, which results in 7 track categories.

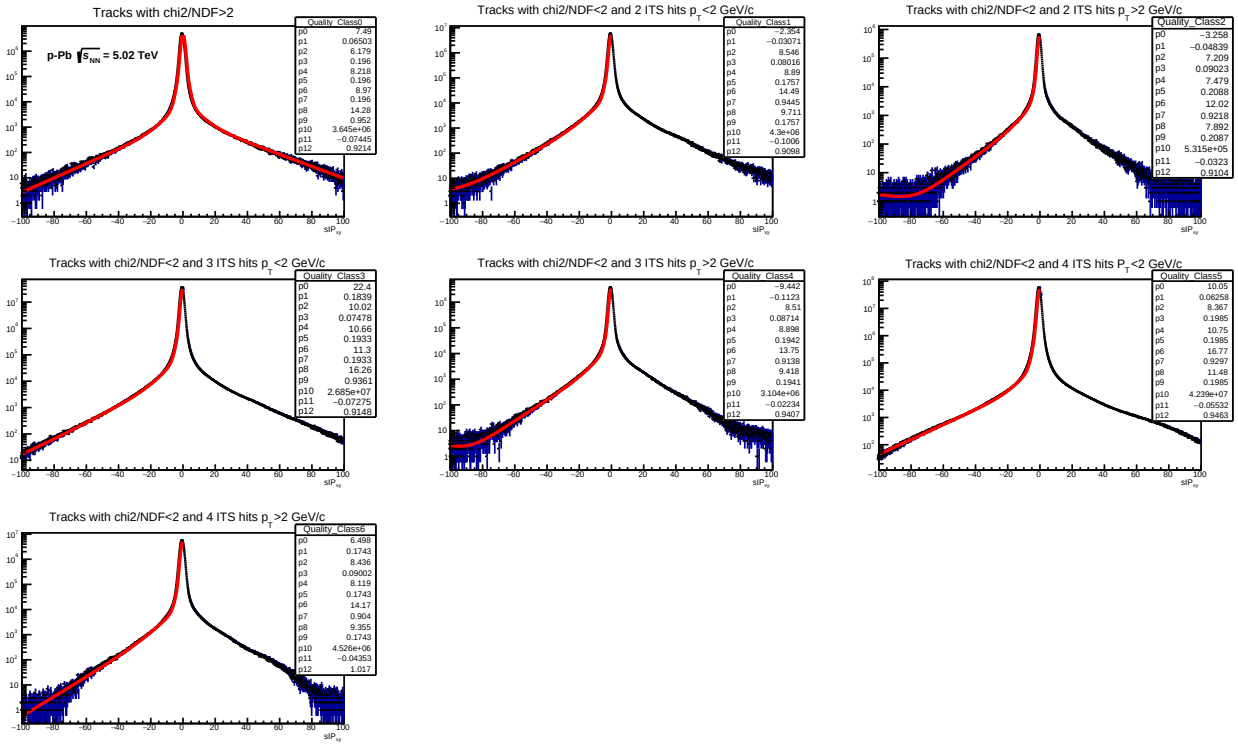

Fig. 4.13 The impact parameter significance distribution for the different tracks categories fitted with a certain function in order to extract the resolution function R.

After extracting the resolution functions from the different categories (Fig. 4.13), this resolution function was used to calculate the track probability (P_{tr}) for a high quality track within the jet to come from the primary vertex with its Sd_{xy} using the following equation:

$$P_{tr}(Sd_{xy}) = \frac{\int_{-\infty}^{-|Sd_{xy}|} R(S)dS}{\int_{-\infty}^{0} R(S)dS}. \tag{4.8}$$

If the jet contains at least two tracks with probability information, then the jet probability is calculated by combining the probabilities of the track inside the jet through the following equation:

$$JP = \prod \times \sum_{k=0}^{N_{trk}-1} \frac{(-\log \prod)^k}{k!} \quad \text{where} \quad \prod = \prod_{i=1}^{N_{trk}} P_{tr}. \tag{4.9}$$

For the calculation of the jet probability only positive d_{xy} tracks are selected. Two forms of jet probability studied. The first form is the normal probability JP Fig. 4.14 (a), and the second form00 is the one that is used by the CMS $-\ln(JP)$ as shown in Fig. 4.14 (b). The figure shows that the JP distribution for b-jets has a very large peak at 0 and is flat for $JP > 0.2$ while the c-jets have a much smaller peak and is flat at $JP > 0.2$, and the

lf-jets are almost flat. For Fig. 4.14 (b) the $-\ln(JP)$ drops much faster for lf-jets and c-jets, while for b-jets it tends to be more flat.

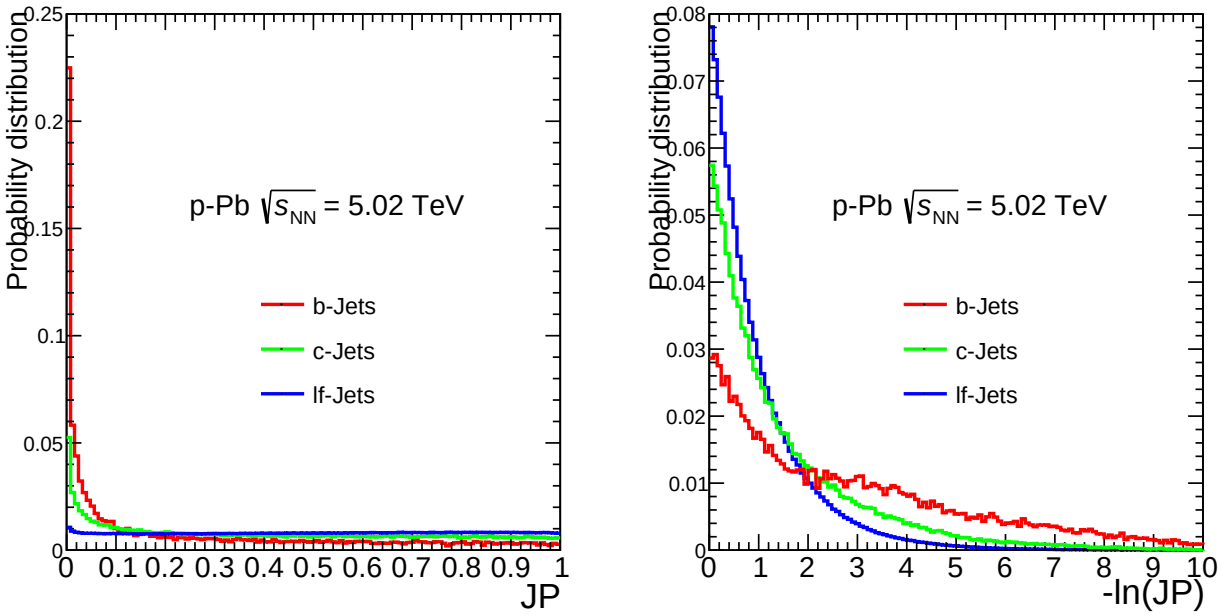

Fig. 4.14 The jet probability discriminator (left) JP, (right) $-\ln(JP)$ for the different jet flavors extracted from MC simulation.

The CMS discriminator ($-\ln(JP)$) was studied in this thesis because it will be used for data driven efficiency and purity calculation using the lifetime reference tagger section 4.5.5.

4.5.4 MC description

In this analysis, we faced several problems with the simulation. The first problem was that the impact parameter and the impact parameter significance of the MC was not describing the data as shown Fig. 4.15. Since the track counting tagger is based on the impact parameter, the discrepancy between the data and MC in d_{xy} may lead to a different tagging efficiency and even different purity. So we decided to investigate data driven methods for efficiency and purity determination.

For the jet probability algorithms, the JP and $-\ln(JP)$ distributions are based on the impact parameter significance distribution, which is different between data and MC. So two different resolution functions were used. In data, the resolution function was built from the impact parameter significance taken from data, while in MC, the resolution function was built from the impact parameter significance taken from MC. The data resolution function is used when building the jet probability distribution in data, and the MC resolution function is used for building the templates used in the data driven methods (section 4.5.5).

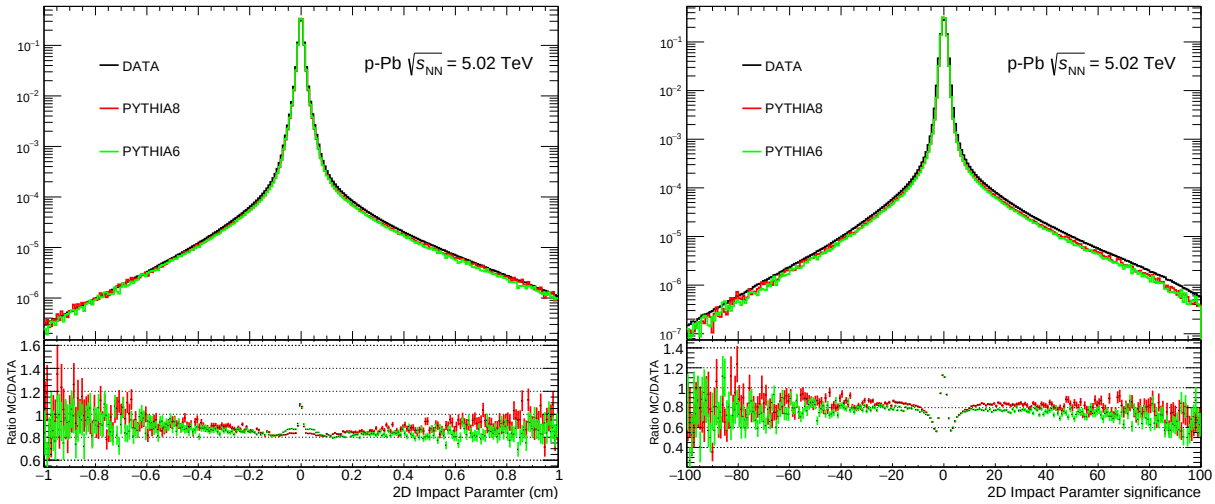

(a) (b)

Fig. 4.15 The the difference between data and MC in impact parameter (left) and impact parameter significance (right) in p–Pb collisions.

4.5.5 Data driven approaches

Data-driven methods are methods that mainly rely on measured distributions extracted from data. These methods require different distributions (or templates) from MC for the signal and background separately. Then, these MC templates are fitted to the data in order to extract the signal fraction and the background fraction.

4.5.5.1 The lifetime reference tagger

The discriminator of the jet probability algorithm is highly discriminating for the different jet flavors for the various jet momenta. According to the jet probability algorithm, tracks with negative impact parameter are used to calculate the probability that those tracks are coming from the primary vertex. The jet probability algorithm can be used as a reference for determining the number of b-jets in a data sample, and also for determining the number of b-jets in any subsample selected by applying a different tagging algorithm. As a result, the efficiency of the applied tagging algorithm can be estimated. Since this method uses a lifetime tagger as a reference tagger, it is called the lifetime reference tagger. This method will be used on an inclusive jet sample.

Since the JP discriminator value is defined for jets with at least two tracks with positive impact parameter significance, this discriminator can be calculated for most of the b-jets with high p_T. So the fraction of b-jets with jet probability information "C_b" (as shown in Fig. 4.16) increases from 90% for jet with p_T= 25 GeV/c to approximately 95% for jets with p_T > 40 GeV/c, but it largely drops to 60% for jets with p_T= 5 GeV/c.

The tagging efficiency of a certain tagger is determined by measuring the fraction of jets that obeys the tagger requirements. The inclusive jet sample was divided into two samples, a sample that represents the jets satisfying the tagger requirement and another sample that represents the inclusive jets before applying the track counting algorithm.

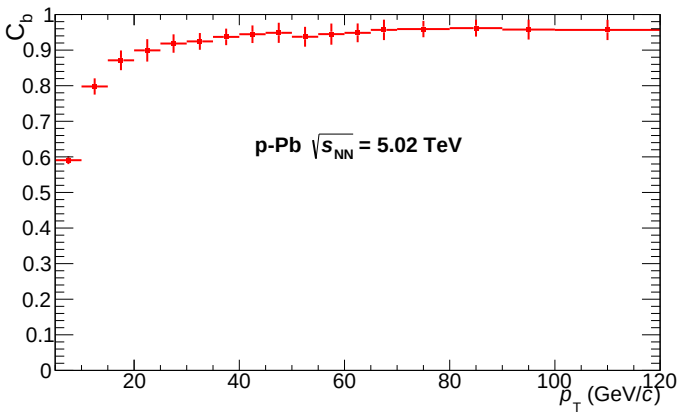

Fig. 4.16 The fraction of b-jet with jet probability information in p–Pb collisions extracted from MC simulation.

These samples will be called (same as before) the "tag" (tagged) sample and the "untag" (untagged) sample respectively.

By fitting JP templates for the b, c, and light parton jets derived from simulation to inclusive jet data with a binned maximum likelihood fit, the fraction of each jet flavor is obtained. The fitting procedure was done separately for the "tag" and the "untag" jet samples. RooFit package was used for this fit [183].

The jet probability discriminator distribution is shown in Fig. 4.17 for the different jet flavors before and after the tagging with the track counting algorithm. In the same figure, the fit to the JP distribution of the data is also shown before and after the tagging using templates reconstructed from MC for the different jet flavors. The tagging efficiency of the b-jets is defined as the ratio of the number of b-jets tagged by the Track Counting tagger to the number of b-jets before applying the tagger as in the equation:

$$\epsilon_b = \frac{C_b \cdot f_b^{tag} \cdot N_{data}^{tag}}{f_b^{untag} \cdot N_{data}^{untag}} \tag{4.10}$$

where f_b^{tag} and f_b^{untag} are b-jet fractions after and before applying the Track Counting tagger respectively, and they are extracted from the fits, N_{data}^{tag} and N_{data}^{untag} are the number of inclusive jets after and before applying the tagger and they are extracted from data, and C_b is the fraction of b-jets that contains a jet probability information which was applied to correct the b-jet tagging efficiency.

The lifetime reference tagger can not be used to determine the tagging efficiency of the jet probability algorithm itself because it uses the JP discriminator in the fitting procedure to obtain the b-jet content of the sample. The jet probability uses cuts on the JP to extract the tagging efficiency and purity so the JP distribution can't be fitted. For more details on the lifetime reference tagger you can refer to [127, 177].

Fig. 4.18 shows the difference in tagging efficiency between the data-driven method and MC. It is clear on this figure that the b-jet tagging efficiency is underestimated by MC. The reason for this big discrepancy is the difference in impact parameter between data and MC. The effect of the tagging efficiency on the measred spectrum is about 20%.

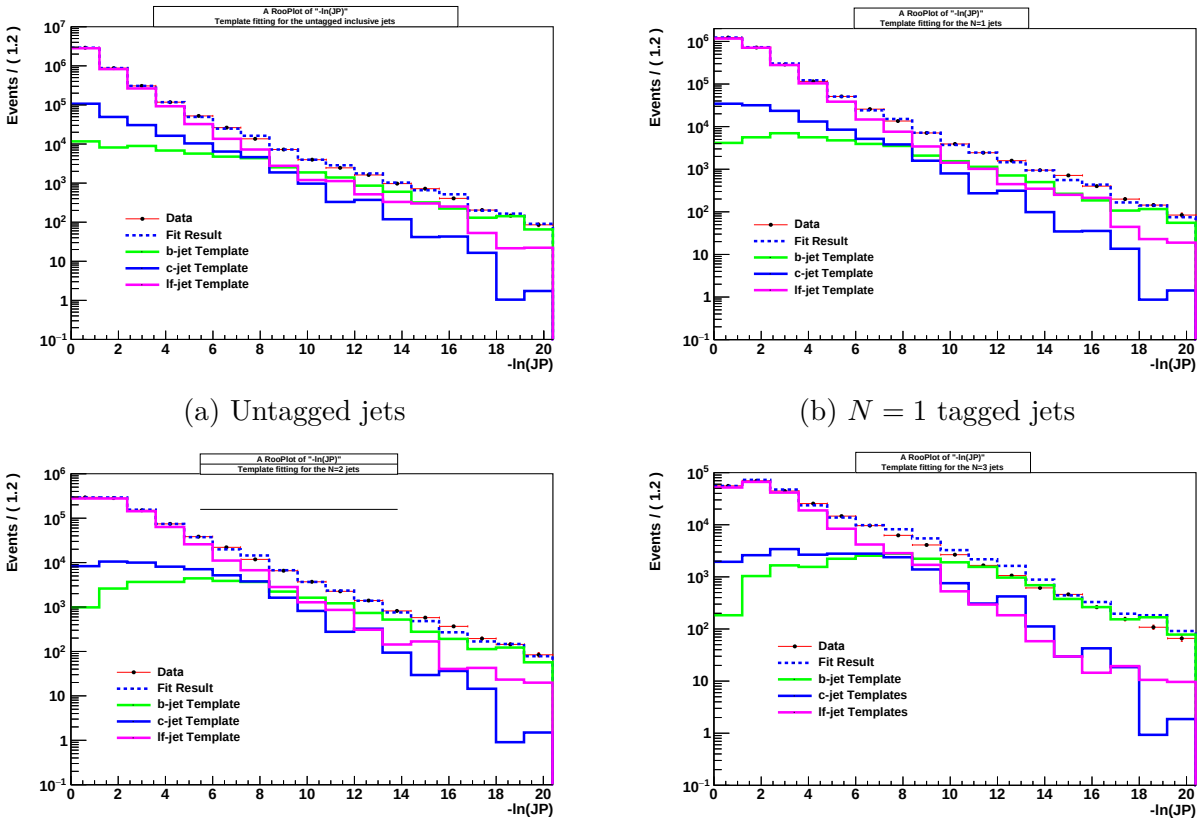

(a) Untagged jets

(b) $N = 1$ tagged jets

(c) $N = 2$ tagged jets

(d) $N = 3$ tagged jets

Fig. 4.17 Template fits of the combined b, c and light-parton jet templates to the JP discriminator distributions from data. (a) For the untagged sample, (b) for the $N = 1$ tagged sample, (c) for the $N = 2$ tagged sample, and (d) for the $N = 3$ tagged sample in the jet p_T range between $10 < p_T < 20$ GeV/c.

4.5.6 b-jet purity

The b-jet tagging algorithms introduced in chapter 4.4 don't only tag b-jets, but it also tag charm and light-parton jets, as was seen in section 4.5.2, and these misidentified jets need to be corrected for. So in order to use the b-jets in physics analyses it is necessary to measure the b-jet tagging purity to correctly identify the amount of b-jets in the tagged sample.

After identifying the flavors of the jets and after applying the tagging algorithm and applying the tagger working point, the b-jet purity which is defined as the number of tagged b-jet in the tagged sample, is estimated as:

$$P(p_T) = \frac{N_{b-jet}^{tagged}(p_T)}{N_{inc.jet}^{tagged}(p_T)} \tag{4.11}$$

where $P(p_T)$ is the b-jet purity as a function of p_T, $N_{b-jet}^{tagged}(p_T)$ in the number of tagged b-jets in the tagged sample or the number of b-jet estimated from b-jet template

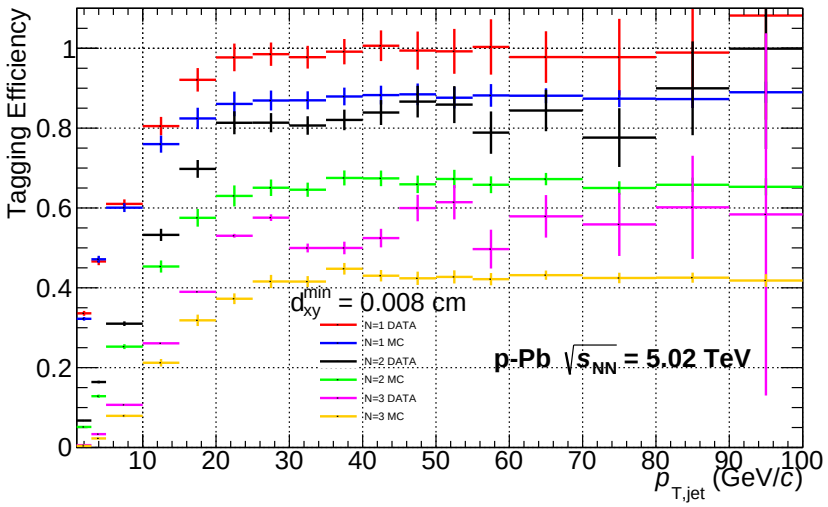

Fig. 4.18 The b-jet tagging efficiency extracted from the data-driven methods compared to the b-jet tagging Efficiency taken directly from MC simulation.

fitting, and $N_{inc.jet}^{tagged}(p_T)$ is the number of all the tagged inclusive jets $i.e$ $N_{inc.jet}^{tagged} = N_{b-jet}^{tagged} + N_{c-jet}^{tagged} + N_{lf-jet}^{tagged}$.

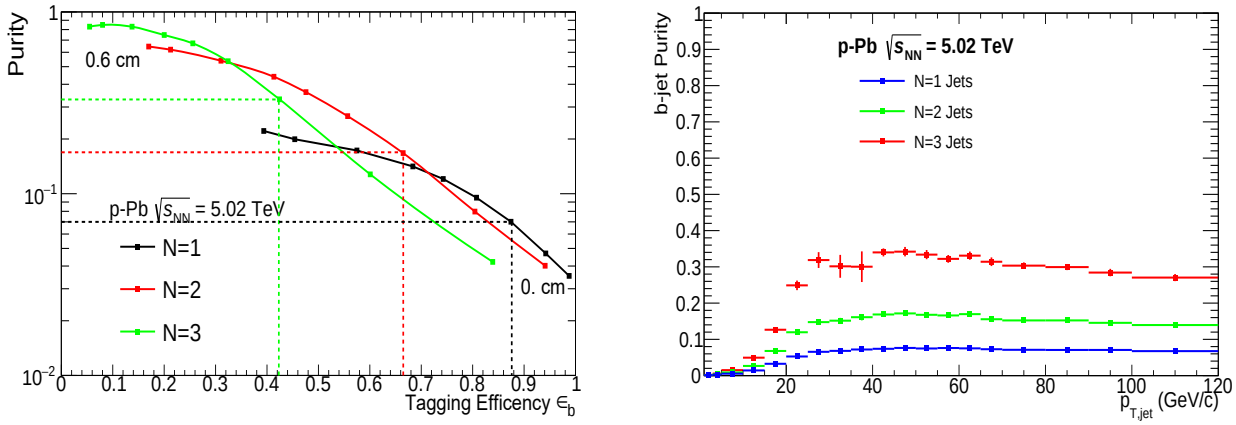

(a) (b)

Fig. 4.19 The b-jet purity versus the tagging efficiency for the different working point in transverse momentum range $30 < p_T < 40$ GeV/c (a) and the b-jet purity as a function of p_T (b) for a medium working point of the Track Counting algorithm at $d_{xy}^{min} = 0.008$ cm.

Figure 4.19 (a) shows the b-jet purity as a function of the tagging efficiency for the three Track Counting taggers. This plot was obtained by varying the tagger working point between $0.0 < d_{xy}^{min} < 0.06$ cm for the Track Counting tagger. This figure shows that as the working point increases the b-jet purity increases largely but the tagging efficiency sharply drops which reduces the statistics of the sample. Fig. 4.19 (b) show the b-jet purity as a function of p_T. The purity increases when increasing the transverse momentum

until it starts to slightly decease after $p_T > 30$ GeV/c. This working point analysis was done in a sample of simulated jets with different flavors.

There is another way to estimate the b-jet purity, it is a data-driven method. In order to do a data-driven purity determination, any discriminating variable that discriminates between b-jet, c-jet and light-jets can be used. For example, in the secondary vertex analysis, the purity is estimated by fitting templates of the secondary vertex mass distribution reconstructed from MC for the different jet flavor [127]. The JP distribution was used in this analysis for the template fitting. Same procedure as above was made by fitting templates reconstructed from MC of the JP distribution for the different jet flavors, and the b-jet purity will be fraction of b-jets obtained from the fits.

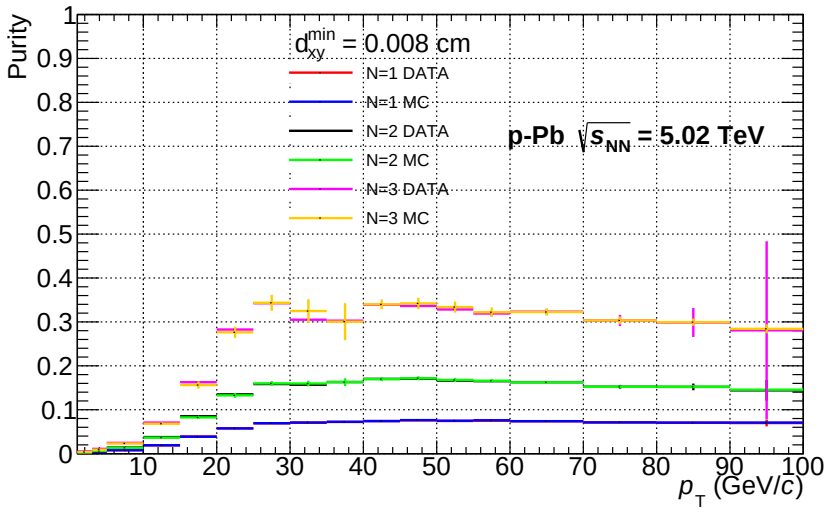

Fig. 4.20 The b-jet purity extracted from the data-driven methods compared to the b-jet purity taken directly from MC simulation.

Fig. 4.20 shows the difference in purity between the data-driven method and MC. It is clear on this figure that the b-jet purity is very well described by MC since it gives a very good agreement with the data-driven method.

Fig. 4.21 shows the raw spectrum before and after applying the tagging efficiency and purity on the tagged jet spectra.

4.5.7 Unfolding

Comparing the jet results obtained from data to the results of other experiments and to the theory predictions requires that both results should be fully corrected to the true, particle level spectrum. To do this comparison, we need a spectrum that is corrected from all detector effects.

After applying background subtraction the obtained jet spectra are not the same as the true spectrum, they differ in two ways. Firstly the background subtracted jet spectra are affected by the detector effects. These jets are reconstructed with transverse momentum that is different from the true transverse momentum because of the tracking efficiency and momentum resolution of the detector. Second, although the jets are corrected for the

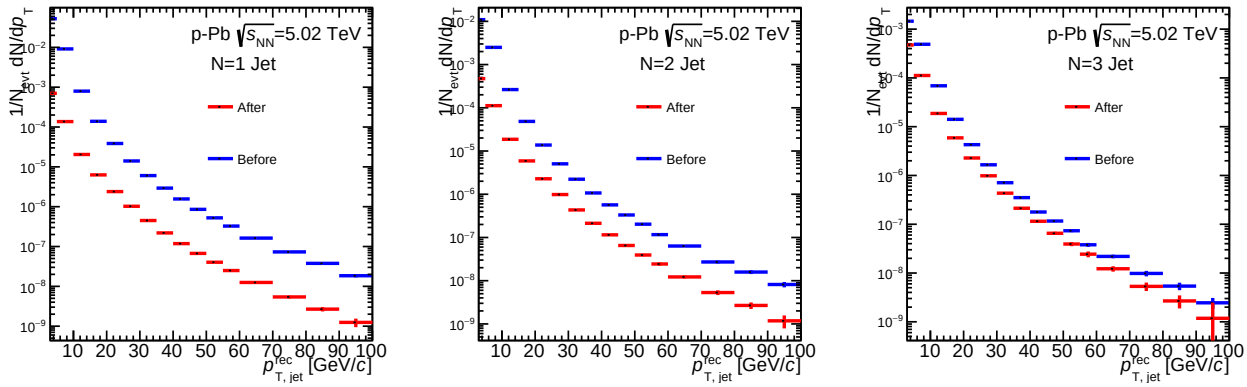

Fig. 4.21 The raw spectrum after and before applying the tagging efficiency and purity correction for $N = 1$ (left), $N = 2$ (middle), and $N = 3$ (right) tagged jets.

average background, they are still affected by the background fluctuations. These two effects can be only corrected on a statistical basis for the whole event sample, and not on an event-by-event basis.

The measured spectrum consists of a true distribution (that represent the true observable) convoluted with the detector (measurement) response (and convoluted with the background fluctuation in case of p-Pb). In general the response can be considered as a function of two variables $f(x, y)$ which represents the probability density that a measured value y in the measured distribution had a true value x before the measurement. In this analysis, the distribution is given as a binned histogram, so the response will be given as a matrix.

The mathematical representation of the effect of the measurement on the true spectrum can be written as:

$$y_i = \sum_j R_{ij} x_j \tag{4.12}$$

where i and j are the bin numbers and R_{ij} are the components of the response matrix. The response matrix R_{ij} corresponds to the detector and the background fluctuation effects on the measurement of the jet spectra.

If the response matrix R_{ij} is known, then unfolding algorithms can be applied to extract the true distribution x from the measured distribution y.

4.5.7.1 Unfolding algorithms

The simple method for extracting the true spectrum from the measured spectrum using equation 4.12 is by inverting the response matrix R. But due to the limitation of the tracking efficiency and momentum resolution of the detector and the finite statistics in simulation, the results may be highly fluctuating. So a kind of regularization has to be included in the unfolding algorithm.

Several unfolding algorithms were applied in this analysis. The Singular Value Decomposition [184] algorithm will be used as the default, while the Bayesian unfolding [185] and the χ^2 unfolding will be used for systematic uncertainty assessment.

Singular value decomposition (SVD)

This unfolding algorithm is based on singular value decomposition known from linear algebra and published in 1996 [184]. This method will be used as the default unfolding algorithm in this analysis. This unfolding algorithm is implemented in the RooUnfold package [186]. Using the matrix representation of (4.12), the unfolding problem can be formulated as a weighted least square problem as:

$$(Rx - y)^T C^{-1} (Rx - y) = \min \tag{4.13}$$

where R is the unfolding matrix, x and y are the true and measured distributions in vector representation, and C is the covariance matrix of the measured spectrum.

In equation (4.13), the "min" factor represents the problem as a minimization problem. The usage of the covariance matrix defines a weighting for the significance of the entries of the measurement vector with respect to the uncertainties on the measurement. The unfolding matrix and the measured distribution vector are rotated and rescaled in such a way that the covariance matrix reduces to the unit matrix and the true distribution is formulated as a ratio relative to the prior, $\tilde{x} = x/x^{prior}$.

The singular value decomposition of the response matrix R can be written as: $R = USV^T$, where U and V are orthogonal matrices and S is a diagonal matrix with positive elements. The elements of the diagonal of S are called the singular values (s_i) of the response matrix, and the columns of U and V are called the left and right singular vectors. The singular values should be gradually decreasing to zero. Small values of s_i corresponds to a large fluctuations. For a smooth measured spectrum, only the first elements (k elements) of the decomposition are significant. The regularization is performed by applying a smooth cut-off on the very small singular value s_i which suppresses the highly fluctuating solutions. The estimation of the optimum regularization parameter is discussed in detail in section 4.5.7.3.

Bayesian unfolding

The Bayesian unfolding [185] depends on Bayes' theorem on conditional probabilities. Bayes' theorem links two differential probabilities by:

$$P(A|B) = \frac{P(B|A) \cdot P(A)}{P(B)} \tag{4.14}$$

where $P(A)$ and $P(B)$ are the probabilities that the events A and B occurring independently of each other, and $P(A|B)$ and $P(B|A)$ are the conditional probabilities that the likelihood of event A occurring under the condition of event B, and vice-versa.

For the case of this analysis, the jet spectra can be treated as a probability distributions and the response matrix can be treated as the distribution of conditional probabilities. With all of these assumptions Bayes' theorem can be rewritten as:

$$S_{ji} = \frac{R_{ij} T_j}{\sum_k R_{ik} T_k} \tag{4.15}$$

where S is the smearing matrix, R is the response matrix, and T is the true spectrum. The denominator of equation 4.15 represents the measured spectrum. In order to extract the true spectrum for a given distribution, the smearing matrix should be used as:

$$T_j = \sum_i S_{ji} M_i \tag{4.16}$$

where M here is the measured spectrum.

In order to extract the true spectrum T in equation 4.16, the smearing matrix S must be known, but looking at equation 4.15, the smearing matrix S can be computed if the true spectrum is known. Which means that a direct computation for S and T is not possible. So in order to calculate S and T an iterative procedure has to be used. First a certain function called "prior" is chosen to replace T, so if T is known then by using equation 4.15 the smearing matrix can be calculated. The prior is a spectrum that should look like the true spectrum as much as possible. Second, equation 4.16 was used to compute the first unfolding in order to produce an unfolded spectrum. In the next iteration, the produced unfolded spectrum is used as the new prior, and this process is repeated several times. In the end the unfolded spectrum should look like the true distribution.

χ^2 unfolding

The χ^2-unfolding is based on a χ^2-function minimization, which can be written as:

$$\chi(x) = \sum_i \left(\frac{y_i - \sum_j R_{ij} x_j}{\delta y_i} \right) + \beta P(x), \tag{4.17}$$

where y_i are the measured values, x_j are the unfolded values, and R_{ij} are entries of the response matrix. The other term $\beta P(x)$ is called the penalty term. The χ^2-unfolding algorithm is a kind of χ^2 fit where y_i corresponds to the free parameters. The χ^2-unfolding algorithm is implemented in AliUnfolding package, which is part of AliRoot. AliUnfolding uses MINUIT [187] for the minimization procedure.

The penalty term is utilized to artificially prefer or penalize a certain property of the unfolded distribution. It represents a regularization of the unfolding procedure by imposing additional constraints to the distribution. These constraints can be such basic properties as smoothness or positiveness of the unfolded spectrum but also detailed restrictions as the preference of a certain spectrum shape. The latter constraint is also used in the present analyses. The penalty term prefers a power-law shape for the unfolded distribution through the following equation:

$$P(x) = \sum_i \left(\frac{\mathrm{d}^2 \ln x_i}{\mathrm{d} \ln p_T^2} \right)^2, \tag{4.18}$$

where x_i are the unfolded values. Equation (4.18) is to be read as the second derivative of the logarithmic representation of the unfolded spectrum. The requirement to minimize this quantity means that the penalty term prefers an unfolded spectrum that is linear in the logarithmic formulation. And the distribution that is linear in this scale is the power-law spectrum.

The regularization strength β should not be chosen too big, otherwise the penalty term dominates the minimization procedure and the unfolded spectrum will be largely affected by the properties induced by the penalty term. On the other hand, regularization strength should not be too small to incorporate the desired properties and to suppress fluctuations.

4.5.7.2 Building the response matrix

The response matrix links two objects together: the measured jet transverse momentum distribution and the true jet distribution. The response matrix includes both the detector effects and the background fluctuations that affect the measurement. In a perfect situation where the detector is perfect and there are no background fluctuations, the response matrix would be a diagonal matrix. The detector response matrix and the background matrix are built separately, so two separate unfolding can be done, but it is better to merge the two matrices into one response matrix by multiplying them so only one unfolding can be performed. The total multiplied response matrix can be represented as:

$$R = F \times DR \tag{4.19}$$

where R is the total response matrix, F is the background fluctuation matrix, and DR is the detector response matrix. The total response matrix can link the true and measured jet spectra by:

$$y_{measured} = (F \times DR) y_{true} \tag{4.20}$$

where $y_{measured}$ is the measured distribution, and y_{true} is the true jet distribution.

The main effect contributing to the total response matrix is coming from the detector response (DR) matrix. The DR is built in a PYTHIA simulated event sample that is propagated through a full detector simulated by GEANT. The particle level (generated level) jet spectra are available from PYTHIA, while the detector level jets can be obtained from PYTHIA+GEANT. The particle level jet spectra are jets that would be measured by a perfect detector, while the detector level jet spectra are jets measured by a detector which includes all detector effects.

The particle and detector level jets are matched by calculating the distance between the jets by using geometrical approach. The jets are said to be matched if the distance between them is smaller than 0.25 as:

$$\Delta R_{part.jet,det.jet} = \sqrt{(\eta_{part.jet} - \eta_{det.jet})^2 + (\phi_{part.jet} + \phi_{det.jet})^2} < 0.25 \tag{4.21}$$

where $\Delta R_{part.jet,det.jet}$ is the distance between particle level jet and the detector level jets in the $\eta - \phi$ plane, and η_{jet} and ϕ_{jet} are the pseudo-rapidity and azimuthal angle of the particle/detector level jets. The number 0.25 stand for the maximum distance between the detector- and particle-level jets. This jet matching links the true particle level jets, and the measured detector level jets. After that, the transverse momenta of the matched jets are used to fill the detector response matrix.

The other contribution to the total detector response is the background fluctuation matrix. This matrix is based on the δp_T distribution estimated for the whole event sample by taking into account that the background fluctuations are independent of the jet p_T.

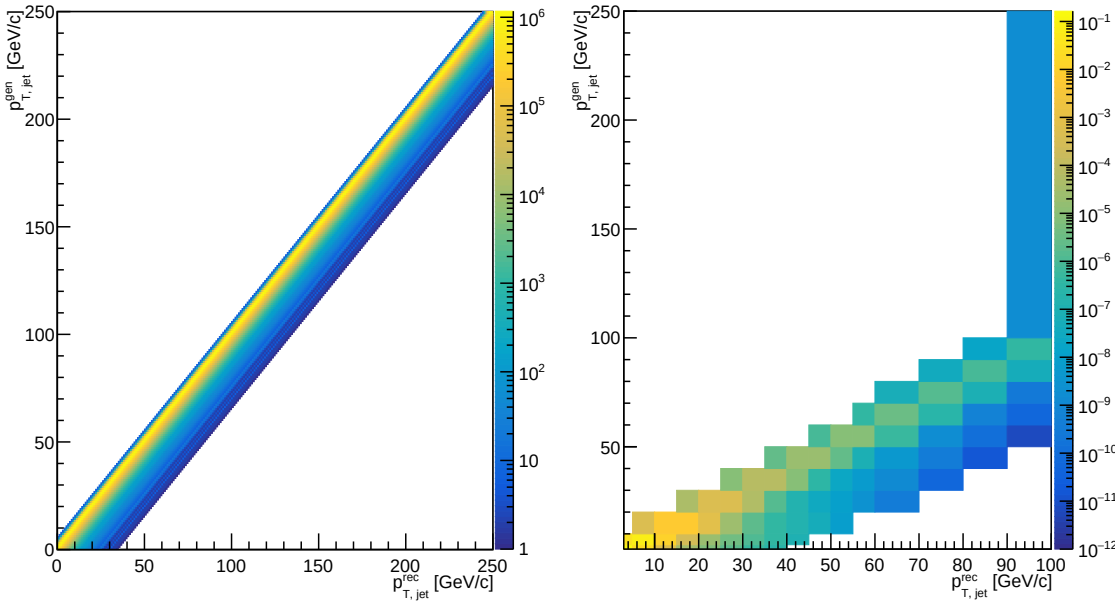

Fig. 4.22 The background fluctuation matrix for the $N = 3$ tagged jet with fine binning in p–Pb collisions (left) and the rebinned and the reweighted version (right). The left palette of the right figure corresponds to probability distribution, and the palette of the left figure corresponds to the number of entries. This matrix will be used in the unfolding procedure of the p–Pb spectra.

The δp_T matrix is built by inserting the one dimensional δp_T distribution in all the slices in the particle level jet transverse momentum. For every single slice, the distribution is shifted by $p_{T,chjet}^{part}$. This is to ensure that the background matrix will give the correct behavior *i.e* symmetric with p_T (it is not p_T dependent). If there was no background fluctuation, the background matrix would be a diagonal matrix with zero off diagonal elements.

Figure 4.22 shows the δp_T matrix with fine binning (left) and with the rebinning and reweighting (right). As discussed in section 4.5.1.1 three δp_T distribution were reconstructed for the different track counting taggers $N = 1$, $N = 2$, and the $N = 3$ taggers, so three background fluctuation matrices were built for the different taggers.

Figure 4.23 shows the detector response matrix with fine binning (left) and the rebinned and reweighted version (right). Also Fig. 4.24 shows the total combined matrix after multiplication. The right matrix of Fig. 4.24 is the rebinned and reweighted version of the total matrix which is the one that will be used in the unfolding.

It should be noted that, the background matrix was used to unfold the p–Pb spectra only, and it will not be used for the b-jets in pp collisions since the background fluctuation are very small in pp collisions.

The response matrix has to be rebinned according to the required binning of the unfolded spectra and also according to the binning of the measured spectrum. The response matrix was rebinned through a weighted rebinning procedure, in which the bin

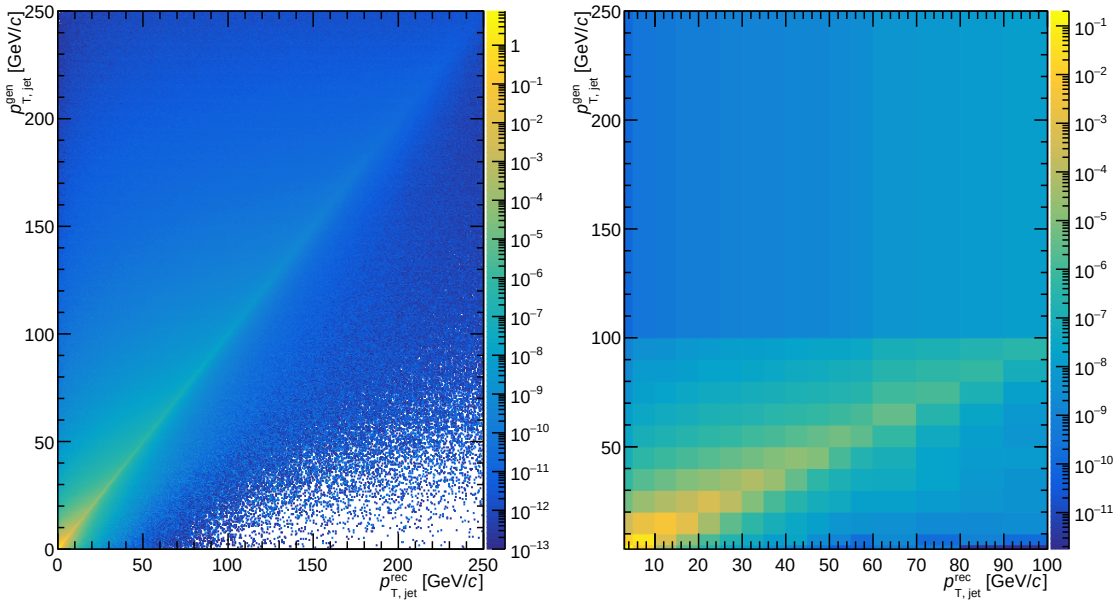

Fig. 4.23 The detector response matrix with fine binning in p–Pb collisions (left) and the rebinned and the reweighted version (right).

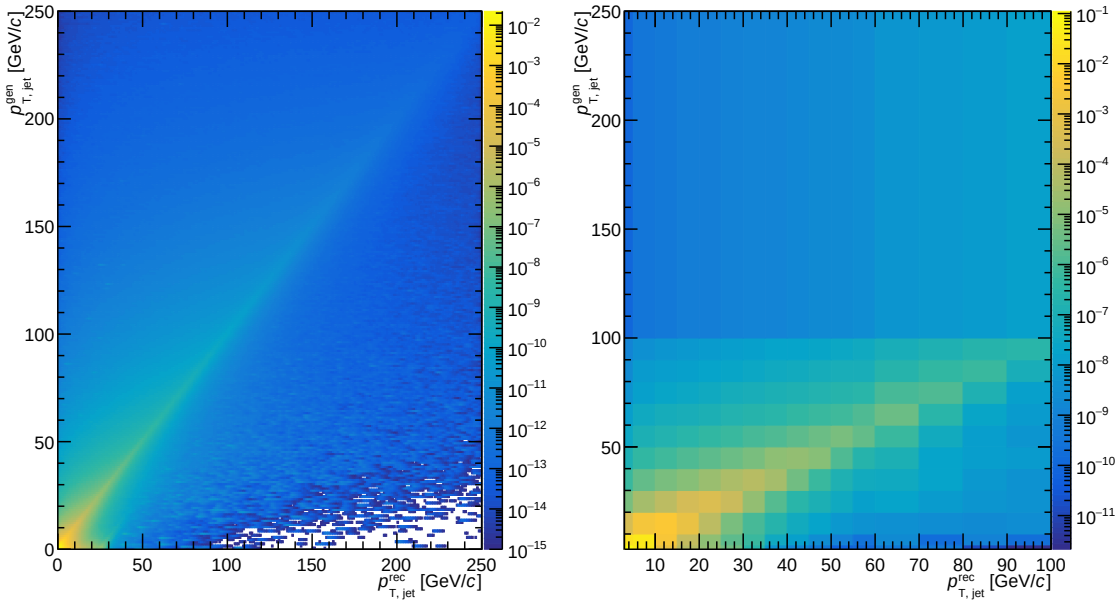

Fig. 4.24 The combined response matrix with fine binning in p–Pb collisions (left) and the rebinned and the reweighted version (right). This response matrix will be used in the unfolding procedure of the p–Pb spectra.

weights is a fit of a Tsallis function to a PYTHIA spectrum:

$$f(p_T) = p_T \left(1 + \frac{p_T}{7.2}\right)^{-8} \tag{4.22}$$

The reason for doing weighted rebinning is because of the large binning used in this analysis. The binning for both spectra is as follows:

- Measured range:
  p–Pb : $\{3, 5, 10, 15, 20, 25, 30, 35, 40, 45, 50, 55, 60, 70, 80, 90, 100\}$,

- Unfolded range:
  p–Pb : $\{3, 5, 10, 20, 30, 40, 50, 60, 70, 80, 90, 100, 250\}$.

The transverse momentum range of the input spectrum truncates the response matrices when rebinning. So some of the particle level jets in a certain p_T ranges ($p_T < 3$ GeV/c and $p_T > 100$ GeV/c) will be lost. This means those jets will be placed in a momentum region which falls outside the measured p_T range.

The kinematic efficiency is the ratio of the particle level jet spectra in the truncated response matrix over the p_T distribution of the true jet. This kinematic efficiency is used after the unfolding procedure by dividing the unfolded spectrum by this efficiency. Another kind of efficiency that has to be used for correcting the jet spectra after unfolding process is the jet reconstruction efficiency. The unfolded jet spectrum is corrected by the reconstruction efficiency by dividing the unfolded spectrum over this efficiency. It is the ratio of the matched particle-level jet spectra in the detector response matrix over the total particle-level jet spectra, it can written as:

$$\epsilon_{jet}^{rec} = \frac{N_{jet}^{matched}}{N_{jet}^{total}} \tag{4.23}$$

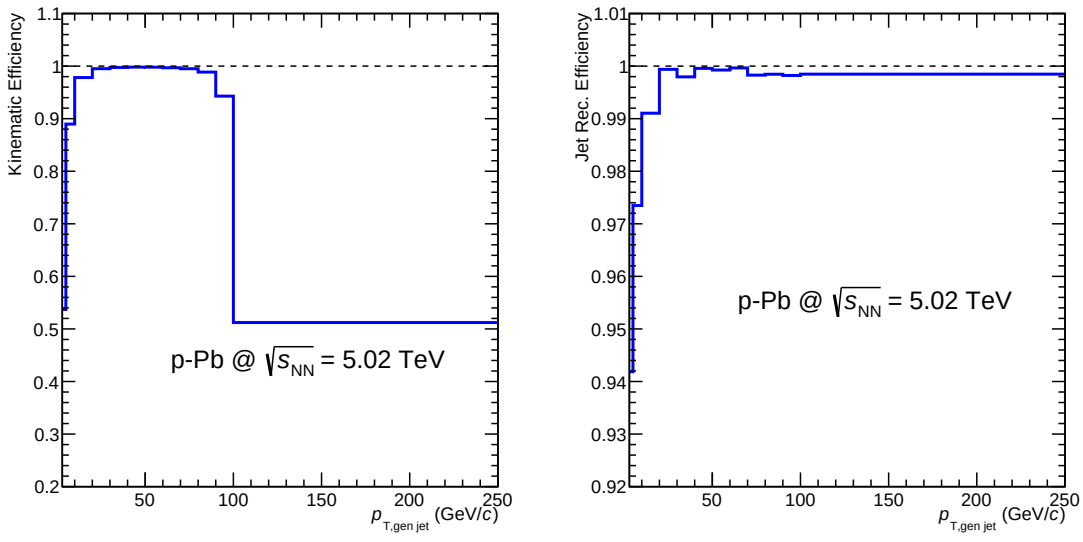

Fig. 4.25 The kinematic efficiency (left) and the b-jet reconstruction efficiency (right).

Figure 4.25 shows the kinematic efficiency for the given response matrix (left) and also shows the b-jet reconstruction efficiency (right). As can be seen in the figure the jet

reconstruction efficiency increases from 0.94 at $p_T = 3$ GeV/c to almost 1 for $p_T > 20$ GeV/c.

The reweighting means dividing the p_T^{gen}-axis of the matrices by the prior distribution. The reweighting of the response matrix introduces a weight for the jets with respect to the probability to find them with a given transverse momentum. The prior distribution determines this probability.

The prior distribution should look like the true spectrum as much as possible. In this analysis the default prior that was used is the PYTHIA b-jet spectrum. It is not clear what prior to use, so different priors were used for systematic uncertainty (section 5.1.2.3). Comparing the left and right panels of Fig. 4.22 shows that the reweighting of the δp_T matrix causes the spectrum to be steeply falling.

4.5.7.3 Regularization parameter analysis

All the unfolding algorithms require a regularization parameter. This regularization parameter describes the regularization strength of the unfolding results. The choice of the best regularization parameter relies on the measured b-jet distribution and needs to be computed for all the different algorithms.

The regularization parameter must be an integer value. The best regularization parameter for the SVD unfolding was obtained by following the procedure described in [184] by looking at the d-vector ($|d_i^k|$) distribution where k is the regularization parameter. The d-vector represents the coefficients of the decomposed measured (and rescaled) histogram with respect to a basis function defined by the columns of the rotation matrix U. For small k, $|d_i^k|$ should be statistically significant $|d_i^k| > 1$, after that, it falls gradually towards zero. The regularization parameter k should be chosen in such a way that the $|d_i^k|$ is close to unity.

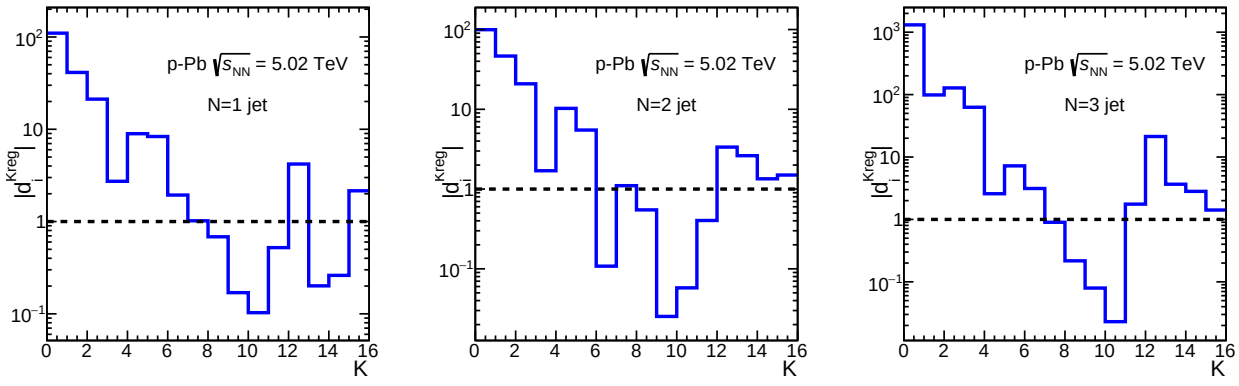

Fig. 4.26 The $|d_i^k|$ (d-vector) distribution for unfolded b-jet spectra in p–Pb collisions.

Fig. 4.26 shows the d-vector distributions, on this figure $|d_i^k|$ starts very large and after that gradually decreases to a very small values $|d_i^k| < 1$. As can be seen on this figure, the $k = 8$ gives $|d_i^k| \approx 1$, so here $k = 8$ should be the optimal regularization parameter.

Also, by comparing the unfolded jet spectrum and the true jet spectrum it is possible to estimate the quality and the validity of the unfolding procedure, this comparison is

called closure test. The unfolding method is said to be perfect if it gives a distribution similar to the true jet distribution.

The best regularization parameter is the one that gives an unfolded spectrum with the least deviation from the true distribution. The optimum regularization parameter in this analysis was chosen to be $N = 1$,$N = 2$,$N = 3$: $k = 8$. The ratio of unfolded over truth is shown for the different regularization parameters in Fig. 4.27. This figure shows that the very small regularization leads to an incorrect unfolded distribution and the very large regularization parameter make the unfolded spectrum to be over-regularized.

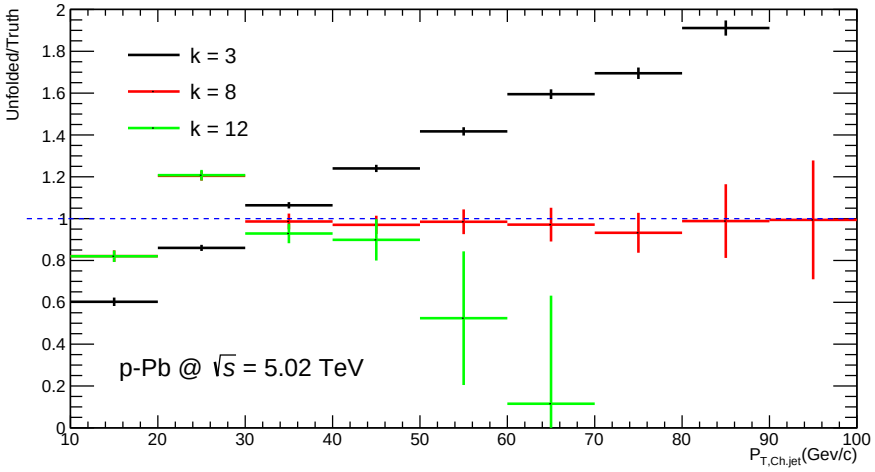

Fig. 4.27 Closure test for the unfolded spectra (ratio unfolded over truth) for the different regularization parameters.

In order to estimate the optimum regularization/number of iteration for the χ^2 and the Bayesian unfolding, the Pearson coefficients are used. The Pearson matrices represent the Pearson coefficients which are a measure of the correlations between the unfolded spectrum and the true jet spectrum, written as:

$$P_{ij} = \frac{Cov(i,j)}{\sigma_i \sigma_j} \tag{4.24}$$

where P_{ij} are Pearson matrix elements, $Cov(i,j)$ is the covariance of the two variables i, j, and $\sigma_{i,j}$ are the standard deviations for i and j. In equation 4.24 i and j represents the bin numbers of the unfolded and the true spectrum.

Figure 4.28 shows the Pearson matrices for different regularization/iteration with the default regularization used is $k = 7$. Unfolded distribution with strong off-diagonal correlations are rejected. So in the optimum case the diagonal elements should be close to unity and the off-diagonal should be close to zero.

Fig. 4.29 shows a comparison between the measured spectrum (after applying the tagging efficiency and purity) and unfolded spectrum for the different tagged jet spectra.

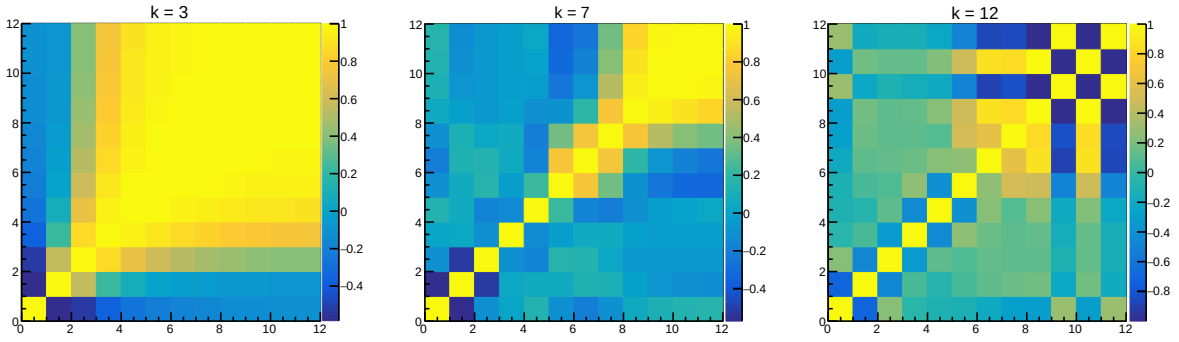

Fig. 4.28 The Pearson coefficient for the different regularization parameters, left $k = 3$, middle $k = 7$, and right $k = 12$.

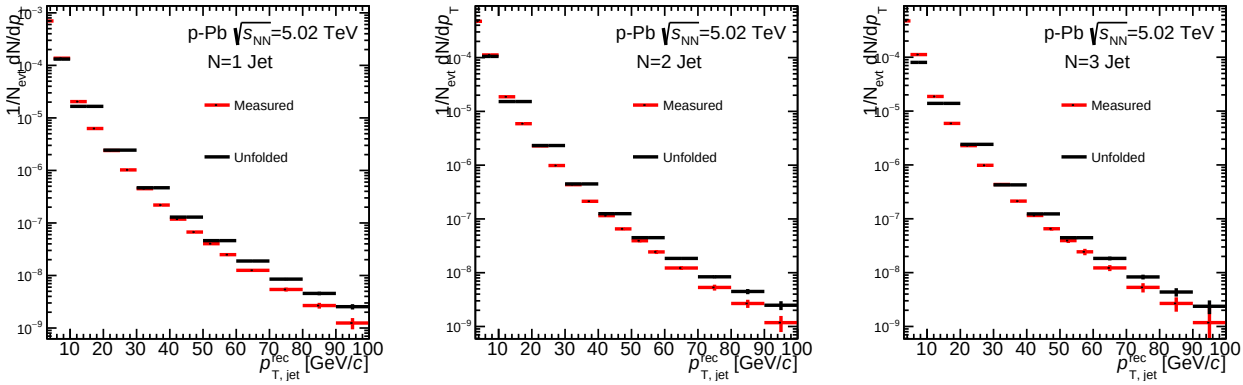

Fig. 4.29 Comparison between the measured spectrum (after applying the tagging efficiency and purity) and unfolded spectrum for $N = 1$ (left), $N = 2$ (middle), and $N = 3$ (right) tagged jets.

4.5.8 Correcting the $N = 1$ jets

Due to the jet probability requirement (section 4.5.3) that the jet has to contain at least two tracks with positive impact parameter, not all the $N = 1$ tagged jets have jet probability information. So when performing the data-driven efficiency determination procedure in section 4.5.5 (which uses the jet probability distribution) not all the $N = 1$ jets will be taken into account. So in order to remove all the $N = 1$ tagged jets with no jet probability information, a certain correction factor has to be applied. This correction factor is the fraction of $N = 1$ tagged jets with jet probability information, and it is determined as:

$$C_{JP}^{N=1} = \frac{N_{tagged}^{JP}}{N_{tagged}} \tag{4.25}$$

where $C_{JP}^{N=1}$ is the fraction of $N = 1$ jets with jet probability information, N_{tagged}^{JP} is the number of $N = 1$ tagged jets with jet probability information, N_{tagged} is total number of $N = 1$ tagged jets.

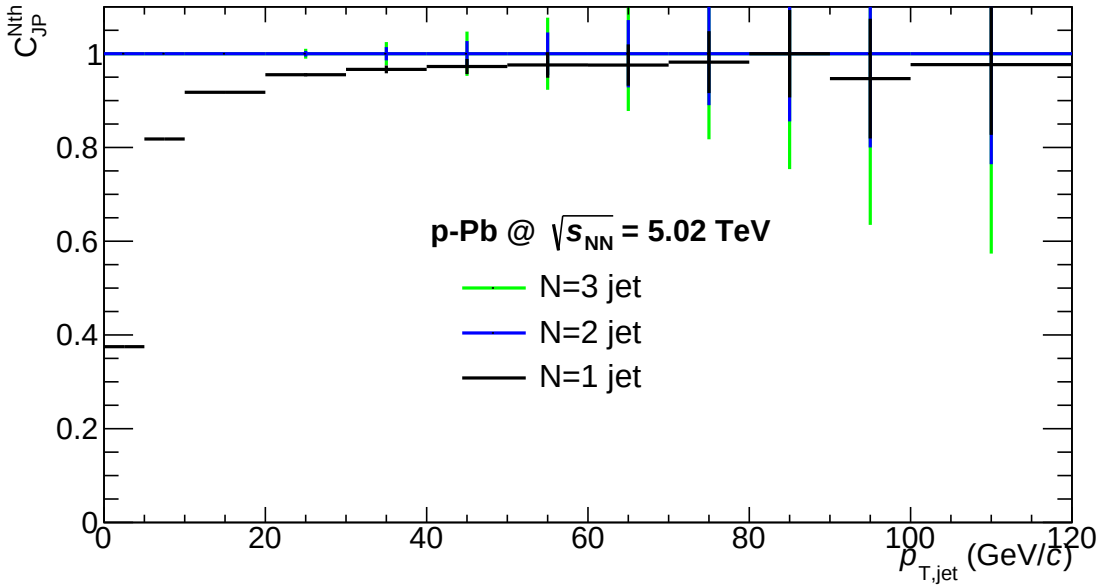

Fig. 4.30 The fraction of $N = 1$ jets with jet probability information in p–Pb collisions.

Fig. 4.30 shows the fraction of $N = 1$, $N = 2$ and $N = 3$ tagged jets that have a jet probability information. As can be seen in the figure, due to the jet probability requirements all the $N = 2$ and $N = 3$ tagged jets have jet probability information which is not the case for the $N = 1$ tagged jets. The fraction of $N = 1$ tagged jets is increasing with p_T until it reaches 1. In order to remove all the $N = 1$ tagged jets with no jet probability information, the unfolded $N = 1$ jet spectrum has to be multiplied by this correction factor.

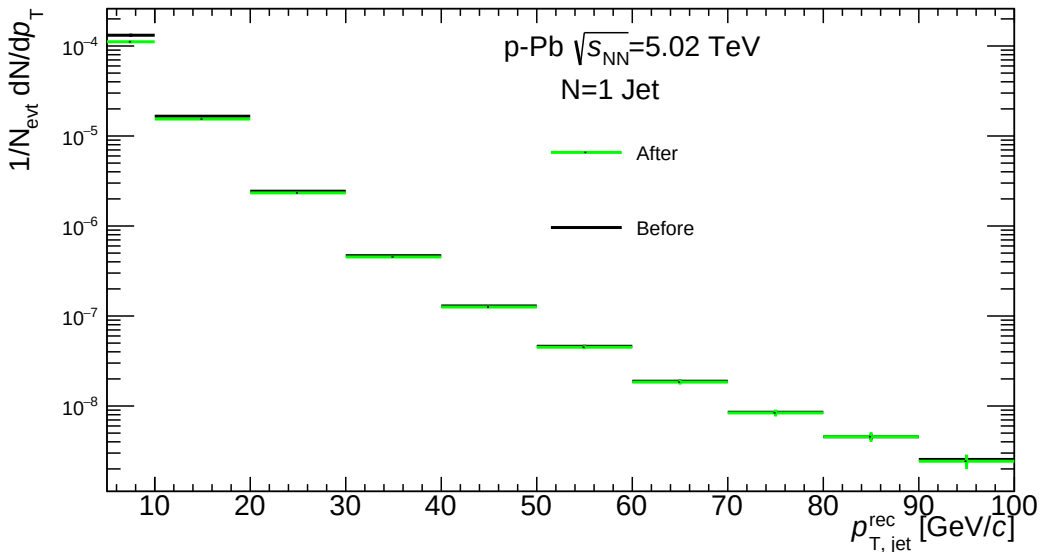

Fig. 4.31 Comparison between the $N = 1$ tagged jets spectra before and after correcting for the jets with jet probability information.

Fig. 4.31 shows a comparison between the $N = 1$ tagged jets spectra before and after correcting for the jets with jet probability information in p–Pb collisions.

4.6 b-jet spectrum in pp collisions

The b-jet spectra in pp collisions were corrected using similar steps used to correct the p–Pb spectra.

4.6.1 Underlying event subtraction

The b-jet spectra in pp collisions were corrected from the underlying events using the same method used for p–Pb collisions (The CMS method) in section 4.5.1. The underlying event density in pp collisions was shown in Fig. 4.8. It is clear on the figure that the underlying event density in pp collisions in much smaller than that of the p–Pb collisions.

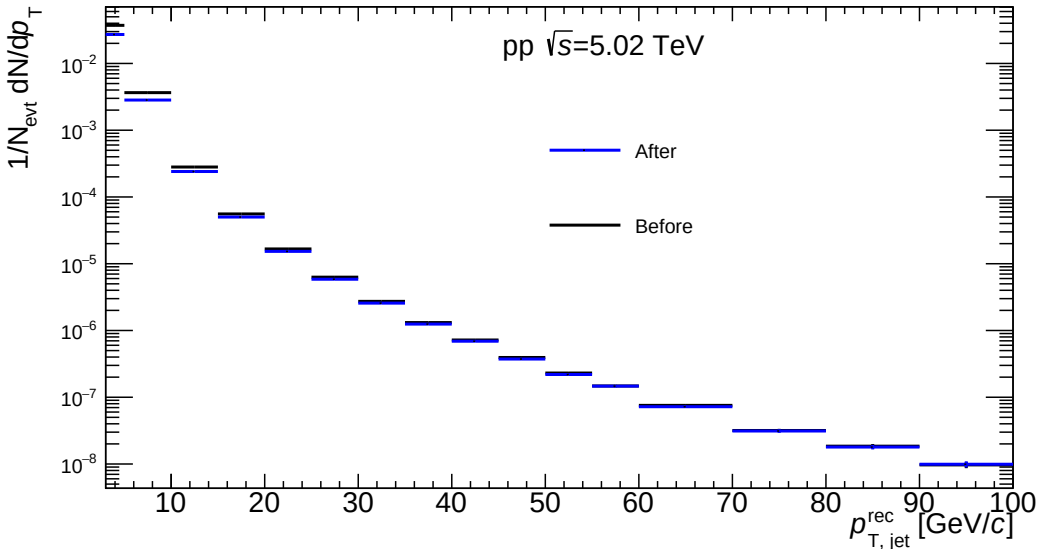

Fig. 4.32 The raw inclusive jet spectrum after and before subtracting the underlying events in pp collisions.

Fig. 4.32 shows the raw inclusive jet spectrum after and before subtracting the underlying events in pp collisions.

4.6.2 Tagging efficiency

The tagging efficiency in pp collisions was estimated in the same way as in p–Pb collisions in section 4.5.2. In this analysis, a PYTHIA8 MC simulations was used for the pp data.

The tagging efficiency in pp collisions is shown for the different jet flavors in Fig. 4.33 as a function of p_T for the $N = 1$, $N = 2$, and $N = 3$ tagged jets. The b-jet tagging efficiency increases steeply at low p_T, and after 30 GeV/c it starts to get flat with p_T. The c-jet tagging efficiency has the similar shape as the b-jet (increasing and then flat).

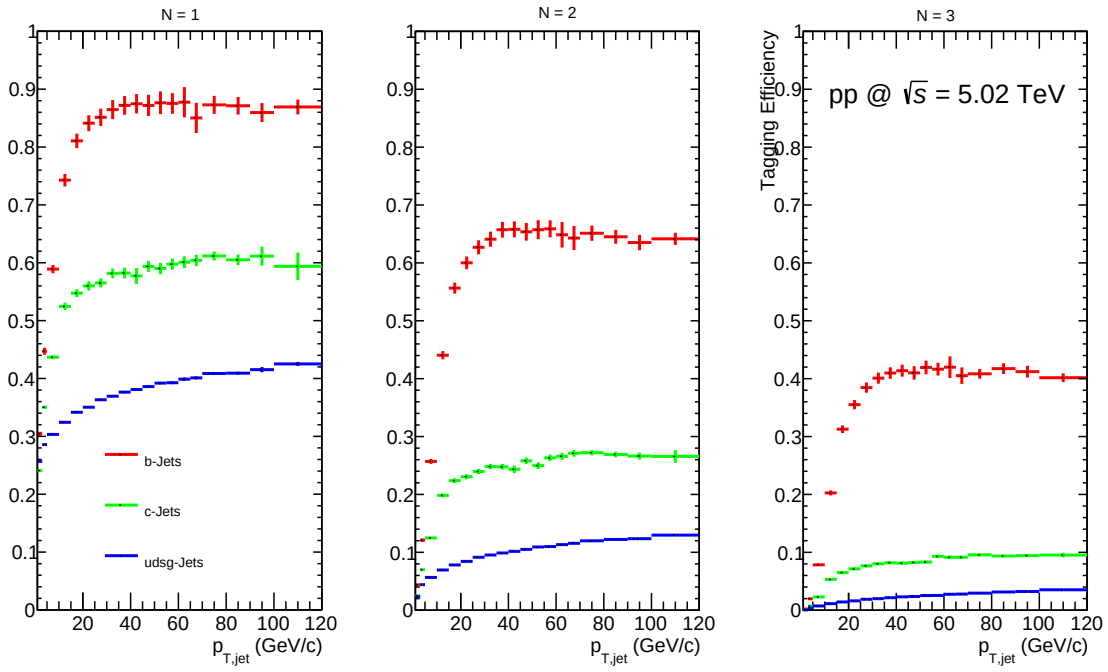

Fig. 4.33 The tagging efficiency and the mistagging rate of the b-jet and c/lf-jets respectively with the tagger working point $d_{xy}^{min} = 0.008$ cm, for the $N = 1$ (left), $N = 2$ (middle), and $N = 3$ (right) tagged jets in pp collisions.

The b-jet tagging efficiency is much larger than the c-jet tagging efficiency, which is in turn larger than that of the lf-jets. The three taggers use the same working point, but for the $N = 3$ the rejection of the c-jet and lf-jets is much larger, while the $N = 1$ b-jet tagging efficiency is larger than the $N = 2$ tagging efficiency, which in turn is larger than the $N = 3$ tagging efficiency. The reason for the different lf-jet mistagging between pp in Fig. 4.33 and p–Pb in Fig. 4.11 at low p_T is due to the EPOS generated soft particles. The MC used in p–Pb is PYTHIA6+EPOS-LHC and in pp is PYTHIA8. EPOS-LHC generates a soft particle which will be clustered into lf-jet, which means the number of lf-jet will be increased so the lf-jet mistag will be increased at low p_T.

the performance of the track counting taggers algorithm are shown in Fig. 4.34 in pp collisions. This figure shows the same behavior as the the one shown for p–Pb collisions (Fig. 4.12). The default working point for the track counting algorithm that was used in this thesis for pp collisions is $d_{xy}^{min} = 0.008$ cm.

4.6.3 MC description

In pp collisions, it was also noticed that the MC doesn't describe the data very well. For example the data impact parameter and the impact parameter significance were not described by MC as shown Fig. 4.35. As the track counting tagger is based on the impact parameter, the discrepancy between the data and MC in d_{xy} may cause a different tagging efficiency and even different purity. So it was decided to investigate data driven methods for determining the efficiency and purity.

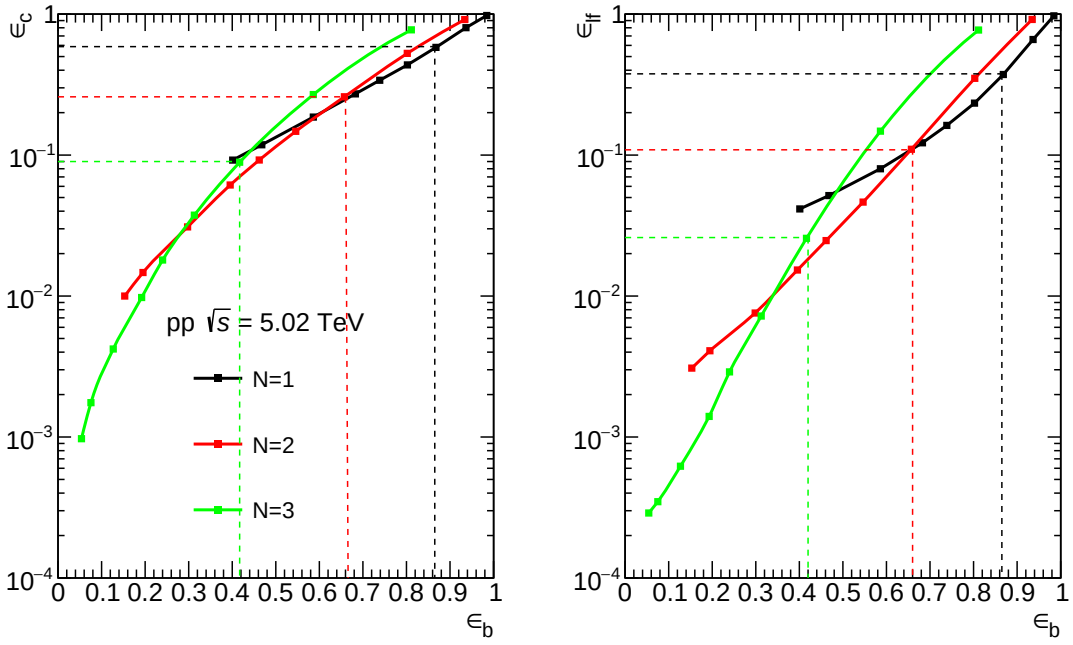

Fig. 4.34 The performance of the N_{th} track counting taggers algorithms for jet transverse momentum in the range $30 < p_T < 40$ GeV/c. The dashed colored line corresponds to the default tagger working point.

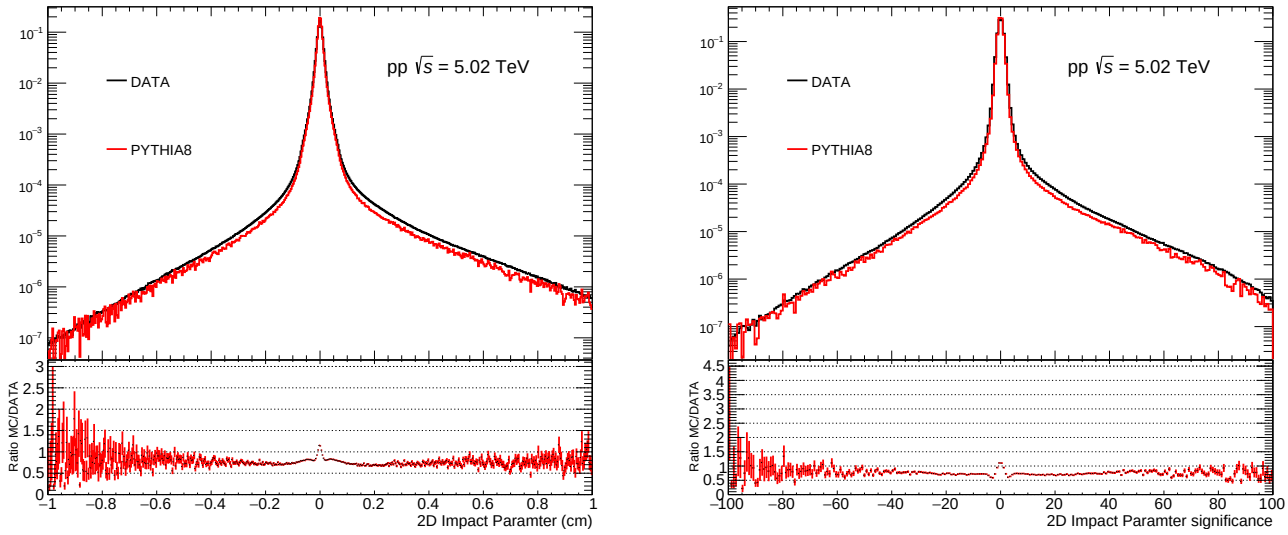

(a) (b)

Fig. 4.35 The the difference between data and MC in impact parameter (left) and impact parameter significance (right) in pp collisions.

4.6.4 Data driven approaches

The lifetime reference tagger was also used for determining the tagging efficiency of the b-jets in pp collisions the same way as was done in p–Pb collisions (section 4.5.5.1).

The JP discriminator value is defined for jets with at least two tracks with positive impact parameter significance, which means a small fraction of the b-jets will not have a jet probability information. The fraction of b-jets with jet probability information "C_b" as shown in Fig. 4.36 sharply increases from 60% for jets with p_T= 5 GeV/c to 90% for jet with p_T= 25 GeV/c after it increases slightly 95% for jets with p_T > 40 GeV/c in which it becomes approximately constant.

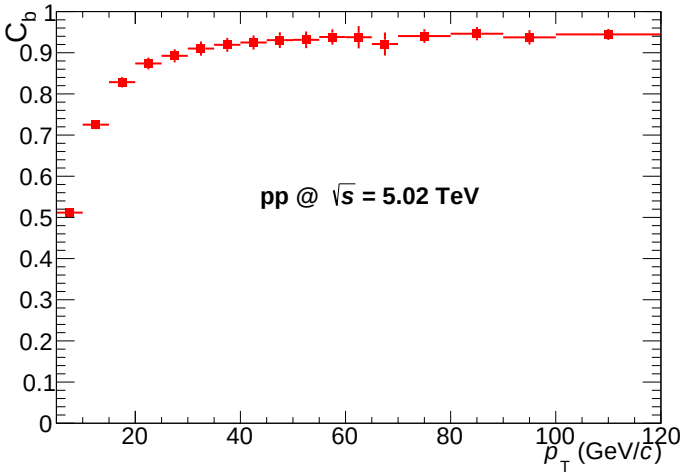

Fig. 4.36 The fraction of b-jet with jet probability information in pp collisions.

The fraction of each jet flavor is obtained by fitting the JP templates for the b, c, and light parton jets derived from simulation to inclusive jet data with a binned maximum likelihood fit. Two jet samples were made, one corresponds to the "tagged" jets and another sample corresponds to the "untagged" (pretagged) jets. The fitting procedure was separately done on both samples.

Fig. 4.37 shows the jet probability discriminator distribution for the different jet flavors before and after applying the track counting algorithm. In the same figure, the fit of the JP distribution using templates reconstructed from MC for the different jet flavors with the JP distribution in data is also shown before and after the tagging . Then the tagging efficiency is calculated the same way as done in p–Pb collisions in section 4.5.5.1.

The difference in tagging efficiency between the data-driven method and MC is shown in Fig. 4.38. It is clear on this figure that MC totally underestimate the b-jet tagging efficiency in pp collisions. The reason for this big discrepancy is the difference in impact parameter between data and MC.

4.6.5 b-jet purity

The b-jet purity in pp collisions was identified in the same way as in p–Pb collisions in section 4.5.6.

The b-jet purity as a function of the tagging efficiency for the three Track Counting taggers is shown in Figure 4.39 (a). This plot was obtained by varying the tagger working point between $0.0 < d_{xy}^{min} < 0.06$ cm for the Track Counting tagger. This figure shows that as the working point increase the b-jet purity increases largely but the tagging efficiency

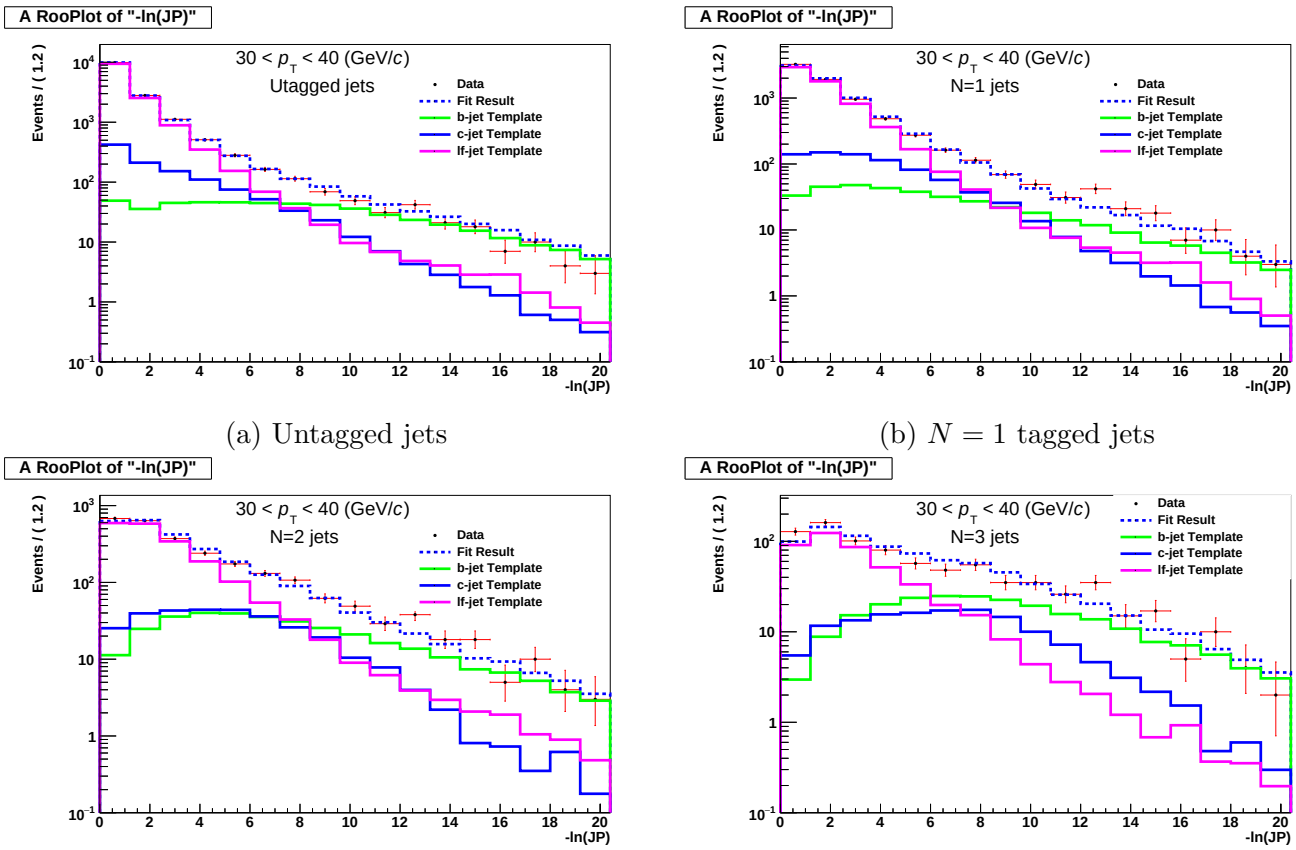

(a) Untagged jets

(b) $N = 1$ tagged jets

(c) $N = 2$ tagged jets

(d) $N = 3$ tagged jets

Fig. 4.37 Template fits of the combined b, c and light-parton jet templates to the JP discriminator distributions from data. (a) For the untagged sample, (b) for the $N = 1$ tagged sample, (c) for the $N = 2$ tagged sample, and (d) for the $N = 3$ tagged sample in pp collisions.

sharply drops. The b-jet purity as a function of p_T is shown Fig. 4.19 (b). When increasing the transverse momentum the purity increases until it starts to slightly decease after $p_T > 30$ GeV/c.

In order to estimate the purity using data-driven methods, same as done for p–Pb (4.5.6) was made by fitting templates reconstructed from MC of the JP distribution for the different jet flavors, and the b-jet purity will be fraction of b-jets obtained from the fits.

The difference in purity between the data-driven method and MC is shown in Fig. 4.40. It is clear on this figure that the MC describe very well the b-jet purity since it gives a very good agreement with the data-driven method.

Fig. 4.41 shows the raw spectrum before and after applying the tagging efficiency and purity on the tagged jet spectra in pp collisions.

4.6.6 Unfolding

The unfolding procedures used in pp collisions are the same as the one used to unfold the b-jets in p–Pb collisions except for the unfolding with fluctuation matrix. The default

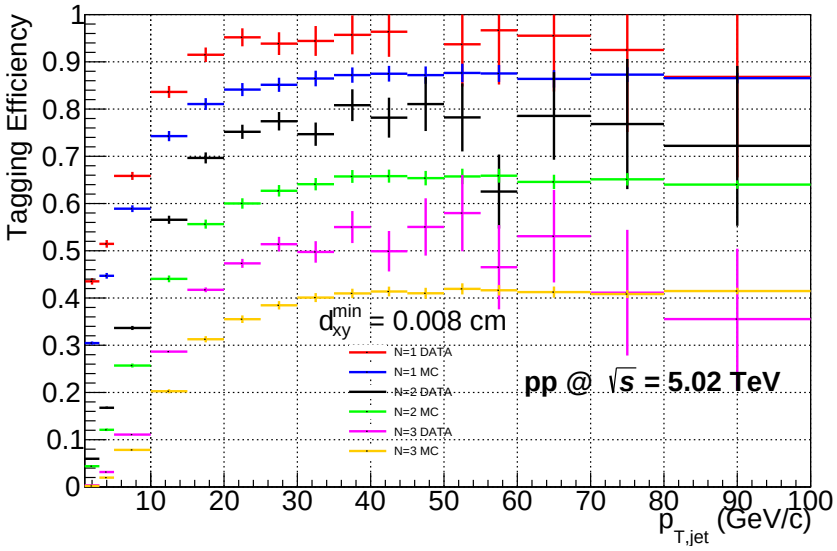

Fig. 4.38 The b-jet tagging efficiency extracted from the data-driven methods compared to the b-jet tagging Efficiency taken directly from MC simulation in pp collisions.

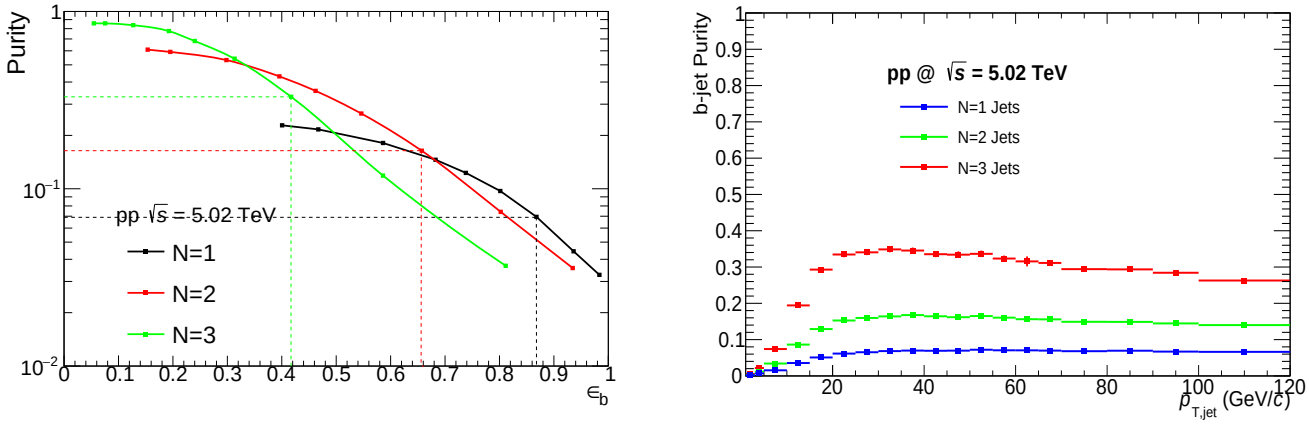

(a) (b)

Fig. 4.39 The b-jet purity versus the tagging efficiency for the different working point in transverse momentum range $30 < p_T < 40$ GeV/c (a) and the b-jet purity as a function of p_T (b) for a medium working point of the Track Counting algorithm at $d_{xy}^{min} = 0.008$ cm in pp collisions.

unfolding algorithm used in pp collisions is the SVD unfolding algorithm (see section 4.5.7.1).

4.6.6.1 Building the response matrix

The response matrix in pp collisions was built in a different way from the p–Pb response matrix. Since the underlying activity in pp collisions in negligible, so the background (δp_T) matrix was not in the unfolding procedure.

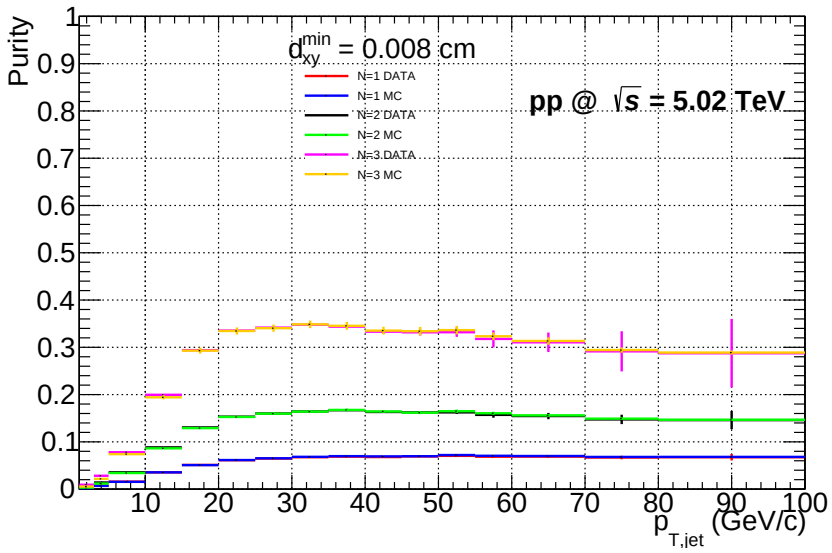

Fig. 4.40 The b-jet purity extracted from the data-driven methods compared to the b-jet purity taken directly from MC simulation in pp collisions.

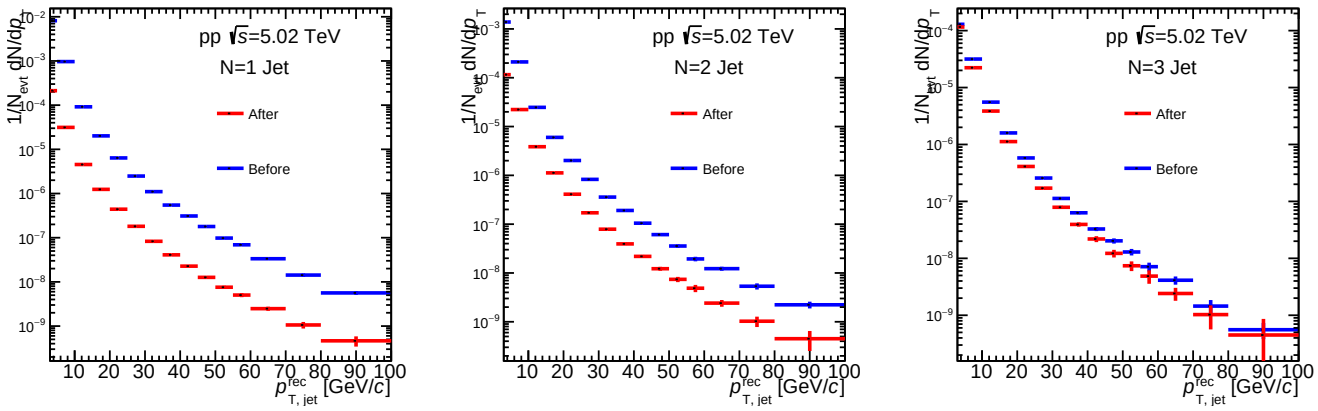

Fig. 4.41 The raw spectrum after and before applying the tagging efficiency and purity correction for $N = 1$ (left), $N = 2$ (middle), and $N = 3$ (right) tagged jets .

The detector response matrix with fine binning is shown in Fig. 4.42 (left) and the rebinned and reweighted version (right), which is the one that will be used in the unfolding.

The response matrix was rebinned through a weighted rebinning procedure as was done in p–Pb collisions in section 4.5.7.2. The binning is as follows:

- Measured range:
  pp: $\{3, 5, 10, 15, 20, 25, 30, 35, 40, 45, 50, 55, 60, 70, 80, 90, 100\}$.
- Unfolded range:
  pp: $\{3, 5, 10, 20, 30, 40, 50, 60, 70, 80, 90, 100, 250\}$.

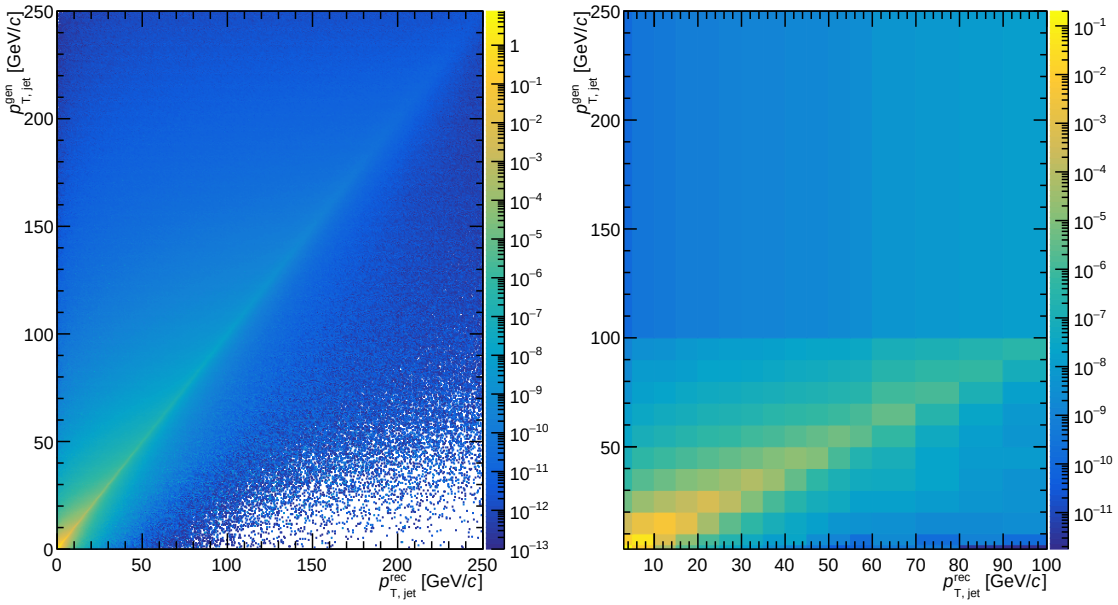

Fig. 4.42 The detector response matrix with fine binning in pp collisions (left) and the rebinned and the reweighted version (right). This response matrix will be used in the unfolding procedure of the pp spectra.

The unfolded spectrum should be corrected for the kinematic efficiency by dividing the unfolded spectrum by this efficiency. The unfolded jet spectrum has also to be corrected for the jet reconstruction efficiency. By dividing the unfolded spectrum over this efficiency, the unfolded jet spectrum will be corrected from the reconstruction efficiency.

The kinematic efficiency for the given response matrix in pp collisions is shown in Fig. 4.43 (left) and also the b-jet reconstruction efficiency is shown in the right panel. As can be seen in the figure, the jet reconstruction efficiency increases from 0.94 at $p_T = 3$ GeV/c to almost 1 for $p_T > 20$ GeV/c.

In this analysis the default prior that was used is the PYTHIA b-jet spectrum. It is not clear what prior to use, so different priors were used for systematic uncertainty (section 5.2.2.3).

4.6.6.2 Regularization parameter analysis

The regularization parameter analysis was done in the same way as was done in p–Pb collisions in section 4.5.7.3.

The best regularization parameter for the SVD unfolding was obtained by looking at the d-vector ($|d_i^k|$) distribution [184].

The d-vector distributions is shown in Fig. 4.44. As can be seen on this figure, non of the regularization parameters is equal to unity, so in this case, we can choose the parameter that is close to unity. So the chosen regularization parameters are: $N = 1$: $k = 7$, $N = 2$: $k = 6$, $N = 3$: $k = 6$.

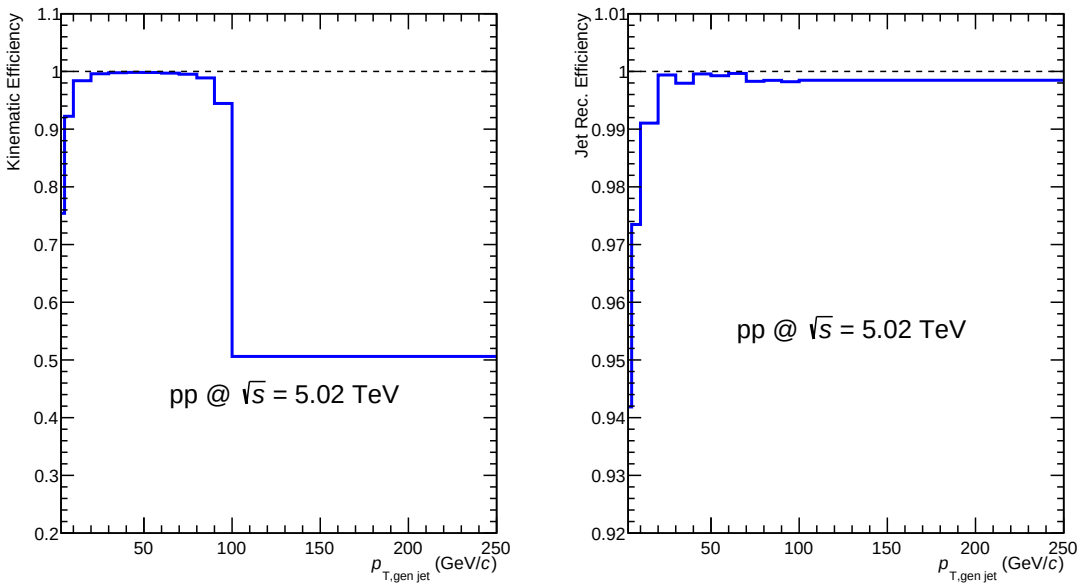

Fig. 4.43 The kinematic efficiency (left) and the b-jet reconstruction efficiency (right) in pp collisions.

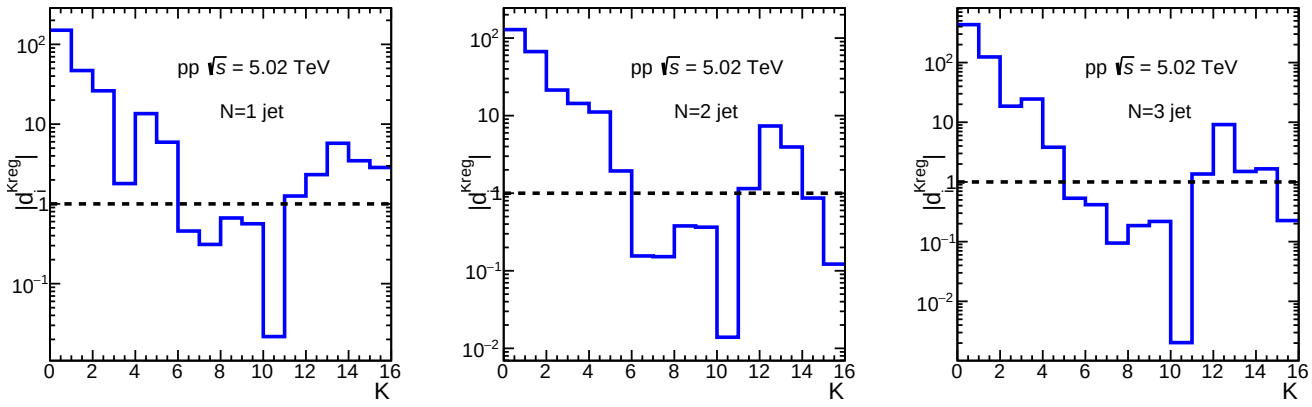

Fig. 4.44 The $|d_i^k|$ (d-vector) distribution for unfolded b-jet spectra in pp collisions.

The ratio of unfolded over truth (closure test) is shown for the different regularization parameters in Fig. 4.45. This figure shows that the very small regularization leads to an incorrect unfolded distribution and the very large regularization parameter make the unfolded spectrum to be over-regularized.

Fig. 4.46 shows a comparison between the measured spectrum (after applying the tagging efficiency and purity) and unfolded spectrum for the different tagged jet spectra in pp collisions.

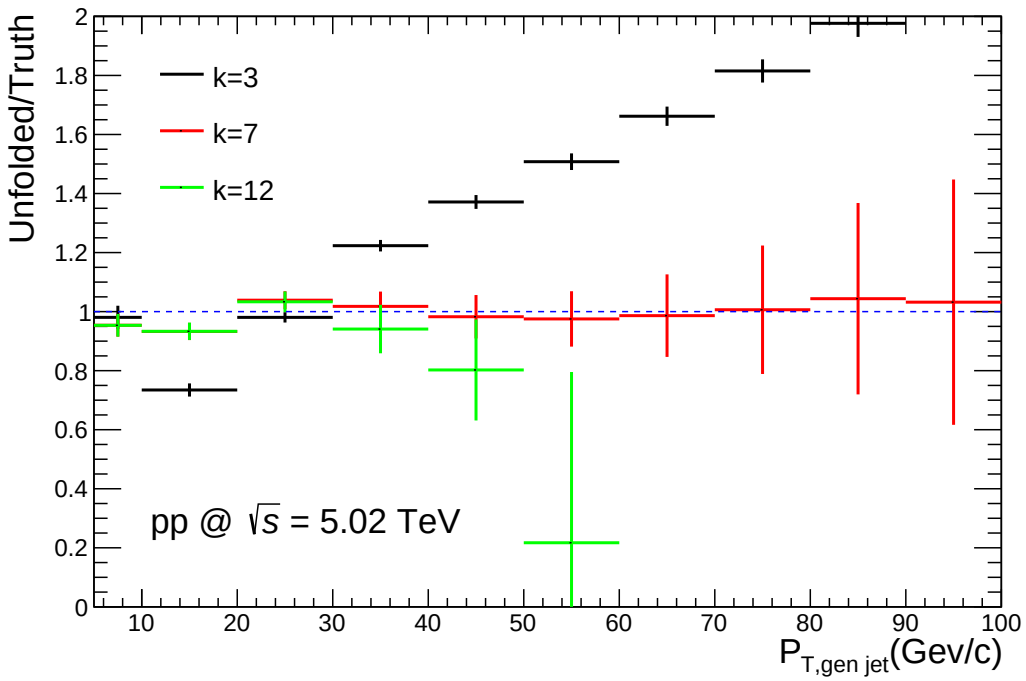

Fig. 4.45 Closure test for the unfolded spectra (ratio unfolded over truth) for the different regularization parameters.

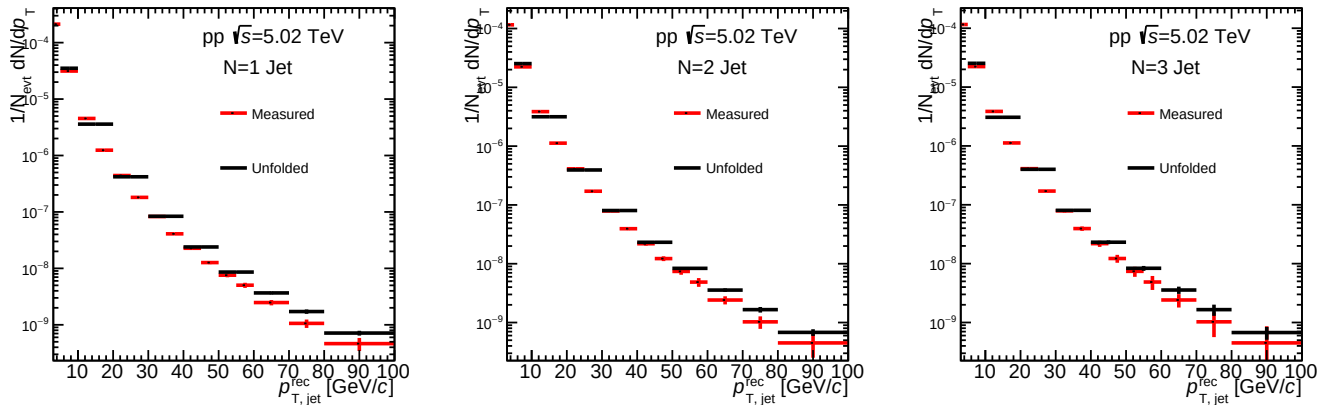

Fig. 4.46 Comparison between the measured spectrum (after applying the tagging efficiency and purity) and unfolded spectrum for $N = 1$ (left), $N = 2$ (middle), and $N = 3$ (right) tagged jets .

4.6.7 Correcting the $N = 1$ jets

In pp collisions, the $N = 1$ tagged was also affected by the same effect as in p–Pb collisions (section 4.5.8) in such a way not all the $N = 1$ jets will be taken into account when performing the data-driven efficiency determination procedure in section 4.5.5 (which uses the jet probability distribution). So in order to remove all the $N = 1$ tagged jets with no

jet probability information, a certain correction factor has to be applied. This correction factor is defined as the fraction of $N = 1$ tagged jets with jet probability information.

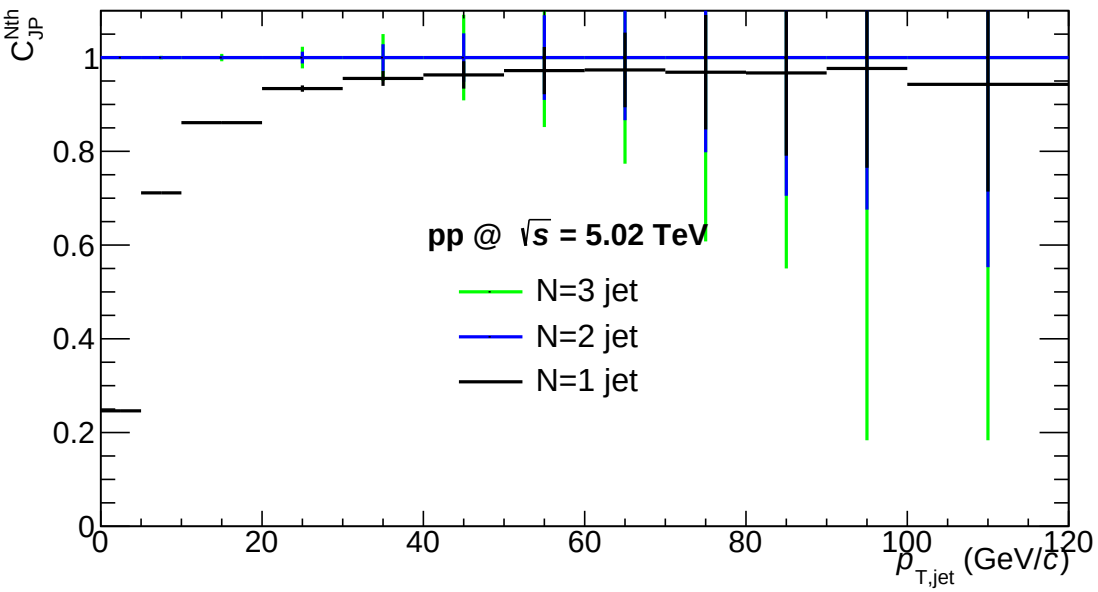

Fig. 4.47 The fraction of $N = 1$ jets with jet probability information in pp collisions.

The fraction of $N = 1$, $N = 2$ and $N = 3$ tagged jets that have a jet probability information is shown in Fig. 4.47. As can be seen in the figure, all the $N = 2$ and $N = 3$ tagged jets have jet probability information (due to the jet probability requirements) which is not the case for the $N = 1$ tagged jets. The fraction of $N = 1$ tagged jets is increasing with p_T until it reaches 98%. The unfolded $N = 1$ jet spectrum has to be multiplied by this correction factor in order to remove all the $N = 1$ tagged jets with no jet probability information.

Fig. 4.46 shows a comparison between the $N = 1$ tagged jets spectra before and after correcting for the jets with jet probability information in pp collisions.

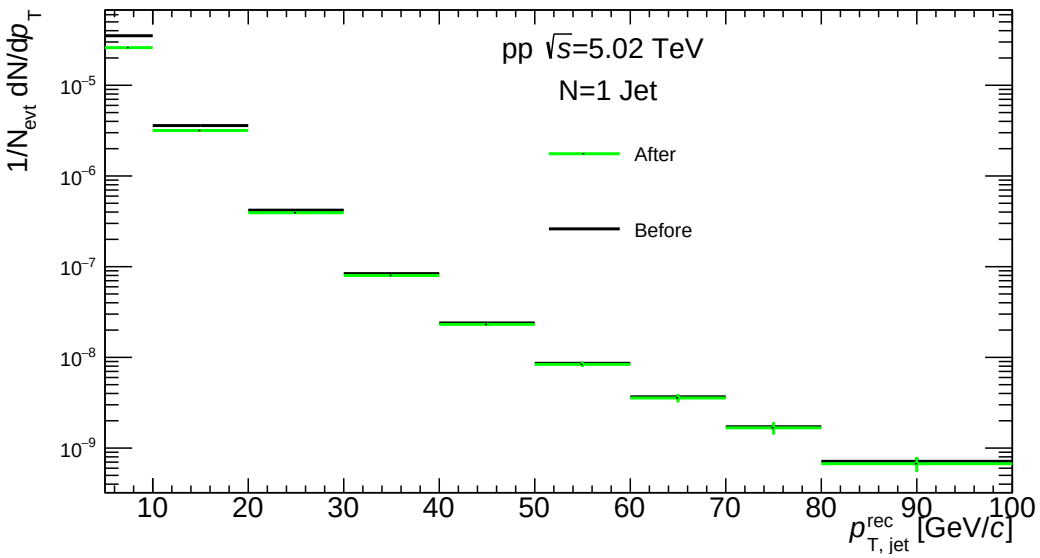

Fig. 4.48 Comparison between the $N = 1$ tagged jets spectra before and after correcting for the jets with jet probability information.

Chapter 5

Systematic and statistical uncertainties

This b-jet analysis implements a complex correction chain (tagging efficiency, purity and also the procedure of unfolding) where each step turns into a systematic uncertainty to be estimated, and due to the many steps it has more uncertainties.

Several sources of systematic uncertainty were studied:

- Uncertainties on the unfolding (section 5.1.2 for p–Pb collisions and section 5.2.2 for pp collisions).
- Uncertainties on the background fluctuation (only for p–Pb collisions in section 5.1.3).
- Tagger working point (section 5.1.4 for p–Pb collisions and section 5.2.3 for pp collisions).
- Tracking efficiency (section 5.1.5 for p–Pb collisions and section 5.2.4 for pp collisions).
- The effect of rejecting the V^0 particles (K_s^0 and Λ) will be discussed in section 5.1.6 for p–Pb collisions only.

In the end, a summary of all the systematic uncertainties will be presented in section 5.1.7 for p–Pb collisions and section 5.2.5 for pp collisions.

For the systematic uncertainties there is no common general procedure for estimating the uncertainty, unlike the statistical. So it is necessary to define an accurate way to compute the uncertainties.

The b-jet measurement depends on several parameters. Some of them are chosen for good reasons like when they define the observable under consideration. Examples include the jet radius and the jet reconstruction algorithm. There are also other parameters which might be considered more arbitrary or at least less justified to be the best and the unique choice like the SVD regularization parameter or the estimation method of background fluctuation. So in order to take into consideration the different parameters, the systematic uncertainties need to be assessed.

Like in most of the particle physics analyses, the following procedure was used to estimate the uncertainties on a bin-by-bin basis:

1. Decide the tunable parameters. Take the jet resolution parameter as an example, this parameter is part of the jet definition so it shouldn't be part of the systematic uncertainty.

2. Choose the parameter that gives the baseline result. This chosen parameter will be the optimal and the least biased parameter.

3. Define an acceptable variations for every tunable parameter. The chosen variation is dependent on the parameter itself. Sometimes for some parameters more than one variation is considered. The chosen parameter can be a number like the SVD regularization parameter, or a method or algorithm like the unfolding algorithm.

4. The physical observable is measured for each variation of the tunable parameter separately.

5. The deviation of these measurements from the measurement of the baseline parameter is taken as the uncertainty $\Delta^{i}_{Sys}(x)$, where i is the varied parameter and x is the bin. If few parameters were used, the maximum deviation from the nominal parameter will be chosen as uncertainty, sometimes an average value is selected depending the parameter. In some cases when there are many parameters to study the RMS of these parameters will be taken as uncertainty.

One of the disadvantages of this procedure is that the systematic uncertainty is largely affected by the statistical fluctuation. So in order to get a better estimate, the uncertainty for some parameters is only allowed to rise with p_T, or if the uncertainty drops for higher p_T bins, the uncertainty value is taken to be the same as the bin before. Or for other parameters, only a single average value is taken as a systematic uncertainty.

The choice of the nominal parameter, the parameter variation range, and the corresponding uncertainty estimate has a small problem - it is not always clear which parameter should be chosen to be the nominal parameter. There is a similar problem also for the variations around the nominal parameter. Even for the uncertainty estimation it is not clear whether to take the maximum deviation from the nominal parameter or take a Gaussian error. In this analysis, the total uncertainty was estimated by propagating all the uncertainties using the Gaussian method and calculated by:

$$\Delta^{tot}_{sys}(x) = \sqrt{\sum_{i} \Delta^{i}_{sys}(x)^2}. \tag{5.1}$$

This equation assumes that the uncertainties are not correlated.

The estimation of the uncertainty on the nuclear modification factor R^{b-jet}_{pPb}, was done by taking the total uncertainty on the b-jet spectra measured in p–Pb , and the pp spectra as uncorrelated uncertainty and propagated except for the tracking efficiency. The tracking efficiency on both systems are correlated since they were taken by the same detector.

For the b-jet fraction, the tracking efficiency and the unfolding uncertainty are treated as correlated and they should be canceled.

5.1 Uncertainties for b-jet production cross section in p–Pb collisions

5.1.1 Statistical uncertainties

After unfolding the b-jet spectra, it was noticed that the SVD unfolding algorithm underestimate the statistical error on the unfolded spectrum. In order to calculate the statistical error, the measured spectrum was smeared (varied) by its statistical errors and then unfolded. Several random numbers in the range of the error bars were generated and filled in histograms, then these histogram were unfolded. The statistical errors are estimated to be the standard deviation of the different varied spectra.

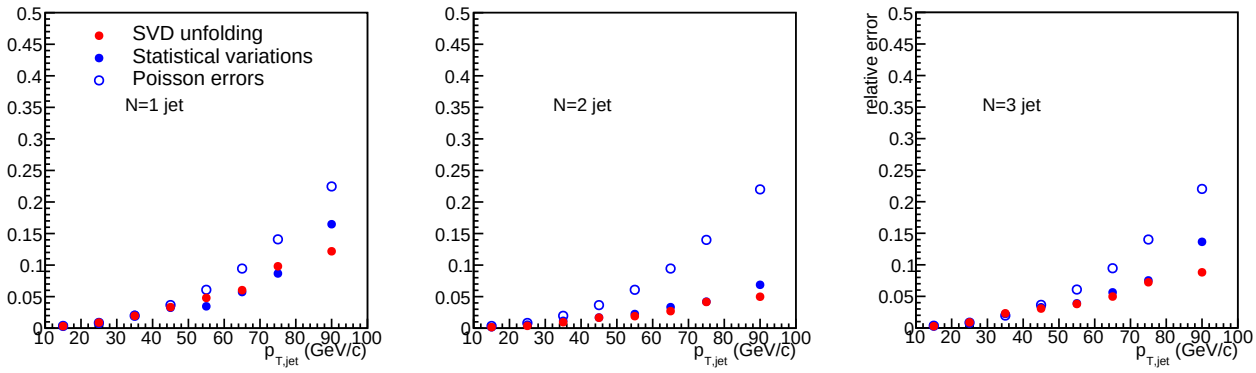

Fig. 5.1 The statistical errors estimated from the different methods: Poissonian errors, SVD errors, and the errors estimated from the statistical variations.

Fig. 5.1 shows the statistical errors estimated from the different methods. As can be seen on the figure, the SVD unfolding method underestimate the statistical errors, and the Poissonian errors overestimate the statistical errors. The statistical variations were taken to be the final statistical errors in this analysis and propagated to the unfolded b-jet spectrum.

5.1.2 Unfolding

For the estimation of the systematic uncertainty of the whole unfolding process, various parameters have been varied.

- The unfolding algorithm.
- The regularization parameter.
- The prior.
- The minimum p_T of the input spectrum.

5.1.2.1 The unfolding algorithm

The nominal unfolding algorithm used in this analysis was the SVD unfolding. The SVD is not the only unfolding algorithm, there is also the χ^2 unfolding and Bayesian unfolding. The systematic uncertainty was estimated by changing the SVD method to the two other methods, and the systematic was estimated from the ratio over the SVD.

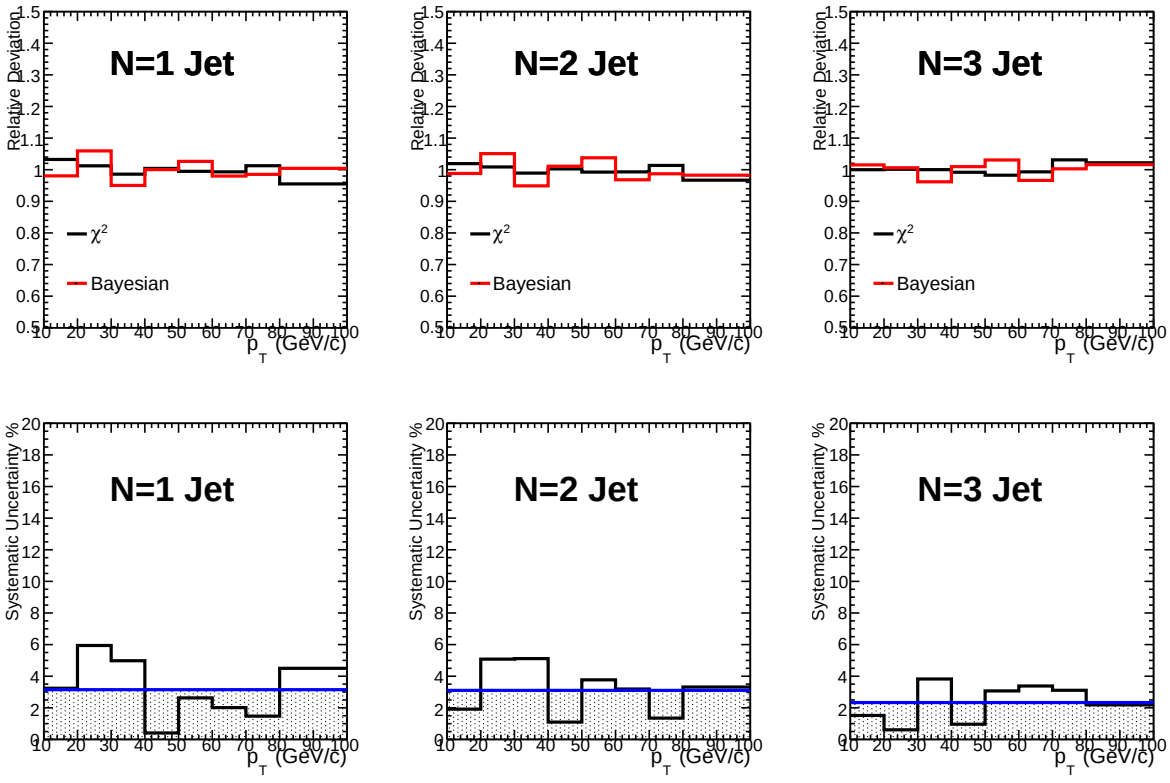

Fig. 5.2 The deviation from nominal of the different unfolding algorithms (upper panel), and systematic uncertainty (maximum deviation) and its average value (lower panel), for the different tagged jets.

Figure 5.2 (upper panel) shows the relative deviation of the χ^2 unfolded spectra and the Bayesian unfolded spectra. The uncertainty values for the different p_T bins is shown in Fig. 5.2 (lower panel), and the black line corresponds to the value that will be considered as a final uncertainty.

The uncertainty value was estimated using the average value of the maximum deviation (the mean value of the all the bins) from the nominal unfolding by the χ^2 unfolded spectra and the Bayesian unfolded spectra as shown in Fig. 5.2. Using the bin-by-bin deviation of the spectra to estimate the uncertainty would overestimate it due to the large statistical fluctuations as shown in Fig. 5.2.

5.1.2.2 Regularization parameter

The change of the regularization parameter in the SVD unfolding process can only be done in integer steps. The nominal parameter was chosen to be $k = 8$ (see section 4.5.7.3), and

the variations were made by changing $k \pm 1$. The relative deviation of the regularization parameter is shown in Fig. 5.3 (upper panel).

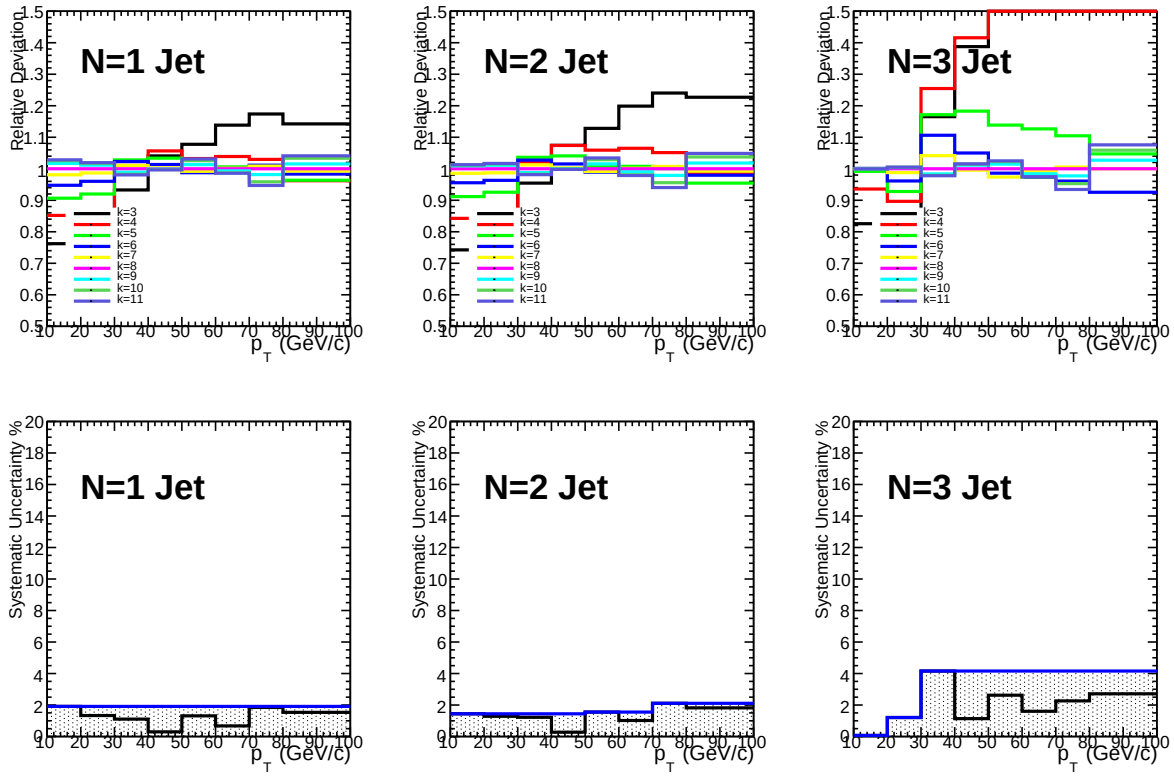

Fig. 5.3 The deviation of the different regularization parameters from the nominal value (upper panel), and the systematic uncertainty estimated from the deviation $k \pm 1$ shown in shaded area (lower panel).

The systematic uncertainty computed from the deviation of the regularization parameter from the nominal value should be increasing with p_T as shown in Fig. 5.3 (lower panel). So if the deviation is decreasing, the uncertainty on this bin will be set at the same value as the bin before. This probably will cause a small overestimation of the systematic uncertainty. The reason behind this condition is that the regularization smooths all the spectrum and specially the high p_T bins which have much lower statistics. This smoothness decreases the statistical fluctuations but also enhances the systematic uncertainties, which is taken into consideration by the regularization parameter.

5.1.2.3 Prior

The prior distribution is required by all the different unfolding algorithms. This prior distribution is expected to be the similar to the true distribution. In this thesis, the default prior distribution used in the analysis is the b-jet spectrum obtained from PYTHIA. The prior distributions used to estimate the uncertainty are the measured spectrum and the χ^2 unfolded spectrum.

Figure 5.4 (upper panel) shows the deviation of the different priors used in this in analysis with a respect to the nominal one. The lower panel of Fig. 5.4 shows the systematic

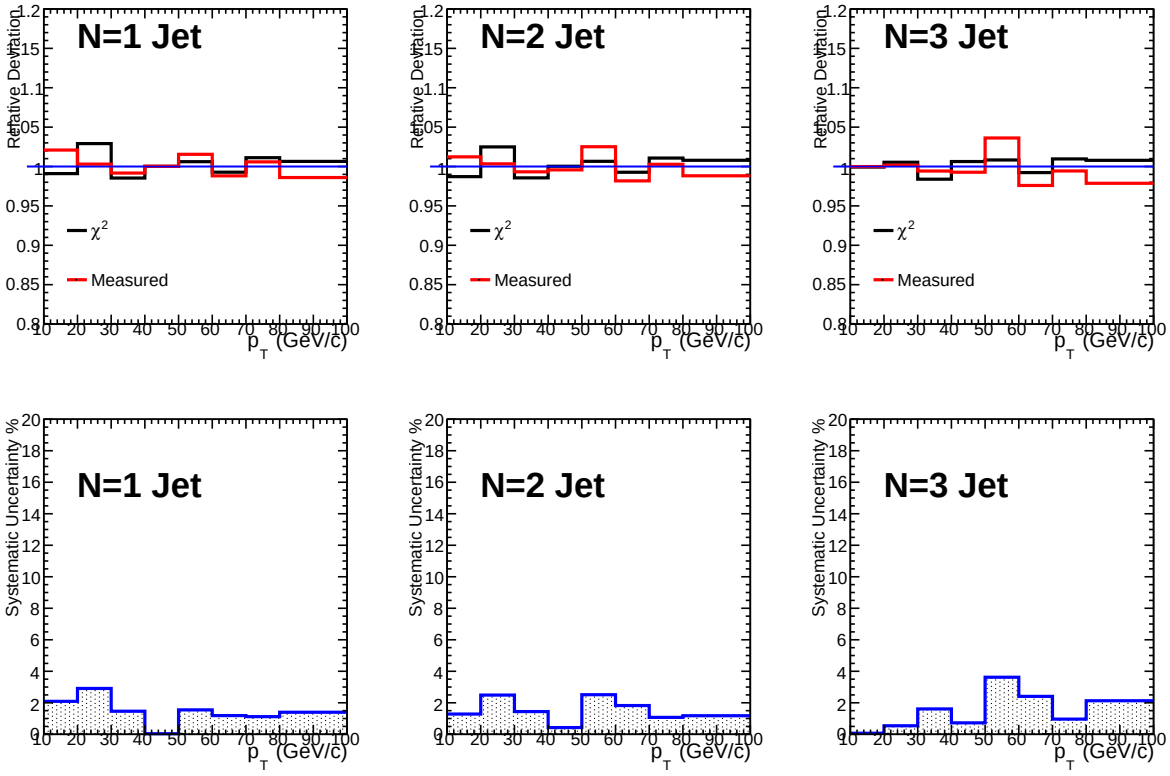

Fig. 5.4 The deviation of the different prior distributions from the nominal value (upper panel), and the systematic uncertainty estimated from the maximum deviation shown in shaded area (lower panel).

uncertainty estimated from the RMS (Root Mean Square) of the deviation shown in the shaded area.

5.1.2.4 The p_T range

The procedures for the unfolding require a certain binning. The uncertainty from the different unfolding ranges and binning is estimated by changing the default binning. The minimum and maximum p_T for the measured and unfolded jet spectra were varied as follows:

- Range 1: $1 < p_T^{unfolded} < 250$ (GeV/c) and $1 < p_T^{measured} < 100$ (GeV/c).
- Range 2: $3 < p_T^{unfolded} < 250$ (GeV/c) and $1 < p_T^{measured} < 100$ (GeV/c).
- Range 3: $1 < p_T^{unfolded} < 250$ (GeV/c) and $3 < p_T^{measured} < 100$ (GeV/c).
- Range 4: $3 < p_T^{unfolded} < 120$ (GeV/c) and $2 < p_T^{measured} < 100$ (GeV/c).

Figure 5.5 (upper panel) shows the relative deviation of the different unfolded spectra with different unfolding ranges, and panel (lower panel) shows the estimated systematic uncertainty from the RMS. As can be seen from the figure, only the very low and the very high p_T bins are largely affected by changing the unfolding range.

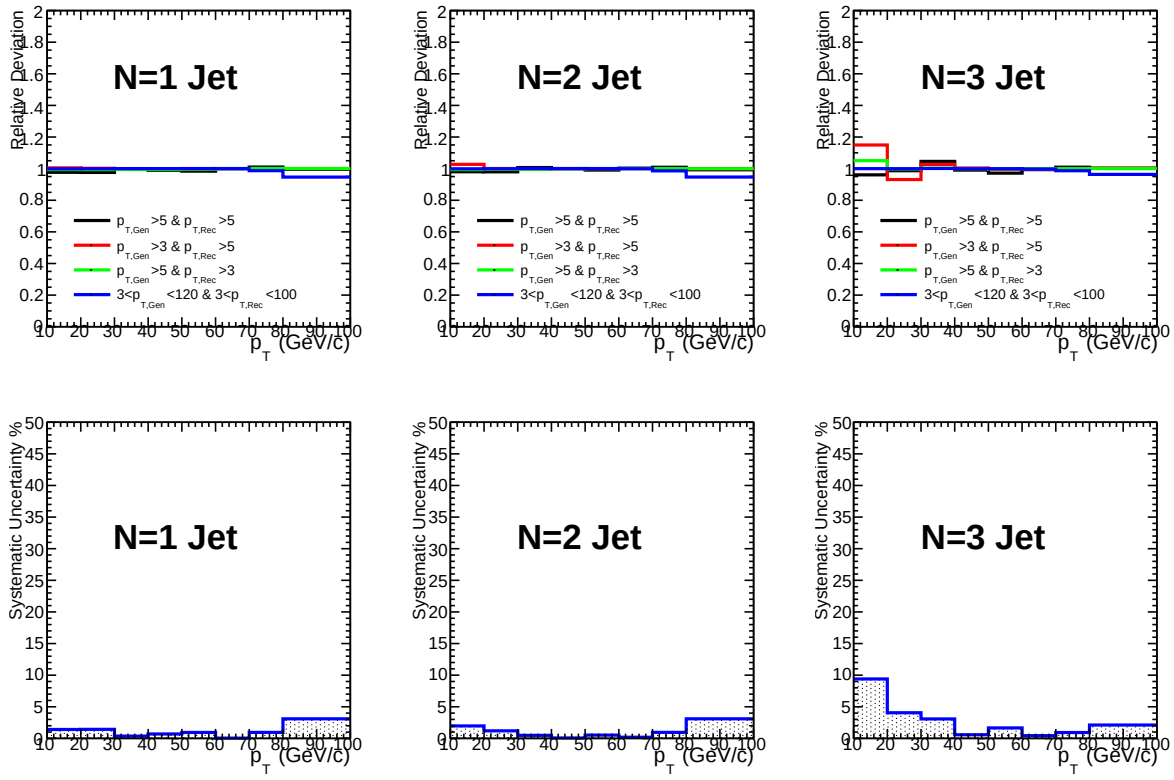

Fig. 5.5 The deviation of the different unfolded spectra with different ranges from the nominal value (upper panel), and the systematic uncertainty estimated from the deviation (RMS) shown in shaded area (lower panel).

5.1.3 δp_T response

The random cone method was used for the extraction of the δp_T as discussed in section 4.5.1.1. The random cone has a probability to overlap with a signal jet produced from the hard scattering. So the leading jet and the sub-leading jets were excluded from the random cone reconstruction. By default for each tagger (N^{th} tagger), a specific δp_T was built for the events that contains only a tagged b-jet by the N^{th} tagger. So for the systematic uncertainty estimation the default δp_T was changed to be the inclusive jet δp_T.

Fig. 5.6 shows the systematic uncertainty estimated from unfolding with δp_T matrix.

5.1.4 Tagger working point

The default working used in the analysis is $d_{xy}^{min} = 0.008$ cm. The uncertainty on the tagger working point (tagging efficiency and purity) was estimated by varying the working point by these parameters $\{0., 0.004, 0.008, 0.012, 0.016\}$ cm. The data driven procedures discussed in section 4.5.5 was repeated for the all the different working points.

Fig. 5.7 (upper panel) shows the deviation of the different b-jets with different working points from the nominal b-jet. The lower panel shows the systematic uncertainty estimated from the RMS of the different variations.

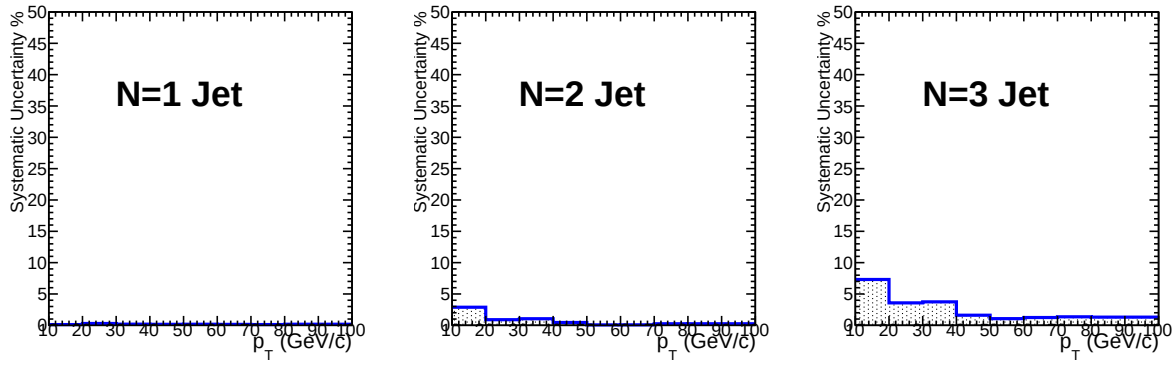

Fig. 5.6 The Systematic uncertainty estimated from unfolding with different δp_T matrix.

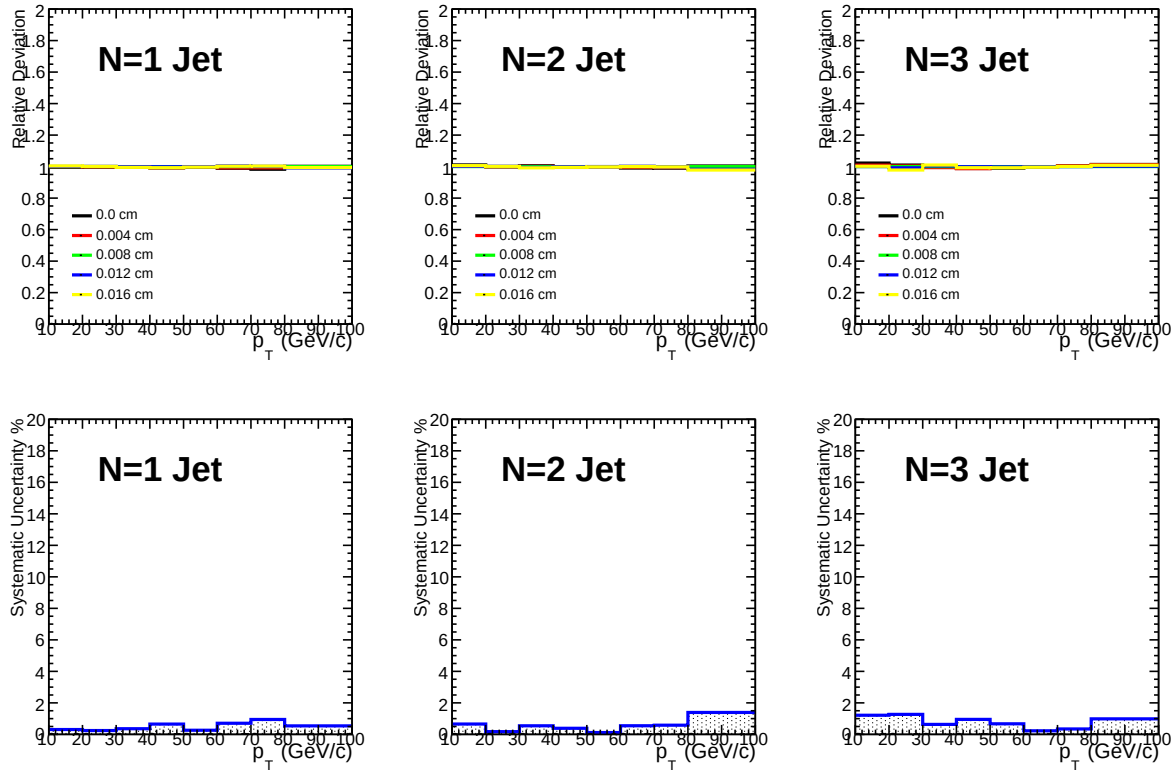

Fig. 5.7 The deviation of the different b-jets from different working points (upper panel), and the systematic uncertainty estimated from the deviation (RMS) shown in shaded area (lower panel).

5.1.5 Tracking efficiency

The effect of the tracking efficiency uncertainty on the b-jet spectra can be estimated by introducing a different tracking efficiency in the detector response. The tracks were randomly discarded with a given probability before building the detector response. This probability is estimated by a random number, if this random number is less than the percentage of the reduced tracking efficiency then this track will be discarded. This method

will also cause some loss of statistics but this process is done on the MC level where there are no problems with the statistics at high p_T.

The detector response matrices that have been created with reduced tracking efficiency, which represent the detector with the reduced tracking efficiency. The tracking efficiency was reduced by (4%, 5%, and 10%). So that means 4%, 5%, and 10% of the tracks will be randomly discarded. These parameters were taken from another jet analyses in ALICE, in pp collisions it was taken from [188, 189], and in p–Pb collisions it was taken from [190]. So the jet spectra unfolded with 90% tracking inefficiency response will be enhanced in comparison with the 5% and 4% inefficiency.

The systematic uncertainty on the unfolded jet spectra are estimated from the deviation of the 4% reduced tracking efficiency detector response matrix from the nominal tracking efficiency as shown in Fig. 5.8 (lower panel). The 5% and the 10% inefficiencies (Fig. 5.8 upper panel) were used to show the effect of the reduced tracking efficiency on the unfolded jet spectra.

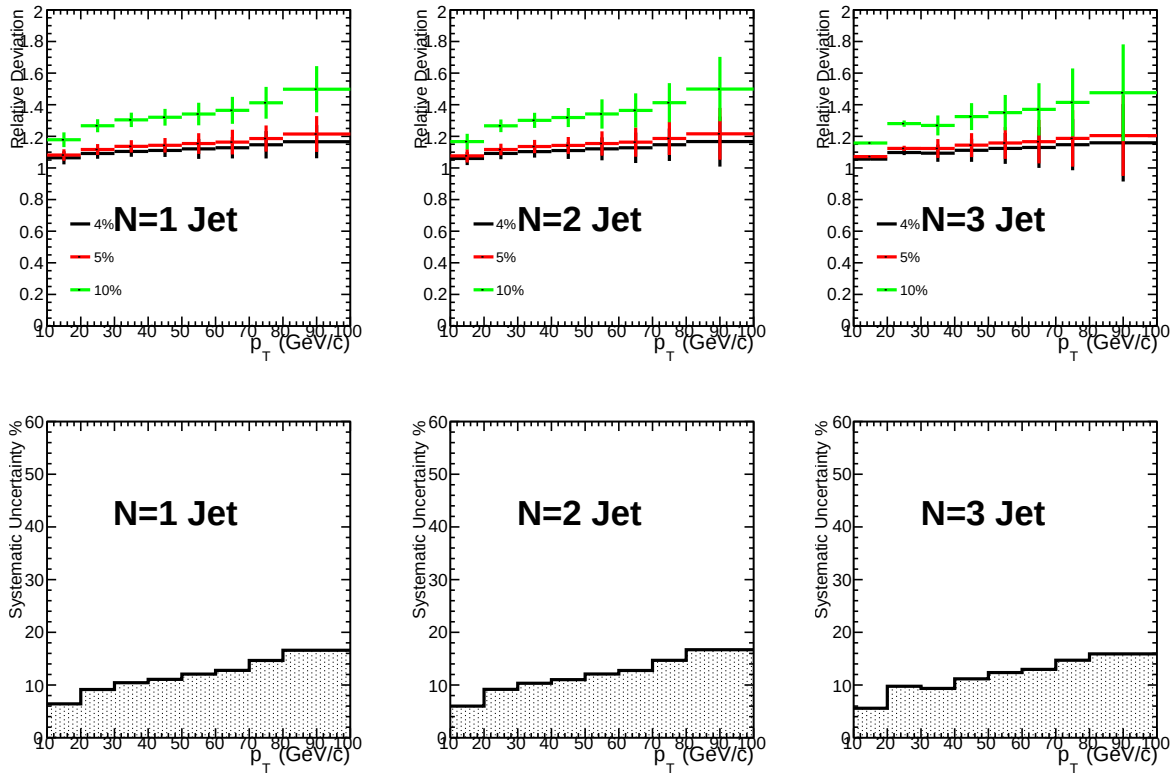

Fig. 5.8 The deviation of the different unfolded spectra with DRM with different tracking inefficiencies (upper panel), and the systematic uncertainty estimated from the deviation of the 4% reduced tracking efficiency shown in shaded area (lower panel).

It should be noted that, the systematic uncertainty yield was estimated by reducing the tracking efficiency by 4%. This uncertainty was evaluated under the assumption that it will be the same if the tracking efficiency was artificially enlarged by the same percent.

The tracking efficiency uncertainty is correlated in pp and p-Pb collisions since these data were collected by the same detector. So systematic uncertainty cancellation should

be done here. According to [191] the uncorrelated uncertainty from tracking efficiency on the R_{pPb} is estimated from reducing the tracking efficiency by 2% on both pp and p-Pb unfolded spectra.

5.1.6 V0 Rejection

The lifetime tagging algorithms (like TC, SV, JP, ...) by definition assume all the measurable lifetime objects (the N^{th} track, the secondary vertex, ...) are indicative of the heavy-flavor jets. But light strange hadrons also have a long lifetime and they also decay in a similar way to the heavy-flavor-hadrons (HF-hadrons). So a small background can arise from the strange hadrons especially K_s^0 and Λ since their lifetime don't largely differ from those of the HF-hadrons. Also $\gamma \to e^+e^-$ conversion in the detector materials may occur at large distance from the beam pipe. These electrons from photon conversion can also contribute to the mistaging rate.

The V^0 particles in jets, mainly K_s^0 and Λ, are reconstructed using their decay most frequent channel: $K_s^0 \to \pi^+\pi^-$, $\Lambda \to p\pi^-$, $\bar{\Lambda} \to \bar{p}\pi+$ using the invariant mass of the decay daughters. The V^0 candidates (and the V^0 daughters) were selected using some topological cuts plus a combination of the different detectors' PID information as follows [192, 193] :

- The pseudo rapidity of the daughters should be $|\eta_{Daughters}| < 0.9$ and that for the V^0 $|\eta_{V0}| < 0.8$.
- $DCA_{Daughters}$ to primary vertex ≥ 0.1 cm.
- DCA between V^0 daughters $\leqslant 1\sigma_{TPC}$.
- $|\Delta\frac{dE}{dx}| < 3\sigma^{TPC}_{\frac{dE}{dx}}$ for protons with $p_T < 1$ GeV.
- Reject Kink daughters.
- The Offline V^0 reconstruction was selected.
- Radius of the decay vertex $5 < R_{decay} < 100$ cm.
- Cosine of pointing angle (CPA) $\leqslant 0.998$.
- Transverse proper lifetime $\leqslant 5\tau$.
- Armenteros Podolanski cut [194] (only for K_s^0) $q^T_{Arm.} \geq 0.2|\alpha|$.

The V^0 reconstruction efficiency is dependent on the transverse momentum of the decay daughters of the V^0 particles. Figure 5.9 shows the K_s^0, Λ and $\bar{\Lambda}$ reconstruction versus p_T. This efficiency was extracted from MC simulation.

Electrons from photon conversion can be recognized by their opening angle (which is very small). These electrons also have similar properties as the electrons from HF decays and they can be mistagged. The photon candidates were selected using some topological cuts [195]:

- The offline V^0 reconstruction was selected.

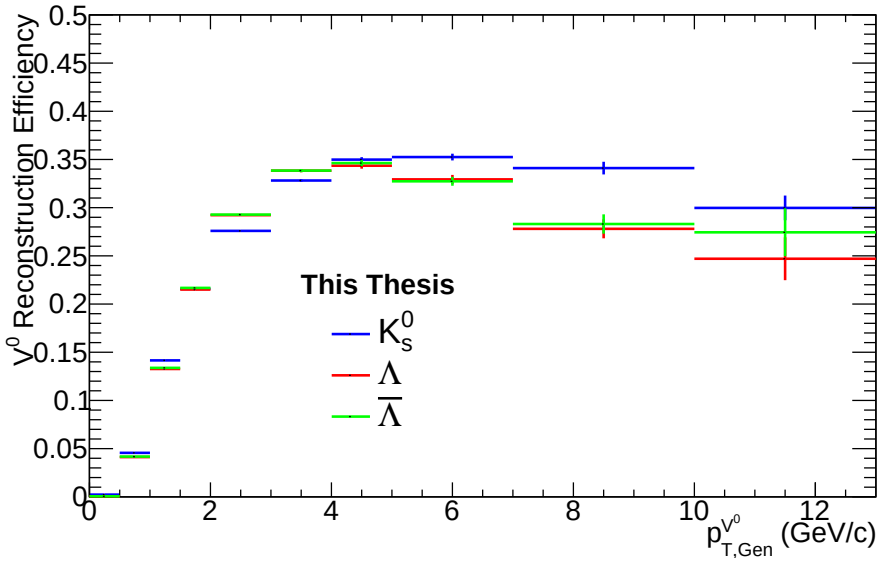

Fig. 5.9 The V^0 reconstruction efficiency for the K^0_s, Λ and $\bar{\Lambda}$ as a function of transverse momentum of the V^0 particle.

- the pseudorapidity of the electrons should be $|\eta_e| < 0.9$.
- Radius of the decay vertex $0 < R_{decay} < 180$ cm.
- TPC cross rows over findable cluster > 0.6.
- $-3 < |\Delta \frac{dE_e}{dx}| < 5\sigma^{TPC}_{\frac{dE}{dx}}$.
- Armenteros Podolanski cut $q^T_{Arm.,max} \leq 0.05$.
- The tracks should have $\chi^2/NDF < 30$.
- Cosine of pointing angle (CPA) $\leqslant 0.85$.
- The opening angle of the e^+ e^- pair should be $\psi_{pair,max} < 0.05$.

Since the V^0 particles have similar properties as the b-hadrons decays, rejecting these particles will improve the b-jet purity. As shown in Fig. 5.10, the b-jet purity increases if rejecting the reconstructed V^0, and it also increases even larger if we make a rejection for all the V^0s by checking their generated MC particle.

In order to estimate the uncertainty from the V^0 rejection, this analysis was repeated with turning on the reconstruction and the rejection of the V^0 and the electrons from photon conversion.

Figure 5.11 shows the systematic uncertainty estimated from rejecting the V^0s and electrons from photon conversion shown in the shaded area.

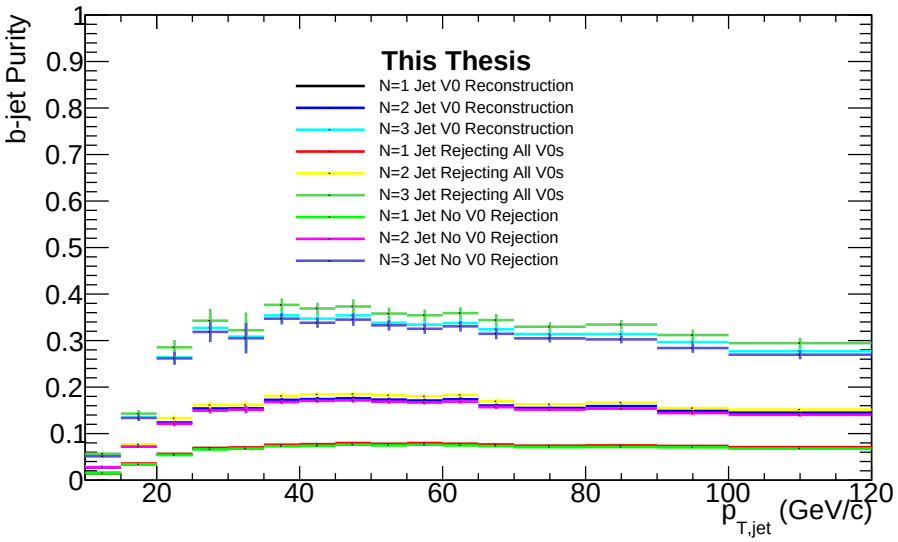

Fig. 5.10 Comparing the b-jet purity with rejecting the reconstructed V^0s, rejecting all the V^0s from MC and without any V^0 rejection.

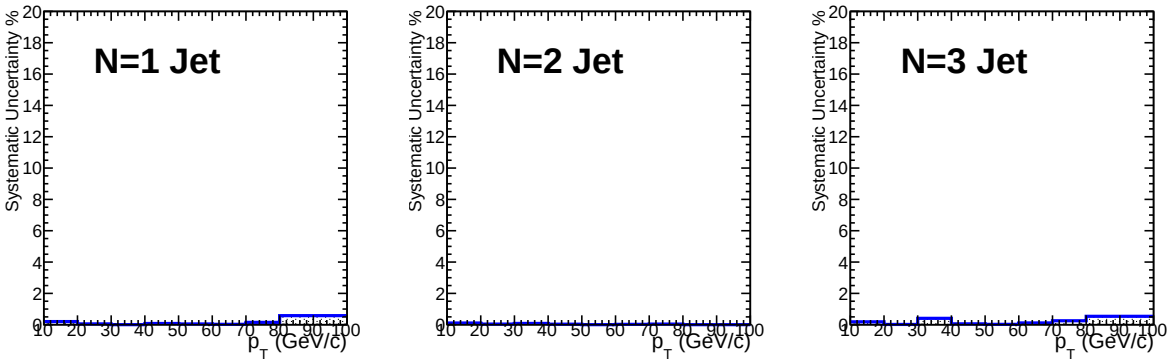

Fig. 5.11 The systematic uncertainty estimated from rejecting the V^0s and electrons from photon conversion (shaded area).

5.1.7 Summary of systematic uncertainties

The dominant uncertainty sources have been identified to be originating from the tracking efficiency and from the unfolding procedure. In Tabs. 5.1 5.2 5.3, the uncertainties are summarized for the different tagged b-jet spectra.

Table 5.1 Summary for all the systematic uncertainty for the N=1 tagged jets in p–Pb collisions.

Uncertainty source	p_T bins							
	10-20	**20-30**	**30-40**	**40-50**	**50-60**	**60-70**	**70-80**	**80-100**
Unfolding algorithm	3.14							
Regularization parameter	2.03							
Prior	2.09	2.91	1.46	0.04	1.55	1.19	1.12	1.40
Unfolding range	1.40	1.43	0.36	0.69	0.94	0.04	0.94	3.09
δp_T	0.12	0.29	0.18	0.16	0.17	0.15	0.12	0.17
Tracking Efficiency	7.67	10.60	11.62	12.11	12.86	13.27	15.18	17.73
Tagger working point	0.31	0.24	0.36	0.65	0.26	0.71	0.95	0.54
V^0 rejection	0.20	0.05	0.00	0.08	0.05	0.03	0.15	0.58
Normalization uncertainty	3.24							

Table 5.2 Summary for all the systematic uncertainty for the N=2 tagged jets in p–Pb collisions.

Uncertainty source	p_T bins							
	10-20	**20-30**	**30-40**	**40-50**	**50-60**	**60-70**	**70-80**	**80-100**
Unfolding algorithm	3.1							
Regularization parameter	1.81						2.24	
Prior	1.28	2.49	1.44	0.43	2.51	1.82	1.07	1.18
Unfolding range	1.97	1.19	0.48	0.06	0.52	0.18	0.95	3.09
δp_T	2.88	0.90	1.05	0.45	0.07	0.07	0.25	0.25
Tracking Efficiency	7.26	10.55	11.53	12.04	12.88	13.27	15.21	17.74
Tagger working point	0.66	0.17	0.54	0.39	0.12	0.55	0.58	1.39
V^0 rejection	0.11	0.04	0.08	0.03	0.00	0.02	0.04	0.00
Normalization uncertainty	3.24							

Table 5.3 Summary for all the systematic uncertainty for the N=3 tagged jets in p–Pb collisions.

Uncertainty source	p_T bins							
	10-20	**20-30**	**30-40**	**40-50**	**50-60**	**60-70**	**70-80**	**80-100**
Unfolding algorithm	2.33							
Regularization parameter	0.05	1.25	4.57					
Prior	0.07	0.54	1.61	0.73	3.62	2.41	0.96	2.13
Unfolding range	9.39	4.05	3.07	0.57	1.65	0.43	0.92	2.11
δp_T	7.31	3.58	3.74	1.61	1.06	1.24	1.36	1.30
Tracking Efficiency	6.80	11.31	10.35	12.15	13.16	13.54	15.28	16.81
Tagger working point	1.21	1.27	0.63	0.95	0.67	0.23	0.34	0.99
V^0 rejection	0.18	0.02	0.41	0.06	0.02	0.11	0.25	0.54
Normalization uncertainty	3.24							

Figs. 5.12 show the total uncertainty after propagating all the different uncertainty sources using Eq. (5.1). In this figure it is shown for all the different tagged jet spectra ($N = 1$, $N = 2$ and $N = 3$).

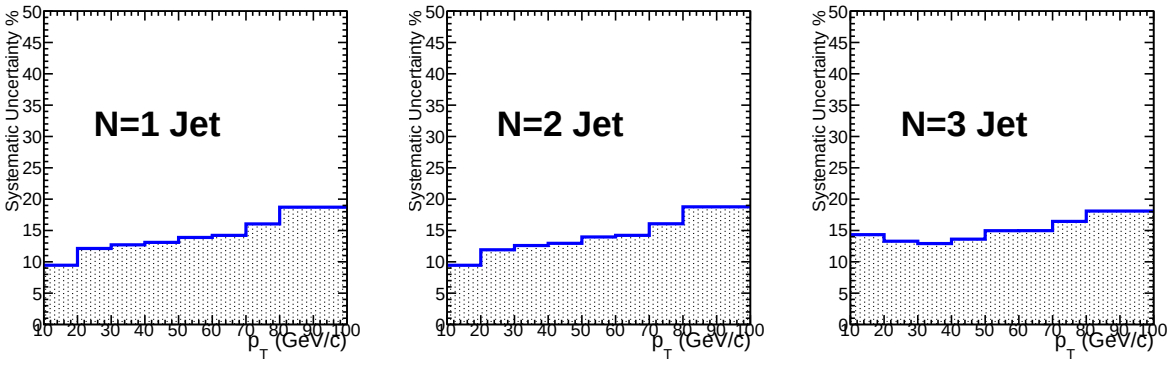

Fig. 5.12 The total system uncertainty after propagating all the uncertainties from the different sources.

5.2 Uncertainties for b-jet production cross section in pp collisions

5.2.1 Statistical uncertainties

The statistical errors in pp collisions are estimated the same way as in p–Pb collisions.

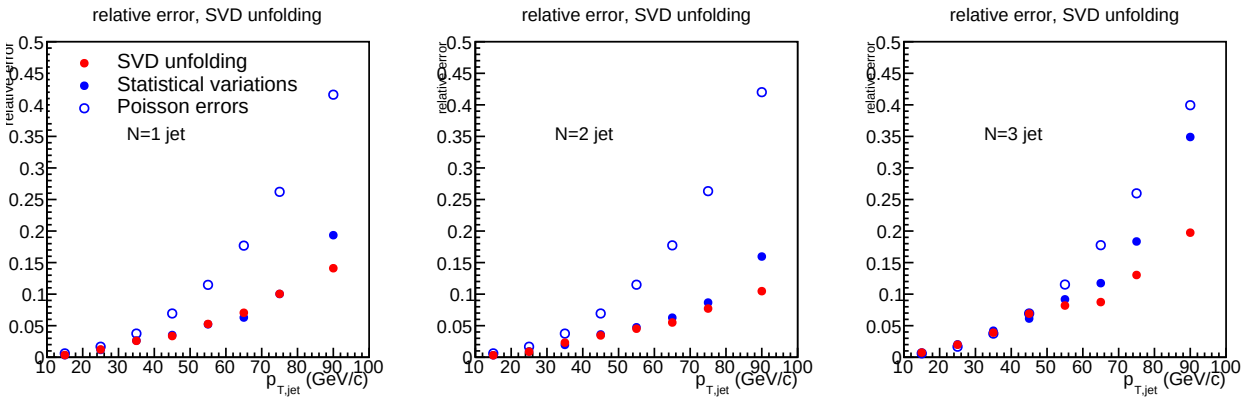

Fig. 5.13 The statistical errors estimated from the different methods: Poissonian errors, SVD errors, and the errors estimated from the statistical variations.

Fig. 5.13 shows the statisitcal errors estimated from the methods. As can be seen on the figure, the SVD unfolding method underestimate the statistical errors, and the poissonian errors overestimate the statistical errors.

5.2.2 Unfolding

5.2.2.1 The unfolding algorithm

The nominal unfolding algorithm used in this analysis was the SVD unfolding. The systematic uncertainty was estimated by changing the SVD method to the the χ^2 unfolding and Bayesian unfolding, and the systematic was estimated from the ratio over the SVD.

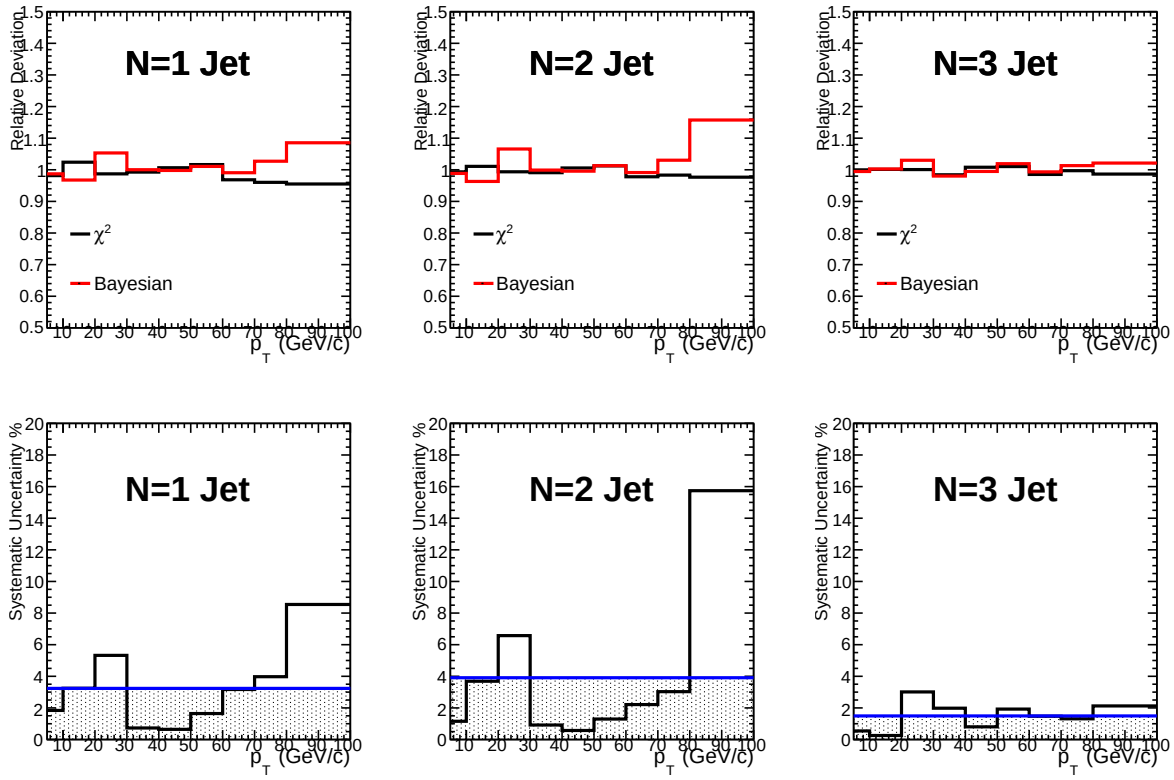

Fig. 5.14 The deviation from nominal of the different unfolding algorithms (upper panel), and systematic uncertainty and its average value (lower panel), for the different tagged jets.

Figure 5.14 (upper panel) shows the relative deviation of the χ^2 unfolded spectra and the Bayesian unfolded spectra. The uncertainty values for the different p_T bins is shown in Fig. 5.14 (lower panel), and the black line corresponds to the value will be considered as a final uncertainty.

The uncertainty value was estimated using the average value of the maximum deviation (the mean value of the all the bins) from the nominal unfolding by the χ^2 unfolded spectra and the Bayesian unfolded spectra as shown in Fig. 5.14. Using the bin-by-bin deviation of the spectra to estimate the uncertainty would overestimate it due to the large statistical fluctuations as shown in Fig. 5.14.

5.2.2.2 Regularization parameter

The nominal parameter was chosen to be $N = 1$: $k = 7$, $N = 2$: $k = 6$, and $N = 3$: $k = 6$ (see section 4.5.7.3), and the variations were made by changing $k \pm 1$ for the $N = 1$ and

only $k+1$ for the $N=2$ and $N=3$ since $k=5$ is not regularized correctly. The relative deviation of the regularization parameter is shown in Fig. 5.15 (upper panel).

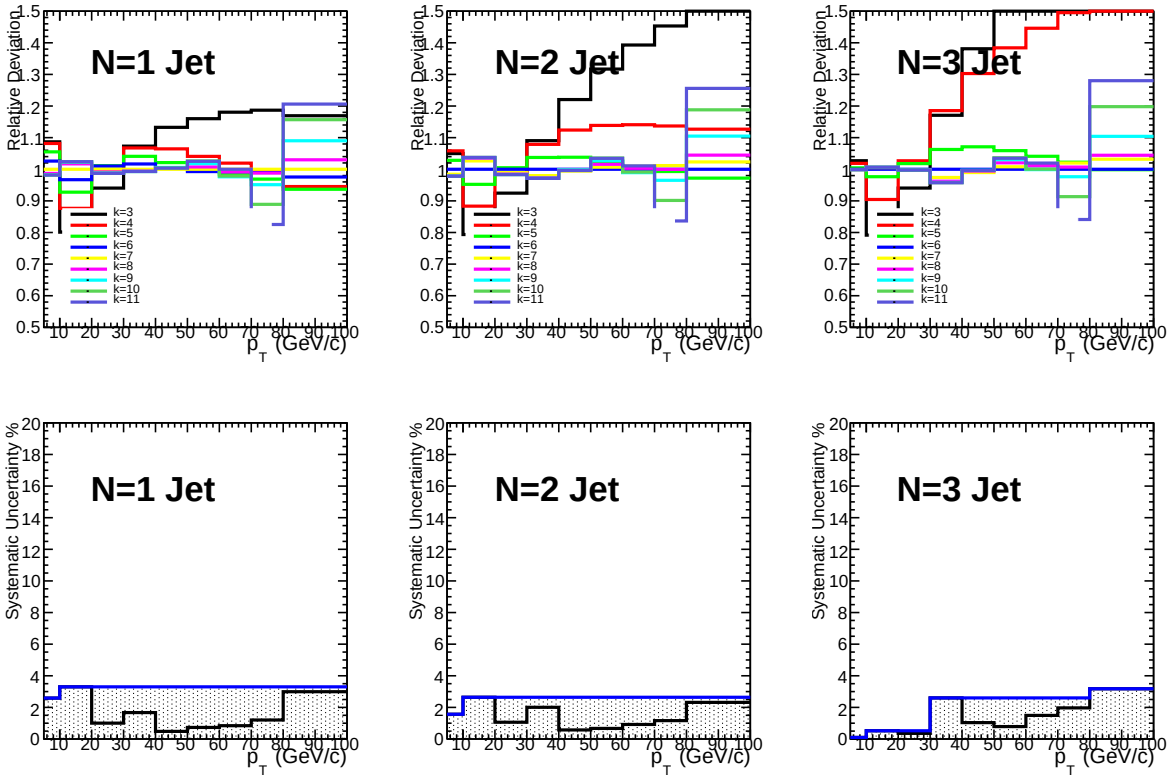

Fig. 5.15 The deviation of the different regularization parameters from the nominal value (upper panel), and the systematic uncertainty estimated from the deviation $k \pm 1$ shown in shaded area (lower panel).

The systematic uncertainty computed from the deviation of the regularization parameter from the nominal value should be increasing with p_T as shown in Fig. 5.15 (lower panel) the shaded area. So if the deviation is decreasing the uncertainty is on this bin will the same as the bin before.

5.2.2.3 Prior

In this thesis, the default prior distribution used in the analysis is the b-jet spectrum obtained from PYTHIA. The prior distributions used to estimate the uncertainty are the measured spectrum and the χ^2 unfolded spectrum.

Figure 5.16 (lower panel) shows the deviation of the different priors used in this in analysis with a respect to the nominal one. Panel (b) of Fig. 5.16 shows the systematic uncertainty estimated from the RMS (Root Mean Square) of the deviation shown in the shaded area.

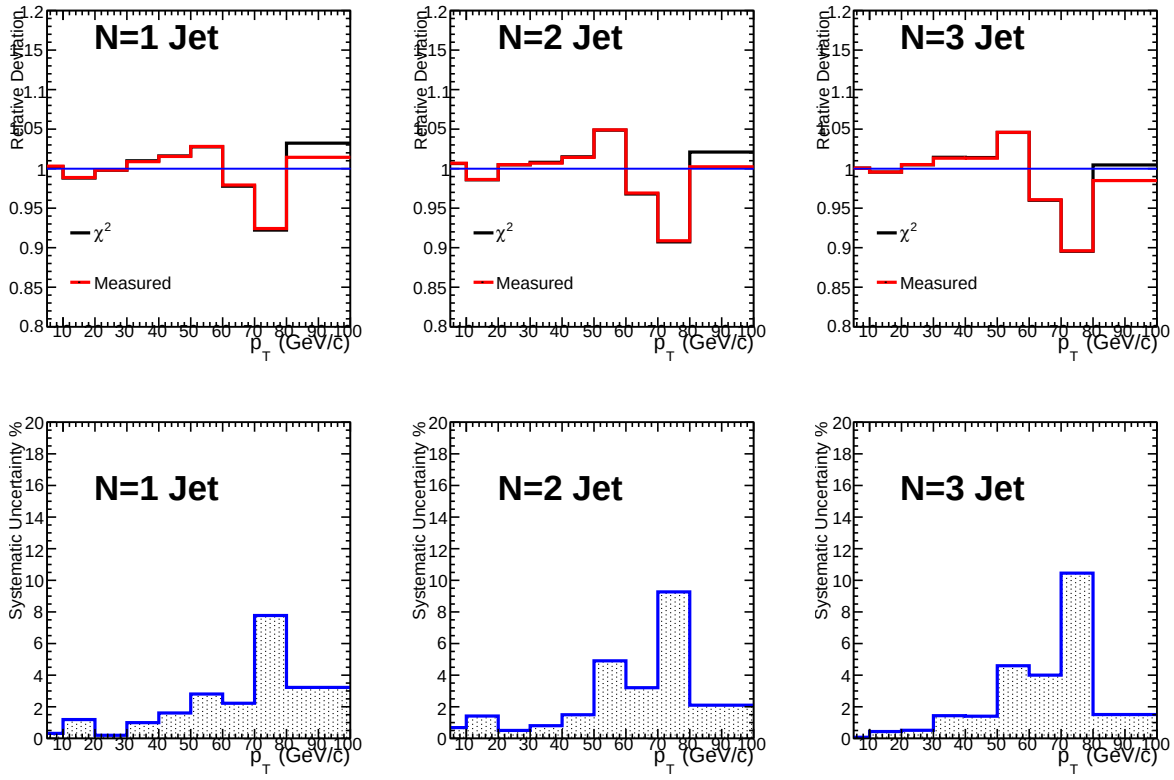

Fig. 5.16 The deviation of the different prior distributions from the nominal value (upper panel), and the systematic uncertainty estimated from the maximum deviation shown in shaded area (lower panel).

5.2.2.4 The p_T range

The uncertainty from the different unfolding ranges and binning is estimated by changing the default binning. The minimum and maximum p_T for the measured and unfolded jet spectra were varied as follows:

- Range 1: $1 < p_T^{unfolded} < 250$ (GeV/c) and $1 < p_T^{measured} < 100$ (GeV/c).
- Range 2: $3 < p_T^{unfolded} < 250$ (GeV/c) and $1 < p_T^{measured} < 100$ (GeV/c).
- Range 3: $1 < p_T^{unfolded} < 250$ (GeV/c) and $3 < p_T^{measured} < 100$ (GeV/c).
- Range 4: $3 < p_T^{unfolded} < 120$ (GeV/c) and $2 < p_T^{measured} < 100$ (GeV/c).

Figure 5.17 (upper panel) shows the relative deviation of the different unfolded spectra with different unfolding ranges, and Fig. 5.17 (lower panel) shows the estimated systematic uncertainty from the RMS. As can be seen from the figure, only the very low and the very high p_T bins are largely affected by changing the unfolding range.

5.2.3 Tagger working point

The default working used in the analysis is $d_{xy}^{min} = 0.008$ cm. The uncertainty on the tagger working point (tagging efficiency and purity) was estimated by varying the working point

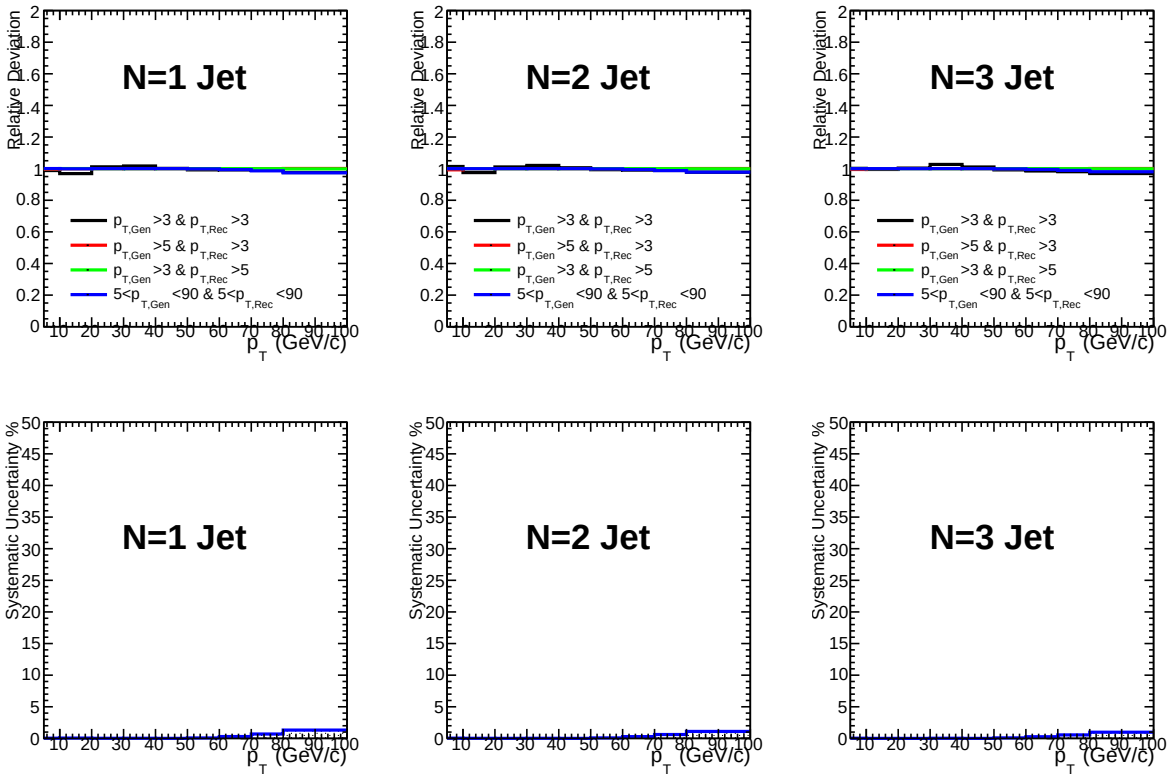

Fig. 5.17 The deviation of the different unfolded spectra with different ranges from the nominal value (upper panel), and the systematic uncertainty estimated from the deviation (RMS) shown in shaded area (lower panel).

by these parameters $\{0., 0.004, 0.008, 0.012\}$ cm. The data driven procedures discussed in section 4.5.5 was repeated for the all the different working points.

Fig. 5.18 (upper panel) shows the deviation of the different b-jets with different working points from the nominal b-jet. The lower panel shows the systematic uncertainty estimated from the RMS of the different variations.

5.2.4 Tracking efficiency

The detector response matrices that have been created with reduced tracking efficiency, which represent the detector with the reduced tracking efficiency. The tracking efficiency was reduced by 4%. So that means 4% of the tracks will be randomly discarded. This percentage was taken from another jet analyses in ALICE, in pp collisions it was taken from [188, 189], and in p–Pb collisions it was taken from [190]. So the jet spectra unfolded with 96% tracking inefficiency response will be enhanced in comparison with the nominal efficiency.

The systematic uncertainty on the unfolded jet spectra are estimated from the deviation of the 4% reduced tracking efficiency detector response matrix from the nominal tracking efficiency as shown in Fig. 5.19 (lower panel).

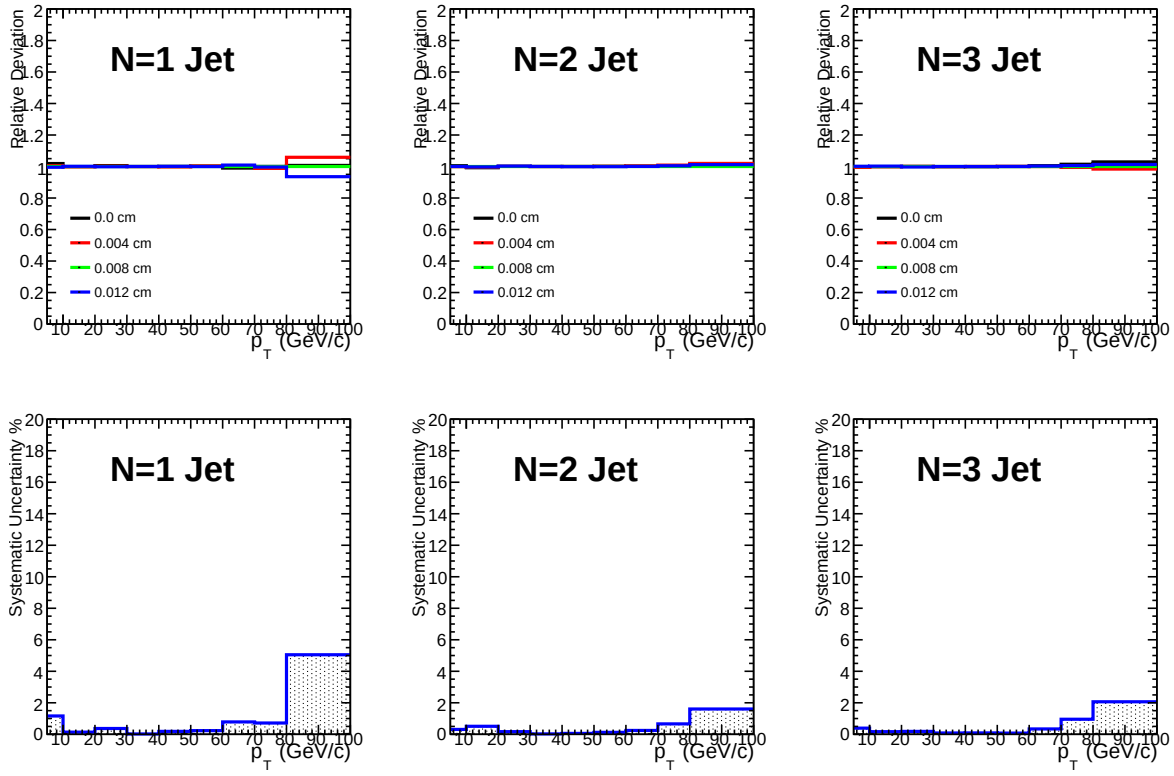

Fig. 5.18 The deviation of the different b-jets from different working points (upper panel), and the systematic uncertainty estimated from the deviation (RMS) shown in shaded area (b).

It should be noted that, the systematic uncertainty yield was estimated by reducing the tracking efficiency by 4%. This uncertainty was evaluated under the assumption that it will be the same if the tracking efficiency was artificially enlarged by the same percent.

5.2.5 Summary of systematic uncertainties

The dominant uncertainty sources have been identified to be originating from the tracking efficiency and from the unfolding procedure. In Tabs. 5.4 5.5 5.6, the uncertainties are summarized for the different tagged b-jet spectra.

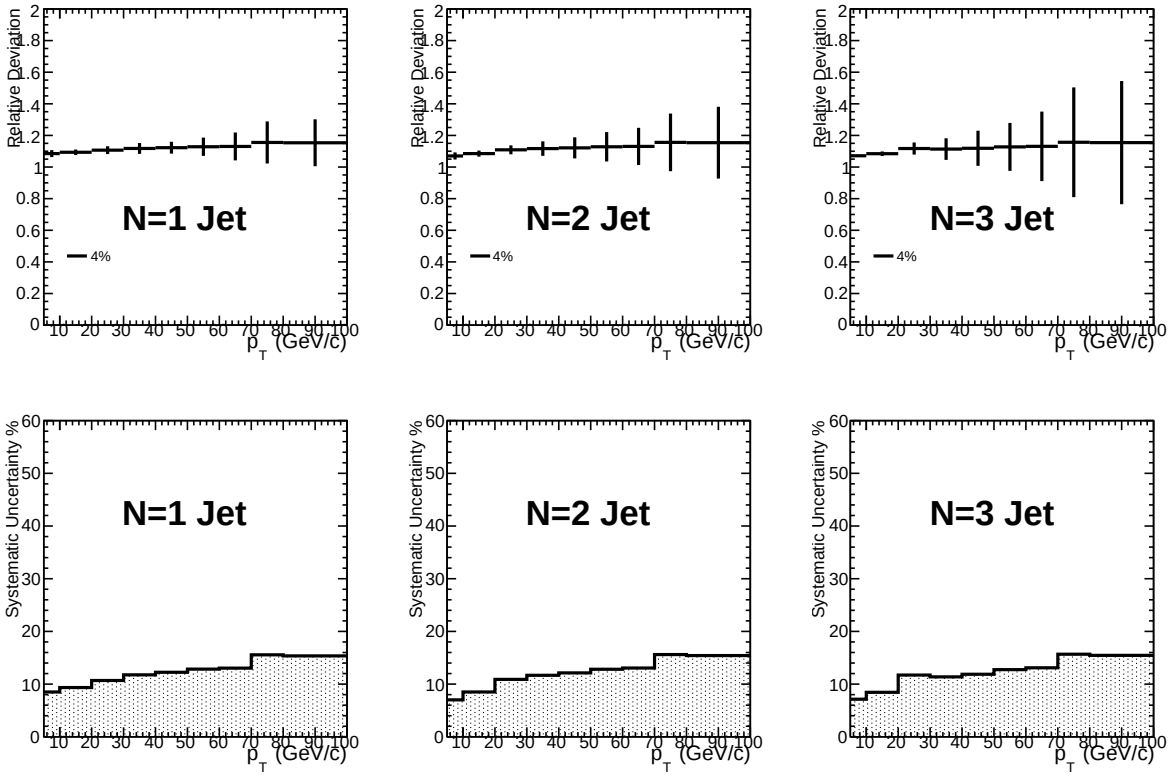

Fig. 5.19 The deviation of the different unfolded spectra with DRM with different tracking inefficiencies (upper panel), and the systematic uncertainty estimated from the deviation of the 4% reduced tracking efficiency shown in shaded area (lower panel).

Table 5.4 Summary for all the systematic uncertainty for the N=1 tagged jets.

Uncertainty source	p_T bins								
	5-10	**10-20**	**20-30**	**30-40**	**40-50**	**50-60**	**60-70**	**70-80**	**80-100**
Unfolding algorithm	3.23								
Regularization parameter	2.59	3.3							
Prior	0.31	1.19	0.19	0.99	1.6	2.8	2.2	7.7	3.2
Unfolding range	0.03	0							
Tracking Efficiency	8.5	9.3	10.6	11.7	12.2	12.8	13.3	15.5	15.3
Tagger working point	1.16	0.13	0.36	0.02	0.18	0.23	0.78	0.72	5.05
Normalization uncertainty	2.29								

Table 5.5 Summary for all the systematic uncertainty for the N=2 tagged jets.

multicolumn1|c| Uncertainty source	p_T bins							
	5-10	**10-20**	**20-30**	**30-40**	**40-50**	**50-60**	**60-70**	**70-80**	**80-100**
Unfolding algorithm	3.9								
Regularization parameter	1.57	2.64							
Prior	0.68	1.41	0.5	0.8	1.49	4.9	3.2	9.2	2.1
Unfolding range	0								
Tracking Efficiency	7	8.5	10.8	11.6	12.12	12.8	13	15.6	15.4
Tagger working point	0.30	0.50	0.16	0.02	0.05	0.12	0.24	0.66	1.6
Normalization uncertainty	2.29								

Table 5.6 Summary for all the systematic uncertainty for the N=3 tagged jets.

Uncertainty source	p_T bins							
	5-10	**10-20**	**20-30**	**30-40**	**40-50**	**50-60**	**60-70**	**70-80**	**80-100**
Unfolding algorithm	2.24								
Regularization parameter	0.10	0.52	0.52	2.60	2.60	2.60	2.60	2.60	3.18
Prior	0.07	0.43	0.51	1.43	1.4	4.59	4	10.54	1.5
Unfolding range	0								
Tracking Efficiency	7.1	8.4	11.7	11.3	11.8	12.7	13	15.6	15.4
Tagger working point	0.39	0.16	0.18	0.08	0.086	0.07	0.34	0.95	2.06
Normalization uncertainty	2.29								

Figs. 5.20 show the total uncertainty after propagating all the different uncertainty sources using Eq. (5.1). In this figure it is shown for all the different tagged jet spectra ($N = 1$, $N = 2$ and $N = 3$).

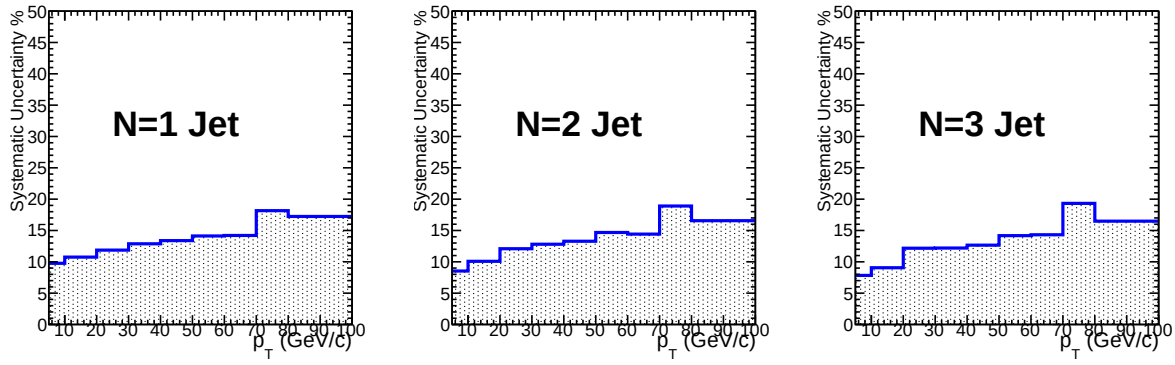

Fig. 5.20 The total systematic uncertainty after propagating all the uncertainties from the different sources.

5.3 Theoretical uncertainties on the b-jet POWHEG spectra

The main sources of systematic uncertainty for the NLO calculations are the renormalization and factorization scale variations. These two uncertainties originates from the finite orders in pertubative calculations. Another source of uncertainty in the NLO simulation is the unertainty arising from the variations of the parameters used to fit the PDFs. The PDF variations are treated as uncorrelated sources of systematic uncertainty on both the PDFs and nPDFs. These errors originate from the uncertainties on the original deep inelastic scatterings, in which the hadron structure is investigated.

For the renormalization and factorization scales uncertainties, they were by varied as follows:

- $\mu_{ren} = 0.5\mu^{ref}_{ren}$ and $\mu_{fact} = 0.5\mu^{ref}_{fact}$
- $\mu_{ren} = 0.5\mu^{ref}_{ren}$ and $\mu_{fact} = 1\mu^{ref}_{fact}$
- $\mu_{ren} = 1\mu^{ref}_{ren}$ and $\mu_{fact} = 0.5\mu^{ref}_{fact}$
- $\mu_{ren} = 1\mu^{ref}_{ren}$ and $\mu_{fact} = 2\mu^{ref}_{fact}$
- $\mu_{ren} = 2\mu^{ref}_{ren}$ and $\mu_{fact} = 1\mu^{ref}_{fact}$
- $\mu_{ren} = 2\mu^{ref}_{ren}$ and $\mu_{fact} = 2\mu^{ref}_{fact}$

where μ_{ren} and μ_{fact} are the varied renormalziation and factorization scales respectively, and μ^{ref}_{ren} and μ^{ref}_{fact} are the original renormalziation and factorization scales.

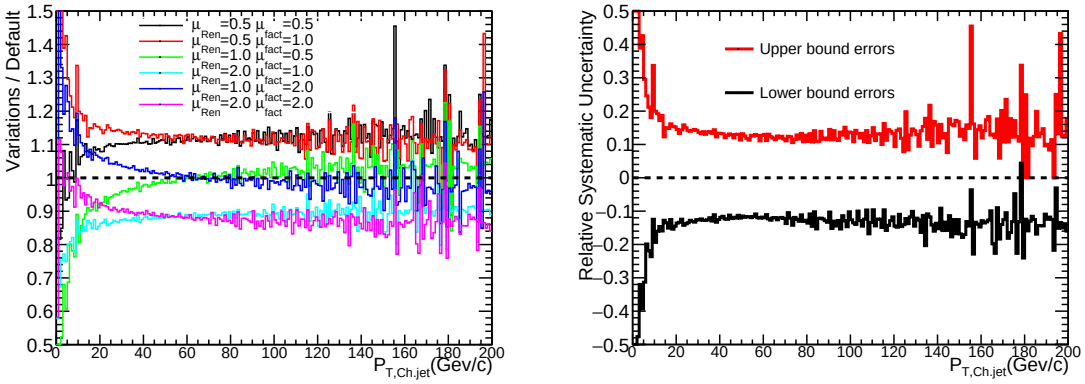

Fig. 5.21 Ratio of transverse momentum spectra of the b-jet with varied renormalization and factorization scales over the default (left), and the estimated systematic uncertainty from the envelop (right).

Fig. 5.21 (left) shows the systematic variation of the renormalization and factorization scales as described above. Also the right panel of Fig. 5.21 shows the estimated total systematic uncertainty using the envelop obtained from the maximal scale variations.

The PDF variation is not very large compared to the scale variations, so the uncertainty from the PDFs and nPDFs was not taken into account in this analysis.

Chapter 6

Results and discussion

The inclusive charged b-jet differential cross section in p–Pb collisions are shown in section 6.1 and compared with theory predictions. Then, the differential cross section of the b-jets in pp collisions will be shown in section 6.2 and also compared with the POWHEG predictions. After that, in section 6.3 the nuclear modification factor of the b-jets will be presented. Next, the b-jet nuclear modification will be compared with that of the inclusive charged jets in section 6.4. Finally, the b-jet fractions in pp and p–Pb collisions will presented in section 6.5.

6.1 b-jet production cross section in p–Pb collisions

After subtracting the underlying events from the inclusive b-jet spectra, applying efficiency and purity correction, and after unfolding the results, the differential production section cross section of the b-jet with resolution parameter $R = 0.4$ is shown in figures 6.1, 6.2, and 6.3 for the $N = 1$, $N = 2$, and $N = 3$ tagged b-jets respectively. The differential production cross section can be written as:

$$\frac{\mathrm{d}\sigma^{b-jet}}{\mathrm{d}p_T} = \frac{C_{vtx}}{N_{evt}}\sigma_{V0} \cdot \text{Unfolded}\left(\frac{\mathrm{d}N^{b-jet}}{\mathrm{d}p_T} \cdot \frac{P_b}{\epsilon_b}\right) \tag{6.1}$$

where $\frac{\mathrm{d}N^{b-jet}}{\mathrm{d}p_T}$ is the p_T differential yield of the b-jets, N_{evt} is the number of minimum bias (MB) events after event selection as described in section 4.1, and σ_{V0} is the total MB trigger cross section and it is equal to $\sigma_{V0} = 2.09 \pm 0.07$ b [173]. The total cross section was multiplied to convert the normalized differential p_T yield into a differential cross section. The factor P_b in equation (6.1) is the b-jet purity in the tagged sample, and ϵ_b is b-jet tagging efficiency. The tagging efficiency and purity corrections are applied before the unfolding.

The cut on the z-coordinate of the primary vertex is not supposed to largely modify the b-jet production cross section. The MB events that don't contain any reconstructed primary vertex were included when the σ_{V0} was measured, but they don't contain any jet. So the total number of selected events should be corrected for the vertex finding efficiency

which is represented by the factor:

$$C_{vtx} = \frac{N_{evt}^{wVtx}}{N_{evt}^{total}}, \tag{6.2}$$

the vertex factor in this analysis was measured to be $C_{vtx} = 0.975$ which is quite high.

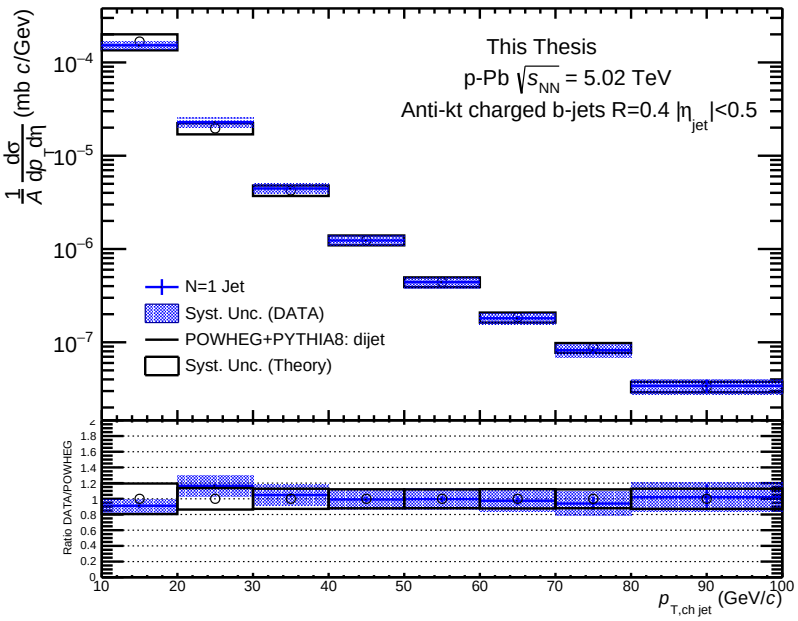

Fig. 6.1 The differential production cross section for N=1 b-tagged jets in p–Pb collisions compared to NLO pQCD prediction.

In figures 6.1, 6.2, and 6.3 the systematic uncertainties are shown in the colored boxes, and the statistical uncertainties are represented by the error bars. The uncertainties were estimated in details in chapter 5.

Figures 6.1, 6.2, and 6.3 also show a comparison to the NLO pQCD calculation made by POWHEG. The systematic uncertainties on POWHEG contain uncertainties from varying the renormalization and factorization scales of the CT14nlo parton distribution function [196] and the EPPS16 nPDF [197].

In order to compare the p–Pb spectra with the pp and the POWHEG spectra, the differential cross section in p–Pb should be normalized by the number of nucleons in the lead ion "A":

$$\frac{\mathrm{d}\sigma_{pPb}^{b-jet}}{\mathrm{d}p_T} = \frac{1}{A}\frac{\mathrm{d}\sigma^{b-jet}}{\mathrm{d}p_T} \tag{6.3}$$

The inclusive charged b-jet spectra presented in figures 6.1, 6.2, and 6.3 shows a good agreement with NLO pQCD calculation done by POWHEG within uncertainties of the measured data and the theoretical uncertainties of the POWHEG.

The b-jet spectra taken from POWHEG+PYTHIA8 are taken after applying the same cuts on the tracks and jets as the discussed in section 4.2 and 4.3.

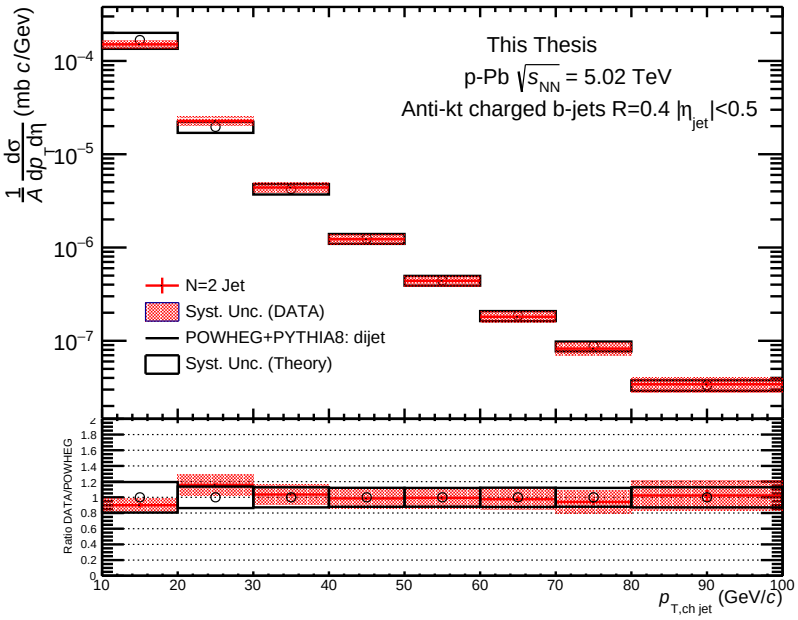

Fig. 6.2 The differential production cross section for N=2 b-tagged jets in p–Pb collisions compared to NLO pQCD prediction.

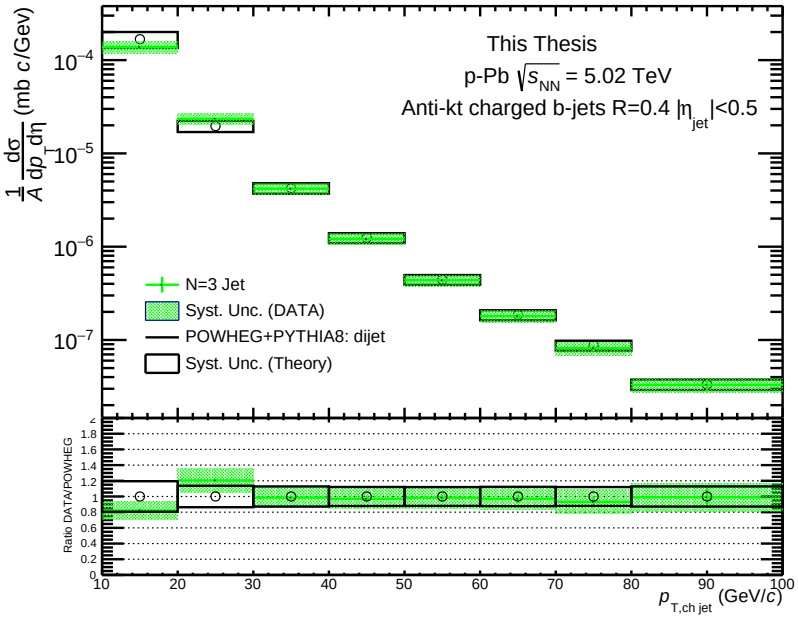

Fig. 6.3 The differential production cross section for N=3 b-tagged jets in p–Pb collisions compared to NLO pQCD prediction.

It should be noted also that the b-jet spectra here are inclusive b-jet spectra. So they contain two contributions to the b-jet production, b-jets produced directly from the hard scattering and b-jets produced from gluon splitting.

6.2 b-jet production cross section in pp collisions

The differential production cross section was measured for the b-jets with resolution parameter $R = 0.4$ after background subtraction and SVD unfolding. The production cross section can be written in a similar way to the p–Pb as in equation (6.1). The difference between the pp cross section and the p–Pb cross section is the total MB trigger cross section which was measured by the Van der Meer scan $\sigma_{V0} = 51.2 \pm 1.2$ mb [174]. Since the average multiplicity in pp collisions is much lower, the vertex reconstruction efficiency is also lower $C_{vtx} = 0.919$.

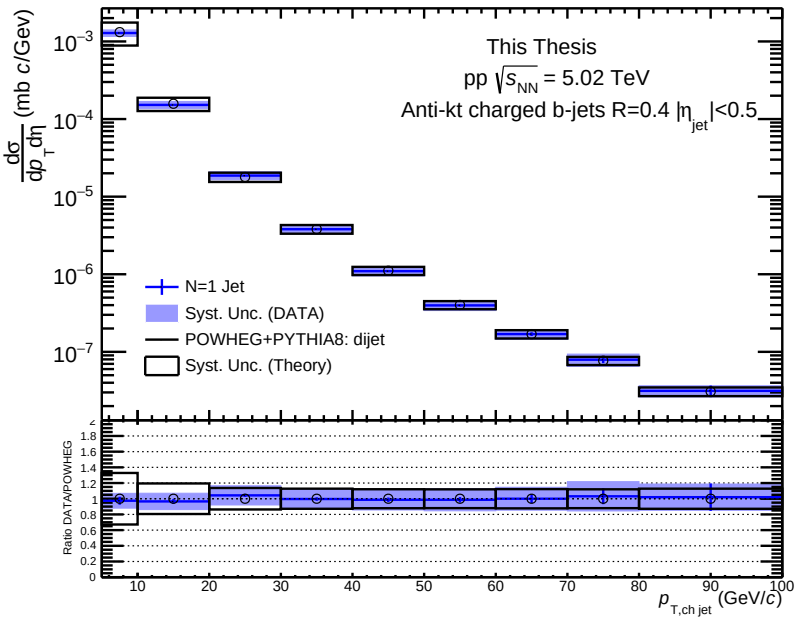

Fig. 6.4 The differential production cross section for N=1 b-tagged jets in pp collisions compared to NLO pQCD prediction.

Figures 6.4, 6.5, and 6.6 show the b-jet differential production cross section as a function of p_T for the $N = 1$, $N = 2$, and $N = 3$ tagged jets respectively. The systematic uncertainties are shown in the colored bars. The measured b-jet cross section is compared with NLO pQCD prediction made by POWHEG dijet package at the same center of mass energy.

The presented inclusive charged b-jet spectra show an excellent agreement with NLO prediction within the measured systematic uncertainty and the theory uncertainties on the POWHEG spectra.

6.3 The b-jet nuclear modification factor R^b_{pPb}

The nuclear modification factor is one of the most common observables for studying the nuclear matter effect. This factor is called R_{pPb} in p–Pb collisions and is defined as the ratio of the p–Pb spectra over the pp spectra, considering also the normalization by the number of nucleons in the Pb ion.

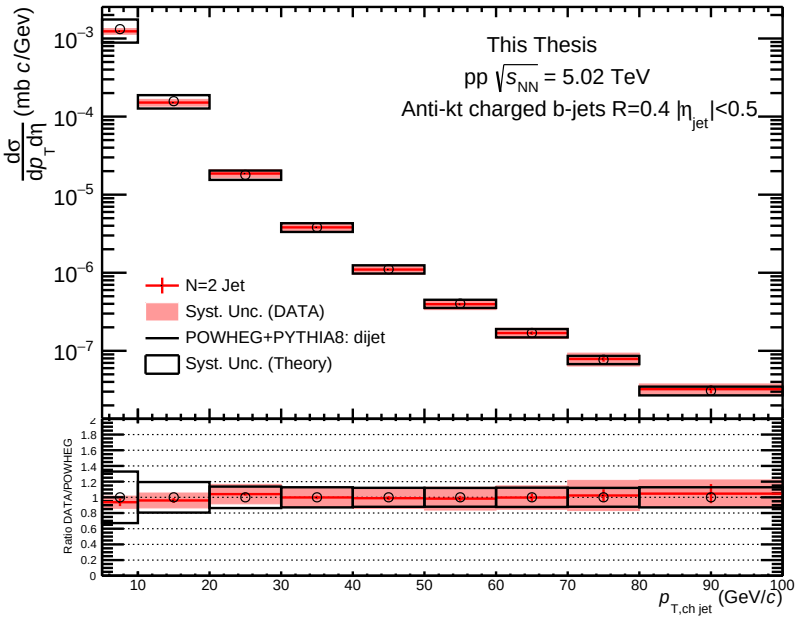

Fig. 6.5 The differential production cross section for N=2 b-tagged jets in pp collisions compared to NLO pQCD prediction.

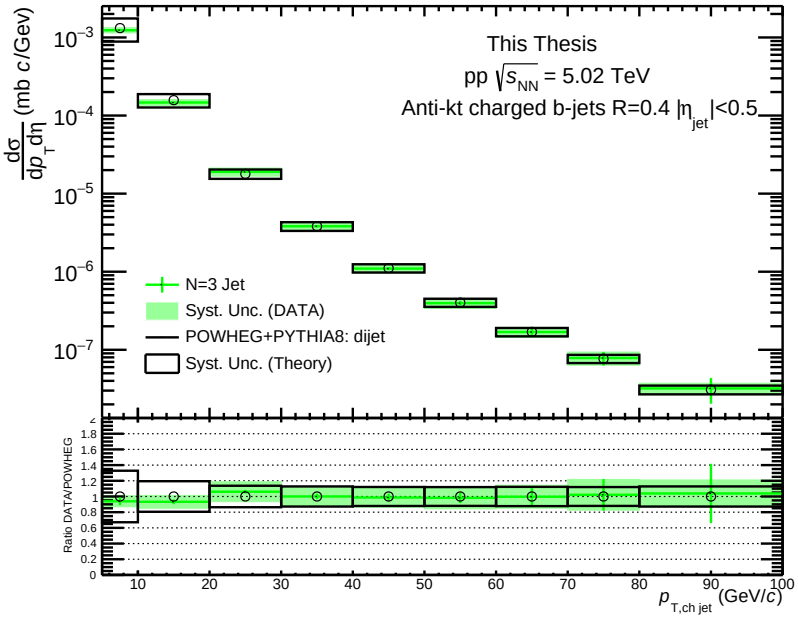

Fig. 6.6 The differential production cross section for N=3 b-tagged jets in pp collisions compared to NLO pQCD prediction.

The b-jet nuclear modification factor in p–Pb collisions R^{b-jet}_{pPb} can be written as:

$$R^{b-jet}_{pPb} = \frac{1}{A}\frac{\mathrm{d}\sigma^{b-jet}_{pPb}/\mathrm{d}p_T}{\mathrm{d}\sigma^{b-jet}_{pp}/\mathrm{d}p_T} \tag{6.4}$$

where A is the number of nucleons in the Pb nucleus, $\mathrm{d}\sigma_{pPb}^{b-jet}/\mathrm{d}p_T$ is the b-jet production cross section in p–Pb , and $\mathrm{d}\sigma_{pp}^{b-jet}/\mathrm{d}p_T$ is b-jet production cross section in pp collisions.

The R_{pPb}^{b-jet} can be explained as follows:

- if the $R_{pPb} > 1$ this means that the b-jet production is enhanced.
- if the $R_{pPb} = 1$ this means that there is no modification for b-jet production.
- if the $R_{pPb} < 1$ this means suppression the b-jet production (jet quenching).

In p–Pb collisions, the deviation from 1 is caused by the interaction with cold nuclear matter effect. While in Pb–Pb collisions the deviation (jet quenching) is due to the interaction with QGP.

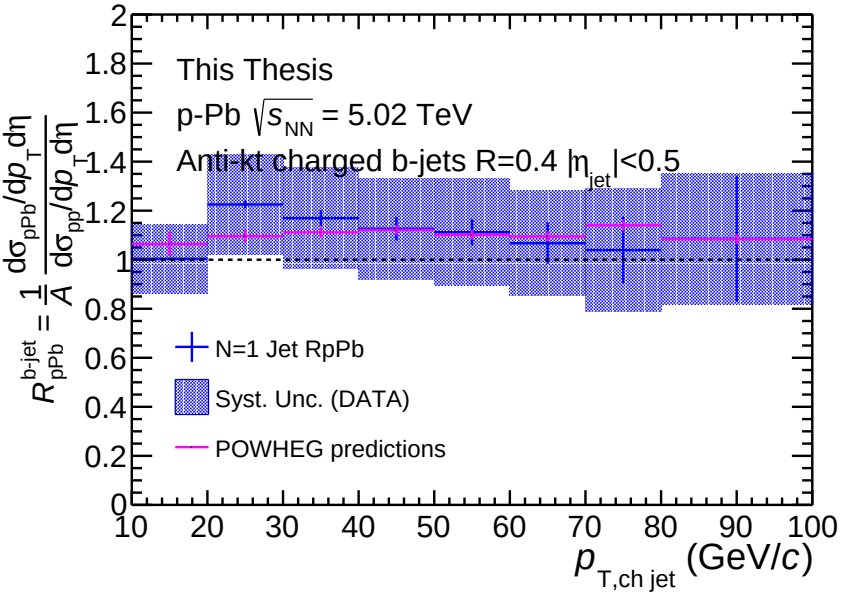

Fig. 6.7 The nuclear modification factor R_{pPb}^{b-jet} for the N=1 inclusive charged b-jets as a function of p_T .

Figures 6.7 6.8 6.9 show the nuclear modification factor of the b-jet R_{pPb}^{b-jet} as a function of p_T. The systematic uncertainties are given as colored boxes.

The R_{pPb}^{b-jet} is consistent with unity within the uncertainties. Also comparing the measured b-jet nuclear modification factor to the theory prediction, they are consistent within uncertainties.

The results of this analysis can also be compared to the results measured by the CMS Collaboration [127] at the same center of mass energies $\sqrt{s_{NN}} = 5.02$ TeV and the same collision system. But it should be noted that, the CMS measurement is done for fully reconstructed b-jets taking the neutral particles in the reconstruction procedure. It should be noted also that the CMS measurement is done for different jet resolution parameter. So no direct comparison can be made for the b-jet spectra, but we can compare the nuclear modification factors.

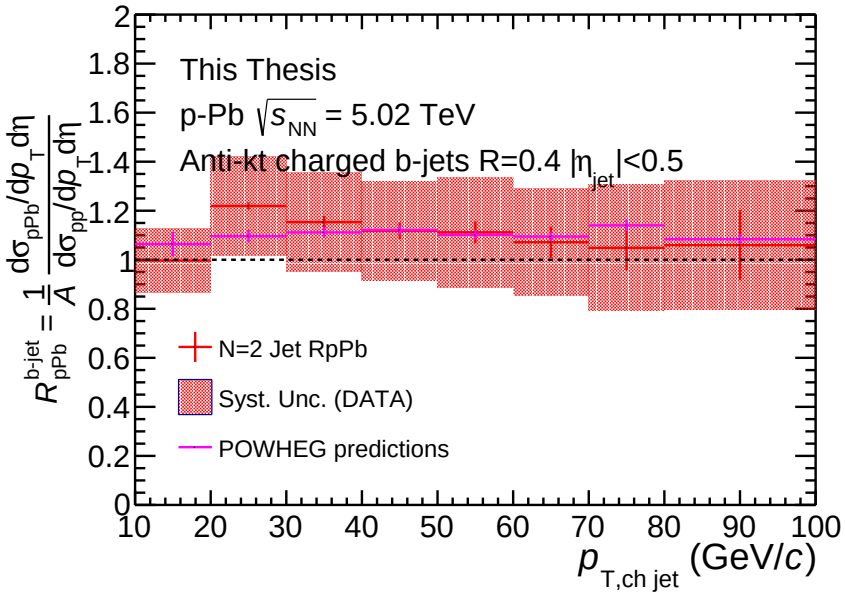

Fig. 6.8 The nuclear modification factor R^{b-jet}_{pPb} for the N=2 inclusive charged b-jets as a function of p_T .

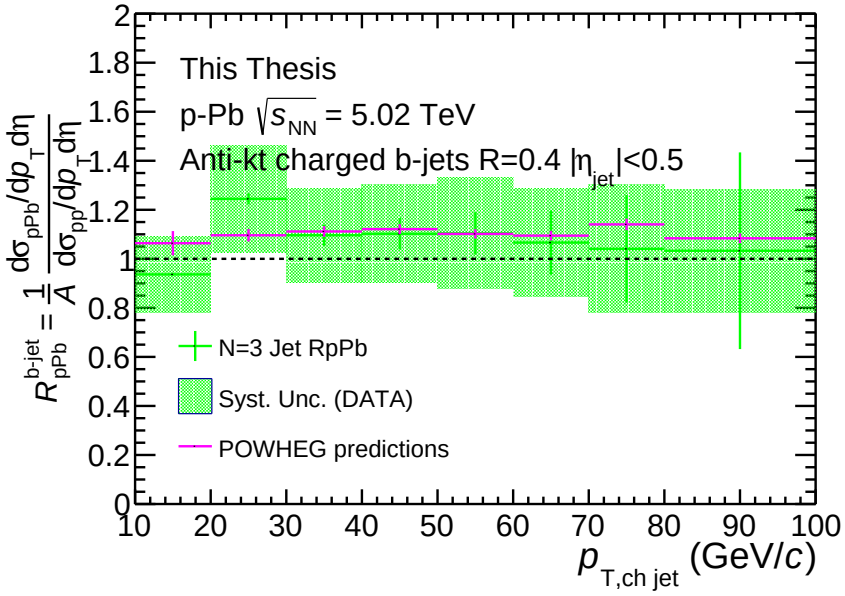

Fig. 6.9 The nuclear modification factor R^{b-jet}_{pPb} for the N=3 inclusive charged b-jets as a function of p_T .

Figure 6.10 shows the R_{pPb} for the b-jets measured by the CMS collaboration compared to that of this analysis. Both nuclear modification factors are consistent within uncertainties.

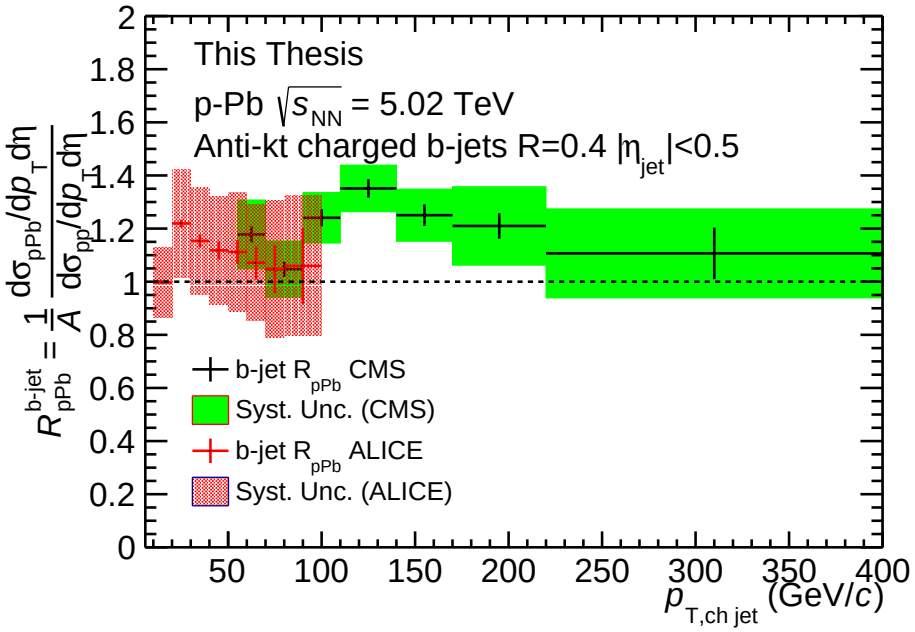

Fig. 6.10 The nuclear modification factor R_{pPb}^{b-jet} for the b-jets as a function of p_T measured by the ALICE expreiment compared to that of the CMS experiment [127].

So the the b-jets are neither quenched (suppressed) nor enhanced in the momentum range $5 < p_T < 70$ GeV/c (ALICE) and $55 < p_T < 400$ GeV/c (CMS). So the interaction of the b-jet with the cold nuclear matter produced in p–Pb collisions has no effect on the b-jet production within the currently measured uncertainties in both experiments.

6.4 Comparison with the inclusive jet R_{pPb}

Figure 6.11 shows the nuclear modification factor R_{pPb} of inclusive charged jets in p–Pb collisions at center of mass energy $\sqrt{s_{NN}} = 5.02$ TeV measured by the ALICE collaboration [198].

The comparison between the nuclear modification factor of the b-jets and the inclusive charged jets R_{pPb}, shows that both R_{pPb}'s are consistent with unity. This also shows that the jet spectra in p–Pb collisions are not affected by the cold nuclear matter effect. Which also shows that the cold nuclear matter doesn't play any role in the jet quenching in Pb–Pb collisions with the current precission.

6.5 The b-jet fraction

The b-jet fraction is the percentage of b-jets in the total inclusive charged jets. The b-jet fraction can be determined by dividing the differential production cross section for inclusive b-jet over the inclusive charged jet cross section.

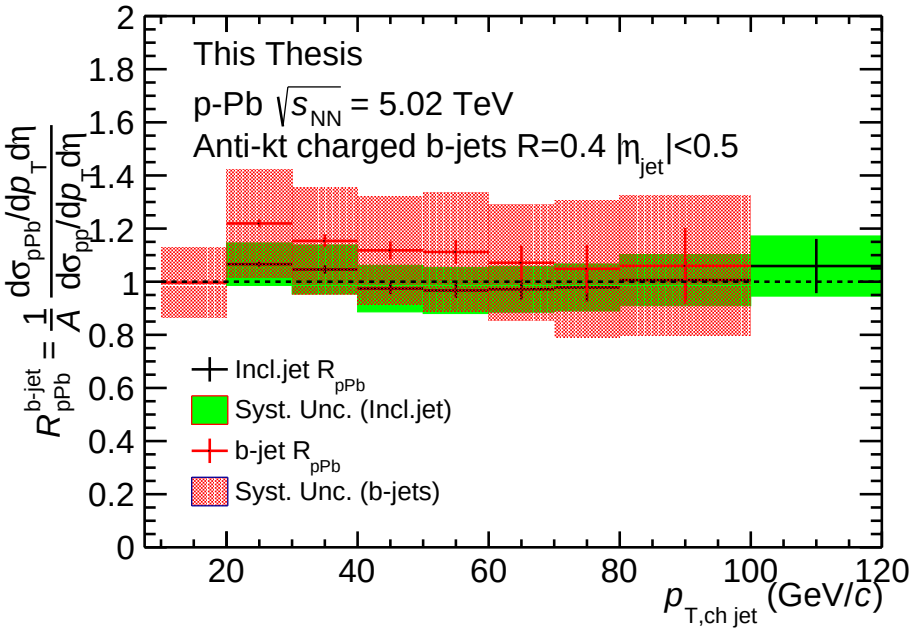

Fig. 6.11 Nuclear modification factor R_{pPb} of the b-jets compared to that of the charged jets measured by the ALICE collaboration [198].

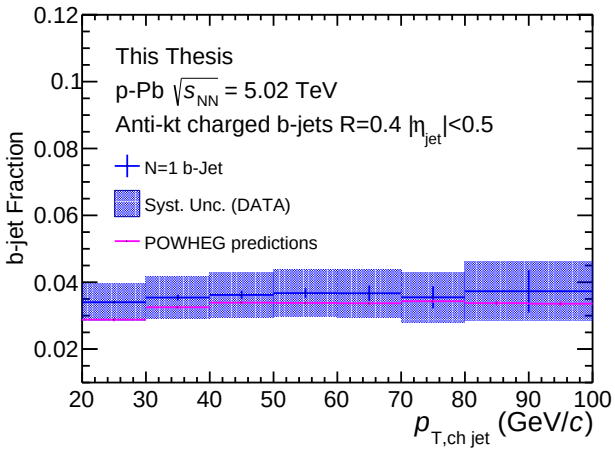

(a) p–Pb collisions

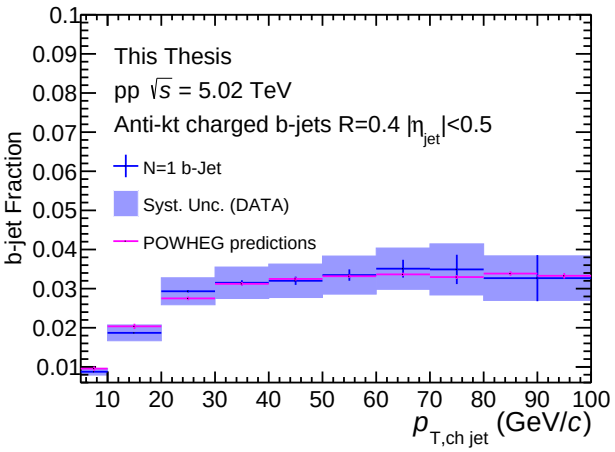

(b) pp collisions

Fig. 6.12 The N=1 b-jet fraction in p–Pb collisions (a) and in pp collisions (b) at $\sqrt{s_{NN}}$ = 5.02 TeV.

Figures 6.12 6.13 6.14 show the b-jet fraction as a function of p_T. The measured b-jet fraction is consistent with the POWHEG predictions within uncertainties. The systematic uncertainties are propagated from the total systematic uncertainty on the b-jet cross section measured in chapter 5. Due to the constraint on the published inclusive charged jet in p–Pb [198] at low p_T because of the high contamination from the background, the b-jet fraction starts from 20 GeV/c. This figure shows that the b-jet increases with p_T

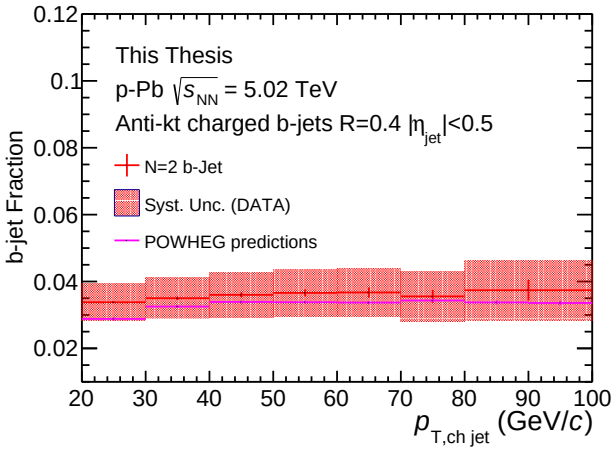

(a) p–Pb collisions

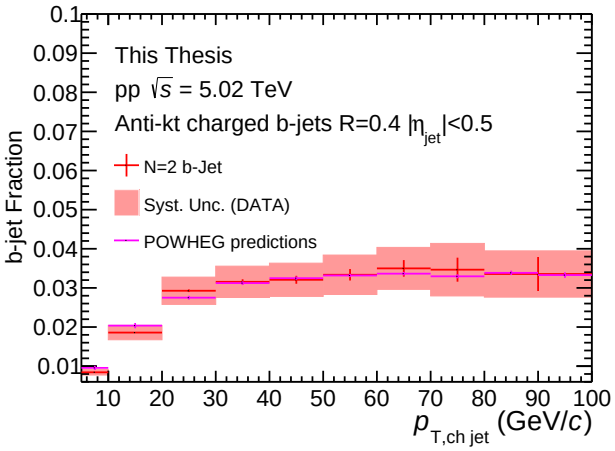

(b) pp collisions

Fig. 6.13 The N=2 b-jet fraction in p–Pb collisions (a) and in pp collisions (b) at $\sqrt{s_{NN}}$ = 5.02 TeV.

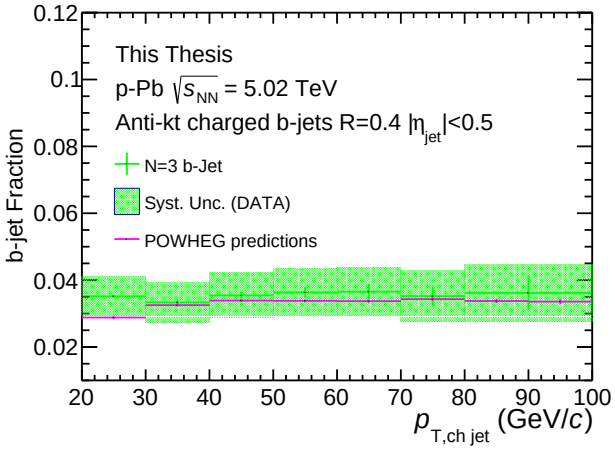

(a) p–Pb collisions

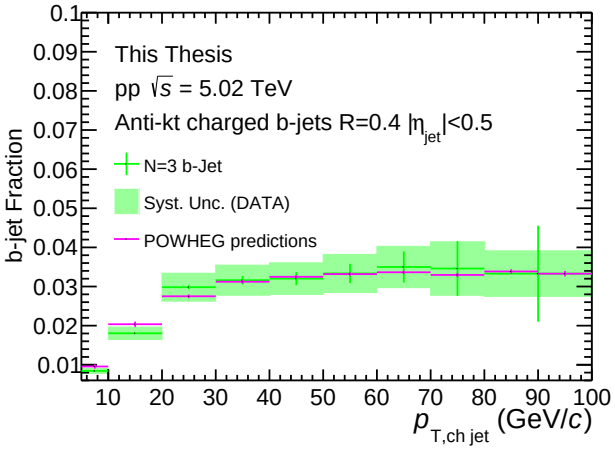

(b) pp collisions

Fig. 6.14 The N=3 b-jet fraction in p–Pb collisions (a) and in pp collisions (b) at $\sqrt{s_{NN}}$ = 5.02 TeV.

until become constant around 0.035 for p_T's above 20 GeV/c. Also the b-jet fraction is almost similar in pp and p–Pb collisions, so the cold nuclear matter effect does not affect the fraction of produced b-jet with respect to the inclusive jets.

The measured b-jet fraction at low p_T in this measurement is consistent with the b-jet fraction measured by the CMS experiment (Fig. 6.15) at high p_T. Which shows that the b-jet fraction is not largely dependent on p_T.

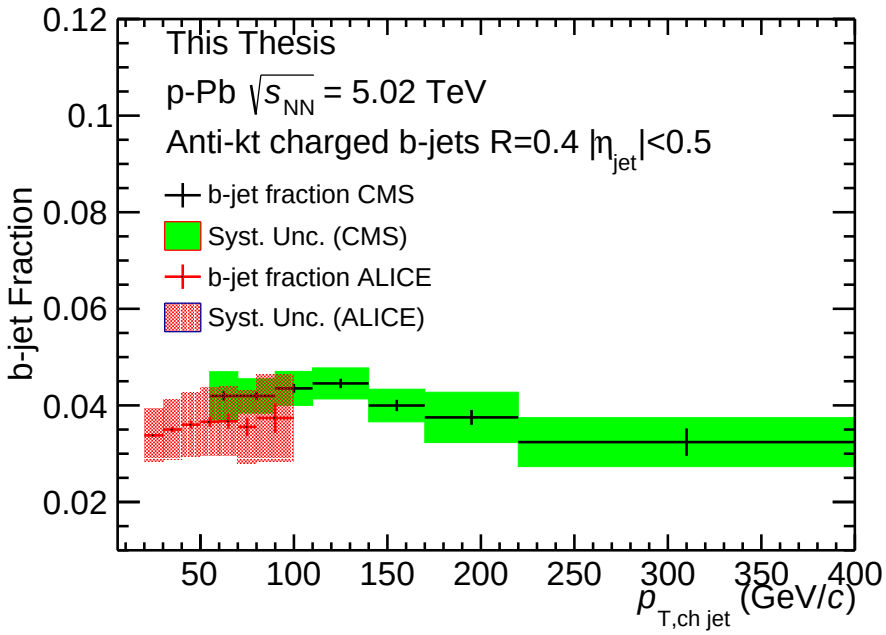

Fig. 6.15 The b-jet fraction in p–Pb collisions at $\sqrt{s_{NN}} = 5.02$ TeV measured by the ALICE experiment at low p_T compared to the CMS results at high p_T [127].

Summary and conclusion

In ultra-relativistic heavy-ion collisions at RHIC and LHC a hot and dense medium of deconfined quark and gluons is created, the quark-gluon plasma (QGP), which is believed to be the state of matter prevailing in the early universe up to a few microseconds after the big bang.

Heavy-ion collisions can be used as a tool to create and study the quark-gluon plasma in the lab. In a hard scattering process the high energy partons interact together producing quarks and gluons. These partons will travel through the QGP, and they will exchange momentum with the medium particles which enhances the gluon emission and the scattering with the other particles with respect to the vacuum leading to an energy loss of the parton, this phenomenon is called jet quenching. This jet quenching will result in a suppression of jet production at high p_T in heavy-ion collisions with respect to jets in pp collisions where there is no QGP.

There are two main kinds of energy loss, radiative and collisional energy loss. In this thesis, I presented a new model for the propagation of an asymptotic parton in a medium described as a collection of random scattering centers in the presence of a chromomagentic background field. Three background field configurations were studied.

In the impulse field configuration, the energy loss turns out to be linearly dependent on the energy E and the medium length L. The dependence on E and L agrees with the results in the literature, however, different color factors have been found which change the sign of the energy loss such that a gain in energy is predicted.

In the zero background field configuration, the energy loss is found to be logarithmically dependent on the energy E and quadratically dependent on the medium length L in agreement with the expressions obtained by Zakharov [147].

Also a constant background field configuration was considered where synchrotron radiation is affected by a multiple soft scattering.

The energy loss calculation were made for massless quarks only, and the experimental side of the thesis was done on b-jets which is massive quark jet. In order to connect the theory side and the experimental side, the heavy-quark mass needs to be added into the calculation. Future calculation on this energy loss model should include the quark mass into all the calculation which can be done by including the spin flip vertex term into the radiation corrected propagator. Including the mass is not enough to reach the b-jet R_{AA}, this model needs to be implemented in a MC simulation. After reaching the modeled R_{AA}, we will be able compare the experimental R_{AA} and the modeled R_{AA}.

Heavy-quarks (charm and beauty) are excellent probes for the study of the QGP, because they are produced before the QGP formation, they are mainly produced in the hard scattering, their production cross section is calculable with pQCD and they also can be tagged using special tagging algorithms. Tagging the HF-jets allows the study of the

mass and color charge (Casimir effect) dependence of parton energy loss. Theory predicts that the mass dependence of the nuclear modification factor R_{AA}, at low momentum $p_T < 50$ GeV/c for b-jets is larger than that of the light-flavor jets (see [11]).

The b-jet production in pp and p–Pb collisions was measured with data collected by the ALICE detector at the LHC at $\sqrt{s} = 5.02$ TeV in years 2017 and 2016, respectively. In this analysis, the jets were reconstructed from charged particles detected in the ALICE central tracking detectors (ITS and TPC). The jets were reconstructed using the anti-k_T algorithm which is implemented in the FastJet package. The b-jets were measured using a resolution parameter $R = 0.4$.

In order to compare the results with theory predictions and measurements from other experiments, correction techniques were applied to the b-jet spectra. First, the jets were corrected from the background by subtracting the average background on an event-by-event basis for each reconstructed jet taking the jet area into account.

Then, the tagged jet spectra spectra were corrected from the tagging efficiency and the purity. A data-driven method was used to determine the tagging efficiency and purity by fitting templates of the jet probability distribution from the different jet flavors to the jet spectrum in data. This fitting procedure was done for the untagged and for the tagged jet spectra in order to estimate the tagging efficiency.

After that, the tagged jets were corrected from detector effects (momentum resolution and tracking efficiency) and background fluctuations using the SVD unfolding algorithm which is implemented in the RooUnfold package.

Next, several parameters were changed to estimate the systematic uncertainties.

After that, the fully corrected b-jet production cross sections in pp and p–Pb collisions were compared with NLO pQCD calculations from POWHEG. The measured spectrum showed a good agreement with the POWHEG prediction within uncertainty in the measured p_T range for both the pp and p–Pb collisions b-jet cross sections.

Finally, the fully corrected b-jet spectra in pp and p–Pb collisions were divided to get the nuclear modification factor of the b-jets R_{pPb}^{b-jet}. The nuclear modification factor shows no nuclear modification for the b-jets in the measured momentum range within the measured uncertainties.

To conclude, the interaction of the b-jet with the cold nuclear matter produced in p–Pb collisions has no visible effect on the b-jet production.

This analysis was performed on the p–Pb data sets collected in 2016, and it is the largest data collected so far. Which makes this analysis unique.

This work is an important mile stone for ALICE which demonstrate the feasibility of b-jet tagging in increasing complexity environment of pp and p–Pb collisions. And it will serve as a preliminary to apply this technique to the Pb–Pb collected in 2015 and in 2018.

Also, since the b-jet production cross section was successfully measured in ALICE, another analysis including b-jets can be done,which is measuring b-jets R_{AA} in Pb–Pb collisions. The b-jet R_{AA} was already done by the CMS experiment for very high p_T. But in ALICE, it can be done for a very low p_T, which is the region where any medium effects dependent on the quark mass might be larger.

Another analysis with b-jets can be done. For example the full b-jet production cross section taking the charged and the neutral particles in the jet reconstruction. Also studying the R_{AA} of the charged b-jets and full b-jets.

The inclusive jet spectra are largely sensitive to the event activity. So it is possible to study the dependence of the b-jet production on the event activity or centrality in p–Pb and Pb–Pb collisions.

The electroweak and the electromagnetic bosons ($W^{\pm}$, Z, and photons) are called electroweak and electromagnetic probes. These probes are very important probes for the study of the QGP since they are produced before the QGP takes place and they don't have any color charge (not sensitive to the strong force), so they are not affected by the nuclear medium produced in heavy-ion collisions. Correlating a photon with a jet can be used to see effect of the QGP on the inclusive jet production. Since the γ-jet analysis was successfully done in ALICE in pp and p–Pb collisions, instead of taking inclusive jets we can take a b-jet (*i.e* γ+b-jet) as was done in [199]. The jet energy will be better calibrated and the modification of the jet energy distribution can be studied more deeply, but the price is much lower statistic. Feasibility studies needed for Run3.

Tagging two b-jets in one event is a good tool for tagging the top quark, in this way it is also possible to study the top quark quenching in heavy-ion collisions. The top quark is a very massive particle, and due to the dead cone effect it may be not largely quenched or even not quenched at all. Also, the tagging the di-b-jets allow for the tagging of the Higgs boson, which allows the study of the Higgs interaction with the QCD medium. The Higgs and top quenching can not be done with current LHC and the current detectors, this will be done in the future collider FCC [200].

Measuring the anisotropic flow in the azimuthal distribution of heavy-flavor hadrons allows for the estimation of the medium transport properties. The dynamical collectivity of the expanding QCD medium transform the initial-state spatial anisotropy into final-state particle momentum anisotropy. The anisotropic flow is described by the Fourier coefficient v_n of the azimuthal angle of the particles ϕ relative to the initial-state symmetry angle plane Ψ_n. v_2 is called the elliptic flow in non-central collisions. The v_2 of the inclusive jets has been already measured in ALICE in [201]. Measuring the b-jet v_2 at low p_T provides an observation into the possible collective flow imparted by the medium to the b quark. While at high p_T, the b-jet v_2 is sensitive to the path-length dependence of the parton energy loss. So since the b-jet measurement in ALICE was successful, so we can measure the b-jet v_2 in p–Pb collisions and even in Pb–Pb collisions.

To conclude, the study of QCD jet observables in heavy-ion collisions is an effort that include both experimentalists and theorist. Significant progress has been made on both from the point of view of the development of experimental techniques as well as from the theoratical development and the theoretical parametric estimates based on scale analysis and modeling within MC parton showers. These developments have lead to a detailed qualitative understanding of how jets are modified in the medium created in heavy-ion collisions. It would be useful to consider strategies that further enhance the jet observables as a valuable probes for the QGP. It is also important to develop common techniques in the broad field of jet physics at colliders, based on modern perturbation QCD methods and on revised tools for high-energy experiments.

The relativistic heavy ion programs at RHIC and the LHC have contributed to considerable advances in our understanding of hot and dense QCD matter. In the near future, the LHC is upgrading the luminosity and energy and also upgrading its detectors, and RHIC is upgrading its detectors. These upgrades will allow for more precise measurements, and examine the limits of the perfect fluid paradigm in terms of system

size, geometry, and beam energy. Also the RHIC is performing a beam energy scan to look for critical fluctuations in order to find the end points of the QCD phase transition. In the longer term, a number of new facilities is coming that will investigate the regime of maximum baryon density. This regime is reached at energies of a few GeV per baryon in the center of mass. The facilities are: FAIR at GSI Germany, NICA in Dubna Russia, and JPARC in Japan. These new facilities will investigate the collisions in the low energy regime with a very high precision, and they will make use of all the knowledge gained at the higher energies.

Appendix A

Datasets and event selection

A.1 Triggering and data taking

The Central Trigger Processor (CTP) of ALICE detector creates the trigger decision derived from detector signals and information about the LHC bunch filling scheme. The CTP computes the trigger inputs from the trigger detector each machine clock cycle (≈ 25 ns). The level 0 trigger (L0) is evaluated each 0.9 μs after the collision using the trigger detectors like V0, T0, EMCal, PHOS, and MTR. If the event was accepted by the L0 then it will be evaluated further by the level 1 (L1) trigger in the CTP, which is evaluated each LHC clock cycle (≈ 6.5 μs. The L0 and L1 decisions are transported to the detectors with a latency of about 300 ns, trigger the buffering of the event data in the electronics of the detectors front-end. The Level 2 (L2) trigger decision, taken after about 100 μs related to the drift time of the TPC, triggers the transfer of the event data to DAQ (Data AcQuisition) and to the High Level Trigger system (HLT) in which the event will be filtered.

The beam-gas interaction events are rejected by the bunch crossing mask (BCMask) which provides information to whether there are bunches coming from both A-side and C-side, or one of them, or neither. Beam-gas interaction triggers bunches without a collision partner, and removed from the physics data with the condition of the presence of both bunches.

The Minimum Bias trigger (MBand and MBor) triggers event with least bias as possible and events trigger by the minimum bias triggers are called minimum bias event (MB). These triggers were used in the all pp and Pb–Pb data taken by the ALICE detector. The high-efficiency MBor trigger was used at low luminosity. When the luminosity and the background level increased, the high-purity MBand trigger become more powerful.In the high luminosity Pb–Pb runs, the V0-based trigger was accompanied by a requirement of signals in both ZDCs (MBZ) in order to reject the electromagnetic interactions between the lead ions. The biased "power-interaction" trigger (SPI) demand a certain number of hits in the SPD. V0 was also used to create central $0-10\%$ (CENT) and semicentral $0-50\%$ (SEMI) Pb-Pb triggers, with thresholds on the summed-up signals. The thresholds were applied separately to the sums of the output charges of V0A and V0C, then the bunches crossing in two sides were required.

There are also another rare triggers which are used for the different physics analyses. The high-multiplicity trigger (HM) is based on the hits in the outer layer of the SPD. The

PHOS and EMCal are implemented at L0 triggers which require a certain energy deposit in the calorimeter cells. The EMCal L1 trigger provides triggers on photons/electrons and on jets. The TRD which is implemented at L1 triggers provide triggers on jets, single electrons, double electrons which are used in the quarkonium analysis, and on a shared electron between TRD and EMCal.

The muon triggers are implemented at L0. There are two single-muon triggers and two dimuon triggers, all in concurrence with MB. The DG (double gap) trigger in pp asks for a particle at midrapidity and no particles in the intermediate pseudo-rapidity ranges of the V0 detector. The CUP (central-rapidity ultraperipheral) trigger execute a similar selection in collision systems including ions. The MUP (muon ultraperipheral) trigger which is similar to the DG except it applies for a forward muon. Finally there is the ACORDE cosmic trigger (COS) which trigger on high multiplicity cosmic muon events.

A.2 Data samples

In the present thesis, several data sets have been analyzed: Monte Carlo simulations (used for cross checks, predictions, and correction techniques), and the ALICE data sets used for the main analyses of the b-jets in pp and p–Pb collisions.

The analysis was performed on data recorded in 2016 (p–Pb) and 2017 (pp) with the ALICE detector at the LHC. p–Pb collisions were taken at a center-of-mass energy of $\sqrt{s_{\mathrm{NN}}} = 5.02$ TeV and pp at $\sqrt{s} = 5.02$ TeV respectively. Around 700 million minimum bias p–Pb events were recorded and 1 billion pp events were recorded. In 2016 and 2017 during the data taking the SDD sub-detector was reaching it busy time too quickly, so a cluster without the SDD was setup to collect as much as possible of the delivered luminosity, which lead to the recording of some events without the SDD information. The events with SDD information fire the CENT trigger class while the events without SDD information fire the FAST trigger class only. Three kinds of events were reconstructed during pass1:

- **pass1_CENT_wSDD**: all events in the CENT cluster, i.e. with SDD in the readout, reconstructed including SDD in the tracking. So these events show the best tracking performance.
- **pass1_CENT_woSDD**: all events in the CENT cluster, i.e. with SDD in the readout, reconstructed excluding SDD from the tracking. It was reconstructed to merge its events with the FAST events.
- **pass1_FAST**: all events that are only in the FAST cluster (and not in the CENT), i.e. without SDD in the readout

The CENT_wSDD events cannot be merged with the FAST events due to the different tracking performance, so pass1_CENT_woSDD was reconstructed, which the same as the pass1_CENT_wSDD but without SDD in the reconstruction to be merged with the FAST. So in order to run on the full statistics of 2016 p–Pb pass1_CENT_woSDD and pass1_FAST datasets were used. Internally, the recorded p–Pb datasets at $\sqrt{s_{\mathrm{NN}}} = 5.02$ TeV periods are called LHC16q and LHC16t. The run numbers that were processed in this analysis are listed below:

- **LHC16q**: 265525, 265521, 265501, 265500, 265499, 265435, 265427, 265426, 265425, 265424, 265422, 265421, 265420, 265419, 265388, 265387, 265385, 265384, 265383, 265381, 265378, 265377, 265344, 265343, 265342, 265339, 265338, 265336, 265335, 265334, 265332, 265309.
- **LHC16t**: 267166, 267165, 267164, 267163.

The pp periods at $\sqrt{s} = 5.02$ TeV are internally called LHC17p and LHC17q. The run numbers that were processed in this analysis are listed below:

- **LHC17p**: 282343, 282342, 282341, 282340, 282314, 282313, 282312, 282309, 282307, 282306, 282305, 282304, 282303, 282302, 282247, 282230, 282229, 282227, 282224, 282206, 282189, 282147, 282146, 282127, 282126, 282125, 282123, 282122, 282120, 282119, 282118, 282099, 282098, 282078, 282051, 282050, 282031, 282030, 282025, 282021, 282016, 282008.
- **LHC17q**: 282367, 282366, 282365.

It should be noted that, the run number 282030 doesn't exist on the FAST cluster.

The p–Pb MC productions used in this thesis at a center-of-mass energy of $\sqrt{s_{\mathrm{NN}}} = 5.02$ TeV are generated using PYTHIA6 [111] and EPOS-LHC [170]. Each one of them consists of two datasets one anchored to (describe the detector configurations of) the pass1_CENT_woSDD and another one anchored to the pass1_FAST:

- LHC17h6a2, LHC17h6b2: $b\bar{b}$ production contains around 10M CENT_woSDDFAST events and 10M FAST event. In this production the final state partons were forced to be beauty partons ($b\bar{b}$). This MC was used for determining the b-jet tagging efficiency and for determining the b-jet reconstruction efficiency used after unfolding.
- LHC17h6c2, LHC17h6d2: $c\bar{c}$ production contains around 10M CENT_woSDDFAST events and 10M FAST event. In this production the final state partons were forced to be charmed partons ($c\bar{c}$). This MC was used for determining the c-jet mistagging rate.
- LHC17h6e2, LHC17h6f2: jet-jet production which contains about 37M CENT_woSDDFAST events and 37M FAST event. The final state of this production is di-jet final state. This MC was used for creating the response matrix which was used for unfolding in section 4.5.7. This MC was also used for determining the mistagging rate for the light-flavor jets and also used for determining the b-jet purity.

The MC productions that are anchored to the pp data are generated using PYTHIA8 [172]. Each one of them consist of two data sets one is anchored to (describe the detector configurations of) the pass1_CENT_woSDD and another one anchored to the pass1_FAST:

- LHC18b8_fast and LHC18b8_cent_noSDD: jet-jet production which contains about 110M FAST events and 60M CENT_woSDD events. The final state of this production is di-jet final state. This MC was used for creating the response matrix which was used for unfolding in section 4.5.7. This MC was also used for determining the b-jet tagging efficiency, c/light-flavor-jet mistagging rate and for determining the b-jet purity. It was also used for the definition of the templates that were used in the data driven efficiency and purity determination in section 4.5.5.

A.3 Quality assurance

Not all the recorded runs in 2016 were used in this analysis, some runs were excluded for quality reasons. For examples some of the runs were excluded since the ZDC detector was off, some of them were also rejected since there was no TOF information. The rest of the runs were checked by the basic quality tests, which are confirming that the spatial track distribution of the detector don't reveal any dead regions in the detector or that the ϕ, η and p_T distributions looks similar in all the runs.

Figure A.1 shows the ϕ and η distributions of the tracks compared to a certain reference in the different run numbers. In this figure the reference is the sum of all the distribution in all the run numbers. It is clear that all the distribution in all the run numbers show a good agreement with the reference except for run 265331 which shows a large dip in the ϕ and η distribution. When this run was recorded by the detector the TPC C-sided IROC (Inner ReadOut Chamber) was not working, so a significant number of tracks was lost which lead to the large dip in ϕ and η. As a result this run was excluded from the analysis.

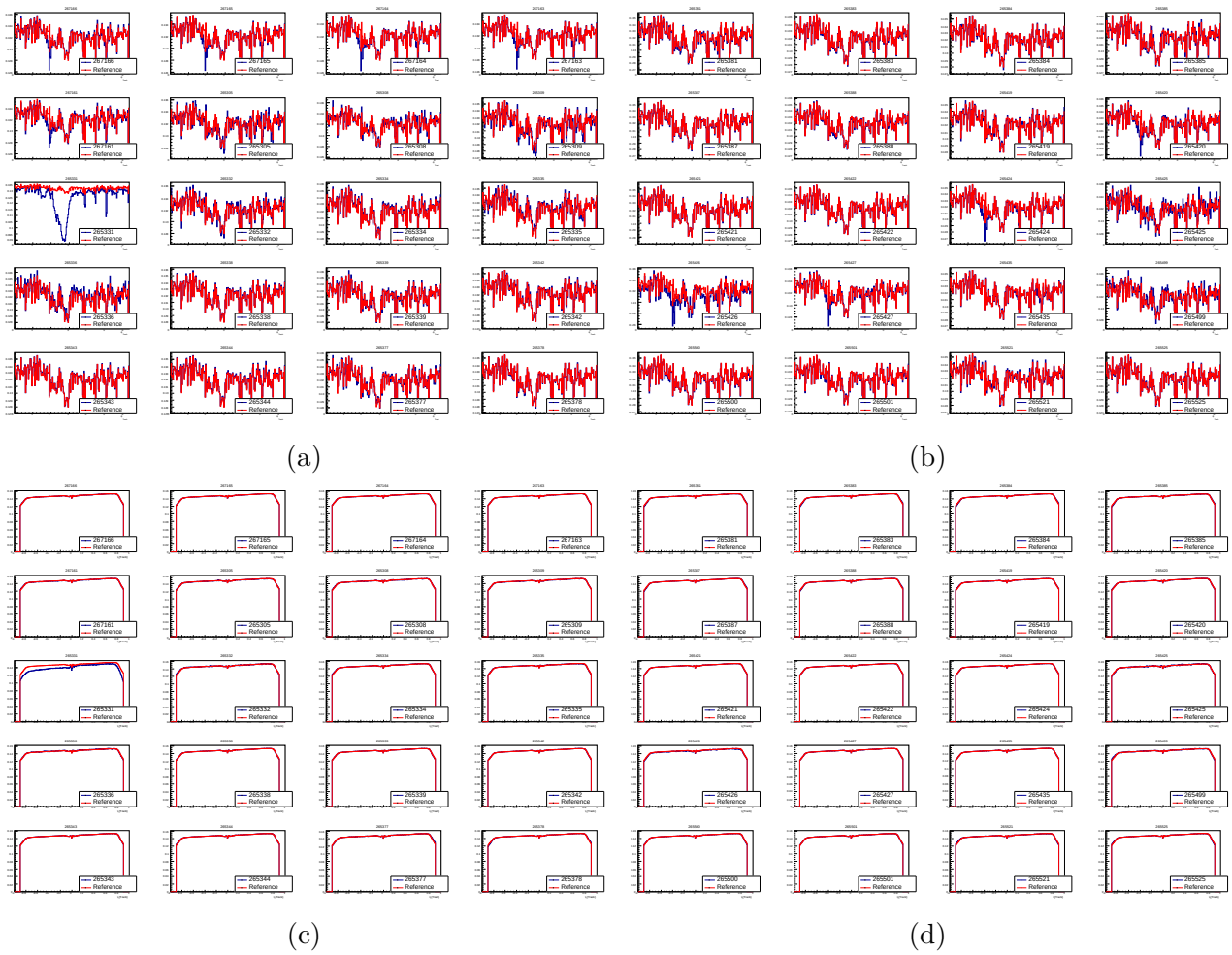

Fig. A.1 The ϕ distribution (a)(b) and the η distribution of the tracks for the different run numbers compared to a reference which is the sum of all distributions of all the runs

A.4 Track selection

Charged jets are constituted from charged tracks reconstructed by the ALICE detectors, and the reconstruction of tracks in the ALICE detector was discussed in details in section 3.3. But they cannot be used directly in the jet finding, several quality selection criteria should be used before.

In order to select high quality tracks, a certain cut should be applied on the reconstructed tracks. Some tracks can be reconstructed in a pseudorapidity region up $|\eta| < 1.4|$, but the tracking efficiency sharply falls in the outer regions of the detector. For this reason, tracks are limited to the pseudorapidity region $|\eta| < 0.9$. Furthermore, the tracking efficiency sharply decreases in the low track-p_T region, so in order to reject these tracks a minimum $p_{T,min} > 0.15$ GeV/c cut was applied.

Also, the high quality track efficiency is not totally constant in $\eta - \phi$ plane due to dead SPD sections. This non uniformity of the tracking efficiency affect of the jet distributions in these regions due to an inefficient clustering of the jet finding in these regions. In order to avoid these inefficiencies the concept of hybrid tracks was introduced. The tracks used in the heavy-flavor analysis are composed of two types, high quality tracks (also referred to as global tracks) and tracks without/without ITS refit and no SPD hits (called complementary tracks). The usage of these two types assures that a uniform track distribution in $\eta - \phi$ plane.

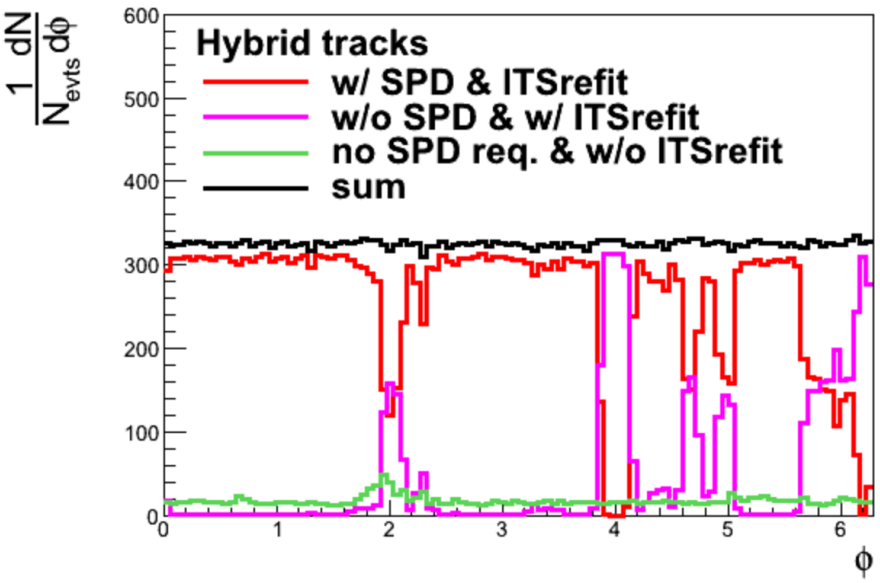

Fig. A.2 Azimuthal distribution of hybrid tracks.

The global tracks use SPD information and ITS refit, so they give the optimal p_T resolution, While the complementary tracks are constrained to the primary vertex in order to improve the p_T resolution even with the missing hits in the SPD or failing the ITS refit.

In AOD hybrid tracks can be selected using 2 filter bits, filter bit for the global tracks (filter bit 4)and filter bit for the complementary tracks (filter bit 9). There are two kinds of global tracks, filter bit 4 and filter bit 8, the difference between these two is that the

impact parameter distribution of filter bit 8 tracks is more constrained (due to the golden χ^2, cut see section B.3), so in order to use a more relaxed impact parameter distribution filter bit 4 was used in this analysis, and it is also used in the heavy-flavor working group.

Appendix B

Hybrid track cuts

The track cuts used in this analysis are commonly used by the ALICE heavy-flavor group in the used data sets. As discussed in the text, the track are mainly consist of two kinds: global (filterbit 4) and complementary (filterbit 9). below is a summary of the track cuts used during filtering the ESD tracks.

B.1 Common cuts between the global and complementary tracks

This is a list of cuts that are applied for both global and complementary tracks.

B.1.1 Minimum number of crossed rows in TPC, Minimum ratio crossed rows/findables

The number of crossed rows is set to 70, and the ratio of crossed row over findable clusters is set to 0.8.

The pads at the end caps of the TPC are ordered in rows relative to the beam line. In total, 160 rows contain sensor pads. Crossed row associated to that the clusters in two pads directly next to a row are founded. The number of crossed rows then is related to the amount of information the track encoded into the ion trace in the TPC on at least partially continuous lines. This cut assures that the tracks have the minimum quality required. It removes the tracks with largely overestimated p_T because of too few information available from the TPC.

The other cut that is related to crossed rows cut is the requirement that at least 80% of the possibly findable rows (predicted from trajectory of the track) are reconstructed. This removes tracks badly reconstructed in the TPC.

B.1.2 Minimum number of TPC clusters

The minimum number of TPC clusters is set to 70 clusters for $p_T < 20$ GeV/c and 100 for tracks with $p_T > 20$ GeV/c.

This cut is in general another version of the previous crossed-rows cut. It also removed badly reconstructed tracks in the TPC. For low transverse momentum tracks, the minimum

number of clusters depends on the transverse momentum. Above $p_T > 20$ GeV/c, at least 100 clusters are needed for a track to pass this cut.

B.1.3 TPC refit

In the third phase of the track reconstruction process, the tracks are reconstructed inwards from the outer side of the central detector barrel tracker to the primary vertex. This procedure is a refit, which uses the TPC and ITS clusters found in previous stages of the reconstruction. Tracks with succeeded TPC and ITS refit have significantly better momentum resolution. A TPC refit is needed for all the tracks.

B.1.4 Maximum fraction of shared TPC clusters

The maximum fraction of shared TPC clusters is set to 40%.

Mainly to discard multiple reconstructed versions of one physical track, a track is only allowed to share a certain fraction of its TPC clusters with another track.

B.1.5 Allow kinks

This flag is off. Tracks that show a kink in their trajectories, like those that originate from a decay process, are rejected.

B.1.6 Maximum χ^2 for TPC and ITS clusters

The maximum χ^2 for TPC clusters is set 4, and the maximum χ^2 for ITS clusters is set 36.

To guarantee that a track is reconstructed with a high precision, a good agreement between the track curve and its corresponding detector clusters is required. As a measure for the agreement,the χ^2 values between track curves and clusters can be calculated. These values are normalized to the number of ITS or TPC clusters. This cut is imposed for ITS and TPC clusters.

B.1.7 Maximum DCA to vertex z and xy-plane

The maximum DCA to vertex z is set to 3.2 cm, the maximum DCA to xy-plane is set to 2.4 cm.

The particle associated to the reconstructed track should be created in the primary collision vertex. So the track should start near the primary vertex. This cut removes many material-generated background particles and also secondaries from weak decays. The smallest distance between the track curve and the primary vertex is evaluated for the z direction (along the beam axis) and in the xy-plane with a distance of closest approach (DCA) technique. Due to differing resolutions in z and xy, the procedure is split. The cut is on the distances of closest approach in both dimensions.

B.2 Cuts applied for global tracks only

This is a list of cuts that are applied for global tracks only.

B.2.1 ITS refit

The ITS refit cut is used for the same reasons as the TPC refit cut, in order to improve the momentum resolution of the tracks.

B.2.2 Minimum hits in SPD

The minimum number of hits in SPD is set to 1 hits.

A hit in the SPD, which is very close to the interaction point, enhance the momentum resolution of the reconstructed tracks.

B.3 The golden χ^2 cut

In ALICE collaboration the default tracks that are usually used by the different PWGs are hybrid tracks with AOD filterbit 8 and filterbit 9. In this analysis the filterbit 4 was used instead of filterbit 8. The reason for the golden χ^2 cut which is applied in filterbit 8 also called the maximum χ^2 for vertex constrained tracks. This cut is set to 36 in filterbit 8 and in filterbit 4 is not applied (it is relaxed). This cut constrain the tracks to the primary vertex. In other words it removes a large fraction of the secondary particles coming from the secondary vertex (like c and b quark decay products), which is not good for the tagging of the heavy-flavor hadrons and HF-jets. Since the tagging procedure requires particles coming from the secondary vertex in order to reconstruct the mother particle (which is HF-hadron).

Appendix C

Different background estimators

In this analysis the CMS method for background estimation was used as a default method. But this is not only method in the literature. There are several methods that could have been used in this analysis, but they were as a systematic uncertainty in [198]. Here are a list of different background estimators.

C.1 Original Pb-Pb approach

This approach works very well in Pb-Pb collisions, but that doesn't mean that it will for a much smaller systems like p-Pb collision system. So it has to be adapted by certain way.

The background density in this approach is calculated by:

$$\rho_{PbPb} = \text{median}\left\{\frac{p_{T,i}}{A_i}\right\} \tag{C.1}$$

where i is the index of k_T jets with p_T >0.15 GeV/c.

The k_T jet sample also includes signal from hard scattering. The usage of the median method already shows a stability with regard to outliers in the jet distribution, in this case outliers from the hard signal. Another method to reduce the effect of the signal is to exclude k_T jet signal. Here, the n leading jets are excluded from the sample. Leading jets are those with the highest transverse momentum p_T. n is usually chosen to be $n = 2$.

The authors of this method proposed to include ghost jets in the jet sample when estimating the background in a sparser environment to consider the empty areas. The acceptance is filled symmetrically with ghost particles that have very small momentum to estimate the area. In relatively sparse environments, the jet algorithm can merge these ghost particles to ghost jets that do not contain any particles. In Pb-Pb, these ghost jets do not ant effect, because of the high average background density. The p-Pb system is a different case, because most of the events, a sizable part of the acceptance does not contain particles.

C.2 Mean-based approach

In the Pb-Pb approach, when including ghost particles, the background density is zero if more than 50% of the jets are ghost jets since the method uses the median as estimator.

The mean-based background density estimation method emerge from a first naive idea to solve the problem. The method is to estimate the background density by:

$$\rho_{mean} = \text{Mean}\left\{\frac{p_{T,i}}{A_i}\right\} \tag{C.2}$$

In contrast to the median approach, the mean of a distribution is continuous but also much more influenced by outliers. So, it is necessary for this method to exclude the hard scattering signal jets from the jet sample. They are excluded by neglecting k_T jets that share tracks with those signal jets.

Another kind of the mean-based approach arises if all the k_T jets have approximately the same area or transverse momentum. In this case, the background density can be estimated by:

$$\rho_{mean} = \text{Mean}\left\{\frac{p_{T,i}}{A_i}\right\} \approx \frac{\text{Mean}\left\{p_{T,i}\right\}}{\text{Mean}\left\{A_i\right\}} = \frac{\sum_i p_{T,i}}{\sum_i A_i} = \rho_{MeanII} \tag{C.3}$$

The two mean approaches suffer from two conceptual problems. First, the mean is sensitive to outliers in the distribution. Even if the exclusion of the signal by excluding signal jets perfectly worked, the background density would be biased to larger values due to fluctuations. This will cause another problem, the exclusion affects signal jets above a certain p_T threshold, which is 5 GeV/c in this case. A jet with $p_T = 4.9$ GeV/c will be reviewed as background but includes signal with a high probability. This conceptual problem needs to distinguish signal and background jets. So again, the background will be biased to larger values. The median-based methods do not have this problem as they are relatively insensitive to signal contamination in sparse events.

C.3 Track-based approach

The background calculation using tracks is the easiest. The summed p_T of all non-signal tracks is divided by the associated area, leading to the estimation of the background density as:

$$\rho_{track} = \frac{\sum_i p_{T,i}}{A} \tag{C.4}$$

Similar to the mean-based approach, the background definition largely depends on the signal definition. In this case, tracks are determined to belong to the background if they lie outside a rigid cone with $R = 0.6$ around the axis of signal jet. The area A is calculated by a Monte Carlo method and corresponds to the acceptance excluding the area of the $R = 0.6$-cones around the jets.

This background estimate has the same problems as the mean-based method and is even more influenced by a signal contamination.

C.4 Perpendicular cone method

It is the same method as used for the pp jet spectra analysis. It is estimated as the sum of track p_T in a perpendicular cone which is defined with respect to a leading jet axis and

divide it by jet area to get jet p_T density:

$$\rho_{\perp} = \frac{\sum_i p_{T,i}}{\pi R^2} \tag{C.5}$$

where i corresponds to the tracks inside the perpendicular cone, and R is the jet resolution parameter.

Appendix D

Other data-driven approaches

The data-driven methods described in this section are another methods which are not use in this analysis.

D.1 The p_T^{rel} method

The p_T^{rel} variable is determined for leptons that are located inside the jets, defined as the lepton transverse momentum relative to the jet's momentum axis (or the combined axis of the jet and the lepton) as shown in Fig. D.1.

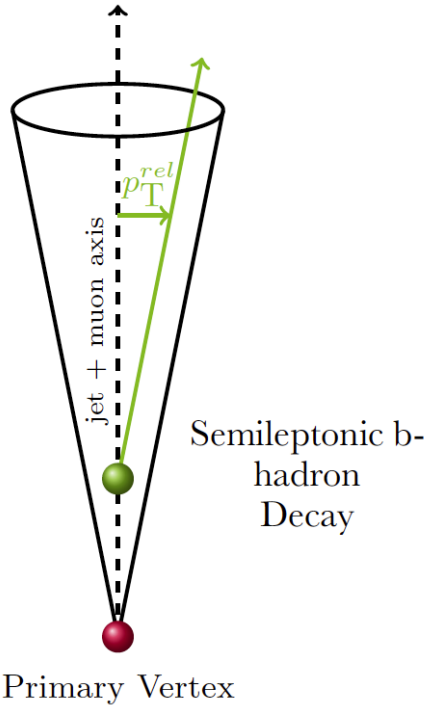

Fig. D.1 The p_T^{rel} variable is defined as the projection of the lepton momentum (green line) transverse to the jet+lepton axis (dashed black line).

Since the ALICE detector doesn't reconstruct muon in the central barrel, electrons were use instead of muons for the p_T^{rel} analysis in this thesis.

From the momentum vector (the three momentum component of the four vector) $\vec{p} = (p_x, p_y, p_z)$ of the background subtracted jet momentum $\vec{p}_j$ and the muon $\vec{p}_\mu$ the transverse projection of the muon can be determined by:

$$p_T^{rel} = \sqrt{\vec{p}_\mu^2 - \left(\frac{\vec{p}_j \cdot \vec{p}_\mu}{|\vec{p}_j|}\right)^2}. \tag{D.1}$$

Due to the heavy b-quark mass, the p_T^{rel} of the leptons from b-hadron decays is much larger than that of the leptons from light-flavor jets or from charm-hadron decays. Which allows the p_T^{rel} to be used as a discriminator.

Also the 3 dimensional impact parameter of the lepton tracks from b-hadrons is larger than that of the leptons from other hadrons. This parameter can also be used as a discriminator but it was not used in this analysis. Both the p_T^{rel} variable and lepton impact parameter can be used as a discriminator for the b-jet tagging efficiency determination. The p_T^{Rel} method depends on the fits to the p_T^{rel} distribution in the data with respect to a b-jet, charm and light jet p_T^{rel} templates from MC.

The electrons were reconstructed using the same procedure done in [118] by using PID of the different detectors with the following cuts:

- Electrons with $p_T > 0.5$ GeV/c were selected.
- The pseudorapidity of the electrons should be in the range $|\eta_{electrons}| < 0.9$.
- The electrons 2D impact parameter should be $DCA_{xy}^{electrons} \leq 2.4$ cm.
- The z-IP is in the range $DCA_{z}^{electrons} \leq 3.2$ cm.
- Number of track SPD hits > 1.
- Number of ITS clusters ≥ 2 and Number of TPC Clusters ≥ 80.
- Reject Kink daughters (*i.e.* secondary vertices not describing the required decay topology which can be e.g. $k^{\pm}$ decays).
- TOF PID: $|n\sigma_{TOF}| > 3$ for electrons with $p_T < 2.5$ GeV/c.
- TPC PID: $-0.5 < n\sigma_{TPC} < 3$ for all electrons.
- EMCal: The $0.8 < E/p < 1.2$ for EMCal electrons with $p_T > 6$ GeV/c.

The p_T^{rel} method requires high p_T electrons, but the MB trigger for the 2016 p–Pb data does not allow for a large number of high p_T electrons, and also no EMCal triggers were used in 2016 p–Pb datasets at $\sqrt{s_{\rm NN}} = 5.02$ TeV. So in order to have a high p_T electrons with acceptable statistics a combination of triggers was used: MB trigger from the 2016 data and the EMCal trigger (EMCEGA) and the TRD trigger from the 2013 p–Pb data as shown in Fig. D.2. As shown in this figure the p_T^{rel} distribution of the EMCal triggered electrons is much larger than that of the MB trigger (with large number of events).

The p_T^{rel} spectra of the electrons in jets were simulated using PYTHIA in order to extract the p_T^{rel} distribution of the different jet flavors to obtain the b-jet content of the sample. The tagging efficiency of a certain tagger is determined by measuring the fraction

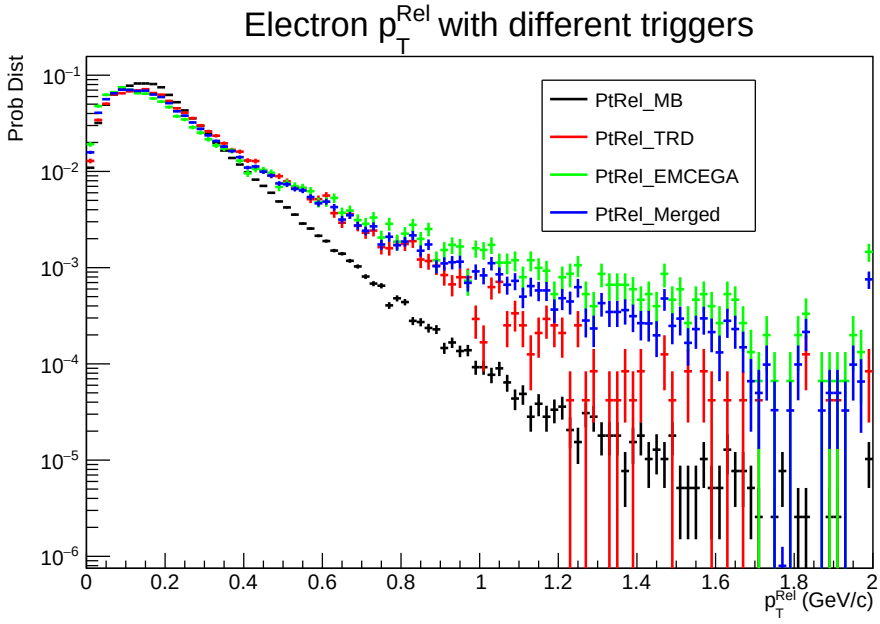

Fig. D.2 The combination of the p_T^{rel} distributions from the different triggers.

of electron jets that obeys the tagger requirements. The lepton jet sample was divided into two samples, a sample with jets satisfying the tagger requirement and another sample that represent the electron jets before applying the tagging algorithms. These samples will be called the "tagged" sample and the "untagged" (or pre-tagged) sample respectively.

In order to obtain a sample with high b-jet purity, the dijet event is required to have two reconstructed jets: an electron jet (jet containing an electron) and another jet satisfying the jet probability b-jet tagging algorithm. Simulated MC events, were used to reconstruct the p_T^{rel} distributions for jets containing electrons originating from the fragmentation of b, c, and light partons. Electrons in the light jets are mainly coming from the decay of charged pions, kaons or from photon conversion. In Fig. D.3, the p_T^{rel} distribution obtained from simulation for electrons in b-jets compared to that of the charm and light jets

By fitting p_T^{rel} templates for the b, c, and light parton jets derived from simulation to inclusive jet data with a binned maximum likelihood fit, the fraction of every jet flavor is obtained. The fitting procedure was executed separately for the "tagged" and the "untagged" electron jet samples.

The tagging efficiency of the b-jet is calculated through the equation:

$$\epsilon_b = \frac{f_b^{tag} \cdot N_{data}^{tag}}{f_b^{untag} \cdot N_{data}^{untag}} \tag{D.2}$$

where f_b^{tag} and f_b^{untag} are b-je fractions after and before applying the tagging algorithm and they are extracted from the fit to the data, and N_{data}^{untag} and N_{data}^{tag} are the total yields in data for the untagged and tagged electron jets respectively. The quantities $f_b^{tag} \times N_{data}^{tag}$ and $f_b^{untag} \times N_{data}^{untag}$ represent the amount of b-jet in data in the tagged and the untagged electron jet samples. For more details on the p_T^{rel} method you can refer to [177, 202].

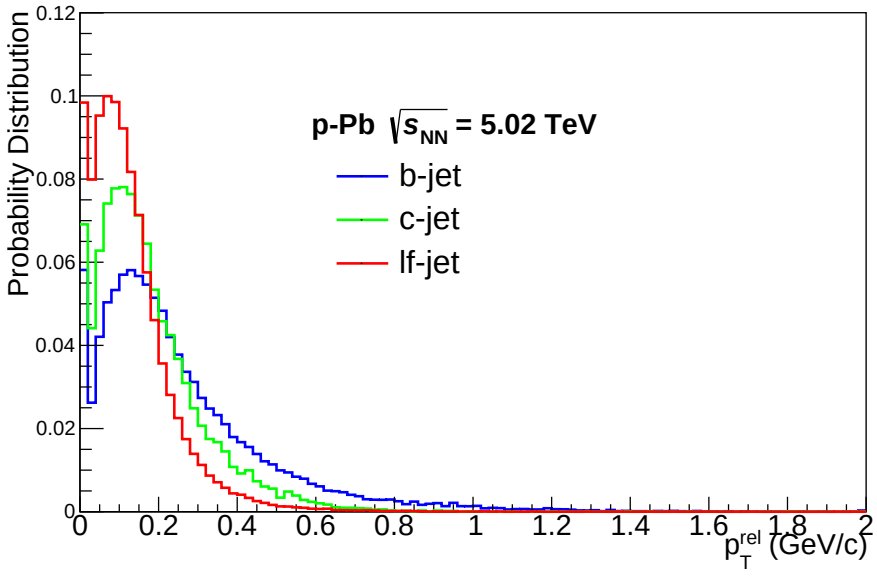

Fig. D.3 Comparison of p_T^{rel} distribution for the different jet flavors.

D.2 Reweighting the MC

This method is an alternative method to reproduce the impact parameter distribution, but it was not used in this thesis since it is time consuming.

PYTHIA fails to reproduce the different particles spectra. The inclusive jet spectra are not sensitive to the different particles composition, but the impact parameter distribution is a combination of the different primary and secondary particles impact parameters. So changing the particle composition will affect the shape of the impact parameter distribution, leading to a different b-jet efficiency and purity.

To reweight the particle spectra, all the impact parameter distributions are filled with a weighting factors. This weighting factor refers to the data/MC fraction of the particle linked with the track under study at a given p_T^{part}. It can be written as:

$$\omega = \frac{Yield^i_{Data}(p_T^{part})}{Yield^i_{MC}(p_T^{part})} \tag{D.3}$$

where ω is the weight, i corresponds to the particle species, and $Yield^i_{Data}(p_T^{part})$ and $Yield^i_{MC}(p_T^{part})$ are the particle yields in data and MC.

The MC reference spectra were selected from PYTHIA simulation in such a way that they match the selection criteria used in the different analyses of the published particle spectra.

The published data of each particles p_T spectra is parametrized using a convenient fitting function like Tsallis-Levi or Bylinkin-Rostovtsev fits, the purpose of the fitting was to allow for a common binning in p_T for all the reference spectra and the MC spectra.

Figure D.4 (left) shows the Tsallis-Levai fit to a certain published data reference. The right panel of Fig. D.4 shows the weighting factors as a function of p_T. These weighting factors are extracted from MC using equation D.3 and they are applied to correct the

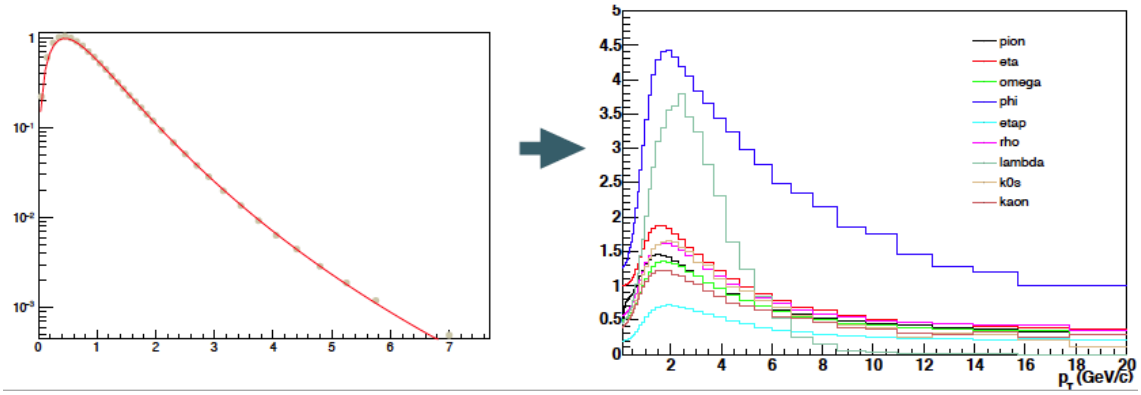

Fig. D.4 Tsallis-Levai fit for a certain published reference particle spectra (left) and the particle weight (right) (Figure adapted from Minjung Kim).

MC in bins of p_T. For the particles spectra that are not available (like B^0, $B^{\pm}$, ...), the particle spectra was simulated using FONNL [203] and then used as a reference.

The procedure if the reweighting is done during the MC analysis on an event-by-event basis, works as follows:

- Loop over all the track inside the jets.
- For each track, match it with its generator level particle through the MC label.
- Follow the chain of mothers until a certain particle species is found.
- Extract the weight of the particle as a function of the particle's p_T (see Fig. D.4).
- Reweight the histogram of the impact parameter distribution with the extracted weight.

This method was used in the b-jet analysis in pp collisions at $\sqrt{s} = 7$ TeV with ALICE by Linus Feldkamp. For more details on the rewighting refer to [204].

Appendix E

General formulas for the energy loss

The quark energy loss in the transverse field case, where $Q \neq 0$ and $q' \neq 0$ was found to be:

$$\Delta E \approx \mathcal{C}\alpha_s \frac{L}{\lambda_g} \frac{\mu_s^2}{q_\perp'^2} E \ . \tag{E.1}$$

where the factor $\mathcal{C}$ reads:

$$\begin{aligned} &-\frac{C_F}{6\pi N^2 qQ(q+Q)^5}\Big[3qQ(2N^2q(2q^2+2qQ+Q^2) \\ &+Q(2q^2+qQ+Q^2))\left(\log(\frac{q^2}{Q^2})\right) \\ &+(q+Q)(12N^2q^4+(5N^2+4)q^3Q+7(N^2-1)q^2Q^2 \\ &+(5N^2-2)qQ^3+3(N^2-1)Q^4)\Big] \end{aligned} \tag{E.2}$$

which is quadratic in μ.

The quark energy loss in the longitudinal field case, where $q_g \neq 0$ and $q_{q'} \neq 0$ was found to be:

$$\Delta E \approx \mathcal{C}'\alpha_s \frac{L}{\lambda_g} E \ . \tag{E.3}$$

where the factor $\mathcal{C}$ can be written as:

$$\begin{aligned}
&\frac{1}{540\pi\left(q_g^2-q_q^2\right)^5}(-q_g^6(145q_q^4(31L_g+3L_q)\\
&+3\mu^4(5L_{gq}+32)+10q_q^2\left(3\mu^2(30-19L_\mu)+172P\right)\\
&+320\mu^2Q)+q_g^4(5q_q^6(825L_g+161L_q)+3q_q^2(\mu^4(95L_{gq}+96)\\
&+296\mu^2Q)+2q_q^4\left(45\mu^2(21-13L_\mu)+1768P\right)+96\mu^4P)\\
&-q_g^2(5q_q^8(432L_g+61L_q)+3q_q^4(\mu^4(175L_{gq}+96)+656\mu^2Q)\\
&+10q_q^6\left(9\mu^2(2-19L_\mu)+292P\right)+192\mu^4Pq_q^2)\\
&+q_g^8\left(5q_q^2(451L_g+42L_q)+\mu^2(367-30L_\mu)+480P\right)\\
&-493L_gq_g^{10}-640\mu^2q_qq_g^7+1712\mu^2q_q^3q_g^5-3872\mu^2q_q^5q_g^3\\
&+2800\mu^2q_q^7q_g+q_q^4(q_q^2\left(3\mu^4(85L_{gq}+32)+1400\mu^2Q\right)\\
&+q_q^4\left(2160P-\mu^2(1080L_\mu+1177)\right)+493L_qq_q^6+96\mu^4P))
\end{aligned} \tag{E.4}$$

Where :

$$\begin{aligned}
&L_\mu=4\log(\mu)-\log\left(q_g^2+\mu^2\right)-\log\left(\mu^2+q_q^2\right)\\
&L_{gq}=\log\left(q_g^2+\mu^2\right)-\log\left(\mu^2+q_q^2\right)\\
&P=(A-B+C-D)\quad and\quad Q=(A-B-C+D)\\
&L_g=2\log\left(q_g\right)-\log\left(q_g^2+\mu^2\right)\\
&L_q=2\log\left(q_q\right)-\log\left(\mu^2+q_q^2\right)\\
&A=X\tan^{-1}\left(\frac{q_g^2}{X}\right)\quad\text{and}\quad B=X\tan^{-1}\left(\frac{q_qq_g}{X}\right)\\
&C=Y\tan^{-1}\left(\frac{q_qq_g}{Y}\right)\quad\text{and}\quad D=Y\tan^{-1}\left(\frac{q_q^2}{Y}\right)\\
&Y=\sqrt{\mu^2q_q^2-q_g^2\left(\mu^2+q_q^2\right)}\quad\text{and}\quad X=\sqrt{q_g^2\left(\mu^2-q_q^2\right)-\mu^2q_q^2}
\end{aligned}$$

References

[1] C. Shen and U. Heinz, "The road to precision: Extraction of the specific shear viscosity of the quark-gluon plasma," *Nucl. Phys. News* **25** no. 2, (2015) 6–11, arXiv:1507.01558 [nucl-th].

[2] J. E. Huth *et al.*, "Toward a standardization of jet definitions," in *1990 DPF Summer Study on High-energy Physics: Research Directions for the Decade (Snowmass 90) Snowmass, Colorado, June 25-July 13, 1990*, pp. 0134–136. 1990. http://lss.fnal.gov/cgi-bin/find_paper.pl?conf-90-249.

[3] M. Gyulassy and M. Plumer, "Jet Quenching in Dense Matter," *Phys. Lett.* **B243** (1990) 432–438.

[4] G.-Y. Qin and X.-N. Wang, "Jet quenching in high-energy heavy-ion collisions," *Int. J. Mod. Phys.* **E24** no. 11, (2015) 1530014, arXiv:1511.00790 [hep-ph]. [,309(2016)].

[5] S. D. Ellis and D. E. Soper, "Successive combination jet algorithm for hadron collisions," *Phys. Rev.* **D48** (1993) 3160–3166, arXiv:hep-ph/9305266 [hep-ph].

[6] M. Cacciari, S. Frixione, N. Houdeau, M. L. Mangano, P. Nason, and G. Ridolfi, "Theoretical predictions for charm and bottom production at the LHC," *JHEP* **10** (2012) 137, arXiv:1205.6344 [hep-ph].

[7] M. Cacciari, S. Frixione, M. L. Mangano, P. Nason, and G. Ridolfi, "QCD analysis of first b cross-section data at 1.96-TeV," *JHEP* **07** (2004) 033, arXiv:hep-ph/0312132 [hep-ph].

[8] B. A. Kniehl, G. Kramer, I. Schienbein, and H. Spiesberger, "Collinear subtractions in hadroproduction of heavy quarks," *Eur. Phys. J.* **C41** (2005) 199–212, arXiv:hep-ph/0502194 [hep-ph].

[9] B. A. Kniehl, G. Kramer, I. Schienbein, and H. Spiesberger, "Inclusive D*+- production in p anti-p collisions with massive charm quarks," *Phys. Rev.* **D71** (2005) 014018, arXiv:hep-ph/0410289 [hep-ph].

[10] S. Frixione, P. Nason, and G. Ridolfi, "A Positive-weight next-to-leading-order Monte Carlo for heavy flavour hadroproduction," *JHEP* **09** (2007) 126, arXiv:0707.3088 [hep-ph].

[11] J. Huang, Z.-B. Kang, and I. Vitev, "Inclusive b-jet production in heavy ion collisions at the LHC," *Phys. Lett.* **B726** (2013) 251–256, arXiv:1306.0909 [hep-ph].

[12] **Particle Data Group** Collaboration, J. Beringer *et al.*, "Review of particle physics," *Phys. Rev. D* **86** (Jul, 2012) 010001. https://link.aps.org/doi/10.1103/PhysRevD.86.010001.

[13] **L3** Collaboration, M. Acciarri *et al.*, "Measurement of mass and width of the W boson at LEP," *Phys. Lett.* **B454** (1999) 386–398, arXiv:hep-ex/9909010 [hep-ex].

[14] **OPAL, DELPHI, L3, ALEPH, Working Group on LEP Energy** Collaboration, L. Arnaudon *et al.*, "Measurement of the mass of the Z boson and the energy calibration of LEP," *Phys. Lett.* **B307** (1993) 187–193.

[15] K. C. Wang, "A suggestion on the detection of the neutrino," *Phys. Rev.* **61** (Jan, 1942) 97–97. https://link.aps.org/doi/10.1103/PhysRev.61.97.

[16] **Super-Kamiokande Collaboration** Collaboration, Y. Fukuda, "Evidence for oscillation of atmospheric neutrinos," *Phys. Rev. Lett.* **81** (Aug, 1998) 1562–1567. https://link.aps.org/doi/10.1103/PhysRevLett.81.1562.

[17] **SNO** Collaboration, G. A. McGregor, "First results from the Sudbury Neutrino Observatory," in *Proceedings, 37th Rencontres de Moriond on Electroweak Interactions and Unified Theories: Les Arcs, France, March 9-16, 2002*, pp. 249–256. 2002. arXiv:nucl-ex/0205006 [nucl-ex]. https://inspirehep.net/record/586804/files/Pages_from_C02-03-09_249.pdf.

[18] **ATLAS** Collaboration, G. Aad *et al.*, "Observation of a new particle in the search for the Standard Model Higgs boson with the ATLAS detector at the LHC," *Phys. Lett.* **B716** (2012) 1–29, arXiv:1207.7214 [hep-ex].

[19] **CMS** Collaboration, S. Chatrchyan *et al.*, "Observation of a new boson at a mass of 125 GeV with the CMS experiment at the LHC," *Phys. Lett.* **B716** (2012) 30–61, arXiv:1207.7235 [hep-ex].

[20] J. Rafelski, "Connecting QGP-Heavy Ion Physics to the Early Universe," arXiv:1306.2471 [astro-ph.CO]. [Nucl. Phys. Proc. Suppl.243-244,155(2013)].

[21] S. Borsanyi, "Thermodynamics of the QCD transition from lattice," *Nucl. Phys.* **A904-905** (2013) 270c–277c, arXiv:1210.6901 [hep-lat].

[22] R. S. Bhalerao, "Relativistic heavy-ion collisions," in *Proceedings, 1st Asia-Europe-Pacific School of High-Energy Physics (AEPSHEP): Fukuoka, Japan, October 14-27, 2012*, pp. 219–239. 2014. arXiv:1404.3294 [nucl-th]. https://inspirehep.net/record/1290394/files/arXiv:1404.3294.pdf.

[23] J. D. Bjorken, "Highly relativistic nucleus-nucleus collisions: The central rapidity region," *Phys. Rev. D* **27** (Jan, 1983) 140–151. https://link.aps.org/doi/10.1103/PhysRevD.27.140.

[24] K. Kovarik *et al.*, "nCTEQ15 - Global analysis of nuclear parton distributions with uncertainties in the CTEQ framework," *Phys. Rev.* **D93** no. 8, (2016) 085037, arXiv:1509.00792 [hep-ph].

[25] J. W. Cronin, H. J. Frisch, M. J. Shochet, J. P. Boymond, P. A. Piroué, and R. L. Sumner, "Production of hadrons at large transverse momentum at 200, 300, and 400 gev," *Phys. Rev. D* **11** (Jun, 1975) 3105–3123. https://link.aps.org/doi/10.1103/PhysRevD.11.3105.

[26] R. Haake, *Measurement of charged jets in p-Pb collisions at 5.02 TeV with the ALICE detector* . PhD thesis, Munster University, 2015. https://www.uni-muenster.de/imperia/md/content/physik_kp/agwessels/thesis_db/ag_wessels/diss-haak-15.pdf.

[27] M. Arneodo, "Nuclear effects in structure functions," *Physics Reports* **240** no. 5, (1994) 301 – 393. http://www.sciencedirect.com/science/article/pii/0370157394900485.

[28] J. Aubert *et al.*, "The ratio of the nucleon structure functions f2n for iron and deuterium," *Physics Letters B* **123** no. 3, (1983) 275 – 278. http://www.sciencedirect.com/science/article/pii/0370269383904379.

[29] K. Saito and T. Uchiyama, "Effect of the fermi motion on nuclear structure functions and the emc effect," *Zeitschrift für Physik A Atoms and Nuclei* **322** no. 2, (Jun, 1985) 299–307. https://doi.org/10.1007/BF01411895.

[30] G. P. Salam, "Towards Jetography," *Eur. Phys. J.* **C67** (2010) 637–686, `arXiv:0906.1833 [hep-ph]`.

[31] M. Cacciari, G. P. Salam, and G. Soyez, "The Anti-k(t) jet clustering algorithm," *JHEP* **04** (2008) 063, `arXiv:0802.1189 [hep-ph]`.

[32] M. Cacciari, G. P. Salam, and G. Soyez, "FastJet User Manual," *Eur. Phys. J.* **C72** (2012) 1896, `arXiv:1111.6097 [hep-ph]`.

[33] D. d. Enterria and B. Betz, *High-pT Hadron Suppression and Jet Quenching*, pp. 285–339. Springer Berlin Heidelberg, Berlin, Heidelberg, 2010. https://doi.org/10.1007/978-3-642-02286-9_9.

[34] J. D. Bjorken, "Energy Loss of Energetic Partons in Quark - Gluon Plasma: Possible Extinction of High p(t) Jets in Hadron - Hadron Collisions,".

[35] E. Braaten and M. H. Thoma, "Energy loss of a heavy quark in the quark-gluon plasma," *Phys. Rev. D* **44** (Nov, 1991) R2625–R2630. https://link.aps.org/doi/10.1103/PhysRevD.44.R2625.

[36] A. Peshier, "Qcd collisional energy loss reexamined," *Phys. Rev. Lett.* **97** (Nov, 2006) 212301. https://link.aps.org/doi/10.1103/PhysRevLett.97.212301.

[37] S. Peigné and A. Peshier, "Collisional energy loss of a fast heavy quark in a quark-gluon plasma," *Phys. Rev. D* **77** (Jun, 2008) 114017. https://link.aps.org/doi/10.1103/PhysRevD.77.114017.

[38] B. G. Zakharov, "Parton energy loss in an expanding quark-gluon plasma: Radiative versus collisional," *JETP Lett.* **86** (2007) 444–450, `arXiv:0708.0816 [hep-ph]`.

[39] D. d'Enterria, "Jet quenching," *Landolt-Bornstein* **23** (2010) 471, `arXiv:0902.2011 [nucl-ex]`.

References

[40] A. B. Migdal, "Bremsstrahlung and pair production in condensed media at high energies," *Phys. Rev.* **103** (Sep, 1956) 1811–1820. https://link.aps.org/doi/10.1103/PhysRev.103.1811.

[41] Y. L. Dokshitzer, V. A. Khoze, and S. I. Troian, "On specific QCD properties of heavy quark fragmentation ('dead cone')," *J. Phys.* **G17** (1991) 1602–1604.

[42] Y. L. Dokshitzer and D. E. Kharzeev, "Heavy quark colorimetry of QCD matter," *Phys. Lett.* **B519** (2001) 199–206, arXiv:hep-ph/0106202 [hep-ph].

[43] R. Abir, C. Greiner, M. Martinez, M. G. Mustafa, and J. Uphoff, "Soft gluon emission off a heavy quark revisited," *Phys. Rev.* **D85** (2012) 054012, arXiv:1109.5539 [hep-ph].

[44] T. Bhattacharyya, S. Mazumder, and R. Abir, "Soft Gluon Radiation off Heavy Quarks beyond Eikonal Approximation," *Adv. High Energy Phys.* **2016** (2016) 1298986, arXiv:1307.6931 [hep-ph].

[45] B. G. Zakharov, "Fully quantum treatment of the Landau-Pomeranchuk-Migdal effect in QED and QCD," *JETP Lett.* **63** (1996) 952–957, arXiv:hep-ph/9607440 [hep-ph].

[46] C. A. Salgado and U. A. Wiedemann, "Calculating quenching weights," *Phys. Rev.* **D68** (2003) 014008, arXiv:hep-ph/0302184 [hep-ph].

[47] R. Baier, Y. L. Dokshitzer, A. H. Mueller, S. Peigne, and D. Schiff, "Radiative energy loss of high-energy quarks and gluons in a finite volume quark - gluon plasma," *Nucl. Phys.* **B483** (1997) 291–320, arXiv:hep-ph/9607355 [hep-ph].

[48] R. Baier, Y. Dokshitzer, A. Mueller, and D. Schiff, "Medium-induced radiative energy loss; equivalence between the bdmps and zakharov formalisms," *Nuclear Physics B* **531** no. 1, (1998) 403 – 425. http://www.sciencedirect.com/science/article/pii/S055032139800546X.

[49] M. Gyulassy, P. Levai, and I. Vitev, "Jet quenching in thin quark gluon plasmas. 1. Formalism," *Nucl. Phys.* **B571** (2000) 197–233, arXiv:hep-ph/9907461 [hep-ph].

[50] M. Gyulassy, P. Levai, and I. Vitev, "Reaction operator approach to nonAbelian energy loss," *Nucl. Phys.* **B594** (2001) 371–419, arXiv:nucl-th/0006010 [nucl-th].

[51] M. Gyulassy, P. Levai, and I. Vitev, "Jet tomography of Au+Au reactions including multigluon fluctuations," *Phys. Lett.* **B538** (2002) 282–288, arXiv:nucl-th/0112071 [nucl-th].

[52] S. Wicks, W. Horowitz, M. Djordjevic, and M. Gyulassy, "Elastic, inelastic, and path length fluctuations in jet tomography," *Nucl. Phys.* **A784** (2007) 426–442, arXiv:nucl-th/0512076 [nucl-th].

[53] U. A. Wiedemann, "Gluon radiation off hard quarks in a nuclear environment: Opacity expansion," *Nucl. Phys.* **B588** (2000) 303–344, arXiv:hep-ph/0005129 [hep-ph].

[54] B.-W. Zhang and X.-N. Wang, "Multiple parton scattering in nuclei: Beyond helicity amplitude approximation," *Nucl. Phys.* **A720** (2003) 429–451, arXiv:hep-ph/0301195 [hep-ph].

[55] X.-N. Wang and X.-f. Guo, "Multiple parton scattering in nuclei: Parton energy loss," *Nucl. Phys.* **A696** (2001) 788–832, arXiv:hep-ph/0102230 [hep-ph].

[56] A. Majumder, E. Wang, and X.-N. Wang, "Modified dihadron fragmentation functions in hot and nuclear matter," *Phys. Rev. Lett.* **99** (Oct, 2007) 152301. https://link.aps.org/doi/10.1103/PhysRevLett.99.152301.

[57] A. Majumder, R. J. Fries, and B. Müller, "Photon bremsstrahlung and diffusive broadening of a hard jet," *Phys. Rev. C* **77** (Jun, 2008) 065209. https://link.aps.org/doi/10.1103/PhysRevC.77.065209.

[58] A. Majumder, "The In-medium scale evolution in jet modification," arXiv:0901.4516 [nucl-th].

[59] X. Guo and X.-N. Wang, "Multiple scattering, parton energy loss, and modified fragmentation functions in deeply inelastic *eA* scattering," *Phys. Rev. Lett.* **85** (Oct, 2000) 3591–3594. https://link.aps.org/doi/10.1103/PhysRevLett.85.3591.

[60] P. B. Arnold, G. D. Moore, and L. G. Yaffe, "Photon emission from quark gluon plasma: Complete leading order results," *JHEP* **12** (2001) 009, arXiv:hep-ph/0111107 [hep-ph].

[61] P. B. Arnold, G. D. Moore, and L. G. Yaffe, "Photon and gluon emission in relativistic plasmas," *JHEP* **06** (2002) 030, arXiv:hep-ph/0204343 [hep-ph].

[62] F. Arleo, "(Medium-modified) Fragmentation Functions," *Eur. Phys. J.* **C61** (2009) 603–627, arXiv:0810.1193 [hep-ph].

[63] N. Armesto, C. A. Salgado, and U. A. Wiedemann, "Medium induced gluon radiation off massive quarks fills the dead cone," *Phys. Rev.* **D69** (2004) 114003, arXiv:hep-ph/0312106 [hep-ph].

[64] U. A. Wiedemann, "Gluon radiation off hard quarks in a nuclear environment: opacity expansion," *Nuclear Physics B* **588** no. 1, (2000) 303 – 344. http://www.sciencedirect.com/science/article/pii/S0550321300004570.

[65] A. Dainese, C. Loizides, and G. Paic, "Leading-particle suppression in high energy nucleus-nucleus collisions," *Eur. Phys. J.* **C38** (2005) 461–474, arXiv:hep-ph/0406201 [hep-ph].

[66] C. Loizides, "High transverse momentum suppression and surface effects in cu+cu and au+au collisions within the pqm model," *The European Physical Journal C* **49** no. 1, (Jan, 2007) 339–345. https://doi.org/10.1140/epjc/s10052-006-0059-8.

[67] I. Vitev, "Jet quenching in relativistic heavy ion collisions," *Journal of Physics: Conference Series* **50** no. 1, (2006) 119. http://stacks.iop.org/1742-6596/50/i=1/a=014.

[68] A. Majumder and X.-N. Wang, "Modification of the dihadron fragmentation function in nuclear matter," arXiv:0806.2653 [nucl-th].

[69] P. B. Arnold, G. D. Moore, and L. G. Yaffe, "Photon emission from ultrarelativistic plasmas," *JHEP* **11** (2001) 057, arXiv:hep-ph/0109064 [hep-ph].

[70] P. B. Arnold, G. D. Moore, and L. G. Yaffe, "Transport coefficients in high temperature gauge theories. 1. Leading log results," *JHEP* **11** (2000) 001, arXiv:hep-ph/0010177 [hep-ph].

[71] S. Jeon and G. D. Moore, "Energy loss of leading partons in a thermal QCD medium," *Phys. Rev.* **C71** (2005) 034901, arXiv:hep-ph/0309332 [hep-ph].

[72] **PHENIX** Collaboration, A. Adare *et al.*, "Suppression pattern of neutral pions at high transverse momentum in Au + Au collisions at s(NN)**(1/2) = 200-GeV and constraints on medium transport coefficients," *Phys. Rev. Lett.* **101** (2008) 232301, arXiv:0801.4020 [nucl-ex].

[73] S. A. Bass, C. Gale, A. Majumder, C. Nonaka, G. Y. Qin, T. Renk, and J. Ruppert, "Systematic Comparison of Jet Energy-Loss Schemes in a 3D hydrodynamic medium," *J. Phys.* **G35** (2008) 104064, arXiv:0805.3271 [nucl-th].

[74] J. C. Collins, D. E. Soper, and G. Sterman, "Factorization for short distance hadron-hadron scattering," *Nuclear Physics B* **261** (1985) 104 – 142. http://www.sciencedirect.com/science/article/pii/0550321385905656.

[75] M. L. Miller, K. Reygers, S. J. Sanders, and P. Steinberg, "Glauber modeling in high energy nuclear collisions," *Ann. Rev. Nucl. Part. Sci.* **57** (2007) 205–243, arXiv:nucl-ex/0701025 [nucl-ex].

[76] **ALICE** Collaboration, B. Abelev *et al.*, "Centrality Dependence of Charged Particle Production at Large Transverse Momentum in Pb–Pb Collisions at $\sqrt{s_{\rm NN}} = 2.76$ TeV," *Phys. Lett.* **B720** (2013) 52–62, arXiv:1208.2711 [hep-ex].

[77] **CMS** Collaboration, V. Khachatryan *et al.*, "Measurement of inclusive jet cross sections in *pp* and PbPb collisions at $\sqrt{s_{NN}} = 2.76$ TeV," *Phys. Rev.* **C96** no. 1, (2017) 015202, arXiv:1609.05383 [nucl-ex].

[78] **PHENIX** Collaboration, A. Adare *et al.*, "Measurement of high-p(T) single electrons from heavy-flavor decays in p+p collisions at s**(1/2) = 200-GeV," *Phys. Rev. Lett.* **97** (2006) 252002, arXiv:hep-ex/0609010 [hep-ex].

[79] G. Aad *et al.*, "Measurements of the electron and muon inclusive cross-sections in proton–proton collisions at s=7 tev with the atlas detector," *Physics Letters B* **707** no. 5, (2012) 438 – 458. http://www.sciencedirect.com/science/article/pii/S037026931101522X.

[80] **ALICE** Collaboration, B. B. Abelev *et al.*, "Measurement of electrons from semileptonic heavy-flavor hadron decays in *pp* collisions at $\sqrt{s} = 2.76$ TeV," *Phys. Rev.* **D91** no. 1, (2015) 012001, arXiv:1405.4117 [nucl-ex].

[81] **ALICE** Collaboration, B. Abelev *et al.*, "Production of muons from heavy flavour decays at forward rapidity in pp and Pb-Pb collisions at $\sqrt{s_{NN}} = 2.76$ TeV," *Phys. Rev. Lett.* **109** (2012) 112301, arXiv:1205.6443 [hep-ex].

[82] **ALICE Collaboration** Collaboration, B. Abelev *et al.*, "Measurement of electrons from semileptonic heavy-flavor hadron decays in *pp* collisions at $\sqrt{s}$=7 TeV," *Phys. Rev. D* **86** (Dec, 2012) 112007. https://link.aps.org/doi/10.1103/PhysRevD.86.112007.

[83] R. Maciula and A. Szczurek, "Open charm production at the LHC - k_t-factorization approach," *Phys. Rev.* **D87** no. 9, (2013) 094022, arXiv:1301.3033 [hep-ph].

[84] **ALICE** Collaboration, B. Abelev *et al.*, "Measurement of electrons from beauty hadron decays in *pp* collisions at $\sqrt{s} = 7$ TeV," *Phys. Lett.* **B721** (2013) 13–23, arXiv:1208.1902 [hep-ex]. [Erratum: Phys. Lett.B763,507(2016)].

[85] **ALICE** Collaboration, B. B. Abelev *et al.*, "Beauty production in pp collisions at $\sqrt{s} = 2.76$ TeV measured via semi-electronic decays," *Phys. Lett.* **B738** (2014) 97–108, arXiv:1405.4144 [nucl-ex].

[86] **STAR** Collaboration, L. Adamczyk *et al.*, "Measurements of D^0 and D^* Production in $p + p$ Collisions at $\sqrt{s} = 200$ GeV," *Phys. Rev.* **D86** (2012) 072013, arXiv:1204.4244 [nucl-ex].

[87] B. Reisert, "Charm production studies at cdf," *Nuclear Physics B - Proceedings Supplements* **170** (2007) 243 – 247. http://www.sciencedirect.com/science/article/pii/S0920563207003738. Proceedings of the 11th International Conference on B-Physics at Hadron Machines.

[88] **CDF** Collaboration, D. Acosta *et al.*, "Measurement of prompt charm meson production cross sections in $p\bar{p}$ collisions at $\sqrt{s} = 1.96$ TeV," *Phys. Rev. Lett.* **91** (2003) 241804, arXiv:hep-ex/0307080 [hep-ex].

[89] **ALICE** Collaboration, B. Abelev *et al.*, "Measurement of charm production at central rapidity in proton-proton collisions at $\sqrt{s} = 2.76$ TeV," *JHEP* **07** (2012) 191, arXiv:1205.4007 [hep-ex].

[90] **ALICE** Collaboration, B. Abelev *et al.*, "Measurement of charm production at central rapidity in proton-proton collisions at $\sqrt{s} = 7$ TeV," *JHEP* **01** (2012) 128, arXiv:1111.1553 [hep-ex].

[91] **ALICE** Collaboration, B. Abelev *et al.*, "D_s^+ meson production at central rapidity in proton–proton collisions at $\sqrt{s} = 7$ TeV," *Phys. Lett.* **B718** (2012) 279–294, arXiv:1208.1948 [hep-ex].

[92] **LHCb** Collaboration, R. Aaij *et al.*, "Prompt charm production in pp collisions at sqrt(s)=7 TeV," *Nucl. Phys.* **B871** (2013) 1–20, arXiv:1302.2864 [hep-ex].

[93] **ALICE** Collaboration, S. Acharya *et al.*, "Measurement of D-meson production at mid-rapidity in pp collisions at $\sqrt{s} = 7$ TeV," *Eur. Phys. J.* **C77** no. 8, (2017) 550, arXiv:1702.00766 [hep-ex].

[94] **E791** Collaboration, E. M. Aitala *et al.*, "Mass splitting and production of sigma(c)0 and sigma(c)++ measured in 500-GeV pi- n interactions," *Phys. Lett.* **B379** (1996) 292–298, arXiv:hep-ex/9604007 [hep-ex].

[95] **FOCUS** Collaboration, J. M. Link *et al.*, "Measurement of natural widths of Sigma0(c) and Sigma++(c) baryons," *Phys. Lett.* **B525** (2002) 205–210, arXiv:hep-ex/0111027 [hep-ex].

[96] **CLEO** Collaboration, M. Artuso *et al.*, "Measurement of the masses and widths of the Sigma++(c) and Sigma0(c) charmed baryons," *Phys. Rev.* **D65** (2002) 071101, arXiv:hep-ex/0110071 [hep-ex].

[97] **CDF** Collaboration, T. Aaltonen *et al.*, "Measurements of the properties of $\Lambda_c(2595)$, $\Lambda_c(2625)$, $\Sigma_c(2455)$, and $\Sigma_c(2520)$ baryons," *Phys. Rev.* **D84** (2011) 012003, arXiv:1105.5995 [hep-ex].

[98] **ALICE** Collaboration, S. Acharya *et al.*, "Λ_c^+ production in pp collisions at $\sqrt{s} = 7$ TeV and in p-Pb collisions at $\sqrt{s_{\rm NN}} = 5.02$ TeV," *JHEP* **04** (2018) 108, arXiv:1712.09581 [nucl-ex].

[99] **ALICE** Collaboration, S. Acharya *et al.*, "First measurement of $\Xi_{\rm c}^0$ production in pp collisions at $\sqrt{\rm s} = 7$ TeV," *Phys. Lett.* **B781** (2018) 8–19, arXiv:1712.04242 [hep-ex].

[100] **CMS** Collaboration, V. Khachatryan *et al.*, "Measurement of the B^+ Production Cross Section in pp Collisions at $\sqrt{s} = 7$ TeV," *Phys. Rev. Lett.* **106** (2011) 112001, arXiv:1101.0131 [hep-ex].

[101] **ATLAS** Collaboration, G. Aad *et al.*, "Measurement of the differential cross-section of B^+ meson production in pp collisions at $\sqrt{s} = 7$ TeV at ATLAS," *JHEP* **10** (2013) 042, arXiv:1307.0126 [hep-ex].

[102] **LHCb** Collaboration, R. Aaij *et al.*, "Measurement of b-hadron masses," *Phys. Lett.* **B708** (2012) 241–248, arXiv:1112.4896 [hep-ex].

[103] **LHCb** Collaboration, R. Aaij *et al.*, "Measurement of B meson production cross-sections in proton-proton collisions at $\sqrt{s} = 7$ TeV," *JHEP* **08** (2013) 117, arXiv:1306.3663 [hep-ex].

[104] **LHCb** Collaboration, R. Aaij *et al.*, "Measurement of the $B^\pm$ production cross-section in pp collisions at $\sqrt{s} = 7$ TeV," *JHEP* **04** (2012) 093, arXiv:1202.4812 [hep-ex].

[105] **CMS** Collaboration, S. Chatrchyan *et al.*, "Measurement of the Strange B Meson Production Cross Section with J/Psi ϕ Decays in pp Collisions at $\sqrt{s} = 7$ TeV," *Phys. Rev.* **D84** (2011) 052008, arXiv:1106.4048 [hep-ex].

[106] **D0** Collaboration, V. M. Abazov *et al.*, "Search for the $X(4140)$ state in $B^+ \to {\rm J}_{\psi,\phi} K^+$ decays with the D0 Detector," *Phys. Rev.* **D89** no. 1, (2014) 012004, arXiv:1309.6580 [hep-ex].

[107] **CMS** Collaboration, S. Chatrchyan *et al.*, "Measurement of the Λ_b cross section and the $_{\bar{\Lambda}_b}$ to Λ_b ratio with $J/\Psi\Lambda$ decays in pp collisions at $\sqrt{s} = 7$ TeV," *Phys. Lett.* **B714** (2012) 136–157, arXiv:1205.0594 [hep-ex].

[108] **CMS** Collaboration, S. Chatrchyan *et al.*, "Inclusive b-jet production in pp collisions at $\sqrt{s} = 7$ TeV," *JHEP* **04** (2012) 084, arXiv:1202.4617 [hep-ex].

[109] **ATLAS** Collaboration, G. Aad *et al.*, "Measurement of the inclusive and dijet cross-sections of b^- jets in pp collisions at $\sqrt{s} = 7$ TeV with the ATLAS detector," *Eur. Phys. J.* **C71** (2011) 1846, arXiv:1109.6833 [hep-ex].

[110] P. Nason, "A New method for combining NLO QCD with shower Monte Carlo algorithms," *JHEP* **11** (2004) 040, arXiv:hep-ph/0409146 [hep-ph].

[111] T. Sjostrand, S. Mrenna, and P. Z. Skands, "PYTHIA 6.4 Physics and Manual," *JHEP* **05** (2006) 026, arXiv:hep-ph/0603175 [hep-ph].

[112] S. Frixione, P. Nason, and B. R. Webber, "Matching NLO QCD and parton showers in heavy flavor production," *JHEP* **08** (2003) 007, arXiv:hep-ph/0305252 [hep-ph].

[113] S. Frixione and B. R. Webber, "Matching NLO QCD computations and parton shower simulations," *JHEP* **06** (2002) 029, arXiv:hep-ph/0204244 [hep-ph].

[114] G. Corcella, I. G. Knowles, G. Marchesini, S. Moretti, K. Odagiri, P. Richardson, M. H. Seymour, and B. R. Webber, "HERWIG 6: An Event generator for hadron emission reactions with interfering gluons (including supersymmetric processes)," *JHEP* **01** (2001) 010, arXiv:hep-ph/0011363 [hep-ph].

[115] **PHENIX** Collaboration, A. Adare *et al.*, "Cold-nuclear-matter effects on heavy-quark production in d+Au collisions at $\sqrt{s_{NN}} = 200$ GeV," *Phys. Rev. Lett.* **109** no. 24, (2012) 242301, arXiv:1208.1293 [nucl-ex].

[116] **PHENIX** Collaboration, A. Adare *et al.*, "Cold-Nuclear-Matter Effects on Heavy-Quark Production at Forward and Backward Rapidity in d+Au Collisions at $\sqrt{s_{NN}} = 200$ GeV," *Phys. Rev. Lett.* **112** no. 25, (2014) 252301, arXiv:1310.1005 [nucl-ex].

[117] **ALICE** Collaboration, S. Acharya *et al.*, "Production of muons from heavy-flavour hadron decays in p-Pb collisions at $\sqrt{s_{\rm NN}} = \mathbf{5.02}$ TeV," *Phys. Lett.* **B770** (2017) 459–472, arXiv:1702.01479 [nucl-ex].

[118] **ALICE** Collaboration, J. Adam *et al.*, "Measurement of electrons from heavy-flavour hadron decays in p-Pb collisions at $\sqrt{s_{\rm NN}} = 5.02$ TeV," *Phys. Lett.* **B754** (2016) 81–93, arXiv:1509.07491 [nucl-ex].

[119] **ALICE** Collaboration, J. Adam *et al.*, "Measurement of electrons from beauty-hadron decays in p-Pb collisions at $\sqrt{s_{\rm NN}} = 5.02$ TeV and Pb-Pb collisions at $\sqrt{s_{\rm NN}} = 2.76$ TeV," *JHEP* **07** (2017) 052, arXiv:1609.03898 [nucl-ex].

[120] **ALICE** Collaboration, J. Adam *et al.*, "D-meson production in p-Pb collisions at $\sqrt{s_{\rm NN}}$ =5.02 TeV and in pp collisions at $\sqrt{s}$ =7 TeV," *Phys. Rev.* **C94** no. 5, (2016) 054908, arXiv:1605.07569 [nucl-ex].

[121] **ALICE** Collaboration, B. B. Abelev *et al.*, "Measurement of prompt D-meson production in $p - Pb$ collisions at $\sqrt{s_{NN}} = 5.02$ TeV," *Phys. Rev. Lett.* **113** no. 23, (2014) 232301, arXiv:1405.3452 [nucl-ex].

[122] **ALICE** Collaboration, J. Adam *et al.*, "Measurement of D-meson production versus multiplicity in p-Pb collisions at $\sqrt{\rm s_{NN}} = 5.02$ TeV," *JHEP* **08** (2016) 078, arXiv:1602.07240 [nucl-ex].

[123] **CMS** Collaboration, A. M. Sirunyan *et al.*, "Measurements of the charm jet cross section and nuclear modification factor in pPb collisions at $\sqrt{s_{NN}} = 5.02$ TeV," *Phys. Lett.* **B772** (2017) 306–329, arXiv:1612.08972 [nucl-ex].

[124] **LHCb** Collaboration, R. Aaij *et al.*, "Study of J/ψ production and cold nuclear matter effects in pPb collisions at $\sqrt{s_{NN}} = 5$ TeV," *JHEP* **02** (2014) 072, arXiv:1308.6729 [nucl-ex].

[125] **CMS** Collaboration, V. Khachatryan *et al.*, "Study of B Meson Production in p+Pb Collisions at $\sqrt{s_{NN}} = 5.02$ TeV Using Exclusive Hadronic Decays," *Phys. Rev. Lett.* **116** no. 3, (2016) 032301, arXiv:1508.06678 [nucl-ex].

[126] G. M. Innocenti, "B-meson reconstruction performance and spectra in pp and ppb collisions in cms," *Nuclear Physics A* **931** (2014) 1184 – 1188. http://www.sciencedirect.com/science/article/pii/S0375947414004540. QUARK MATTER 2014.

[127] **CMS** Collaboration, V. Khachatryan *et al.*, "Transverse momentum spectra of inclusive b jets in pPb collisions at $\sqrt{s_{NN}} = 5.02$ TeV," *Phys. Lett.* **B754** (2016) 59, arXiv:1510.03373 [nucl-ex].

[128] **STAR** Collaboration, B. I. Abelev *et al.*, "Transverse momentum and centrality dependence of high-p_T non-photonic electron suppression in Au+Au collisions at $\sqrt{s_{NN}} = 200\,\mathrm{GeV}$," *Phys. Rev. Lett.* **98** (2007) 192301, arXiv:nucl-ex/0607012 [nucl-ex]. [Erratum: Phys. Rev. Lett.106,159902(2011)].

[129] **PHENIX** Collaboration, A. Adare *et al.*, "Heavy Quark Production in $p + p$ and Energy Loss and Flow of Heavy Quarks in Au+Au Collisions at $\sqrt{s_{NN}} = 200$ GeV," *Phys. Rev.* **C84** (2011) 044905, arXiv:1005.1627 [nucl-ex].

[130] **PHENIX** Collaboration, A. Adare *et al.*, "Energy Loss and Flow of Heavy Quarks in Au+Au Collisions at s(NN)**(1/2) = 200-GeV," *Phys. Rev. Lett.* **98** (2007) 172301, arXiv:nucl-ex/0611018 [nucl-ex].

[131] **PHENIX** Collaboration, S. S. Adler *et al.*, "Nuclear modification of electron spectra and implications for heavy quark energy loss in Au+Au collisions at s(NN)**(1/2) - 200-GeV," *Phys. Rev. Lett.* **96** (2006) 032301, arXiv:nucl-ex/0510047 [nucl-ex].

[132] **ALICE** Collaboration, J. Adam *et al.*, "Measurement of the production of high-p_{T} electrons from heavy-flavour hadron decays in Pb-Pb collisions at $\sqrt{s_{\mathrm{NN}}} = 2.76$ TeV," *Phys. Lett.* **B771** (2017) 467–481, arXiv:1609.07104 [nucl-ex].

[133] S. Sakai, "Heavy-flavour decay electrons raa in pbpb at 5.02 tev." Alice public figures., July, 2017. http://aliceinfo.cern.ch/Figure/node/10196.

[134] **ALICE** Collaboration, J. Adam *et al.*, "Elliptic flow of muons from heavy-flavour hadron decays at forward rapidity in Pb–Pb collisions at $\sqrt{s_{\mathrm{NN}}} = 2.76$ TeV," *Phys. Lett.* **B753** (2016) 41–56, arXiv:1507.03134 [nucl-ex].

[135] **ALICE** Collaboration, S. Acharya *et al.*, "Measurement of D^0, D^+, D^{*+} and $\mathrm{D}_{\mathrm{s}}^+$ production in Pb-Pb collisions at $\sqrt{\mathrm{s}_{\mathrm{NN}}} = 5.02$ TeV," *Submitted to: JHEP* (2018) , arXiv:1804.09083 [nucl-ex].

[136] **ALICE** Collaboration, J. Adam *et al.*, "Transverse momentum dependence of D-meson production in Pb-Pb collisions at $\sqrt{\mathrm{s}_{\mathrm{NN}}} = 2.76$ TeV," *JHEP* **03** (2016) 081, arXiv:1509.06888 [nucl-ex].

[137] **ALICE** Collaboration, J. Adam *et al.*, "Centrality dependence of high-p_T D meson suppression in Pb-Pb collisions at $\sqrt{s_{\rm NN}} = 2.76$ TeV," *JHEP* **11** (2015) 205, arXiv:1506.06604 [nucl-ex]. [Addendum: JHEP06,032(2017)].

[138] **CMS Collaboration** Collaboration, T. C. Collaboration, "D^0 meson nuclear modification factor in PbPb collisions at $\sqrt{s_{\rm NN}} = 5.02$ TeV," Tech. Rep. CMS-PAS-HIN-16-001, CERN, Geneva, 2016. http://cds.cern.ch/record/2157844.

[139] **CMS Collaboration** Collaboration, T. C. Collaboration, "Nuclear Modification Factor of prompt D^0 meson in PbPb collisions at $\sqrt{s_{\rm NN}} = 2.76$ TeV," Tech. Rep. CMS-PAS-HIN-15-005, CERN, Geneva, 2015. http://cds.cern.ch/record/2055466.

[140] **CMS Collaboration** Collaboration, T. C. Collaboration, "Studies of beauty suppression via measurements of nonprompt D0 mesons in PbPb collisions at sqrt(sNN)=5.02 TeV," Tech. Rep. CMS-PAS-HIN-16-016, CERN, Geneva, 2018. http://cds.cern.ch/record/2318338.

[141] **ALICE** Collaboration, J. Adam *et al.*, "Inclusive, prompt and non-prompt J/ψ production at mid-rapidity in Pb-Pb collisions at $\sqrt{s_{\rm NN}} = 2.76$ TeV," *JHEP* **07** (2015) 051, arXiv:1504.07151 [nucl-ex].

[142] **CMS** Collaboration, S. Chatrchyan *et al.*, "Suppression of non-prompt J/ψ, prompt J/ψ, and Y(1S) in PbPb collisions at $\sqrt{s_{NN}} = 2.76$ TeV," *JHEP* **05** (2012) 063, arXiv:1201.5069 [nucl-ex].

[143] **CMS** Collaboration, S. Chatrchyan *et al.*, "Evidence of b-Jet Quenching in PbPb Collisions at $\sqrt{s_{NN}} = 2.76$ TeV," *Phys. Rev. Lett.* **113** no. 13, (2014) 132301, arXiv:1312.4198 [nucl-ex]. [Erratum: Phys. Rev. Lett.115,no.2,029903(2015)].

[144] A. Andronic *et al.*, "Heavy-flavour and quarkonium production in the LHC era: from proton–proton to heavy-ion collisions," *Eur. Phys. J.* **C76** no. 3, (2016) 107, arXiv:1506.03981 [nucl-ex].

[145] A. Kovner, L. D. McLerran, and H. Weigert, "Gluon production from non-Abelian Weizsacker-Williams fields in nucleus-nucleus collisions," *Phys. Rev.* **D52** (1995) 6231–6237, arXiv:hep-ph/9502289 [hep-ph].

[146] D. Kharzeev, A. Krasnitz, and R. Venugopalan, "Anomalous chirality fluctuations in the initial stage of heavy ion collisions and parity odd bubbles," *Phys. Lett.* **B545** (2002) 298–306, arXiv:hep-ph/0109253 [hep-ph].

[147] B. G. Zakharov, "On the energy loss of high-energy quarks in a finite size quark - gluon plasma," *JETP Lett.* **73** (2001) 49–52, arXiv:hep-ph/0012360 [hep-ph]. [Pisma Zh. Eksp. Teor. Fiz.73,55(2001)].

[148] B. G. Zakharov, "Parton energy loss due to synchrotron-like gluon emission," *JETP Lett.* **88** (2008) 475–480, arXiv:0809.0599 [hep-ph].

[149] A. Dbeyssi, D. Al Dirani, and H. Zaraket, "Synchrotron radiation in a chromo-magnetic field," *Phys. Rev.* **D84** (2011) 105033, arXiv:1111.4968 [hep-ph].

[150] R. P. Feynman and A. R. Hibbs, *Quantum Mechanics and Path Integrals*. McGraw-Hill,New York, 1965.

[151] G. P. Lepage and S. J. Brodsky, "Exclusive Processes in Perturbative Quantum Chromodynamics," *Phys. Rev.* **D22** (1980) 2157.

[152] R. K. Ellis, W. J. Stirling, and B. R. Webber, "Qcd and collider physics," 1996.

[153] B. G. Zakharov, "Transverse spectra of radiation processes in-medium," *JETP Lett.* **70** (1999) 176–182, arXiv:hep-ph/9906536 [hep-ph].

[154] S. Peigné, F. Arleo, and R. Kolevatov, "Coherent medium-induced gluon radiation in hard forward $1 \to 1$ partonic processes," *Phys. Rev.* **D93** no. 1, (2016) 014006, arXiv:1402.1671 [hep-ph].

[155] N. N. Nikolaev and B. G. Zakharov, "The Pomeron in diffractive deep inelastic scattering," *J. Exp. Theor. Phys.* **78** (1994) 598–618. [Zh. Eksp. Teor. Fiz.105,1117(1994)].

[156] J. F. Gunion and G. Bertsch, "HADRONIZATION BY COLOR BREMSSTRAHLUNG," *Phys. Rev.* **D25** (1982) 746.

[157] U. Kakade and B. K. Patra, "Quarkonium dissociation at finite chemical potential," *Phys. Rev.* **C92** no. 2, (2015) 024901, arXiv:1503.08149 [hep-ph].

[158] E. V. Shuryak and I. Zahed, "Jet quenching in high-energy heavy ion collisions by QCD synchrotron - like radiation," *Phys. Rev.* **D67** (2003) 054025, arXiv:hep-ph/0207163 [hep-ph].

[159] O. S. Brüning, P. Collier, P. Lebrun, S. Myers, R. Ostojic, J. Poole, and P. Proudlock, *LHC Design Report*. CERN Yellow Reports: Monographs. CERN, Geneva, 2004. https://cds.cern.ch/record/782076.

[160] T. A. Collaboration, G. Aad, *et al.*, "The atlas experiment at the cern large hadron collider," *Journal of Instrumentation* **3** no. 08, (2008) S08003. http://stacks.iop.org/1748-0221/3/i=08/a=S08003.

[161] T. L. Collaboration, A. A. A. Jr, *et al.*, "The lhcb detector at the lhc," *Journal of Instrumentation* **3** no. 08, (2008) S08005. http://stacks.iop.org/1748-0221/3/i=08/a=S08005.

[162] T. C. Collaboration, S. Chatrchyan, *et al.*, "The cms experiment at the cern lhc," *Journal of Instrumentation* **3** no. 08, (2008) S08004. http://stacks.iop.org/1748-0221/3/i=08/a=S08004.

[163] T. A. Collaboration, K. Aamodt, *et al.*, "The alice experiment at the cern lhc," *Journal of Instrumentation* **3** no. 08, (2008) S08002. http://stacks.iop.org/1748-0221/3/i=08/a=S08002.

[164] J. Alme, Y. Andres, H. Appelshäuser, S. Bablok, N. Bialas, R. Bolgen, U. Bonnes, R. Bramm, P. Braun-Munzinger, R. Campagnolo, P. Christiansen, A. Dobrin, C. Engster, D. Fehlker, Y. Foka, U. Frankenfeld, J. Gaardhøje, C. Garabatos, P. Glässel, C. G. Gutierrez, P. Gros, H.-A. Gustafsson, H. Helstrup, M. Hoch, M. Ivanov, R. Janik, A. Junique, A. Kalweit, R. Keidel, S. Kniege, M. Kowalski, D. Larsen, Y. Lesenechal, P. Lenoir, N. Lindegaard, C. Lippmann, M. Mager, M. Mast, A. Matyja, M. Munkejord, L. Musa, B. Nielsen, V. Nikolic, H. Oeschler, E. Olsen, A. Oskarsson, L. Osterman, M. Pikna, A. Rehman, G. Renault,

R. Renfordt, S. Rossegger, D. Röhrich, K. Røed, M. Richter, G. Rueshmann, A. Rybicki, H. Sann, H.-R. Schmidt, M. Siska, B. Sitár, C. Soegaard, H.-K. Soltveit, D. Soyk, J. Stachel, H. Stelzer, E. Stenlund, R. Stock, P. Strmeň, I. Szarka, K. Ullaland, D. Vranic, R. Veenhof, J. Westergaard, J. Wiechula, and B. Windelband, "The alice tpc, a large 3-dimensional tracking device with fast readout for ultra-high multiplicity events," *Nuclear Instruments and Methods in Physics Research Section A: Accelerators, Spectrometers, Detectors and Associated Equipment* **622** no. 1, (2010) 316 – 367. http://www.sciencedirect.com/science/article/pii/S0168900210008910.

[165] **ALICE** Collaboration, B. B. Abelev *et al.*, "Performance of the ALICE Experiment at the CERN LHC," *Int. J. Mod. Phys.* **A29** (2014) 1430044, arXiv:1402.4476 [nucl-ex].

[166] R. Frühwirth, "Application of kalman filtering to track and vertex fitting," *Nuclear Instruments and Methods in Physics Research Section A: Accelerators, Spectrometers, Detectors and Associated Equipment* **262** no. 2, (1987) 444 – 450. http://www.sciencedirect.com/science/article/pii/0168900287908874.

[167] R. Brun and F. Rademakers, "ROOT: An object oriented data analysis framework," *Nucl. Instrum. Meth.* **A389** (1997) 81–86.

[168] ALICE Collaboration, *The ALICE Offline Bible*, 2007. http://alice-offline.web.cern.ch/sites/alice-offline.web.cern.ch/files/uploads/OfflineBible.pdf.

[169] K. Werner, F.-M. Liu, and T. Pierog, "Parton ladder splitting and the rapidity dependence of transverse momentum spectra in deuteron-gold collisions at RHIC," *Phys. Rev.* **C74** (2006) 044902, arXiv:hep-ph/0506232 [hep-ph].

[170] T. Pierog, I. Karpenko, J. M. Katzy, E. Yatsenko, and K. Werner, "EPOS LHC: Test of collective hadronization with data measured at the CERN Large Hadron Collider," *Phys. Rev.* **C92** no. 3, (2015) 034906, arXiv:1306.0121 [hep-ph].

[171] J. Alwall *et al.*, "A Standard format for Les Houches event files," *Comput. Phys. Commun.* **176** (2007) 300–304, arXiv:hep-ph/0609017 [hep-ph].

[172] T. Sjostrand, S. Mrenna, and P. Z. Skands, "A Brief Introduction to PYTHIA 8.1," *Comput. Phys. Commun.* **178** (2008) 852–867, arXiv:0710.3820 [hep-ph].

[173] **ALICE** Collaboration, B. B. Abelev *et al.*, "Measurement of visible cross sections in proton-lead collisions at $\sqrt{s_{\rm NN}} = 5.02$ TeV in van der Meer scans with the ALICE detector," *JINST* **9** no. 11, (2014) P11003, arXiv:1405.1849 [nucl-ex].

[174] **ALICE Collaboration** Collaboration, "ALICE luminosity determination for pp collisions at $\sqrt{s} = 5$ TeV,". https://cds.cern.ch/record/2202638.

[175] DPG., "Event selection and properties.." Twiki page. https://twiki.cern.ch/twiki/bin/view/ALICE/AliDPGtoolsEventProp.

[176] J. Montejo Berlingen, *Reconstruction of Physics Objects*, pp. 61–85. Springer International Publishing, Cham, 2016. https://doi.org/10.1007/978-3-319-41051-7_4.

[177] **CMS** Collaboration, S. Chatrchyan *et al.*, "Identification of b-quark jets with the CMS experiment," *JINST* **8** (2013) P04013, arXiv:1211.4462 [hep-ex].

[178] **D0** Collaboration, V. M. Abazov *et al.*, "b-Jet Identification in the D0 Experiment," *Nucl. Instrum. Meth.* **A620** (2010) 490–517, arXiv:1002.4224 [hep-ex].

[179] S. Sakai, "Measurement of heavy-flavour jets via electrons from heavy-flavour hadron decays in p-Pb at $\sqrt{s_{\rm NN}} = 5.02$ TeV," Analysis Note ANA-842, ALICE Collaboration, 2018. https://alice-notes.web.cern.ch/node/842.

[180] **ALICE** Collaboration, G. Eyyubova and L. Kramárik, "Performance of the ALICE secondary vertex b-tagging algorithm," *EPJ Web Conf.* **126** (2016) 05004, arXiv:1605.00143 [physics.ins-det].

[181] **CMS** Collaboration, S. Chatrchyan *et al.*, "Measurement of the underlying event activity in pp collisions at $\sqrt{s} = 0.9$ and 7 TeV with the novel jet-area/median approach," *JHEP* **08** (2012) 130, arXiv:1207.2392 [hep-ex].

[182] **ALICE** Collaboration, B. Abelev *et al.*, "Measurement of Event Background Fluctuations for Charged Particle Jet Reconstruction in Pb-Pb collisions at $\sqrt{s_{NN}} = 2.76$ TeV," *JHEP* **03** (2012) 053, arXiv:1201.2423 [hep-ex].

[183] W. Verkerke and D. Kirkby, *RooFit Users Manual*, v2.91 ed., Oct., 2008. https://root.cern.ch/download/doc/RooFit_Users_Manual_2.91-33.pdf.

[184] A. Hocker and V. Kartvelishvili, "SVD approach to data unfolding," *Nucl. Instrum. Meth.* **A372** (1996) 469–481, arXiv:hep-ph/9509307 [hep-ph].

[185] G. D'Agostini, "Bayesian inference in processing experimental data: principles and basic applications," *Reports on Progress in Physics* **66** (Sept., 2003) 1383–1419, physics/0304102.

[186] T. Adye, "Unfolding algorithms and tests using RooUnfold," in *Proceedings, PHYSTAT 2011 Workshop on Statistical Issues Related to Discovery Claims in Search Experiments and Unfolding, CERN,Geneva, Switzerland 17-20 January 2011*, pp. 313–318, CERN. CERN, Geneva, 2011. arXiv:1105.1160 [physics.data-an].

[187] F. James and M. Roos, "Minuit: A System for Function Minimization and Analysis of the Parameter Errors and Correlations," *Comput. Phys. Commun.* **10** (1975) 343–367.

[188] E. Epple and J. Mulligan, "Inclusive full jet measurements in pp collisions at $\sqrt{s} = 5.02$ TeV with ALICE," Analysis note ANA-852, ALICE Collaboration, 2018. https://alice-notes.web.cern.ch/node/852.

[189] A. P. Mohanty, "D0-tagged jets in pp collisions at 5.02 TeV," Analysis Note ANA-840, ALICE Collaboration, 2018. https://alice-notes.web.cern.ch/node/840.

[190] S. Aiola, F. F. Colamaria, A. Rossi, A. C. O. da Silva, B. A. Trzeciak, and A. Mohanty, "D-tagged jets in p-Pb collisions at 5.02 TeV," Analysis Note ANA-784, ALICE Collaboration, 2018. https://alice-notes.web.cern.ch/node/784.

[191] R. Haake, "Measurement of charged jet production in minimum bias p-Pb collisions at $/sqrts_{\rm NN} = 5.02$ TeV," Analysis Note ANA-178, ALICE Collaboration, 2015. https://alice-notes.web.cern.ch/node/178.

[192] A. Zimmermann and J. Stachel, *Production of strange hadrons in charged jets in Pb–Pb collisions measured with ALICE at the LHC*. PhD thesis, Oct, 2016. https://cds.cern.ch/record/2235461. Presented 26 Oct 2016.

[193] V. Kucera, J. Bielčíková, and C. Kuhn, *Study of strange particle production in jets with the ALICE experiment at the LHC*. PhD thesis, Aug, 2016. https://cds.cern.ch/record/2239143. Presented 15 Nov 2016.

[194] J. Podolanski and R. Armenteros, "Iii. analysis of v-events," *The London, Edinburgh, and Dublin Philosophical Magazine and Journal of Science* **45** no. 360, (1954) 13–30, https://doi.org/10.1080/14786440108520416. https://doi.org/10.1080/14786440108520416.

[195] **ALICE** Collaboration, S. Acharya *et al.*, "Neutral pion and η meson production in p-Pb collisions at $\sqrt{s_{\rm NN}} = 5.02$ TeV," *Eur. Phys. J.* **C78** no. 8, (2018) 624, arXiv:1801.07051 [nucl-ex].

[196] S. Dulat, T.-J. Hou, J. Gao, M. Guzzi, J. Huston, P. Nadolsky, J. Pumplin, C. Schmidt, D. Stump, and C. P. Yuan, "New parton distribution functions from a global analysis of quantum chromodynamics," *Phys. Rev.* **D93** no. 3, (2016) 033006, arXiv:1506.07443 [hep-ph].

[197] K. J. Eskola, P. Paakkinen, H. Paukkunen, and C. A. Salgado, "EPPS16: Nuclear parton distributions with LHC data," *Eur. Phys. J.* **C77** no. 3, (2017) 163, arXiv:1612.05741 [hep-ph].

[198] **ALICE** Collaboration, J. Adam *et al.*, "Measurement of charged jet production cross sections and nuclear modification in p-Pb collisions at $\sqrt{s_{NN}} = 5.02$ TeV," *Phys. Lett.* **B749** (2015) 68–81, arXiv:1503.00681 [nucl-ex].

[199] T. Stavreva, F. Arleo, and I. Schienbein, "Prompt photon in association with a heavy-quark jet in Pb-Pb collisions at the LHC," *JHEP* **02** (2013) 072, arXiv:1211.6744 [hep-ph].

[200] Z. Citron *et al.*, "Future physics opportunities for high-density QCD at the LHC with heavy-ion and proton beams," 2018. arXiv:1812.06772 [hep-ph].

[201] **ALICE** Collaboration, J. Adam *et al.*, "Azimuthal anisotropy of charged jet production in $\sqrt{s_{\rm NN}} = 2.76$ TeV Pb-Pb collisions," *Phys. Lett.* **B753** (2016) 511–525, arXiv:1509.07334 [nucl-ex].

[202] I. Burmeister, R. Klingenberg, and J. Albrecht, *Measuring the b-tagging efficiency in ATLAS data at $\sqrt{s} = 8$ TeV and $\sqrt{s} = 13$ TeV using the $p_{\rm T}^{\rm rel}$-method*. PhD thesis, 2017. https://cds.cern.ch/record/2631518. Presented on 2017.

[203] M. Cacciari, M. Greco, and P. Nason, "The P(T) spectrum in heavy flavor hadroproduction," *JHEP* **05** (1998) 007, arXiv:hep-ph/9803400 [hep-ph].

[204] L. Feldkamp, "Statistical reconstruction of beauty jets in proton-proton collisions 7 TeV using track impact paramet," Analysis Note ANA-747, ALICE Collaboration, 2018. https://alice-notes.web.cern.ch/node/747.